ALMA MATER STUDIORUM
UNIVERSITÀ DI BOLOGNA

DOTTORATO DI RICERCA IN

NANOSCIENZE PER LA MEDICINA E PER L'AMBIENTE

Ciclo 36

Settore Concorsuale: 02/B1 - FISICA SPERIMENTALE DELLA MATERIA

Settore Scientifico Disciplinare: FIS/03 - FISICA DELLA MATERIA

ORGANIC MIXED IONIC-ELECTRONIC CONDUCTORS FOR BIOELECTRONIC INTERFACES

Presentata da: Filippo Bonafè

Coordinatore Dottorato

Matteo Calvaresi

Supervisore

Beatrice Fraboni

Co-supervisore

Tobias Cramer

Esame finale anno 2024

Abstract

Using electrical signals to interact with biological systems has shed light on different fundamental signaling principles of living organisms, leading to the development of a broad spectrum of healthcare devices. However, conventional (inorganic) electronic materials significantly differ from living matter in critical aspects including mechanical rigidity, three-dimensional structure, and predominant electronic conductivity. For these reasons, due to their "soft" nature, biocompatibility, and ability to conduct ions in addition to electrons and holes, organic materials with mixed ionic and electronic conductivity (OMIECs) have emerged in recent years as a promising material platform for new and highly efficient interfaces with biology. Faster and significative progresses in organic bioelectronics are predicated on a comprehension of fundamental material processes and their relation to device functionality, but the mixed conductivity renders the experimental characterization of ionic or electronic carrier transport difficult as both are intrinsically entangled. The objective of this thesis is to investigate these phenomena and exploit the resulting knowledge to develop optimized bioelectronic applications. The experimental work required different methods, ranging from the design and microfabrication of micro-structured devices to electrical and electrochemical analyses, including the development of novel operando characterization techniques for organic mixed conductors. We introduced the electrolyte-gated van der Pauw's method for the characterization of electronic transport in OMIEC materials, allowing for a simple and accurate determination of the electronic mobility and threshold voltage; and we demonstrated that contact resistance effects complicate the interpretation of organic electrochemical transistor (OECT) characteristics. We developed the modulated electrochemical atomic force microscopy (mEC-AFM) to monitor fast local ion exchange processes causing electroactuation in OMIECs. By combining multidimensional spectroscopies studying the mechanical deformations resulting from charge injection with multichannel imaging, we revealed the dynamics of the drift transport of hydrated ions in OMIEC layers operating at liquid interfaces. We then extended mEC-AFM to a depth-sensitive technique to acquire subsurface profiles of ion migration and swelling in OMIEC thin films, revealing the spatiotemporal dynamics of electroactuation in the electroactive polymer bulk for different film morphologies and redox states. We finally studied OMIEC applications in bioelectronic devices, including the microfabrication and characterization of flexible microelectrode arrays for *in-vivo* neural recording and stimulation, and the realization of impedance sensors for *in-vitro* cell adhesion experiments. In this contest, we investigated the AC amplification properties of organic electrochemical transistors, and we developed a model experiment to optimize biosensors reaching the single cell resolution limit. The quantitative findings obtained in his work are expected to contribute to the development of enhanced organic bioelectronics interfaces for future healthcare, biomedicine, and biosensing devices.

Table of Contents

List of Acronyms

AFM - Atomic Force Microscopy
AP - Action Potential
CE - Counter Electrode
CEA - Conductivity Enhancing Agents
CNS – Central Nervous System
CP - Conjugated Polymer
CSC_c - Cathodic Charge Storage Capacity
CV - Cyclovoltammetry
DBS - dodecylbenzene sulfonate
DBSA – dodecylbenzene sulfonate acid
DOS - Density of States
EC-AFM - Electrochemical Atomic Force Microscopy
ECF - Extracellular Fluid
ECoG – Electrocorticography
EEG – Electroencephalography
EG - Ethylene Glycol
EgVDP – Electrolyte-gated Van der Pauw
EIS - Electrochemical Impedance Spectroscopy
FET - Field-Effect Transistor
gFPP - gated Four Point Probe
GOPS - 3-glycidoxypropyltrimethoxysilane
GSA - Geometric Surface Area
HOMO - Highest Occupied Molecular Orbital
LFP - Local Field Potential
LUMO - Lowest Unoccupied Molecular Orbital
MEA - Microelectrode Array
mEC-AFM - modulated Electrochemical Atomic Force Microscopy
MOSFET- Metal-Oxide-Semiconductor Field-Effect Transistor
OECT - Organic Electrochemical Transistor
OMIEC - Organic Mixed Ionic-Electronic Conductor
p(g2T-TT) - poly(2-(3,3 -bis(2-(2-(2-methoxyethoxy)ethoxy)ethoxy)-[2,2 -bithiophen]- 5-yl)thieno[3,2-b]thiophene)
PAc - Polyacetylene
PBS - Phosphate-Buffered Saline
PDMS - Polydimethylsiloxane
PEDOT - Poly(3,4-ethylenedioxythiophene)
PEEK - Polyether Ether Ketone
PEN - Polyethylene Naphthalate

Ppy – Polypyrrole
PSPD - Position Sensitive Photodetector
PSS - Polystyrene Sulfonate
RE - Reference Electrode
SMU - Source-Measure Unit
SNR - Signal-to-Noise Ratio
TLM - transmission line model
VDP - van der Pauw
WE - Working Electrode

1 Introduction

Ever since the mid-1750s when Galvani documented the electrical stimulation of frog legs, we have known that human-made, conducting materials can be used to stimulate bioelectrical signals and generate physiological responses.[1] Experiments with electricity and living tissues have not only shed light on the workings of the brain and provided a deeper understanding about how cells communicate with each other and with their environment, but also led to the development of implantable electronic devices such as the cardiac pacemaker and the cochlear implant.[2] However, current bioelectronics realizations are limited by the materials which act as the biotic/abiotic interface. Differently from conventional electronics, which is based on electron conduction, bioelectrical signals in living organisms predominantly consist of the movements of ionic species (currents) and local differences in ion concentrations (potentials). Furthermore, conventional (inorganic) electronic materials significantly differ from living matter in critical aspects including mechanical rigidity, three-dimensional structure, and exposed functional groups at the interface.[3] For these reasons, due to their "soft" nature and ability to conduct ions in addition to electrons and holes, organic materials with mixed ionic and electronic conductivity (OMIECs) have risen up in recent years as a promising material platform for new and highly efficient interfaces with biology.[4]
Since their first introduction in the late 1980s,[5] research on OMIEC materials has led to key advancements in a host of technological developments ranging from sensing, actuation and computation to energy harvesting/storage, and information transfer. OMIECs multifunctional properties arise from their ability to simultaneously participate in redox reactions and modulate the ionic and electronic charge density throughout the bulk of the material.[6] Owing to ionic and electronic interactions and coupled transport properties, OMIECs demand special understanding beyond the knowledge derived from the study of organic thin films and membranes meant to support either electronic or ionic processes only, motivating fundamental research.[7]

This thesis explores the potential of organic mixed ionic-electronic conductors (OMIECs) for bioelectronic interfaces. The research project is structured into two main phases. First, I investigated fundamental processes governing OMIEC behavior, seeking a quantitative understanding of charge transport properties and their connection to material functionality. The resulting knowledge served as conceptual basis for the second phase, regarding the development, modeling, and optimization of bioelectronic devices based on OMIEC materials.
The first thesis chapter provides a general introduction on the state of the art of organic bioelectronics research. The attention is initially focused on the physicochemical properties and charge transport processes occurring in organic mixed conductors. Then, the second section introduces the concept of bioelectronic interface, and some promising applications of OMIEC materials in organic bioelectronics are thoroughly discussed.
The second chapter focusses in detail on the open research issues specifically addressed by this work.

The third chapter describes the adopted experimental methods, starting from the fabrication techniques used to realize micro-structured OMIEC-based devices, which involve photolithography procedures to fabricate micropatterned electrodes and transistors. Then, the experimental techniques employed to study material and device properties are introduced, including electrical, electrochemical, and atomic force microscopy characterizations.
The fourth chapter presents the main experimental results of this thesis. The first section introduces the electrolyte-gated van der Pauw's method for the contact-independent characterization of electronic transport in OMIEC materials, allowing for a simple and accurate determination of the electronic mobility and threshold voltage in poly(3,4-ethylenedioxythiophene):poly(styrenesulfonate) (PEDOT:PSS) thin films. The second section introduces the modulated electrochemical atomic force microscopy (mEC-AFM) to monitor fast local ion exchange processes causing electroactuation in OMIECs, and to provide maps of local electroswelling in PEDOT:PSS through multichannel imaging. In the third section, mEC-AFM is exploited as a depth-sensitive technique on polypyrrole doped with dodecylbenzenesulfonate (Ppy:DBS) to acquire subsurface profiles of ion migration and swelling, revealing the spatiotemporal dynamics of electroactuation in the electroactive polymer bulk for different film morphologies and redox states. The last two subchapters deal with applications of OMIEC materials in bioelectronic devices. The fourth section presents the microfabrication and characterization of flexible microelectrode arrays (MEAs) based on PEDOT:PSS for *in-vivo* neural recording and stimulation of electrocorticography (ECoG) activity. In the fifth section, organic electrochemical transistors (OECTs) based on PEDOT:PSS are used as impedance sensors for *in-vitro* cell adhesion experiments, and the ultimate limit of single cell resolution is achieved through the rational optimization of biosensors guided by a model experiment.

1.1 Organic mixed ionic-electronic conductors

OMIECs are soft electrical (semi-)conductors that transport mobile ionic species. At first, electronically conducting polymers and ionically conducting polymers were developed separately. Electronically conducting polypyrrole was discovered in 1963,[8] but the field of conjugated polymers (CPs – see **1.3.1**) has been widely explored only after the discovery of conducting polyacetylene in 1977.[9] Around roughly the same time, poly(ethylene oxide) (PEO) was found to be capable of dissolving salts and displaying significant ion conduction.[10] Despite both systems were very quickly recognized as promising for electrochemical applications, for many OMIECs their ion conducting properties were inadvertent and overlooked as the focus was often purely on their electrical properties.[7] For instance, the most widely studied mixed conductor, poly(3,4-ethylenedioxythiophene):poly(styrenesulfonate) (PEDOT:PSS) was developed as an antistatic coating and as a hole-conducting interlayer in optoelectronic devices, neither of which require ionic conductivity.[11] Many other OMIECs were the product of investigations into water soluble conjugated polymers allowing the fabrication of all-solution-processed organic optoelectronic devices.[12] Organic mixed ionic-electronic conductors were

explicitly recognized and studied beginning in the late 1980s as potential battery electrodes,[5] but after that a robust field of material formulations has emerged. Modern tools in organic chemistry offer multiple means to design the molecular backbone, side chains, and other additives, resulting in an almost infinite design space for the corresponding materials properties, including energy levels, electronic and ionic conductivity, optical, volume, and moduli.[6] Additionally, one or more of these properties can be modified during device operation, thereby transducing an input (e.g., ionic) into an output (e.g., electronic), allowing OMIECs to be used for a variety of applications (**Figure 1.1**) including actuators,[13] light-emitting electrochemical cells,[14] batteries and supercapacitors,[15] chemical sensors,[16] sensing and stimulating bioelectronic probes,[17] ion pumps,[18] and organic electrochemical transistors for sensing, circuits and neuromorphic computing.[19,20]

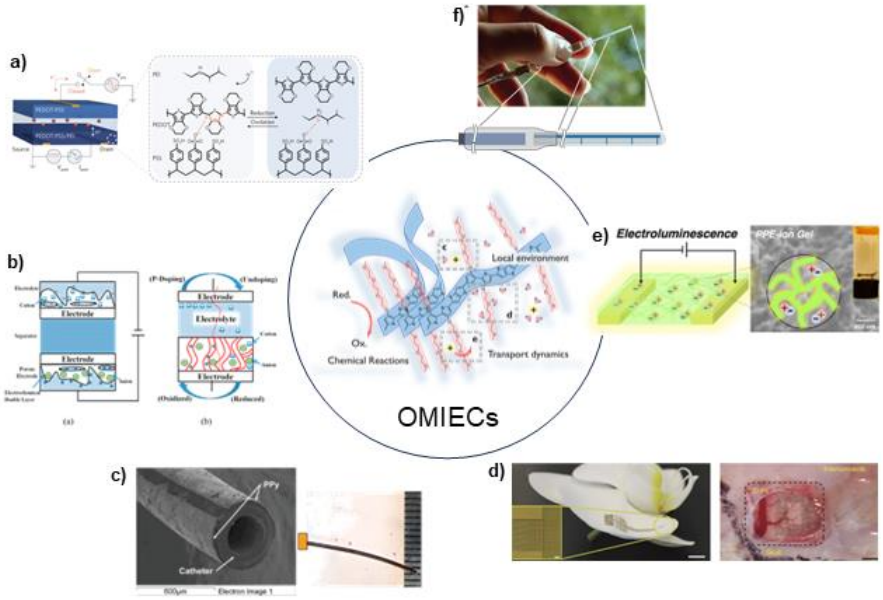

Figure 1.1: Application of OMIECs in current material research. Central figure: schematics of a typical OMIEC structure. **a)** Organic electrochemical transistor for neuromorphic computing.[20] **b)** Electrochemical supercapacitor for energy storage.[15] c) Soft actuator for self-motile bioelectronics devices.[13] **d)** Neural recording and stimulation probes.[17] **e)** Light-emitting electrochemical cells.[14] **f)** Organic electrochemical ion pump for selective drug delivery.[18]

The variation of material properties in OMIEC devices is always connected to the modulation in electronic and ionic charge density. The large variation in charge density impact on electron energy levels, electronic and ionic transport, volumetric capacitance, free volume, optical bandgap, and modulus. Controlled changes in the OMIEC material properties occur throughout the bulk of the material and can be induced by both dynamic external stimuli and (static) structural design (**Figure 1.2**).[6] This enables new design parameters that were previously untouched in traditional electronic devices where typically material property modulation occurs at interfaces (for example field effect).

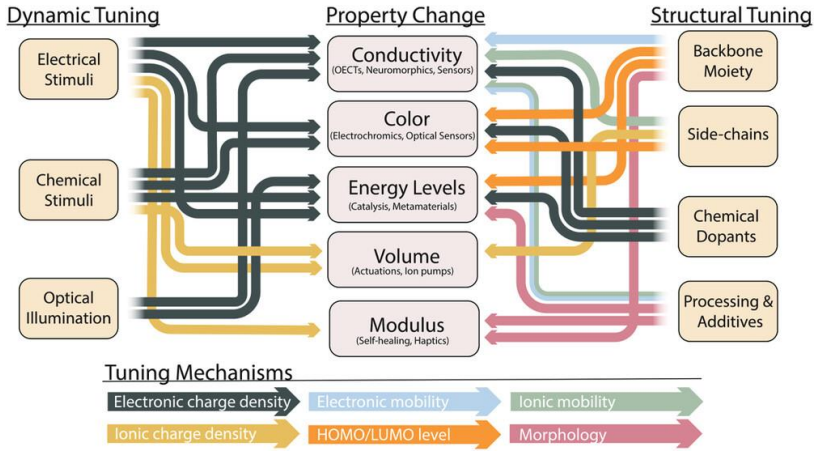

Figure 1.2: Multifunctional property tuning in OMIEC materials. Various device relevant properties can be tuned both by dynamical stimuli and by (static) structural design. For example, controlling the electrical potential applied to a device can dynamically modify the conductivity of an OMIEC material by modifying its charge carrier density (top left). At the same time, the material conductivity can be changed by substituting various backbone components into the OMIEC structure (top right). Similar associations are depicted for a wide range of properties, while the corresponding mechanisms through which these properties are controlled are illustrated at the bottom of the diagram. [6]

1.2 Types and structures of OMIEC materials

Organic mixed ionic-electronic conductors combine properties of conjugated polymers, polymer electrolytes, and polyelectrolytes to simultaneously transport and couple ionic and electronic charges.[7] The most common solid polymer electrolytes leverage periodically repeating ether oxygen groups to coordinate and solvate cations (like polyethylene oxide (PEO) in **Figure 1.3a**), while anions are present but unsolvated.[21] Alternatively, in polyelectrolytes such as poly(styrene sulfonate) (PSS) (**Figure 1.3b**) the polymer is a component of the salt itself, paired with charge-balancing counterions.

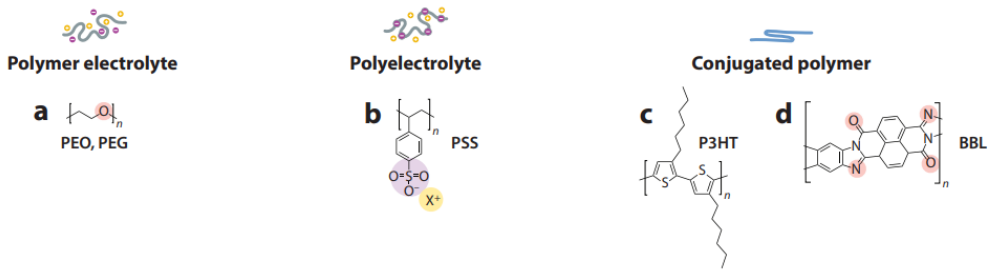

Figure 1.3: Chemical structures of representative polymer electrolytes **(a)**, polyelectrolytes **(b)**, and conjugated polymers **(c, d)**.

On the other hand, electron conductive conjugated polymers (CPs) have low dielectric constants, lack of (a high density of) ion coordinating functional groups, and often contain long nonpolar alkyl side chains (**Figure 1.3c**) and thus do not readily dissolve most salts. In OMIECs, such limitation is overcome via the incorporation of either polyelectrolytes or

polymer electrolytes. This structural difference naturally distinguishes OMIECs into two categories, those intrinsically containing ionic charge carriers **(Figure 1.4 - I, III and V**), and those which do not (**Figure 1.4 - II, IV and VI**). Ionic charge-bearing OMIECs contain a stable ionic moiety that is either accompanied by a counterbalancing ion, exists as a self-balanced zwitter ion,[22] or stabilizes an electronic charge on a conjugated segment, acting as a dopant for the (semi)conducting CP. Alternatively, there exist OMIECs that themselves are not intrinsically charged, yet contain polar polymer electrolytes that can solvate ions. In such non-charged OMIECs the ionic species are incorporated physically during deposition or from contact with an electrolyte.

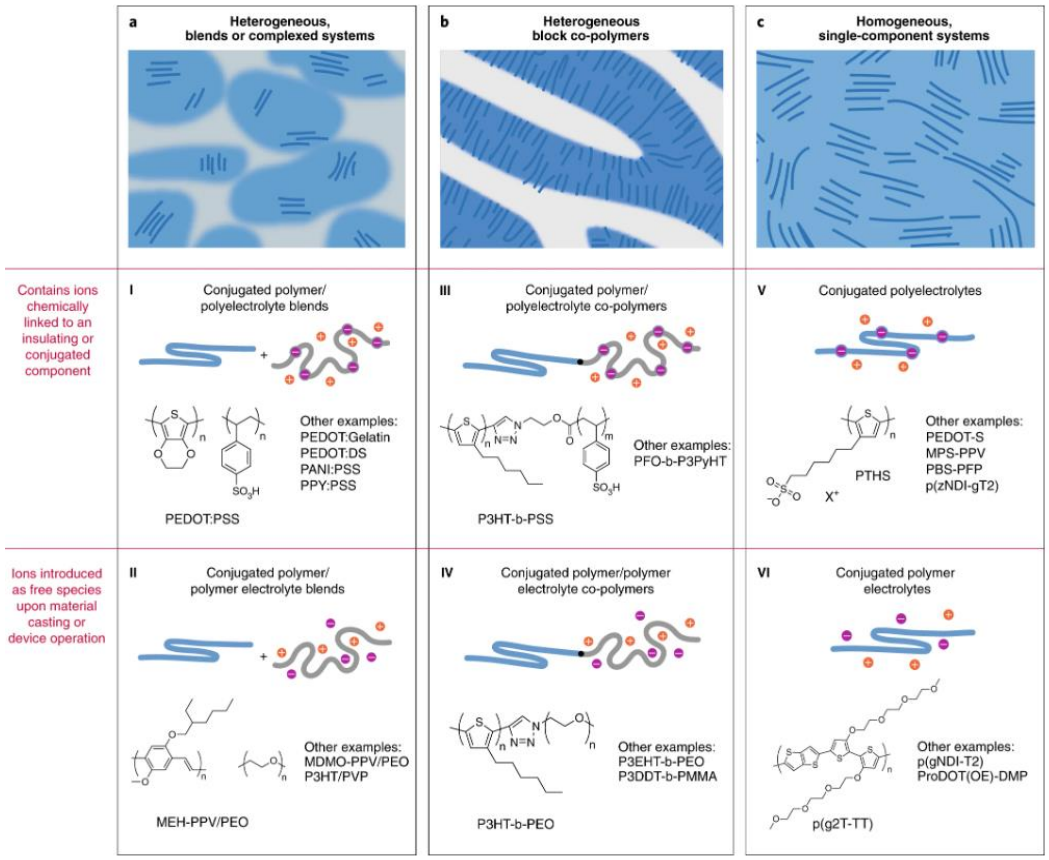

Figure 1.4: OMIECs material classes. **a)** Heterogeneous blends of an electronically conducting conjugated polymer with (I) an ionic charge bearing polyelectrolyte or (II) an ion solvating polymer electrolyte. **b)** Heterogeneous block copolymers of an electronically conducting conjugated polymer with (III) an ionic charge bearing polyelectrolyte or (IV) an ion solvating polymer electrolyte. **c)** Fully conjugated (V) ionic charge bearing polyelectrolytes and (VI) ion solvating polymer electrolytes. Conceptual sketches (grey, ionic transport component; blue, electronic transport component; orange, cations; magenta, anions) and example chemical structures and selected examples are reported for type I, II, III, IV, V, and VI OMIECs.[7]

The second useful categorization is between heterogeneous (**Figure 1.4 a,b**) and homogeneous OMIECs (**Figure 1.4 c**). In the second case, mixed transport occurs concurrently throughout a single material, while in the first regions of predominantly ion conducting material and regions of predominantly electronic conducting material coexist as separated phases.[23]

Evaluating OMIECs based on these two categories gives rise to a taxonomy containing (at least) six types of OMIEC **(Figure 1.4**):

Type I and II: heterogeneous blends or complexes of an electrically conducting π-conjugated polymer and an ionically conducting polyelectrolyte (Type I) or a solid polymer electrolyte (Type II) (**Figure 1.4 a**). Type I OMIECs include PEDOT:PSS, which represents a prototypical OMIEC material.[11] Alone, PEDOT has poor water solubility, so to produce dispersible suspensions it must be polymerized onto a polymer acid template, most commonly polystyrene sulfonic acid (PSS). Given its central role in this thesis work, the main properties of PEDOT:PSS are discussed in detail in **Sect. 1.6**. Other PEDOT blends were developed using several polyelectrolytes, including tosylate[24] or dextran sulphate[25], and other CPs have been templated on PSS[26] to produce type I OMIEC materials. On the other hand, CPs incorporated in type II OMIECs are obtained by traditional polymerization/synthetic techniques and require sufficient solubility to be deposited with a polymer electrolyte producing phase separated bicontinuous microstructures.[27] Both types I and II represent composites of predominately electronic and ionic conducting materials that phase separate into mostly ionic and electronic conducting phases, but frequently feature impure phases and can be largely disordered on multiple length scales.

Type III and IV: heterogeneous block co-polymers based on single macromolecules that contain a distinct ionic and electronic conducting segment (**Figure 1.4 b**). These block OMIECs contain a π-conjugated segment covalently tethered to a fixed ionic charge bearing segment (type III) or a polar ion solvating segment (Type IV). Thermodynamics drives the phase separation of the segments on length scales determined by the segment lengths.[28] By tuning relative segment/block size and processing conditions, a wide variety of defined structures are achievable, including spherical, cylindrical, lamellar and gyroid phases.[29] Given mesoscale morphological disorder, such structures should provide extended, interconnected domains for separated ionic and electronic transport.

Type V and VI: homogeneous OMIECs where there is no microphase separation between ion conducting and π-conjugated components (**Figure 1.4 c**). The distribution of ion solvating moieties along their entire molecular structure produces a single mixed conducting phase. Charged Type V OMIECs typically contain pendant ion sidechains, while polar Type VI OMIECs often contain ether oxygens incorporated into the repeat units or side chains. Single-component OMIECs share the most in common with traditional CPs, though with added functionality that improves ion miscibility even in the absence of solvent swelling. While Type V conjugated polyelectrolytes including sulfonate bearing poly alkylthiophenes[30] and poly ethylenedioxythiophenes[31] have been widely investigated, conjugated polymer electrolytes (Type VI) represent a recent addition to the OMIECs field, but they have rapidly demonstrated both hole (p-type)[32] and electron (n-type)[33] transport using proven backbone motifs with oligo ethylene glycol side chain.

Despite the wide variety of OMIEC material types and their diverse properties and figures of merit in OMIEC-based devices, all of them have in common three fundamental physical processes occurring throughout the bulk and interfaces of the material: electronic transport, ionic transport, and ionic–electronic coupling. For example, energy storage in Type IV OMIEC-based batteries and capacitors depends on the strength of ionic–electronic coupling, whereas the available power and charging rates are often limited by the rate of ion transport.[34] Light-emitting electrochemical cells using Type V OMIEC blends cannot turn on until ions have migrated to form dopant gradients or junctions.[27] The magnitude of ionic–electronic coupling in Type I blends determines the optical absorbance changes in electrochromics,[35] swelling induced strain in actuators and artificial muscles,[36] and the number of states accessible in neuromorphic devices.[37] Ion transport and ionic–electronic coupling together determine the time constants that limit frequency bandwidth and response time of Type I and Type VI OMIEC sensors,[38] and affect the amplification gain of active electrolyte-gated transistors.[39] Given the primary relevance and complex interplay, the three fundamental processes underlying OMIECs behavior are discussed in details in the following paragraphs.

1.3 Electronic transport in OMIECs

1.3.1 Conjugated Polymers

The electronic structure hosting mobile electronic charge carriers in OMIECs is achieved through conjugated π-orbitals present along a polymer backbone or along an ordered stack of planar molecules. Chemical conjugation arises from the different types of bonds that carbon atoms can make in organic molecules. These depend on the structure of carbon atomic orbitals, which can superimpose to form hybrid orbitals and reduce the total energy with respect to the original configuration.[40] Depending on the number of orbitals involved in the hybridization process, carbon can have hybridization sp^3, sp^3 or sp (**Figure 1.5**).[41]

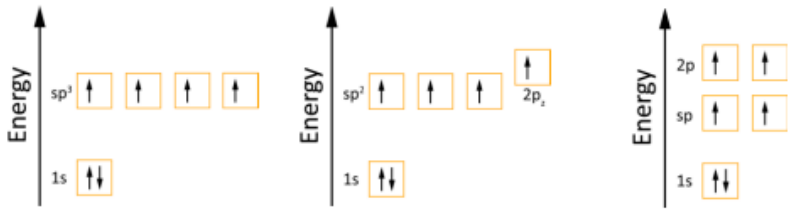

Figure 1.5: Electronic configuration of hybrid orbitals in a carbon atom. [41]

Consequently, depending on its hybridization, carbon will be able to form four, three or two covalent bonds with a corresponding number of atoms, and the resulting molecular orbitals will arrange as far as possible to minimize the electronic repulsion. When the two atomic orbitals overlap on the line joining the two nuclei, the resulting molecular orbital is called sigma (σ bond). Carbon atoms form σ bonds with hybrid orbitals. When the overlapping between the two atomic orbitals occurs perpendicularly with respect to the line joining the nuclei, the formed

molecular orbital is called pi (π bond). Carbon atoms form π bonds with p orbitals. For example, in the molecule of ethylene **(Figure 1.6a**) σ bonds are formed between carbon ad hydrogen, while two carbon atoms are bonded together by a σ bond and a π bond.[42] The C=C distance in ethylene (1.34 Å) is lower with respect to the C-C distance in ethane (1.55 Å), as the double bond held the two atoms more closely than the single bond.[43] The linear combination of atomic orbitals (LCAO) method predicts that two molecular orbitals will be formed for each bond: a bonding orbital, having low energy, and an antibonding orbital. From the scheme in **Figure 1.6b**, we identify the π bonding orbital as the highest occupied molecular orbital (HOMO) and the π^* antibonding orbital as lowest unoccupied molecular orbital (LUMO).

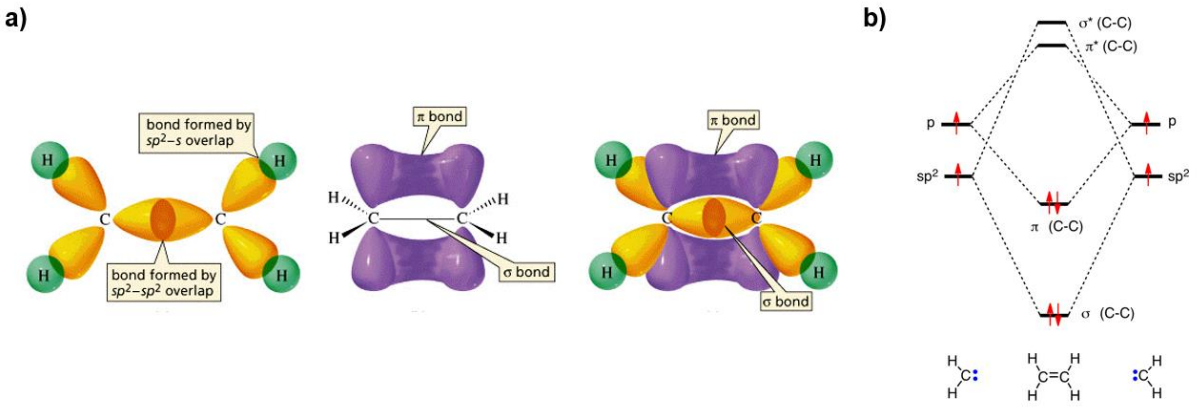

Figure 1.6: **a)** Representation of the electronic structure of the ethylene molecule,[42] and corresponding molecular orbital **(b)**.

Conjugated polymers repeat the electronic structure of the ethylene molecule on a larger scale. Each carbon atom on the polymer backbone forms three σ-bonds with neighboring atoms, while the remaining p orbitals overlap with successive atom orbitals engaging a π system, which originate electronic delocalization and therefore conductivity. The simplest model of electrical conductivity in conjugated polymers is polyacetylene (PAc, with molecular formula $[-C_2H_2]_n$), reported in **Figure 1.7a**. PAc molecule can be modeled with a linear chain, constituted by *N* atoms separated by distance *d*. The total length of the chain will be *(N-1)*d*, which can be approximated with *N*d* if *N* tends to infinite. If we assume π electrons completely delocalized, we can apply the quantum mechanical model for a free particle in a one-dimensional box (with zero potential inside the box, which corresponds to the polymeric backbone, and infinite outside). The wave functions correspond to a set of eigenvalues:[44]

$$E_n = \frac{n^2 h^2}{8m(Nd)^2} \qquad 1.1$$

where *h* is the Planck's constant, *m* the electron mass and *n* a quantum number (n = 1,2,3…). If every orbital is occupied by two electrons with opposite spin, the energies of the HOMO and LUMO levels are

$$E_{HOMO} = \frac{\left(\frac{N}{2}\right)^2 h^2}{8m(Nd)^2}; \quad E_{LUMO} = \frac{\left(\frac{N}{2}+1\right)^2 h^2}{8m(Nd)^2} \qquad 1.2$$

and the energy required to excite an electron from HOMO to LUMO is

$$\Delta E = E_{LUMO} - E_{HOMO} = \frac{(N+1)h^2}{8m(Nd)^2} \approx \frac{h^2}{8mNd^2} \qquad 1.3$$

which tends to zero if *N* tends to infinite. According to this model, macroscopic conjugated polymers should behave as conductors, but experimentally their bandgap does not decrease as in **Eq. 1.3**. The discrepancy between theory and experiments was explained in the 1930s using Peierls' theorem, which states that a one-dimensional and equally spaced atomic chain is unstable.[45] Such instability is solved through a chain distortion which reduces the system symmetry and consequently rearranges the levels of the orbitals. The distortion of the lattice leads to a repeated unit with two carbon atoms closer together and two other carbon atoms more distant, and the resulting conjugated structure alternates single (σ) and double (π) bonds along the polymeric backbone. Consequently, energy gap (E_g) appears between the HOMO and LUMO levels. At the same time, an increase of the length of the conjugated chain leads to an increase of atomic orbitals with slightly dissimilar energy overlapping to form molecular orbitals. The resulting broadening of the energy levels of the frontier orbitals results into the formation of π (filled) and π* (empty) bands **(Figure 1.7a)**,[46] and the conductivity of PAc depends on the concentration of thermal carriers and is limited to 10^{-7}-10^{-5} S/m

1.3.2 Effect of disorder on electronic transport

As result of spatial disorder, conjugated polymers do not have flat energy bands, as exhibited in **Figure 1.7a**. Typically, the distribution of energy levels in HOMO and LUMO bands is approximated by a Gaussian function:

$$g(E) = \frac{N_0}{\sigma_{DOS}\sqrt{2\pi}} exp\left[\frac{-(E-E_0)^2}{2\sigma_{DOS}^2}\right] \qquad 1.4$$

where *g(E)* is the density of states (DOS) as function of energy, N_0 is the total number of states including spin degeneracy per unit volume, σ_{DOS} is the width of the Gaussian DOS, *E* is the energy level of an individual state, and E_0 is the mean energy of all states (energy at the center of the DOS).[47]

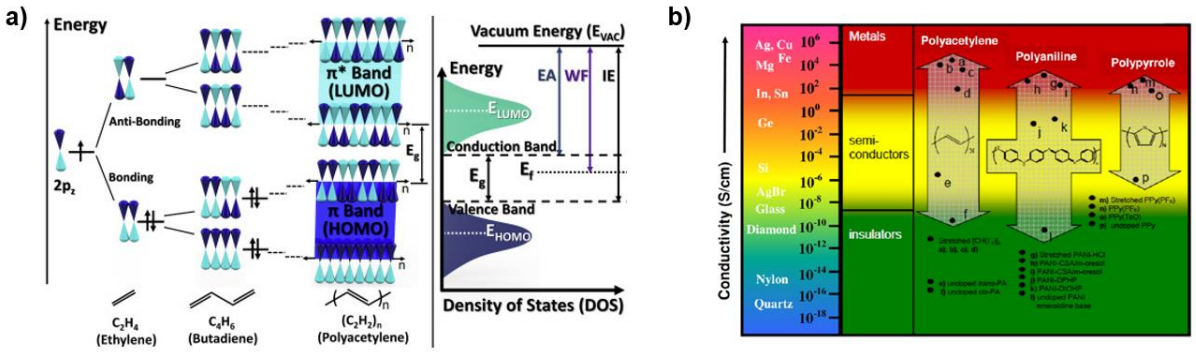

Figure 1.7: Conjugated polymers are organic semiconductors. **a)** Electronic structure of conjugated polymers. Increasing the number of carbon atoms on the polymer backbone reduces the energy gap between HOMO and LUMO levels, but Peierls' distortions in Polyacetylene split the energy levels to π (filled) and π* (empty) bands. The band gap (E_g), Fermi level (E_f), vacuum level energy (E_{VAC}), work function (*WF*), ionization energy (*IE*), and electron affinity (*EA*) can be defined accordingly.[46] **b)** Electrical conductivity in conjugated polymers, reaching high values for high doping levels.

1.3.3 Doping of conjugated polymers

Since there are no partially full bands, pure conjugated polymers are typically semiconductors, with low conductivity. As the energy gap depends on the molecular structure of the repeated unit, it is possible to control it during the synthesis phase through molecular level design. Beside this possibility, other methods are available to increase the conductivity of the conjugated polymer in a successive phase (but always before deposition), which are called doping methods and essentially represent a charge transfer reaction which involves the partial oxidation or reduction of the polymer. The successful doping of conjugated polymers was first demonstrated in 1977 by Heeger, McDiarmid and Shirakawa, who exposed polyacetylene films to halogens vapors increasing their conductivity 10^9 times.[48] The discovery was awarded the Nobel Prize in 2000 and resulted in a paradigm shift from the idea of plastic as insulating material to the new concept of highly conductive plastic for uses in electronics.

While in inorganic semiconductor physics the term "doping" usually refers to the introduction of an external neutral atom (of a different element) in a host lattice to change its electronic structure,[49] for conductive polymers the process typically consists in a redox reaction.[50] The insulating neutral polymer is converted into an ionic complex, consisting of a polymeric cation (p-type doping) and a counterion which is the reduced form of the oxidizing agent, or conversely, into a polymeric anion (n-type doping) and a counterion which is the oxidized form of the reducing agent. Many OMIEC formulations result from the research on counterions able to efficiently dope conjugated polymers.[7] Through doping the optical and electrical properties of conductive polymers can be controlled, in the range from insulators to conductors: for example, electrical conductivity of polyacetylenes, polyanilines, polypyrrole, and polythiophenes compositions[51,52] can be increased up to 10-12 orders of magnitude, reaching 1000 S/cm [11] (see **Figure 1.7b**).

Traditional band theory considers electrons and holes as the charge carriers within a fixed atomic lattice.[53] However, in conducting polymers, electrons and holes have significant coupling to the phonons of the lattice and thus the atomic positions are not entirely fixed.[50] The nature of the charged state is related to the ground state properties of the polymer, as shown in **Figure 1.8**. Conjugated polymers can be classified in degenerate or non-degenerate. In the case of degenerate ground state, all monomers are energetically equivalent with no change in energy of possible alternation of single and double bonds. On the other hand, a non-degenerate ground-state–conjugated polymer has energetically non-equivalent structures, usually given by the energy difference of aromatic (benzoid) and quinoid structures.[54] The schematic illustrations of the change in potential energy (electronic plus lattice distortion energy) in two different types of degenerate and non-degenerate ground-state–conjugated polymers are exhibited **Figure 1.8 a** and **d**, respectively. The double minimum potential energy is related to the spontaneous symmetry breaking in the polymer chain. The non-degeneracy of the ground-state energy in most conjugated polymers appears because of the energy difference of aromatic (benzoid) and quinoid structures.[55]

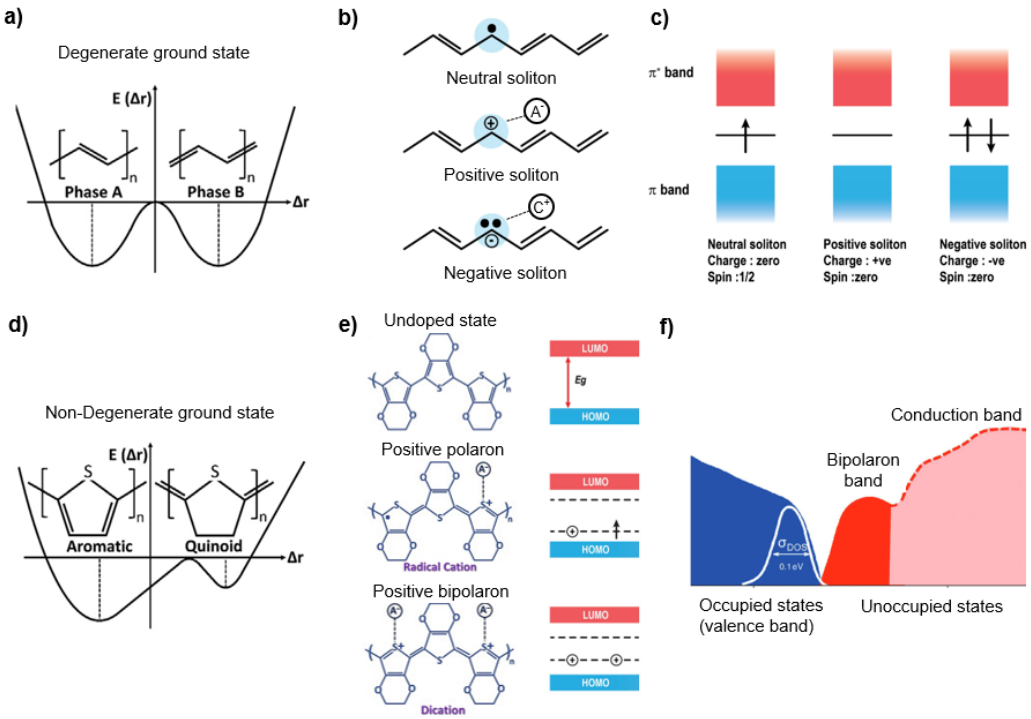

Figure 1.8: Doping of conjugated polymers. **a)** The degenerate ground state of polyacetylene induces the formation of soliton defects **(b)** located in the transition region between phase A and phase B. Both positive and negative solitons can be stabilized by dopant counterions, introducing new levels in the energetic band gap **(c)**. **d)** Non-degenerate ground state in conjugated polymers, and **e)** formation of polarons and bipolaron states induced by doping in poly(3,4-ethylenedioxythiophene) (PEDOT). The structure of a neutral PEDOT chain has an aromatic characteristic, whereas the structure of a polaron or bipolaron distortion has a quinoid characteristic. **f)** Density of states of PEDOT thin films, indicating the formation of bipolaron bands for high doping level. Adapted from[46,54,55].

PAc is a conjugated polymer with a degenerate ground state. By changing the alternation in the bond length pattern (adjacent single and double bonds and changed to double and single

bonds), the energy of the molecular system remains same. These two different structures of trans-polyacetylene have the identical energy, i.e., the equal probability of occurring and can thus coexist in two domains on the same chain.[50] This creates a transition region between the two domains (with different bond length alternation), which is associated with an unpair electron, and it is known as a soliton (**Figure 1.8 b**).[55] A soliton introduces a new energy level (for the unpair electron) in the middle of the intrinsic polymer band gap (**Figure 1.8 c**). Such defect is neutral and present in chains of uneven numbers of carbons, but can be charged negatively or positively by reduction or oxidation with counterions (**Figure 1.8 b** and **c**). A typical example of a conjugated polymer with a non-degenerate ground state is polythiophene, where its aromatic form has lower energy than the quinoid form (**Figure 1.8 d**).[56] The introduction of a positive charge into the polymer creates a local conformational change from the aromatic to the quinoid structure. **Figure 1.8 d**).[56] This structural deformation due to the auto-localization of the introduced charge is known as polaron (**Figure 1.8 e**). Polarons possess a spin of ½ and are formed at low doping levels. Their energy spectrum is characterized by two new energy levels within the intrinsic band gap of the semiconducting polymer. As the doping increases, two polarons located close to each other can form a single spinless bi-polaron defect.[56] The bipolaron can be thought of as analogous to the Cooper pair in the BCS theory of superconductivity,[57] which consists of two electrons coupled through a lattice vibration, i.e., a phonon. The formation of a bipolaron implies that the energy gained by the interaction with the lattice ("sharing" the same lattice distortion) is larger than the Coulomb repulsion between the two charges of same sign confined in the same location.[58] By increasing the doping level of the polymer (a high doping level is considered to be when the dopant to monomer percentage exceeds 33% [59]), bipolaronic states overlap and delocalize resulting in bipolaron bands which provide metal-like conductivity to the structure.[60] The schematic illustration of the energy band diagram obtained from an averaging of the energy spectra of individual crystallites using DFT for a most common conducting polymer thin film, PEDOT, is depicted in **Figure 1.8f**.[60] As can be noted in **Figure 1.8f**, the DOS of both bipolaron and valence band (can be considered as HOMO) display the Gaussian tails toward the gap. The width of the Gaussian DOS (σ_{DOS}) in the valence band is an indication of the energetic disorder of a system and is approximately reported in the range of 0.1 eV for PEDOT thin films.[61]

1.3.4 Interchain transport

The intrachain coupling of charged defect states provides the pathway of charge carriers along the polymer backbone among adjacent localized segments (see **Figure 1.9a**). Similarly, when the distance between different polymer chains is small, there is a high chance of interchain polaron/bipolaron coupling between adjacent localized states through π–π stacking.[62] The resulting interchain coupling provides the hopping pathway between localized coupled segments, either between two individual chains or on one chain that is folded back on itself (see **Figure 1.9b**). In conjugated polymer films, intrachain coupling is strongly favored in crystalline regions, while interchain coupling avoids charge localization in the presence of defects and amorphous regions. The overall rate of charge carrier transport in the film will be

determined by the slower of the two processes occurring in series.[63] Tuning the process parameters and post-processing treatments of CP films increases the degree of crystallinity, crystallite size, and crystallite orientation, so that intercrystallite transport is not rate limiting,[53] that is, moving from a region I (low order) to region II (high order) as depicted in **Figure 1.9c**. In this scheme, the overall rate of charge carrier transport reaches a plateau in the region II and reveals that further enhancement of crystalline order and orientation do not dramatically change the total charge transport rate in the case of large π–π stacking distance. Smaller π–π stacking distances can be obtained by engineering the doping level and the dopant identity, leading to a further enhancement of the film conductivity.[64]

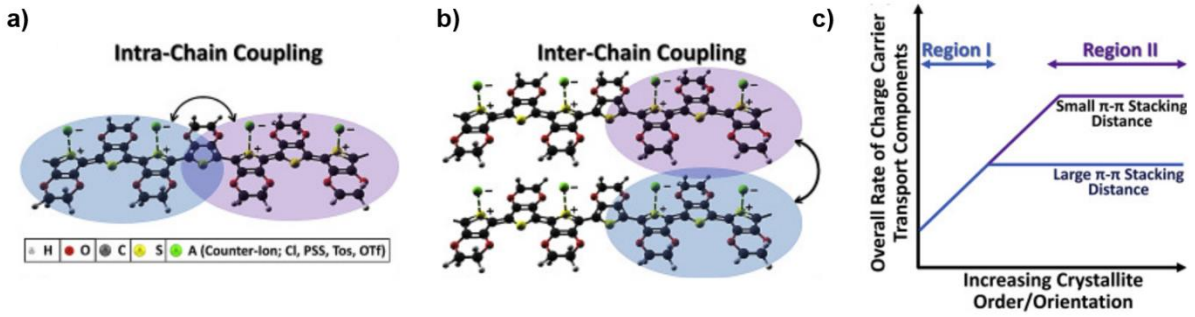

Figure 1.9: Intra-chain and interchain coupling in conjugated polymer films. The wave function of localized charge defects (polaron or bipolaron) can overlap along a polymer chain **(a)** or between adjacent polymer chains **(b)** through π–π stacking. **c)** Schematic illustration of overall rate of charge carrier transport for intercrystallite and interchain processes in conjugated polymer films. For limited order (region I), increasing the degree of crystallinity leads to enhanced electrical conductivity. With increased order (region II), the overall rate of charge carrier transport is limited by the π–π stacking distance and reaches a plateau according to its value.[46]

1.3.5 Mechanism of Electronic Transport in OMIECs

The overall electroneutrality of matter dictates that oppositely charged ions balance electronic carriers in doped conjugated polymers. The fixed polyelectrolyte charge in type I/III/V OMIECs can serve this function (**Figure 1.4**), while type II/IV/VI materials require the injection of counterbalancing dopant anions or cations.

Due to large structural disorder in OMIEC materials limiting the degree of electronic delocalization, charge transport in doped CPs is often described as Efros–Shklovskii variable-range hopping,[65] in which the electronic conductivity (σ_{el}) has the following temperature dependence:

$$\sigma_{el} = \sigma_{ES}\, exp\left[\left(\frac{T_{ES}}{T}\right)^{-\frac{1}{2}}\right] \qquad 1.5$$

where σ_{ES} is the conductivity prefactor and T_{ES} is the characteristic temperature. The fundamental insight of this model is the presence of a Coulomb gap in the density of states (DOS). At very low concentrations the dopant ions act as Coulombic traps for electronic charge carriers and charge transport mostly consists in thermally activated hops between localized

states (see **Figure 1.10a**).[66] With increasing doping levels the activation energy of charge hopping decreases and carrier mobility increases, with some OMIECs displaying diffuse band-like charge transport.[65] Thereby, the Coulomb gap can be qualitatively rationalized as the energetic distance between the highest filled localized states (Fermi level) and the lowest empty delocalized states (transport level or mobility edge). Increasing the charge density should decrease T_{ES} such that at or above T_{ES}, the thermal energy should be sufficient to collapse the Coulomb gap, resulting in high (metallic) conductivity.

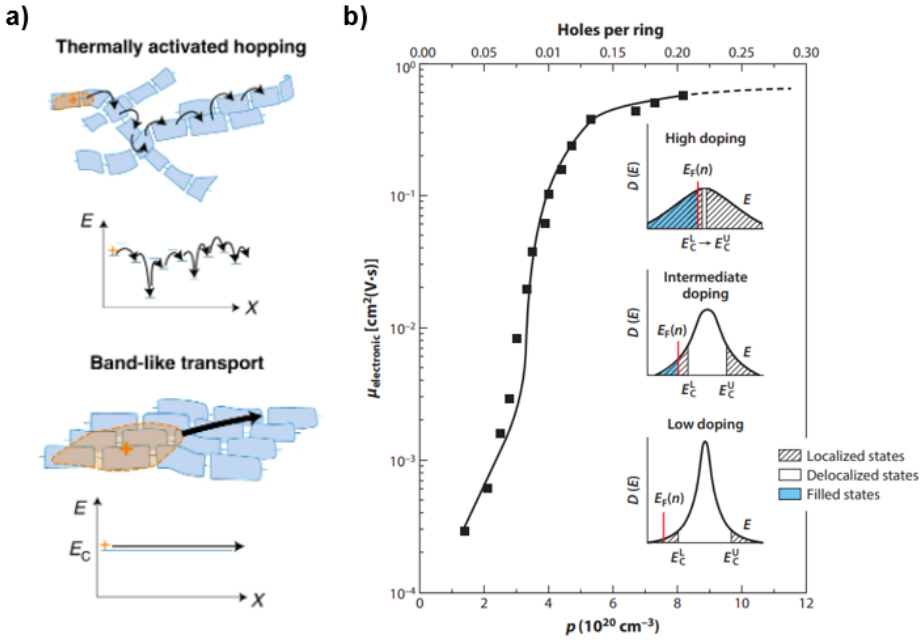

Figure 1.10: Electronic conduction in OMIECs, ranging from thermally activated hopping to band like transport depending on the doping level **(a)**.[7] As a result, the electronic mobility in the prototypical CP P3HT shows a dramatic rise and plateau with increased hole concentration p **(b)**. The insets in panel **b** show the HOMO (valence band) density of states filled up to the Fermi level (E_F). The difference between E_F and the transport level E_C is the Coulomb gap. E_C^L and E_C^U are the lower and upper transport levels, respectively. The broadening of the density of states distribution with increased doping drives the localization of states and shifts E_C, which complicates the transition to true band-like or metallic transport. Adapted from [66].

However, this has not been unequivocally achieved,[67] likely due to dopant-induced disorder that accompanies high carrier densities, as indicated by the broadening of the DOS in **Figure 1.10c**. Over smaller temperature ranges, electronic mobility is commonly (if not strictly accurately) described as thermally activated hopping with an Arrhenius relationship:

$$\mu = \mu_0 \, exp\left(-\frac{E_a}{RT}\right) \qquad 1.6$$

where the activation energy (E_a) and exponential prefactor (μ_0) are carrier density dependent. The activation energy is a useful parameter to approximate the difference between the Fermi level and transport level to compare the mobility at different carrier densities and in different materials.[68]

Despite differences in the chemical structure and composition of OMIECs, stochastic hopping processes occurring at the microscale result into macroscopic electronic currents, which can be described with a general drift-diffusion approach. The one-dimension current density for electrons (J_n) and for holes (J_p) can be defined as

$$J_n = e\mu_n \frac{d\phi}{dx} + eD_n \frac{dn}{dx} \quad 1.7$$

$$J_p = e\mu_p \frac{d\phi}{dx} - eD_p \frac{dp}{dx} \quad 1.8$$

where n and p are the carrier densities, μ_n and μ_n are mobilities, and D_n and D_p are the diffusivities for the electrons and holes, respectively. Absent molecular doping,[69] n and p are equal to the excess cation and anion concentrations, respectively.

1.4 Ionic transport in OMIECs

What sets OMIECs apart from other π-conjugated organic semiconductors is their ability to conduct ionic currents in addition to electronic currents. In the case of dry OMIECs, ion transport is unipolar for types I, III and V (**Figure 1.4**) as one of the ionic charged species is fixed on a polyelectrolyte, whereas both anions and cations are mobile in types II, IV and VI. When OMIECs are placed in contact with an electrolyte, swelling processes of the polymeric matrix allows for the infiltration of excess ions from the electrolyte, and thus both mobile anions and cations may contribute to ion transport. In both cases, the negatively charged anions and positively charged cations can be thought analogous to electrons and holes. Thereby, in dilute systems in one dimension, the ionic current density can be expressed analogously to Eq. 1.7 and 1.8:

$$J_{ion} = \sum_i \left[n_i |z_i| e\mu_n \frac{d\phi}{dx} + eD_n z_i \frac{dn_i}{dx} \right] \quad 1.9$$

where the index i refers to the different ionic species in the OMIEC material. However, assumptions of infinite dilution often do not hold. Ion-ion interactions in OMIECs can produce neutral ion pairs (that can diffuse but do not migrate), net charged ion triplets, and larger clusters or aggregates that can be neutral or charged.[21] Thus, raw anion and cation concentrations are not informative, and when known concentrations of each ion and multi-ion species are absent, anion and cation thermodynamic activities should be used. Additionally, depending on local pH, there may be non-negligible proton, hydronium, or hydroxide transport in hydrated or aqueous systems. Given this complexity, ionic conductivity in polymer MIECs is often quantified as simple σ_{ionic}, but reported mobility or diffusion coefficients should be considered apparent or effective unless rigorously proven otherwise. Moreover, while in typical

electrolytes electroneutrality requires the local cation and anion concentrations to be equal, in OMIECs ions can accumulate to counterbalance electronic carriers:

$$F\sum_i c_i z_i + ep - en = 0 \qquad 1.10$$

where F is Faraday's constant, c_i is the individual ion concentrations, and p and n are the electron and hole concentrations, respectively.

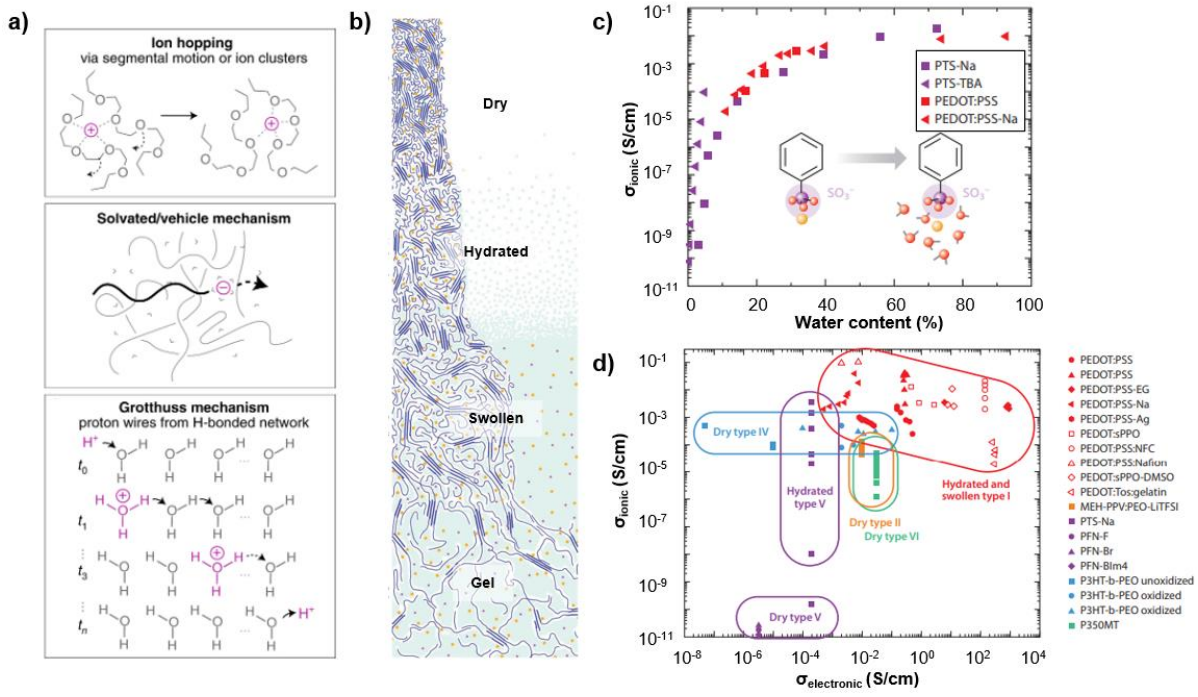

Figure 1.11: Ionic conduction in OMIECs. a) Mechanism of ionic transport in mixed conductors according to their hydration state in (b). Ion hopping occurs in the dry state, while vehicle and Grotthuss transport take place in hydrated materials. c) Impact of water content on ionic conduction in OMIECs formulations. c) Ionic and electronic conductivity map in organic mixed conductors at different hydration conditions. Adapted from 7,73.

Ion transport in OMIECs can occur through different mechanisms (**Figure 1.11a**) depending on the hydration state of the polymeric film (**Figure 1.11b**). In dry and minimally hydrated conditions, ion motion occurs through ion hopping coupled with the segmental motion of the OMIEC side chains or backbone.[70] Ionic transport is dependent on chain fluctuations, and extended conjugation is detrimental to the process. The segmental motion assisted transport can be improved with the incorporation of ion-coordinating moieties. Dry type V polyelectrolytes and type II blends have ion mobilities of order 10^{-10} and 10^{-9} cm^2 V^{-1} s^{-1}, respectively.[71]
Hydration has a tremendous effect on ionic transport in mixed conductors. Many OMIECs (especially types I, III, and V) show such low σ_{ionic} in the dry state that they can be considered as simply electrical (semi)conductors due to strong ion association with the polymer and limited chain motion. With hydration, water plasticizes chains, increasing chain motion, and begins to solvate the ions, partially displacing the polymer in the cation solvation shell.[72] In conjugated

polyelectrolytes, water dissociates the counterion. A sufficient degree of hydration produces a mobile solvation shell of water, allowing vehicle transport. At room temperature, the ionic conductivity of conjugated polyelectrolytes (type VI) spans seven to eight orders of magnitude depending on the degree of hydration (**Figure 1.11c**).[73] Moreover, as OMIECs incorporate poly(4-styrenesulfonic acid) (PSSH), parallel proton transport via the Grotthuss mechanism becomes significant in the highly hydrated state.[74]

Many mixed conductor applications require direct contact with a liquid electrolyte.[75] This complicates the description of transport, as ions and solvent are now in a concentration- and electrochemical potential–dependent equilibrium between the contacting liquid electrolyte the electroactive material. This is most obvious in potential-dependent swelling of OMIECs in response to electrochemically induced electronic charge. In this environment, many marginal polymeric MIECs that minimally solvate/transport ions become surprisingly effective mixed conductors. For example, the type VI material poly(2-(3,3 -bis(2-(2-(2-methoxyethoxy)ethoxy)ethoxy)-[2,2 -bithiophen]- 5-yl)thieno[3,2-b]thiophene) [p(g2T-TT)] passively swells only ∼10% when in contact with aqueous NaCl, independent of electrolyte concentration. However, upon the application of an oxidizing potential, p(g2T-TT) reversibly swells an additional 42% to 86%.[76] Electrolyte swollen PEDOT:PSS shows an ionic conductivity with the same concentration dependence as liquid electrolytes. As excessive swelling can be detrimental to device stability, cross-linkers are often employed to stabilize the polymeric matrix, reducing the ionic mobility up to one order of magnitude.[77] Both highly hydrated and electrolyte swollen polymeric MIECs are more accurately described as conductive hydrogels, where ionic transport is decoupled from polymer chain dynamics as continuous liquid pathways are available for ionic transport. In such a condition, ionic conductivity reaches maximum values, and research efforts are focalized on maintaining a percolative path for effective electronic transport.[78]

A final overview on mixed transport in OMIECs is given by **Figure 1.11d**, showing the ionic and electronic conductivity map of different materials under dry, hydrated, electrolyte swollen, and gelled conditions.[73] The degree of doping and hydration leads to a several orders of magnitude range of electronic and ionic conductivity, respectively. Dry polymer electrolyte-based materials (types II, IV, and VI) show much better ionic conductivity than dry polyelectrolyte-based materials (type V), but maxima ionic and electronic conductivities are measured in hydrated and solvent swollen type I polyelectrolyte/conjugated polymer composites.

1.5 Ionic-electronic interactions in OMIECs

Ionic-electronic interactions in OMIECs involve the entire material bulk and determine the charging properties of mixed conductors. Electroneutrality requires that every electronic charge in the conjugate segment of an OMIEC is counterbalanced by a stabilizing excess ionic charge (net ionic charge) of the opposite sign. As specified in **Sect. 1.3.3**, ionic-electronic coupling is commonly referred to as doping, as it modulates the electrical conductivity of the

OMIEC formulation. In the case of types II, IV and VI OMIECs the stabilizing doping is induced by the injection of mobile ions, while in types I, III and V materials, net ionic charges charge are fixed in the OMIEC, thus they can be inherently doped. Since these dopant ions cannot be removed, de-doping can occur via the incorporation of oppositely charged mobile ions that compensate the fixed ionic charge present in the OMIEC (**Figure 1.12a**). In some mixed conductors ionic–electronic coupling can occur through direct charge transfer processes, such as the protonation of polyaniline, which leads to the stabilization of electronic charge (**Figure 1.12b**). In the absence of an externally applied potential, there is some preferred equilibrium concentration of electronic charge and counterbalancing excess ionic charge. This depends on the energetic position of the HOMO and LUMO bands of the conjugated segment in the OMIEC composition. A sufficiently shallow HOMO energetically favors the stabilization of positive electronic hole charges by excess anions (p-type doping), while a deep LUMO band favors n-type doping involving electrons stabilized by excess cations. The amount of coupling between electronic charge and excess ionic charge (degree of doping) in OMIECs can be modulated with an applied bias when coupled through an electrolyte. Homogeneous single phase OMIECs (types V and VI) display larger magnitudes of ionic–electronic coupling and larger values of volumetric capacitances than biphasic OMIECs (types I–IV).[79] This potential-dependent coupling is the fundamental mechanism of charge storage in OMIEC-based supercapacitors and batteries,[15] and of transduction between ionic and electronic signals in OMIEC-based sensing and stimulating probes.[80] Ion-electron interactions lead to the filling or emptying of electronic states allowing for the reversible bleaching of optical transitions needed in electrochromic devices.[35] Furthermore, the modulation of the degree of doping naturally controls the electrical conductivity of the OMIEC and is leveraged in a variety of OMIEC-based organic electrochemical transistors[38] and neuromorphic devices.[81]

Ion-electron coupling in organic mixed conductors takes place in a disordered, weakly interacting, low dielectric constant, molecular system infiltrated by an electrolyte. Electronic charge can be injected from metallic electrodes underlying the OMIEC layer, transported through the π-conjugated system, and most often electrostatically stabilized by a dopant ion supplied from the electrolyte. Given the complexity of the process, OMIEC charging is often inconsistently described as alternatively faradaic, capacitive (electrostatic) or pseudocapacitive.[82] Faradaic charging of OMIECs implies a current corresponding to the oxidation/reduction of some molecular entity, which follows Faraday's law relating moles of product to coulombs of charge through Faraday's constant.[83] Cases do exist of CPs and OMIECs that undergo archetypal integer electron redox reactions,[84] where the charging process can be described as

$$P^0 + C^+ + e^- \leftrightarrow P^-(C^+) \quad \text{or} \quad P^0 + A^- + h^+ \leftrightarrow P^+(A^-) \qquad 1.11$$

and integer electron processes are localized to single polymer repeat units (*P*), via stabilization with a cation (*C*) or anion (*A*) supplied from the electrolyte. However, such exceptions only prove the more common rule that most CPs generally do not undergo neat redox processes of clearly defined molecular entities. More often, charge is delocalized and distributed fractionally

over a non-constant number of repeat units, and the degree of delocalization depends greatly on the intermolecular ordering. Thereby, charging in OMIECs cannot be rationalized as an equilibrium between a neutral and integer charged species, but instead is a continually evolving equilibrium between incrementally differing degrees of fractional charge,[85] making difficult to properly define reactants, products and integer electron processes. Further complicating matters is the common perception that faradaic and electrostatic are mutually exclusive, but most ionic–electronic charge coupling phenomena in OMIECs are both faradaic and electrostatic. Even in the case of ideal redox polymers (described above), the interaction between electronic charge on the reduced repeat unit and the stabilizing cation is electrostatic. Charge transfer occurs between the OMIEC and the contacting metal electrode, and not between repeat units and the stabilizing (dopant) cations. Understanding OMIEC charging to be faradaic does not preclude electrostatic charge interactions, and the accurate description of charging must better connect to the physical phenomena, opening intriguing challenges for material research.

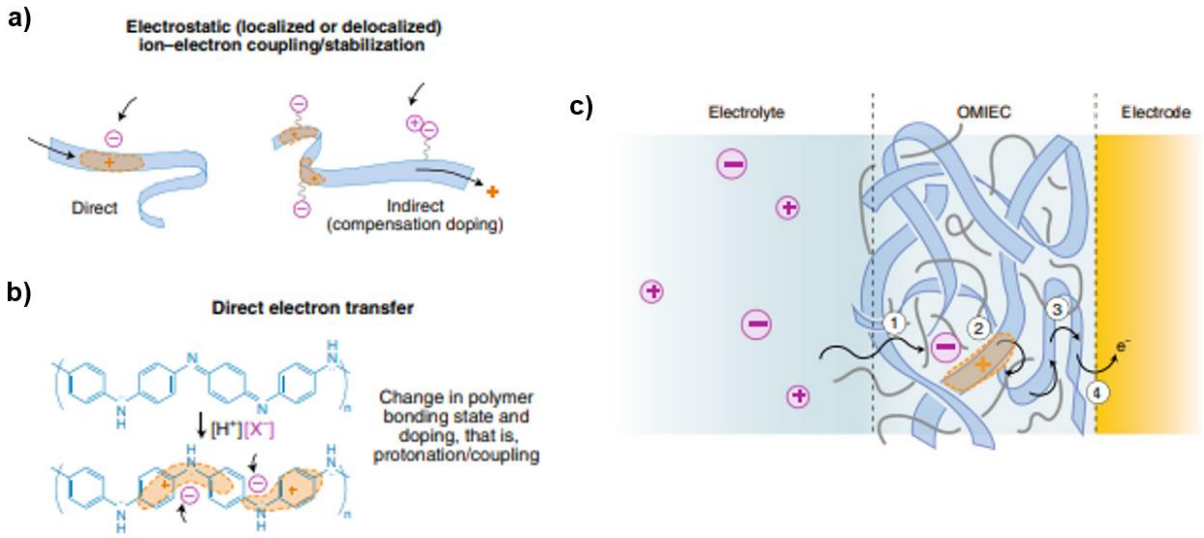

Figure 1.12: Ionic-electronic coupling in OMIECs. The stabilization of electronic carriers with net ionic charges can occur through electrostatic interactions **(a)** or direct charge transfer (protonation) **(b)**. **c)** Charging of an OMIEC material in contact with a metal electrode and an electrolyte, highlighting dopant ion injection and transport (1), electronic carrier (hole) stabilization by a dopant ion (anion) (2), electronic carrier hopping (3) and charge transfer between the metal electrode and the OMIEC (4). Numbering does not indicate the order of the processes.[7]

1.6 PEDOT:PSS as a model OMIEC material

After the discovery of electrically conducting polymers in 1977[48] and more than 30 years of worldwide intense research and huge efforts, PEDOT, or poly(3,4-ethylenedioxythiophene), sets various standards for the entire field. PEDOT, which was invented in 1988 by Bayer AG, Leverkusen, establishes the benchmark in terms of conductivity, processability, and stability among all conductive polymers.[11] One of the main reason for PEDOT success as conducting polymer is its availability in aqueous dispersion. Although

PEDOT is an insoluble polymer, combined with poly(styrenesulfonic acid) (PSS) as a counterion it creates a conjugated polymer-polyelectrolyte blend (type I OMIEC) that can be prepared in stable dispersions, produced on industrial scale, and used through several deposition techniques. PSS is commercially available with different molecular weights and polydispersities the trade name Clevios™ (see **Figure 1.13**). It is soluble in water and forms durable and transparent films.[86] As PEDOT counterion, PSS is always used in excess, thus as host polyelectrolyte.

Trade Name	Solids Content in Water (w/w) (%)	PEDOT:PSS Ratio (w/w)	Viscosity at 20°C (mPas)	Particle Size d_{50} (nm)	Conductivity (S/cm)
Clevios P	1.3	1:2.5	80	80	<10
Clevios PH	1.3	1:2.5	20	30	<10
Clevios P VP AI 4083	1.5	1:6	10	40	10^{-3}
Clevios P VP CH 8000	2.8	1:20	15	25	10^{-5}
Clevios PH 500	1.1	1:2.5	25	30	500
Clevios PH 750	1.1	1:2.5	25	30	750
Clevios PH 1000	1.1	1:2.5	30	30	1000

Figure 1.13: Commercial PEDOT:PSS dispersions in water and their properties.

In standard PEDOT:PSS dispersions, the molar ratio between thiophene groups and sulfonic acid groups is in the range of 1:1.9 to 1:15.2 (weight ratio range 1:2.5 up to 1:20). Since there is one charge every three to four thiophene rings, the charge excess of PSS is between 6-fold and 46-fold.[11] According to the delocalization of positive charges in PEDOT, the weak polar groups and the different spacing of PEDOT charges compared to PSS ones, there is no molecular or supramolecular order in PEDOT:PSS, but only a random interaction between polymer chains giving the so-called "pancake-like" structure, as shown in **Figure 1.14**.[87]

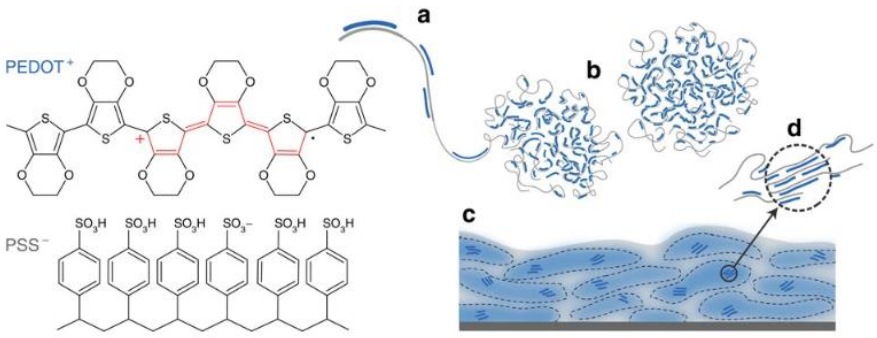

Figure 1.14: Chemical structure of PEDOT:PSS, where holes (positive (bi)polarons) in PEDOT are stabilized by fixed anions in PSS. The commonly described microstructure of the type I OMIEC blend involves the PEDOT synthesis onto PSS template **(a)**, formation of colloidal gel particles in dispersion **(b)** and resulting film with PEDOT:PSS-rich (blue) and PSS-rich (grey) phases **(c)**. PEDOT aggregates/crystallites support enhanced electronic transport **(d)**.[87]

PEDOT:PSS represents a workhorse of organic electronics and bioelectronics, and is in fact one of the most studied and explored materials in current research.[88] Further to its commercial availability and its solubility in water, the polymeric blend forms durable films and shows no absorption in the visible range of light, resulting in transparent films. The density of holes in PEDOT:PSS can be reversibly modulated over a wide range by the compensation with ions provided from an electrolyte. This makes PEDOT:PSS ideal as the electrode in ion-based energy storage devices, such as supercapacitors,[89] and as the channel in electrochemical transistors[90] and sensors.[91] The swift and reversible modulation of the hole density is also accompanied with a switch in color between dark blue and transparent, and PEDOT:PSS has therefore served as the pixel electrode in electrochromic displays.[35] Moreover, PEDOT:PSS is a first choice as the signal translating device in various bioelectronics devices operating in physiological media, such as in biosensors, electrochemical transistors,[92] and electrodes interfacing with neuronal systems.[93]

1.6.1 Deposition and properties of PEDOT:PSS

PEDOT:PSS dispersed in water can be deposited in principle by all common techniques employed for the deposition of waterborne coatings (**Figure 1.15**). Common deposition techniques to obtain uniform coatings are slit coating, drop casting, bar coating, spin coating, electrospinning, and spraying.[94] In case a structured deposition is required, other techniques are commonly employed such as screen printing, inkjet, nozzle printing, and various forms of contact printing (that is, relief, flexo, gravure, and offset printing). Other ways for structured deposition of PEDOT:PSS have been achieved by modifying the wetting properties of the surface, or by using photo-lithographical techniques.[95] The deposition of PEDOT:PSS dispersions by spin coating has proven to be an easily accessible technique to obtain uniform films in a thickness range of 0 to 300 nm.[96] PEDOT:PSS films have to be dried prior to further processing. The water is removed by baking the layers at elevated temperatures, under infrared

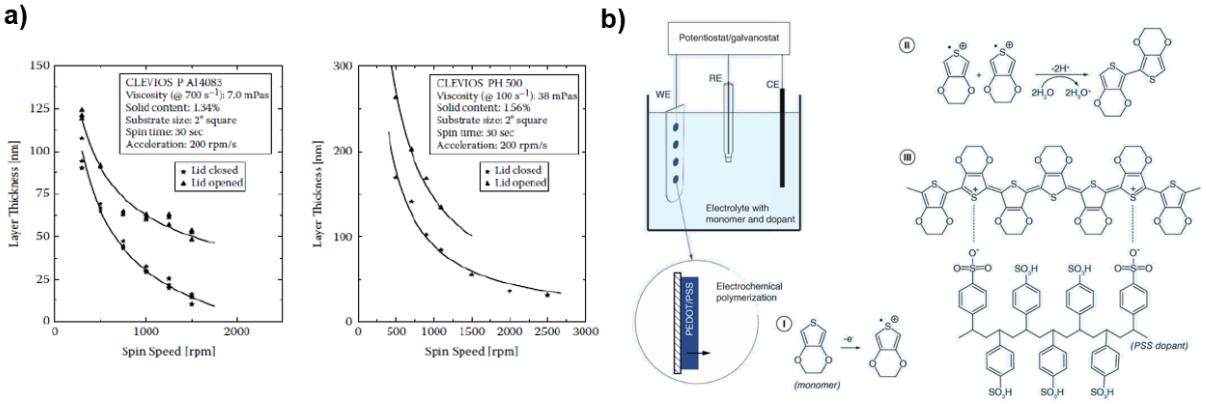

Figure 1.15: Deposition of PEDOT:PSS. **a)** Spin coating curves for CLEVIOS P AI 4083 and CLEVIOS PH 500 PEDOT:PSS dispersions using a Carl Süss RC8 spin-coater (featuring a closed or opened rotating lid).[11] **b)** Electrochemical deposition of PEDOT:PSS from EDOT monomers.[99]

(IR) radiation, or by applying vacuum. Alternatively, highly conductive and stable PEDOT:PSS thin films can be prepared by electrochemical polymerization. Developed at the beginning for polypyrrole,[97] and then extended to many other polymers, this method allows for a precise control of the quantity of the material deposited on the substrate, also providing an easy way of functionalization with inorganic or bio-molecules.[98]

PEDOT:PSS films are stable in a wide temperature range, as demonstrated by thermo-gravimetrical analysis (TGA) of thick layers. **Figure 1.16a** depicts the weight loss over time while the sample is heated at a constant rate in helium.[11] Between 100°C and 200°C the weight loss is solely determined by evaporation of remaining water. Like other polymers containing sulfonic acid groups, PEDOT:PSS is strongly hygroscopic and will take up moisture when handled under ambient conditions. At about 250°C the sample weight decreases significantly.

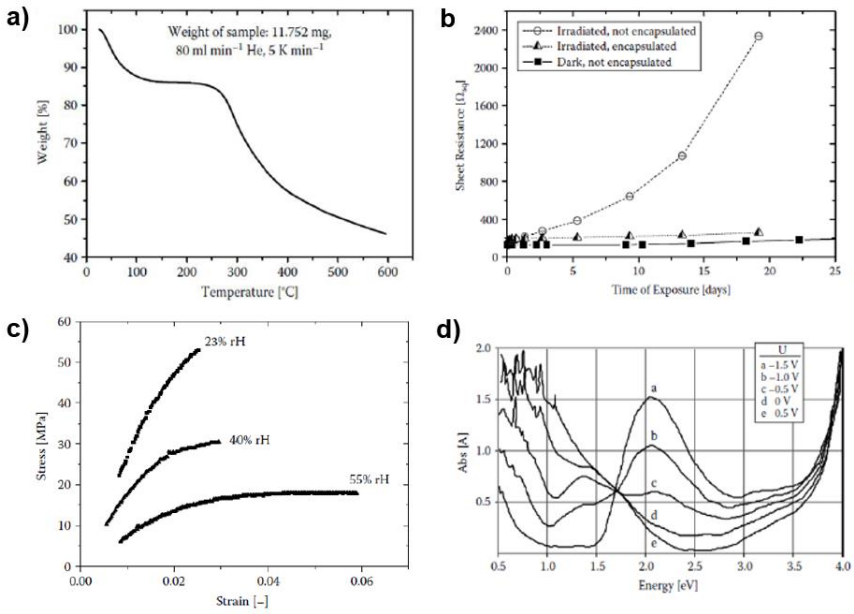

Figure 1.16: Some properties of PEDOT:PSS films. **a)** Thermo-gravimetrical analysis (TGA) indicating thermal stability up to 200°C. **b)** Effect of UV absorption on the sheet resistance of PEDOT:PSS. **c)** Stress-strain curves at different humidity conditions. **d)** Optical absorption of PEDOT:PSS films at different electrochemical potentials.[11]

This is attributed to SO_2 ions evaporation and indicates the fragmentation of the PSS sulfonate group. At higher temperatures of T > 350°C other fragments due to carbon oxidation are detected. Following the analytical data obtained by TGA the material is considered to be thermally stable up to temperatures of T = 200°C. In contrast to many other conjugated highly conductive polymers, PEDOT:PSS exhibits a very stable conductivity. However, like all carbon compounds, PEDOT-type polymers will be subject to degradation, especially when exposed to harsher conditions. The overall decay mechanism seems to be oxidation by oxygen enhanced by UV light (**Figure 1.16a**). Attack to the sulfur atom of the thiophene ring will yield nonconducting sulfoxide and sulfone structures, and ultraviolet (UV)-light exposure must be avoided.

PEDOT:PSS films are mechanically flexible compared to inorganic materials like metal oxides. The mechanical properties of PEDOT:PSS have been investigated by tensile strength tests on

free-standing PEDOT:PSS films (**Figure 1.16c**). Young's modulus and tensile strength were found to be strongly depending on the relative humidity (rH) level during the tests. The polymer exhibits brittle fracture behavior at rH = 23% which changes to plastic fracture behavior at an intermediate rH = 55%. The Young's modulus of films increases from 0.9 GPa at 55% rH to 2.8 GPa at 23% rH.[99]

The optical spectrum of PEDOT:PSS is almost identical to the absorption of in situ chemically polymerized PEDOT without PSS. Thin films (<500nm) of PEDOT: PSS are highly transparent in the visible range (transmittance> 80%). Part of the absorption occurs in the region of red (600 -750 nm), which gives the films a light blue appearance. Gustafsson et al. have studied the optical properties of PEDOT:PSS films deposited on ITO as electrode in an electrochemical cell.[100] **Figure 1.16d** depicts the optical absorption spectra as a function of photon energy at different bias. The peak at 2.2 eV (560 nm), the band gap absorption, reduces as the applied bias is increased. At the same time, two new peaks appear at lower energies (<0.5 eV and 1.4 eV) indicating that the charge inserted into the polymer electrode is stored as bipolarons.[101] The partly neutralized polymer obtained at a bias of –1.5 V is strongly absorbing in the visible range, while PEDOT in its oxidized form at +0.5 V is almost transparent in this region. This behavior may be exploited in electrochromic applications, like displays and smart windows.[102]

1.6.2 Morphology model for PEDOT:PSS

PEDOT:PSS is a type I OMIEC with a relatively high ionic conductivity and specific capacitance. Charging properties (electron-ion coupling) of mixed conductor are commonly studied using cyclic voltammetry (CV). In a cyclic voltammetry experiment, an electrochemical potential is applied to a working electrode typically consisting of an OMIEC layer patterned on a metallic electrode. The applied potential is ramped linearly with respect to time, and the electrochemical current induced by the process is recorded.[103] Typical CV data traces recorded for PEDOT:PSS in 0.1 m KCl solution are shown in **Figure 1.17a**.[23] In the forward potential scan, there is a current peak (at $V \approx -0.7$ V) attributed to the injection of holes into the undoped polymer and expulsion of cations. Accordingly, on the reverse scan the voltammogram shows one cathodic peak ($V \approx -0.7$ V) corresponding to electron injection and cation uptake responsible for the de-doping process of PEDOT. At the same time CV curves exhibit a characteristic rectangular shape in the range from −0.5 to 0.5 V, indicating capacitive charge accumulation in the OMIEC material,[104] with volumetric specific capacitance values reported from 30 to 50 F/cm^3.[105]

The origin of the volumetric capacitance of PEDOT:PSS can be attributed to a phase separation in the polymeric microstructure (see **Figure 1.4**), which can be investigated at different scales. Grazing incidence wide-angle X-ray scattering (GIWAXS) provides information at the Ångström scale.[106] The GIWAXS pattern presented in **Figure 1.17b** indicates a mostly amorphous film, but with some weak and broad, isotropic scattering, indicating π–π stacking in small ordered domains of PSS and PEDOT, respectively.[64] From the broadening of the diffraction peaks it is possible to estimate that each PEDOT crystallite domains is composed by

of up to five chains.[107] The morphology of the PEDOT:PSS film on the scale above 1 nm can be characterized with tapping-mode atomic force microscopy (AFM). **Figure 1.17c** and **d** show the phase and topography images of a 500 × 500 nm^2 area of the PEDOT–PSS film. The 10–20 nm wide grains observed in the phase image with relatively strong contrast are associated with a different chemical composition. For polymer systems, bright areas (high phase signal) in the phase image can be assigned to the relatively hard PEDOT:PSS rich phase[108], while the lower phase signal is referred to areas with an excess of PSS. Surface areas rich in this hygroscopic polyelectrolyte are expected to swell and soften due to ambient humidity, explaining why the PSS region is slightly higher in the corresponding topography image.[109]
The combined observations indicate the PEDOT:PSS morphology model sketched in **Figure 1.17e**. PEDOT:PSS represents a two phase-system consisting of PEDOT-rich and PSS-rich grains of the dimensions of about 10–30 nm. PEDOT-rich grains support primarily hole conductivity, whereas PSS-rich grains support the ionic conductivity. The PEDOT-rich grains consist of PEDOT crystallite domains of 1–2 nm (composed of up to ≈5 chains) embedded in the amorphous PSS matrix. Because the system exhibits high conductivity in the oxidized state, the PEDOT crystallites and chains form a percolative network (presumably via π–π stacking) providing transport paths for the holes throughout the whole structure.

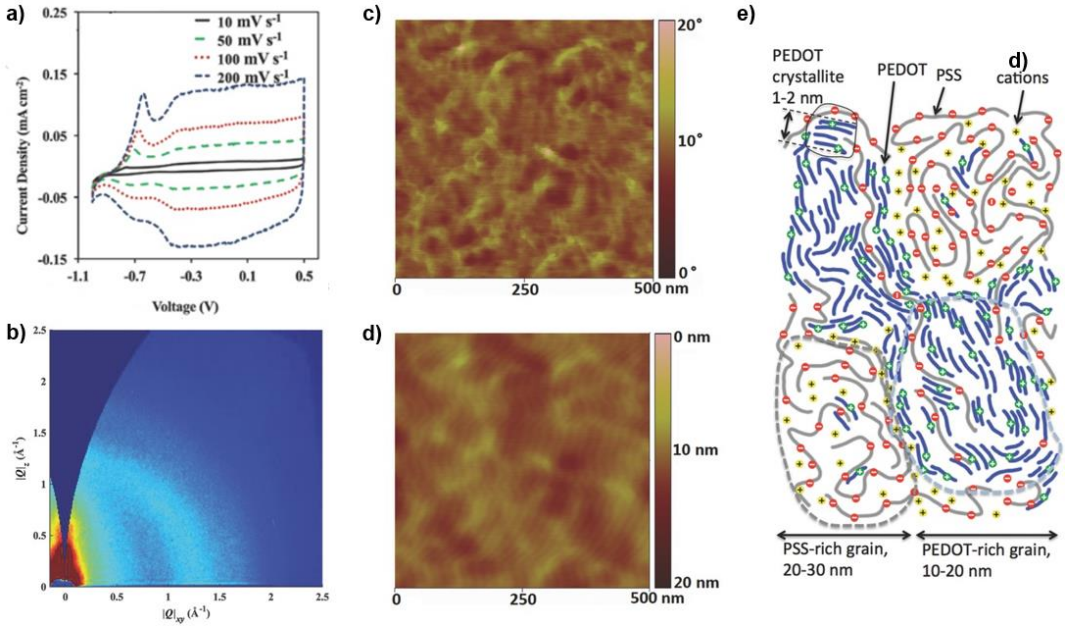

Figure 1.17: Morphology of PEDOT:PSS. **a)** Cyclic voltammetry of a PEDOT:PSS. **b)** GIWAXS data of PEDOT:PSS represented in a coordinate system of scattering vectors Q_{xy}, Q_z, parallel to the substrate plane and substrate normal, respectively. **c)** Phase images and **d)** topography of a PEDOT–PSS film obtained with tapping-mode AFM. **e)** Schematic diagram of the morphology model for PEDOT:PSS.[23]

1.6.3 Secondary doping of PEDOT:PSS

The term "secondary doping" was introduced by MacDiarmid and Epstein to refer to chemical additives used to further enhance the conductivity of a doped conjugated polymer.[110]

Secondary dopants do not actually change the PEDOT doping level, thus they are often referred a conductivity enhancing agents (CEA). Typically, CEA are added to PEDOT:PSS water dispersion (but they can also be added after the film formation) and the effects on conductivity are clearly visible once the film is formed. The most common secondary dopants for PEDOT:PSS are dimethyl sulfoxide (DMSO), copper (II) chloride, and ethylene glycol (EG).[11] Secondary doping processes often require thermal annealing and show two important features: i) the presence of the secondary dopant is not necessary to maintain the conductivity once the film is formed[11], and ii) small quantities of secondary dopants can strongly influence the conductivity of the PEDOT:PSS film, but the conductivity increase rapidly reaches a plateau for large CEA concentrations (**Figure 1.18a**).[111]

The effect of secondary dopant can be interpreted as follows. During the PEDOT:PSS film deposition from aqueous dispersion, polymer chains are "frozen" in a non-equilibrium state, but in presence of a high boiling point solvent the blend rearrange and the PEDOT oligomers find a new thermodynamically favorable position, similarly to the effect of a platicizer.[112] In this way, highly polar secondary dopants interact with $PEDOT^+$ and PSS^- chains, favoring crystalline aggregation. After such rearrangement, the film remains in its new thermodynamically favorable state, even upon the CEA thermal removal.[113] EG content increases have been shown by grazing incidence wide-angle X-ray scattering (GIWAXS) to incur slightly tighter π–π stacking across different polymer chains and increase crystallite size.[87] The growth in domain sizes was accompanied by increases in the heterogeneity of the PEDOT:PSS cores and PSS-rich matrices (**Figure 1.18b**), enhancing the electronic conductivity, but slightly decreasing the ionic mobility. As a consequence, maximized mixed conduction is achieved with 5 vol% EG. Other additives commonly employed in PEDOT:PSS composites to ensure good OECT performance are the molecular surfactant 4-dodecylbenzenesulfonic acid (DBSA) and the cross-linking agent 3-glycidoxypropyltrimethoxysilane (GOPS). Unlike the aforementioned secondary dopants, the primary purpose of these additives is not to boost OECT performance but instead to facilitate organic semiconductor processing or thin-film stabilization onto device substrates.[93] Typical DBSA ratios used for depositing PEDOT:PSS layers onto devices lie below 0.5 v/v%. A different class of additives is given by cross-linkers, which increase the formation of covalent bonds between the polymer chains, thus changing their physical features. Since PSS is highly hygroscopic, PEDOT:PSS films exposed to water swell and usually delaminate. The addition to the mixture solution of the cross-linking agent 3-glycidoxypropyltrimethoxysilane (GOPS) has proved to enhance the PEDOT:PSS film stability in aqueous solutions,[111] as reported in **Figure 1.18c**. Although the films containing GOPS show superior mechanical stability, the addition of GOPS yields thicker films (at a given spin-coating speed) containing a larger amount of hydrophilic PSS^- units. Consequently, the hydration of the PEDOT:PSS film increases causing irreversible morphological changes, which lead to a decrease in conductivity.[114] Anyway, water absorption of PSS^- likely reaches a saturation state after a short time (about 3 h) and, afterwards, the film becomes stable.[111] Due to the presence of multiple components in the deposited films, GOPS exact cross-linking mechanism is yet to be fully elucidated. According to literature, the methoxy groups in GOPS can react with surface silanol groups

present in silicon-based surfaces (e.g. glass).[115] In parallel, the highly strained nature of GOPS's epoxide ring and the availability of the C–O σ* orbitals render it reactive toward numerous nucleophiles, including water, alcohols (e.g. ethylene glycol), thiols, amines, and acids (e.g. the toluene sulfonic acid group in PSS) to form network-like structures (**Figure 1.18d**).[116]

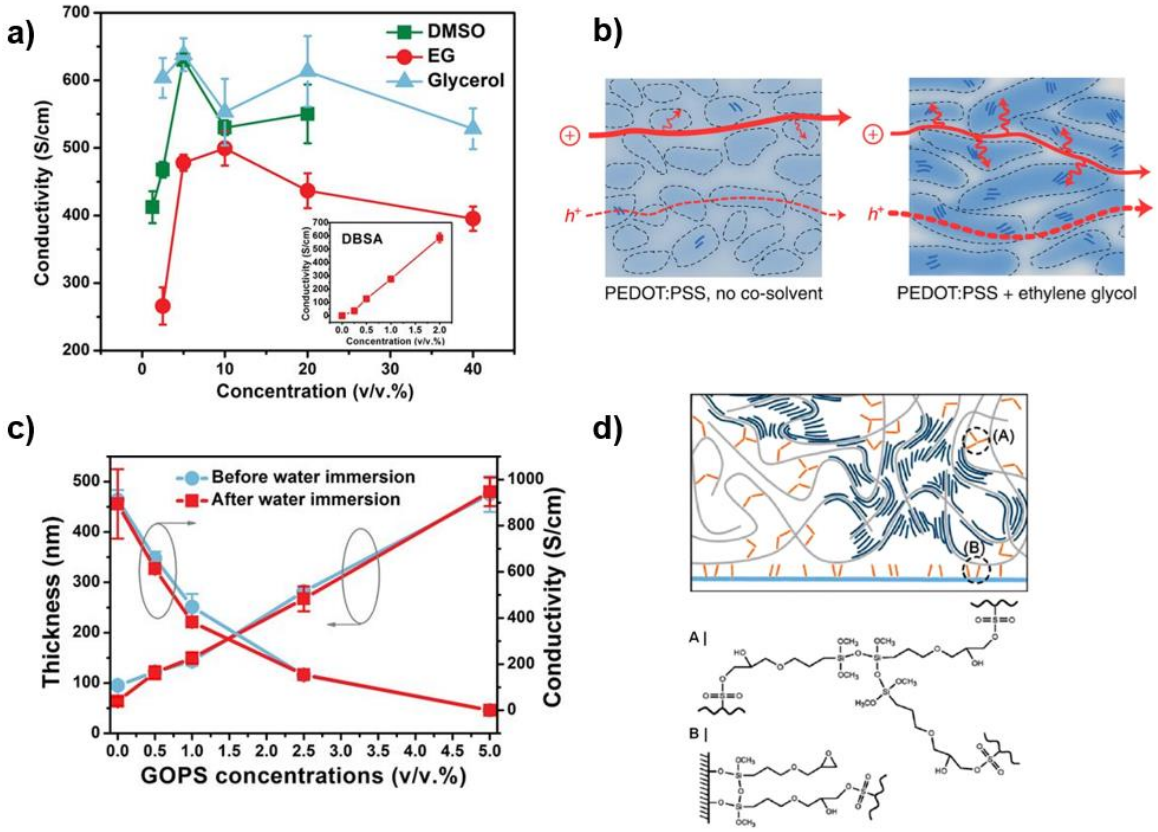

Figure 1.18: Secondary doping of PEDOT:PSS. **a)** Effect of conductivity enhancing agents with different concentrations on PEDOT:PSS conductivity.[111] **b)** Schematic highlighting the impact of ethylene glycol addition on the morphology of PEDOT:PSS and the associated changes in ionic and electronic charge carrier transport. The width of the red arrows denotes the relative ease of electronic and ionic charge carrier transport across the material.[87] **c)** Effect of GOPS concentration on PEDOT:PSS conductivity[111] and **(d)** correspondent cross linking mechanism when blended with PEDOT:PSS on a glass substrate.[116]

1.7 Modeling charge accumulation and transport in OMIECs

Although OMIEC materials have been extensively studied and explored in several applications, fundamental knowledge and accurate quantitative models of the coupled ion-electron functionality and transport are still a challenging field of research, essential for future developments and optimizations of devices based on this class of materials. Early models of dynamic systems with mixed transport have typically been based on classical electrochemical Butler-Volmer models[117] with an additional phenomenological term to account for the capacitive current.[118] More recent works have been based on the drift-diffusion approach,

assuming that charge transport in electrolyte-coupled OMIECs is mediated by the diffusion and drift (also called migration) of charged particles.[119] Diffusion occurs in the presence of concentration gradients, and is called Fickian when the probabilities for particle movement are equal in all directions, i.e., if the medium is isotropic. Drift is the movement of a particle under a driving force, such as the movement of a charged particle under an applied voltage. Since both ions and holes are charged species, one cannot a priori neglect neither their movement driven by the electrical fields inside the OMIEC layer, nor their electrostatic interactions. Preliminary works based on the drift-diffusion approach were able to reproduce some dynamic current characteristics of type I OMIECs, but fail to reproduce the experimentally observed volumetric capacitance of these materials.[119] At the same time, purely capacitive model do not successfully reproduce the ionic and electrical potential distributions in OMIEC layers when used as active materials in electrolyte-gated transistors.[120] For this reason, more complex modeling approaches have been explored in recent years, including thermodynamics-based analyses of the OMIECs charging and transport processes,[121] or quasi-field drift-diffusion models supported by in situ measurements of electrochemical (de)doping of mixed conductors.[85] Despite the variety of modeling approaches present in current literature, the interpretation of results obtained in this thesis is mostly based on the drift-diffusion model introduced by Tybrandt et al. in 2017 for type I OMIECs.[122] In that work, two distinct electrostatic potentials were assumed for the electronic and ionic phases of PEDOT:PSS (see **Figure 1.17**), and electronic properties such as the chemical potential (Fermi level) of holes were coupled to the ionic phase through a diffuse electric double layer.

1.7.1 Chemical potential–electric double layer coupling in type I OMIECs

In amorphous or highly disordered mixed conductors, such as PEDOT:PSS films, electronic transport mainly occurs by hopping or tunneling among localized states (see **sec.** Electronic transport in OMIECs**1.3**), and the hole density of states *g (E)* can be calculated through the Gaussian disorder model. Considering the fermionic nature of electronic carriers, the hole concentration *p* in PEDOT is given by the integration of the density of occupied states (DOOS):

$$p = \int_{-\infty}^{+\infty} DOOS(E)dE = \int_{-\infty}^{+\infty} \frac{g(E)}{1 + exp\left[\frac{(E - \mu_p)}{k_b T}\right]} dE \qquad 1.12$$

where *g(E)* is given by **Eq. 1.4**, k_b is the Boltzmann's constant, and μ_p is the chemical potential of holes, which can be found by solving **Eq. 1.12**. Anyway, when the carrier concentration is small (with respect to total number of states available in the HOMO band), $E_{F,p}$ can be expressed through the Boltzmann's approximation:

$$\mu_p = k_b T \ln(p) - \frac{\sigma^2}{2k_b T} + E_0 = k_b T \ln(p) + eB \quad 1.13$$

where *e* is the elementary charge and *B* a constant. The hole transport in the conjugated polymer phase can then described by a modified drift-diffusion equation (**Eq. 1.14)**, which includes the quasi-electric field arising from the shift in chemical potential due to changes in hole concentration.[123] Although the Boltzmann approximation is only accurate for lower hole concentrations (expressed in mol/cm^3), it can also be used for higher concentrations because a capacitive term dominates the system in that regime, given by the electrostatic interaction between the ionic and electronic phases, as discussed below. The ionic species ($c_\pm$) in the polyelectrolyte phase are described by the standard drift-diffusion equation (**Eq. 1.15**), and changes in concentrations are governed by the continuity equations (**Eq. 1.16** and **Eq. 1.17**):

$$J_p = -D_p \left[\nabla p + \frac{F}{RT} p \nabla \left(V_p + \frac{\mu_p}{e}\right)\right] \quad 1.14$$

$$J_{c_\pm} = -D_{c_\pm} \left(\nabla c_\pm + \frac{F}{RT} c_\pm \nabla V_c\right) \quad 1.15$$

$$\frac{\partial p}{\partial t} = -\nabla J_p \quad 1.16$$

$$\frac{\partial c_\pm}{\partial t} = -\nabla J_{c_\pm} \quad 1.17$$

where *F* indicates the Faraday's constant, and we assume isotropic diffusion using Einstein's relation $D = \mu k_b T/e$ (being μ the carrier mobility). It should be stressed that the electrostatic potential has two different distinct values within the electronic (V_p) and ionic (V_c) phases. This difference causes charging of the interface with holes and ions, thereby creating an electric double layer (EDL) with a voltage-independent volumetric capacitance (c_v) implemented through Poisson's equation

$$-\frac{\varepsilon}{e}\nabla^2 V_p = p - c_v(V_p - V_c) \quad 1.18$$

Similarly, the polyelectrolyte phase is governed by Poisson's equation (**Eq. 1.19**), with **Eq. 1.18** and **1.19** coupling the charging and transport of the electronic and ionic charge carriers:

$$-\frac{\varepsilon}{e}\nabla^2 V_c = p + c_+ - c_- - c_{fix} \quad 1.19$$

where c_{fix} indicates the concentration of fixed sulfonate acceptors on PSS. The hole concentration needs to be included in eq. 1.3.16 because a portion of the anionic charges are compensating for the holes in the electric double layer.

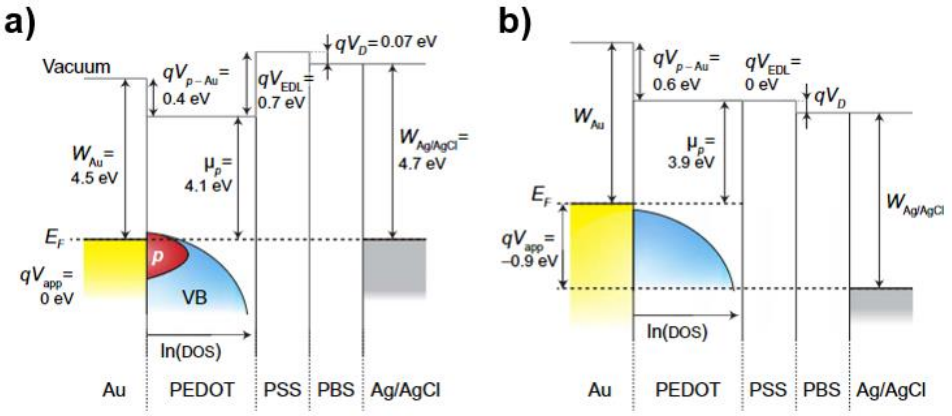

Figure 1.19: Energy diagram of a PEDOT:PSS electrode immersed in an electrolyte (PBS) with a Ag/AgCl reference electrode. The work function of pristine PEDOT is lower than that of gold, giving rise to an interface potential difference and heavy doping at V_{app}= 0 V **(a)**. The charging of the PEDOT-PSS interface creates an electric double layer, where the potential difference is approximately proportional to the hole concentration. **b)** For V_{app} =−0.9 V, PEDOT is essentially de-doped, which increases the potential at the gold-PEDOT interface while the EDL is discharged.[120]

Figure 1.19 shows the energy diagrams for a PEDOT:PSS electrode immersed in an electrolyte (phosphate-buffered saline) with a Ag/AgCl reference electrode. Two different voltages are applied: V_{app} = 0 **(a)** and V_{app}= −0.9 V **(b)**. The work function of the nonclean gold surface is set to W_{Au} = 4.5 eV and $W_{Ag/AgCl}$ = 4.7 eV. The vacuum level for the Ag/AgCl electrode is set to 0 eV as a reference. The system can be understood on the basis of three energy levels/potential differences, which depend on the doping level: the electric double layer potential difference, which causes the charging of the interface and thereby doping of the semiconductor; the chemical potential of holes, which increases with doping level; and the gold-PEDOT interface potential difference, caused by differences in the work function for gold and PEDOT. From the energy diagram, the standard boundary conditions for highly doped semiconductor-metal contacts are used for the gold-PEDOT contact (x = 0) by equating the Fermi levels:

$$E_{F,Au} = W_{Ag/AgCl} + eV_{app} = E_{F,p}(0) = k_b T \ln(p(0)) + eB + eV_p(0) \qquad 1.20$$

and by requiring charge neutrality in **Eq. 1.18**:

$$p(0) - \left[-k_b T \ln\frac{(p(0))}{e} - B + \frac{W_{Ag/AgCl}}{e} + V_{app} - V_c(0)\right] c_v = 0 \qquad 1.21$$

where we isolated $V_p(0)$ from **Eq. 1.20** and we replaced it in eq. **Eq. 1.18**. At the steady state, the hole concentration is constant throughout the film, and V_C in **Eq. 1.21** can be replaced by

the Donnan potential. In fact, the polyelectrolyte/electrolyte interface acts as a semi-permeable membrane, which can be penetrated by the mobile ions provided by the electrolyte solution but cannot be crossed by the SO_3^- fixed anions of the PSS.[124] This behavior resembles the Donnan equilibrium in semipermeable membranes, and is expressed by:

$$V_D = -\frac{RT}{F}\operatorname{arcsinh}\left(\frac{c_{fix}}{2c_{\pm}}\right) \qquad 1.22$$

This yields eq. 1.3.20, which relates the applied voltage to the steady-state hole concentration:

$$V_{app} = \frac{p}{c_v} + \frac{k_b T ln(p)}{e} + B - \frac{W_{Ag/AgCl}}{e} + V_D \qquad 1.23$$

1.7.2 Modeling PEDOT:PSS/electrolyte interfaces

The full set of equation introduced in the previous section can be solved to study the charging dynamics of PEDOT:PSS electrodes placed in contact with an electrolyte for V_{app}=0 and −0.7 V (see **Figure 1.20a** and **b**). The concentration of holes is strongly affected by the applied potential, whereas the relative change in ion concentrations is less pronounced, because the concentration of fixed counterions is much higher. For the same reason, the electrolyte/PSS

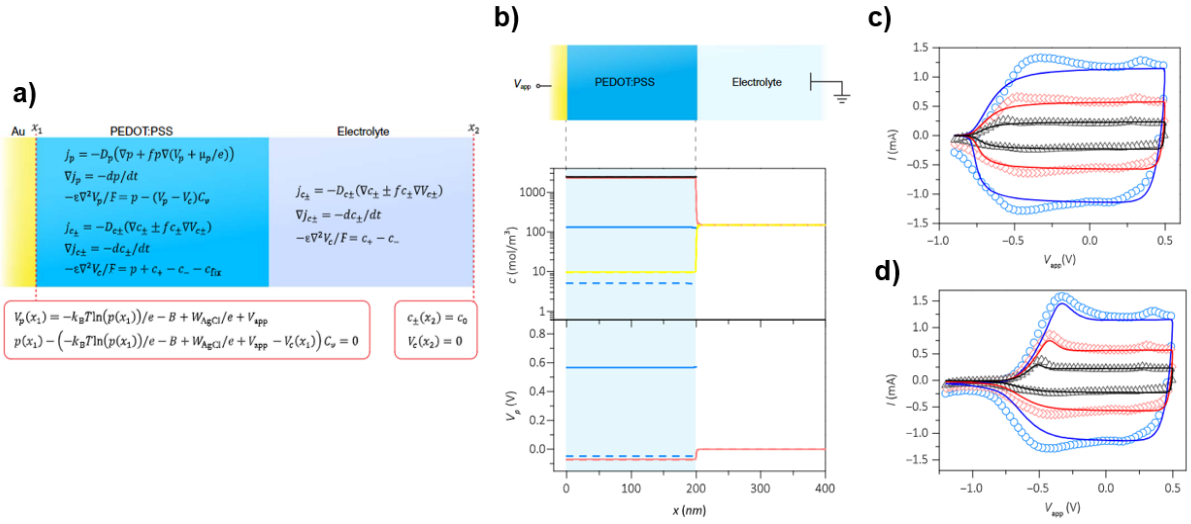

Figure 1.20: Modeling vertical ionic transport in PEDOT:PSS electrodes. **a)** The drift-diffusion, Poisson's equations and boundary conditions for a CP-PE electrode. **b)** Potentials and concentrations for V_{app} = 0 V (solid lines) and −0.7 V (dashed lines). The hole concentration (blue lines) markedly changes with the applied voltage, whereas relative changes in the cation (red lines) and anion (yellow lines) concentrations are small due to the high concentration of fixed PSS^- charges (black line). The electrostatic potential in the PEDOT phase (blue lines) changes a lot, whereas the potential in the PSS and electrolyte phases (red lines) is nearly constant. **c)** The main features of the measured cyclic voltammograms at different scan rates (○, 1.0 V/s; ◊, 0.5 V/s; and Δ, 0.2 V/s) are predicted by the model. d) By reducing the hole mobility, the commonly observed peaks in the forward scan direction can be reproduced.[120]

potential is nearly identical in both cases. Starting from these evidences, we can apply Tybrandt's model to reproduce cyclovoltammetry data acquired at different scan rates for a 600-nm-thick PEDOT:PSS film. Cyclic voltammograms of OMIECs show peaks and plateaus which are typically difficult to decouple. The model offers explanations for three of these distinct features: (1) The box-like shape curve measured for potentials higher than -0.5 V (**Figure 1.20c**) is due to the internal electrical double layer within the material. (2) The gradual decrease in current for lower potentials is a consequence of changes in the chemical potential of the semiconductor. The electrochemical de-doping of PEDOT induced by negative potentials shifts the chemical potential of holes towards the tail of the Gaussian DOS. (3) The asymmetry of the backward and forward scans observed when V_{app} is pushed up to -1.2 V (**Figure 1.20d**) is explained by slow hole transport (the mobility of holes is reduced by seven orders of magnitude). This manifests itself as a delay followed by a peak in the forward scan current. As introduced in **Sect.** 1.3.5, the de-doping of PEDOT at -1.2 V significantly reduce the carrier mobility due to the coulombic interaction with dopant counterions which localizes electronic carriers.

The drift-diffusion model introduced in this paragraph quantitatively reproduces well-known characteristics of type I OMIECs, confirming that these should be viewed as two-phase materials comprising nanostructured semiconductors embedded in polyelectrolyte matrixes. The authors used only PEDOT:PSS experimental data as a comparison with the model predictions, but other type I mixed conductors such as polypyrrole:PSS,[98] polypyrrole:DBS,[125] and polyaniline:PSS,[126] show similar CV characteristics which can be interpreted in an analogue way. Despite Tybrandt's model is restricted only to one dimension and does not consider internal phases with inhomogeneous conductivity, it provides a coherent theoretical framework which is central for the interpretation of physical processes occurring in the OMIEC applications considered in this work.

1.8 Bioelectronic Interfaces

Using electrical signals to interact with biological systems has helped us to understand different fundamental signaling principles of living organisms and to develop important therapy tools.[3] Starting from the 18th century, scientists have developed a huge variety of bioelectronic devices that offer improved healthcare and accelerate the pace of scientific progress.[2] Today, brain–machine interfaces are being developed to assist individuals with restricted mobility in controlling prosthetic limbs, and deep-brain stimulation protocols are used as a therapy to alleviate Parkinson's disease symptoms. At the same time, the pharmaceutical industry is beginning to explore "bioelectronic medicines", aiming to replace systemic administration of certain drugs with electrical stimulation from implanted devices.[127] Due to the great potential in the scientific, sanitary and biomedical fields, along with the associated economic opportunities, research interest in bioelectronics field is growing at increasing rate. This is proved by the rising number of scientific publications and citations in the period from 1985 to 2022 (**Figure 1.21**).

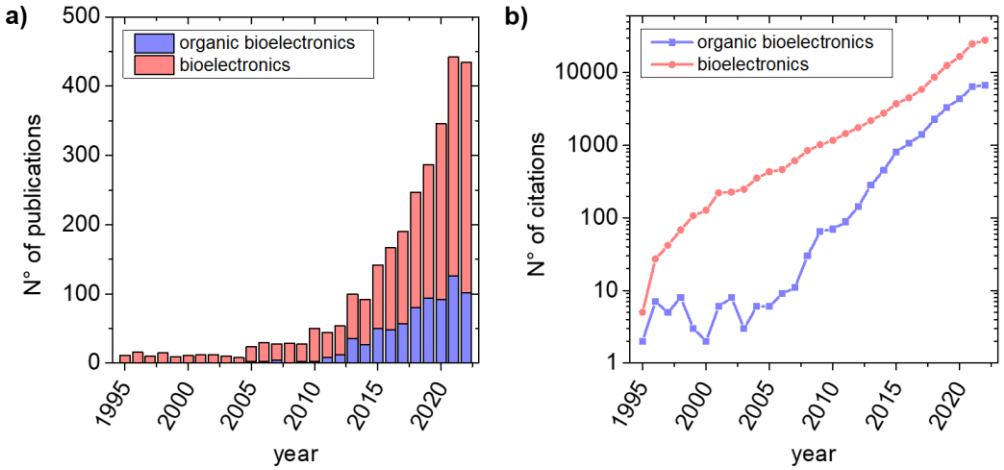

Figure 1.21: Scientific production in the Bioelectronics field, including number of publications **(a)** and literature citations **(b)**. Source: Web of Science™ Core Collection Database.

The ultimate goal of bioelectronics research is the development of highly efficient interfaces that operate as translators between the signals and functions of biology and those of human-made electronic processing systems. When employed in one translation direction, bioelectronics interfaces can be used to precisely control the physiology and functions of cells, tissues, and organs with chemical specificity and high spatiotemporal precision. In the opposite direction, bioelectronics can serve to selectively detect, record, and monitor various signals and physiological conditions within biological systems, as well as convert relevant parameters into electronic data for subsequent processing and decision-making.[128] Initially driven by the solid-state-electronics revolution, allowing to interface biological specimens with electrical devices operating beyond 1 GHz,[129] the field of Bioelectronics has experienced a breakthrough with the introduction of organic materials.[4] The "soft" nature of organics provides superior mechanical compatibility with biological tissues compared to conventional electronic materials, and their natural affinity for mechanically flexible substrates makes them suitable for nonplanar form

factors often required for implants. More importantly, the ability of organics to conduct ions in addition to electrons and holes opens up a new and highly efficient communication channel with biology.[4] For these reasons, "organic bioelectronics" has risen up in recent years as a challenging and multidisciplinary research field, involving material physics and chemistry, electrical engineering, biology, and biomedicine.

1.8.1 Signals in Biology

Bioelectricity refers to the presence of potential gradients (voltages) and the movement of charge carriers (the flow of current) within living organisms. These endogenous electric fields exist at the organelle, cellular, tissue, and organism level (**Figure 1.22**).[130] They originate from charge carrier gradients, established by the diffusion or active transport of charge across membranes.

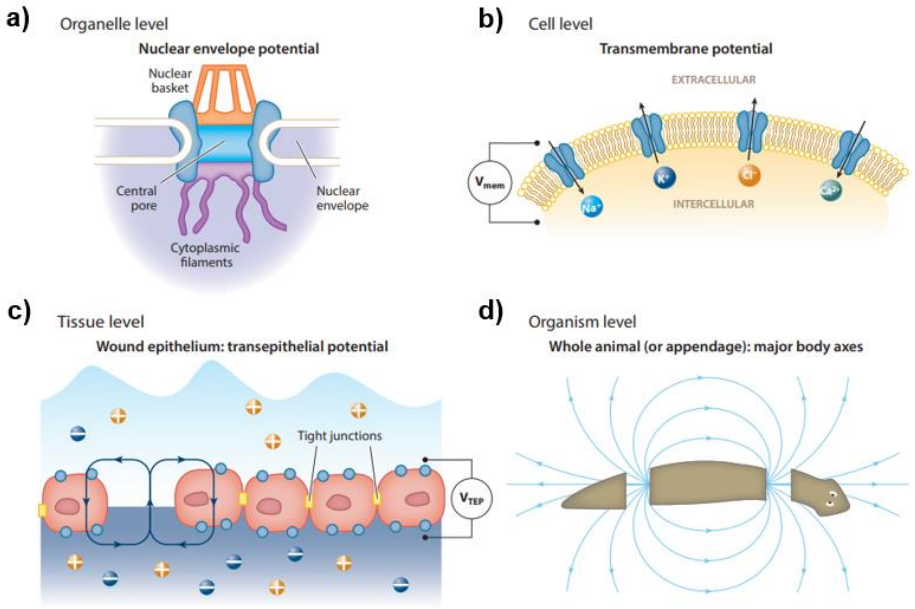

Figure 1.22: Endogenous bioelectric properties. **a)** Subcellular organelles (such as the nuclear envelope) maintain electrical potentials across their membranes. **b)** An electrical potential V_{mem} is also maintained across the cell membrane through ion channels and pumps. **c)** Cells organized into tissues drive a transepithelial potential, which gives rise to electric fields that provide a vector to points of damage. **d)** Combinations of these local and long-range properties result in gradients across entire anatomical body axes.[130]

Biosignals are associated to various molecular carriers ranging in size from small cations and neurotransmitters to giant-sized macromolecules such as DNA and proteins.[131,132] They regulate the life cycle of one individual cell as well as the function of multicellular systems such as tissues and organs. Inside an organism these signals can be transported within the blood stream (the vasculature) and along neurons.[3] The propagation of signals along neural cells is an optimal case study for bioelectric phenomena induced by the perturbation of ionic homeostasis. For electronically excitable cells such as neurons, the cellular membrane can be described using the

Hodgkin–Huxley model.[133] In this model, the cytosol of neurons is separated from the extracellular environment by the capacitive lipid bilayer (**Figure 1.23a**), while the cellular membrane is equipped with resistive, transmembrane ion-selective channels and pumps, which are capable of transferring different kinds of ions across the membrane. At the resting state, the transmembrane potential of excitable cells has a negative value (about -75 mV) mainly caused by the imbalanced ion dispersion of excessive extracellular sodium (Na^+) and intracellular potassium (K^+) ions as well as the different permeability of the cellular membrane to these ions.[134] The communication between neurons occurs through a special apposition of membranes and intermembrane machineries called synapse, which bridges the axon of one neuron (presynaptic terminal) and the dendrite of the other one (postsynaptic terminal) (**Figure 1.23b**). The chemical transmission across the synaptic cleft (width around 200–400 Å) is primarily unidirectional in the mammalian brain.[135] Close to the presynaptic terminal, there is an accumulation of vesicles filled with neurotransmitters, which are directly associated with specific neurological functions or, if misbalanced, with neurological diseases.[136] Neurotransmitters are packaged inside vesicles by the Golgi apparatus, an organelle that is a part of the endomembrane system. The vesicles remain inside the cells until a proper trigger signal (i.e., action potential) is received, forcing the vesicles to migrate toward the membrane boundary where they fuse with the outer membrane at a synapse and "burst", releasing their contents (neurotransmitters) through the process known as exocytosis.[137] The chemical substances then diffuse to the receptor sites on the postsynaptic membrane, which changes the permeability of Na^+, thus inducing an alteration of the postsynaptic potential. If this exceeds a certain threshold (≈−50 mV), voltage-gated Na^+ channels open, enabling the rapid influx of Na^+ ions into the cell, which is accompanied with a depolarization. Correspondingly, the membrane potential increases significantly to roughly 35 mV in a short time (>2ms), followed by an efflux of K^+ ions to the extracellular environment. The resulting depolarization is associated with voltage changes on the order of 100 mV (action potential) and travels along the axon at a speed up to∼100 m/s.[128] Fast transport of the neuronal signal is promoted by the partial coating of the axon with a fatty electrical insulator (myelin). In myelinated nerves, the action potential is regenerated at the so-called Nodes of Ranvier, found in between the myelin sheets, until it reaches the axon terminal and triggers neurotransmitter release.

Other signals affecting the shape and functionality of cells may originate from the extracellular environment.[138] These interactions between cells and biological or artificial surfaces are facilitated by intrinsic protein complexes, including cell adhesion molecules like integrins, intermediary filaments such as F-actin bundles, and versatile adhesive matrix proteins like fibronectin.[139] When combined with intracellular signaling within the organ and signals from other tissues, these factors collectively influence the overall structure and morphology of a tissue, highlighting the intricate nature of signaling in biological systems.

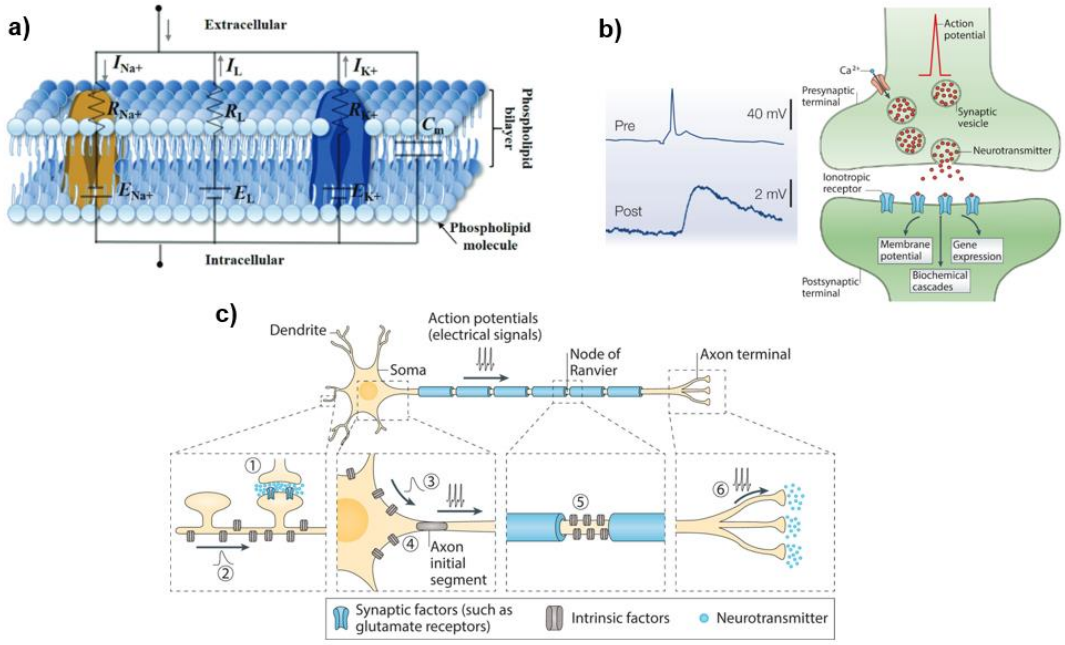

Figure 1.23: Mechanism of propagation of neural signals. **a)** Hodgkin–Huxley equivalent circuit model for the cellular membrane. **b)** Signal propagation between the pre-synaptic and the post-synaptic cells. The action potential at the presynaptic terminal causes vesicles to migrate toward the synaptic cleft and release their contents. **c)** Mechanism of propagation of signals along a neural cell. Adapted from [128,134].

1.8.2 The electrode/electrolyte interface

Highly efficient recording and stimulation of the electrical activity in biological system is a central objective of bioelectronics research. When an electrode is placed inside a physiological medium such as extracellular fluid (ECF), an interface is formed between the two phases. In metallic electrodes and in the attached electrical circuits, charge is carried by electrons. In the physiological medium, or in more general electrochemical terms the electrolyte, charge is carried by several entities, mainly ions, including sodium, potassium, and chloride in the ECF. The central process that occurs at the electrode/electrolyte interface is a transduction of charge carriers from electrons in the electrical circuit to ions in the electrolyte. In the simplest system, two electrodes are placed in an electrolyte, and electrical current passes between the electrodes through the electrolyte. One of the two electrodes is termed a working electrode (WE), and the second is termed a counter electrode (CE). The working electrode is defined as the electrode that one is interested in studying, with the counter electrode being necessary to complete the circuit for charge conduction. An electrophysiology experiment may also contain a third electrode termed the reference electrode (RE), which is used to define a reference for electrical potential measurements.[140] During bioelectronics recording and stimulation, changes in the electrical potential occur upon crossing from the electrode to the electrolyte in a very narrow interphase region, thus forming an electric field at the interface. This change in potential exists even in the equilibrium condition (no current). Electrochemical

reactions may occur in this interphase region if the electrical potential profile is forced away from the equilibrium condition. In the absence of current, the electrical potential is constant (no gradient) throughout the electrolyte beyond the narrow interphase region. During current flow, a potential gradient also exists in the electrolyte, generally many orders of magnitude smaller than at the interface.

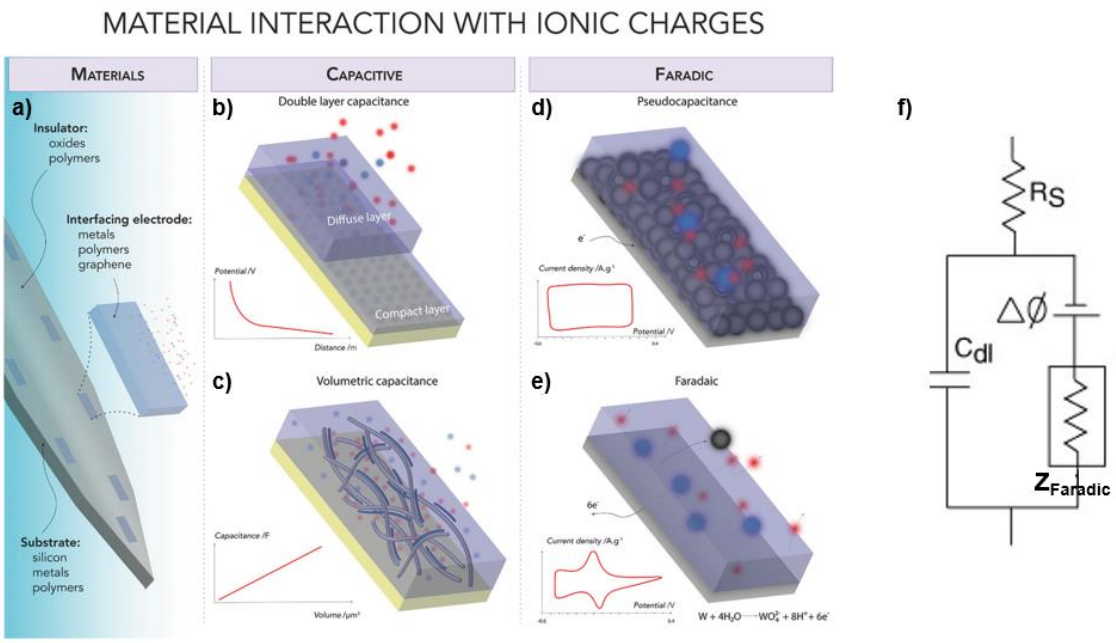

Figure 1.24: The electrode/electrolyte interface. **a)** A bioelectronics probe can be composed by different materials, ranging from metals to conductive polymers. The electrode substrate can be rigid to penetrate soft tissues or flexible to reduce invasiveness and improve biocompatibility. **b)** Capacitive coupling between the electrode and the surrounding electrolyte. The electrode material is represented in yellow, and a positive potential is applied. A first solvation layer (i.e., compact layer) is presented as a light blue volume with anion densely packed (blue spheres) close to the electrode surface. A second layer, also known as the diffuse layer, is presented as a section of light blue volume of electrolyte with both anions and cations (red spheres). **c)** Capacitive coupling by volumetric capacitance and its corresponding characteristic properties. The backing metallic electrode is presented in yellow and a PEDOT:PSS coating is represented using PSS fibers (light grey) and PEDOT aggregates in dark blue. The polymer structure swells in the electrolyte, which is represented in a light blue volume. **d**) Faradic coupling by pseudocapacitance and its characteristic properties. The example of a platinum electrode is presented, where platinum atoms are represented in solid black spheres, adsorbed protons are small dark-red spheres, Pt:H_{ads} atoms are represented as modified black spheres with a concentric shell, and water molecules are light blue, larger spheres. Although electrochemical reactions occur, the CV characteristic plot is similar to a pure capacitive material. **e)** Faradaic reaction. The electrode material presented in this example is Tungsten (light grey material). The volume of electrolyte in which the electrochemical reaction is happening is represented in the light blue volume. Water molecules are schematized by the large blue spheres, the proton in small dark red spheres and the tungsten oxide is presented dark solid sphere.[143] **f)** Equivalent circuit for the electrode/electrolyte interface.

There are two primary mechanisms of charge transfer at the electrode/electrolyte interface, illustrated in **Figure 1.24**. One is a non-Faradaic (or capacitive) reaction, where no electrons are transferred between the electrode and electrolyte. Non-Faradaic reactions include redistribution of charged chemical species in the electrolyte. The second mechanism is a Faradic

process, in which electrons are transferred between the electrode and electrolyte, resulting in reduction or oxidation of chemical species in the electrolyte. These can be divided into Faradaic or pseudocapacitive processes according to the reaction kinetics.

Capacitive charge transfer: if only non-Faradaic redistribution of charge occurs, the electrode/electrolyte interface may be modeled as a simple electrical capacitor called the double layer capacitor C_{dl} (**Figure 1.24b**). This capacitor is formed due to several physical processes.[141,142] First, when an electrode is placed in an electrolyte, charge redistribution occurs as metal ions in the electrolyte combine with the electrode. This involves a transient transfer of electrons between the two phases, resulting in a plane of charge at the surface of the electrode, opposed by a plane of opposite charge, as "counterions", in the electrolyte. A second reason for formation of the double layer is that some chemical species such as halide anions may specifically adsorb to the solid electrode, acting to separate charge. A third reason is that polar molecules such as water may have a preferential orientation at the interface, and the net orientation of polar molecules separates charge.[140] Capacitive charging is quite fast, with minimal redistribution of ions required to create the potential at the material surface. As an example, consider a +2 mV local field potential produced by a set of neurons recorded by a 10 µm diameter electrode with C_{dl} = 10 µF/cm^2. The number of excess positive charge required to accumulate at the surface from this potential is ≈10 000 ions, which is negligible compared to the ≈10^{12} ions/µm^3 present in physiological solutions. Indeed, this represents moving all the positive ions within 0.1 fm above the electrode to the surface, which is less than the diameter of a hydrogen atom.[143] The impedance of a capacitor is frequency dependent, $Z = 1/j\omega C$, implying the electrode is more effective at picking up higher frequency signals. Since the capacitance per unit area of metallic electrodes is relatively constant, engineering lower impedance is done by increasing the surface area, at the cost of losing spatial resolution. For this reason, bioelectronics microelectrodes based on organic mixed ionic electronic conductors can achieve higher signal-to-noise ratios due to their capacitive charge accumulation in the entire film bulk (**Figure 1.24c**).

Faradic charge transfer: charge may also be injected from the electrode to the electrolyte by Faradic processes of reduction and oxidation, whereby electrons are transferred between the two phases:

$$O + ne^- \leftrightarrow R \qquad 1.24$$

Reduction, which requires the addition of an electron, occurs at the electrode that is driven negative, while oxidation, requiring the removal of an electron, occurs at the electrode that is driven positive. Unlike the capacitive mechanism, Faradic charge injection forms products in solution that cannot be recovered upon reversing the direction of current if the products diffuse away from the electrode. Such possibility naturally divides Faradic processes into reversible and irreversible reactions.[144] The degree of reversibility depends on the relative rates of kinetics (electron transfer at the interface) and mass transport. In a Faradaic reaction with slow kinetics

(**Figure 1.24e**), large potential excursions away from equilibrium are required for significant currents to flow. In such a reaction, the potential must be forced very far from equilibrium before the mass transport rate limits the net reaction rate. In the lengthy time frame imposed by the slow electron transfer kinetics, chemical reactants can diffuse to the surface to support the kinetic rate, and product diffuses away quickly relative to the kinetic rate. If the direction of current is reversed, product will not be reversed back into its initial (reactant) form, since it has diffused away within the slow time frame of the reaction kinetics. Diffusion-limited faradaic reactions can alter the functionality of bioelectronics interfaces as there is a limited potential window in which the reaction can take place before the electrolysis of aqueous media occurs.[145] Such detrimental process can create reactive species such as O_2^- and change local pH.[146] Thereby, bioelectronics electrodes must be used within the "safe" water window range designated for each material. This usually only affects their use for stimulation, where larger currents are necessary.

On the other hand, a Faradaic reaction with very fast kinetics relative to the rate of mass transport is reversible. With fast kinetics, large currents occur with small potential excursions away from equilibrium. Since the electrochemical product does not move away from the surface extremely fast (relative to the kinetic rate), there is an effective storage of charge near the electrode surface, and if the direction of current is reversed then some product that has been recently formed may be reversed back into its initial (reactant) form. Such behavior is often referred as pseudocapacitive (**Figure 1.24d**), as it appears like a capacitor with large hysteresis, but in fact it results from a series of electrochemical reactions occurring at different potentials. A classic example for this process is given by hydrogen atoms adsorption occurring in platinum electrodes: $Pt + H_3O^+ + e^- \rightarrow Pt{:}H_{ads} + H_2O$, where the voltage required depends on the surface coverage of the H^+.[147] The differential capacitance is given as $C = dQ/dV$ and quantifies the change in redox states available per unit voltage.

As Faradic and capacitive electrode processes are not mutually exclusive, the charging properties of the electrode/electrolyte interface can be simplistically modeled with the equivalent circuit in **Figure 1.24f**. Faradic processes are represented by a resistor indicating the flow of electrons at the interface. A voltage generator $\Delta\phi$ is also added as the equilibrium potential E_{eq}

$$E_{eq} = E^{\theta} + \frac{RT}{nF} ln\left\{\frac{[O]}{[R]}\right\} \qquad 1.25$$

associated to the process in **Eq. 1.24** is generically different from zero.[148] Finally, the resistance R_s models ionic charge transport in the electrolyte bulk between the working and counter electrode.

1.8.3 Organic materials for biointerfaces

Biological events involve controlled ionic fluxes in an aqueous environment. Constructing devices that sense or trigger biological events therefore requires the use of materials that are not only biocompatible but also transduce biological signals into electrical ones and vice versa. The effectiveness and long-term stability of bioelectronics devices is therefore determined by the different electrochemical processes that can take place at electrode/electrolyte interface. Highly efficient biointerfaces avoid the onset of irreversible Faradaic processes which may potentially create damaging chemical species, and keep the injected charge at a low enough level where it may be accommodated strictly by reversible charge injection processes. Consequently, a major requirement to be asked to the material acting at biotic/abiotic interface is to generate electrode processes that transduce signals by charging and discharging of electric double layers.[128] The measure of how easily the conversion between electronic and ionic currents is performed is given by the impedance of the electrode.[149] To achieve low impedance characteristics per electrode area, a high amount of charge needs to be stored at the interface and the interface needs then to be easily accessed by the ions from the electrolyte. Current electrode technologies use materials such as metals and inorganic semiconductors, where ionic-electronic coupling occurs only at the electrode surface. Capacitive charging processes are furtherly limited by oxide layers that often appear after material cleavage and exposure to atmosphere.[2] As a consequence, the information transfer between the realms of biology and electronics is limited, diminishing the scope and lifetime of the bioelectronic system.

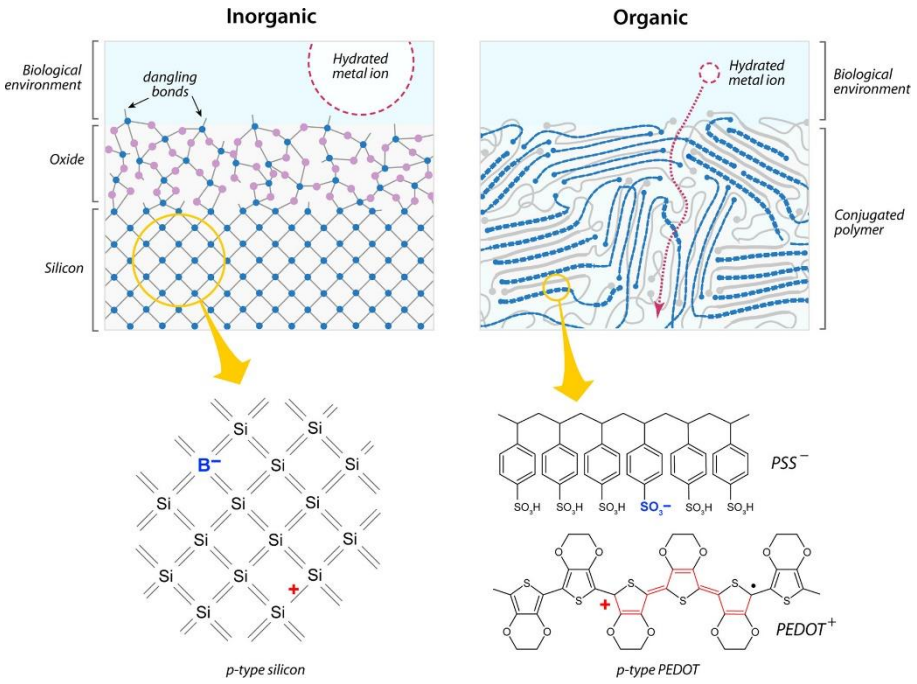

Figure 1.25: Schematics of an inorganic semiconductor, silicon, and an organic semiconductor, PEDOT, at the interface with an electrolyte. The hydrated ion is meant to be the same in both schematics, defining the relative scale. The insets show the action of p-type dopants, boron in silicon, and PSS in PEDOT.[2]

A significant improvement can be obtained using organic mixed ionic-electronic conductors as active materials for biointerfaces. This is evident from **Figure 1.25**, showing schematics of silicon and of an OMIEC material (PEDOT:PSS) in contact with an electrolyte solution. Both materials are p-type doped, silicon with boron and PEDOT with poly(styrene sulfonate) (PSS). A solvated ion is shown in the electrolyte to define a relative scale. Silicon is held together by a network of covalent bonds, where each atom shares valence electrons with four neighbors. In contrast, PEDOT:PSS has covalently bounded (macro-)molecular blocks (typically planar, rigid aromatic repeated units that create a macromolecular conformation) which are held together by weak van der Waals intermolecular interactions, together with dipolar and electrostatic interactions between the charged conjugated polymer and polyelectrolyte phases.[150] The resulting soft polymeric matrix offers a oxide-free electrolyte interface which allows for the exchange of ions between the biological milieu and the bulk of the electronic material. Thereby, in organic mixed conductors, the whole volume of the film, not just its surface, electrically interacts with the biological environment. As a consequence, OMIEC-based electrode coatings achieve a volumetric capacitive coupling with the surrounding electrolyte, reducing the impedance of biointerfaces by order of magnitudes,[151] and minimizing "unsafe" Faradaic charge injection during their operation.[152]

Another relevant advantage of organic materials for bioelectronics is their superior mechanical compatibility with the soft biological tissues,[153] as reported in **Figure 1.26a**. When inorganic materials operate at biointerfaces, the mechanical mismatch between the implanted device and local tissue can result in the formation of a foreign-body response, where the body effectively tries exclude the implanted device through an inflammatory response.[154] Such process is especially detrimental for chronic in-vivo applications, resulting in the formation of scar tissues around devices which effectively insulate them from the biological system (**Figure 1.26b**).[155] Given their smaller Young modulus (in the order of 10 MPa to 3 GPa),[156] flexibility,[157] and stretchable properties,[158] OMIECs not only reduce the mechanical mismatch at biointerfaces, but also are naturally compatible with mechanically flexible and stretchable substrates, suiting the nonplanar form factors often required for low-invasive implants.[4] Mechanical compatibility plays a major role also in in-vitro experiments. At a cellular level, cells directly sense the mechanical nature of their microenvironment through complex mechanotransduction machinery. Minor changes in material stiffness or surface properties can result in profound changes in cellular phenotype.[159] Hence, the ability to tune these properties is important for cell sensing and cell stimulating applications. Conjugated polymers, modifiable both intrinsically through chemical synthesis and extrinsically through subsequent material processing, are therefore well-suited to the development of cell and tissue stimulating interfaces.

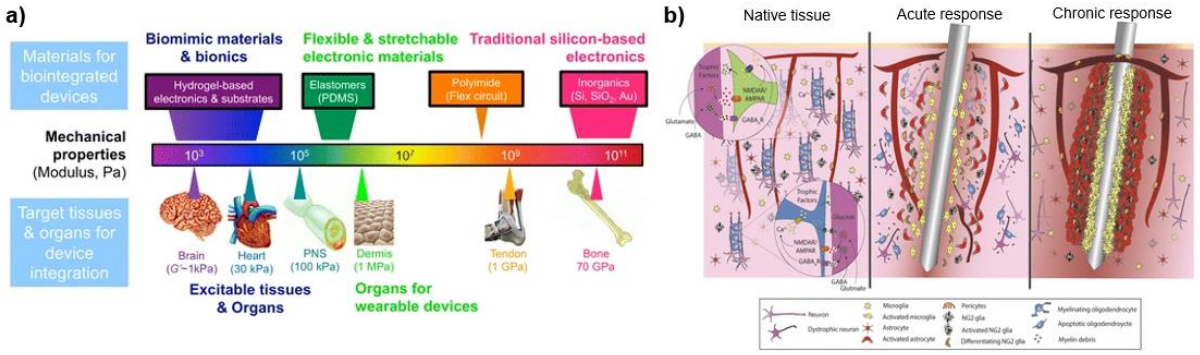

Figure 1.26: a) Mechanical properties of tissues compared with materials used for biointerfaces.[153] **b)** Foreign-body response caused by the implantation of a penetrating neural probe. The chronic immune response leads to the formation of a glial cell layer and angiogenesis which insulate the metallic electrode.[155]

Low temperature processing and facile chemical modification are typical properties of organics, much exploited in organic light emitting diodes and solar cells to endow features such as low-cost fabrication through roll-to-roll processing techniques, as well as and tunable optical absorption/emission spectra.[2] Decades of research has helped develop structure–property relationships between the polymer molecular structure and its optoelectronic properties.[160] These properties are also applicable in bioelectronics. Low-temperature processing allows the fabrication of devices with novel form factors, such as transistors integrated on woven fibers.[161] Conjugated polymers can be chemically altered to tailor material properties, for example, from hydrophobic to hydrophilic, allowing the formation of semiconducting and conducting inks, which facilitate solution-processing fabrication techniques.[162] A wide-range of manufacturing techniques can be used to process conjugated polymers into devices, ranging from cleanroom-based manufacture, to desktop printing technologies, and more. These manufacturing approaches lend themselves well to the production of affordable, electronic, point-of care diagnostic tests, that fulfil the requirements set out by the diagnostics research community.[163] Conjugated polymers are not only patternable in 2D, but also via 3D printing methods.[164] Highly conjugated polymers can be patterned onto flexible plastics, glass, paper, or incorporated directly into composite gel systems.[165] They can be drawn into fibers, nanofibers, or used to coat existing fibers which can subsequently be woven into organic electronic fabrics.[166] The variety of intrinsically weak bonding interactions present between adjacent polymer chains can be harnessed through a variety of approaches to form "self-healing" systems, namely where a previously cut or damaged material can reform their initial network.[167]

In organics, excitations couple strongly to the structure of the molecule, and by extension, of the film. In silicon, the presence of electronic charge does not modify the lattice appreciably, as atoms are bonded with each other in a 3D manner. In contrast, removing an electron from a thiophene chain in PEDOT:PSS causes part of the chain to revert from an aromatic to a quinoid structure.[11] When doping is performed in an electrolyte solution, the corresponding uptake/release of ions can cause large dimensional changes in the organic film. The corresponding variations in both optical and mechanical properties upon have been used to great advantage for making electrochromic displays[168] and actuators for artificial muscles,[169]

respectively. At the same time, the semiconducting properties of OMIECs make them well suited to building devices such as transistors, which can act as amplifiers, transducing small voltage changes into large changes in current.[170,171]

This unique material property combination makes OMIECs as principal candidates for biointerfaces in future bioelectronic devices. The crosstalk between electronics and biology works in two directions, as depicted in **Figure 1.27**: on one side, a biological process or reaction can transfer a signal to an organic electronic device (for example an enzymatic reaction that leads to a current modulation in a polymeric transistor);[16] on the opposite, an organic electronic device can stimulate a biochemical reaction or process (i.e. the polarization of a conducting polymer electrode stimulates a neural potential action).[172] In the former, the device acts as a sensor, transducing an analyte/ion/chemical variation in an electric output, while in the latter it behaves as an actuator, electrically stimulating a biological response.[173]

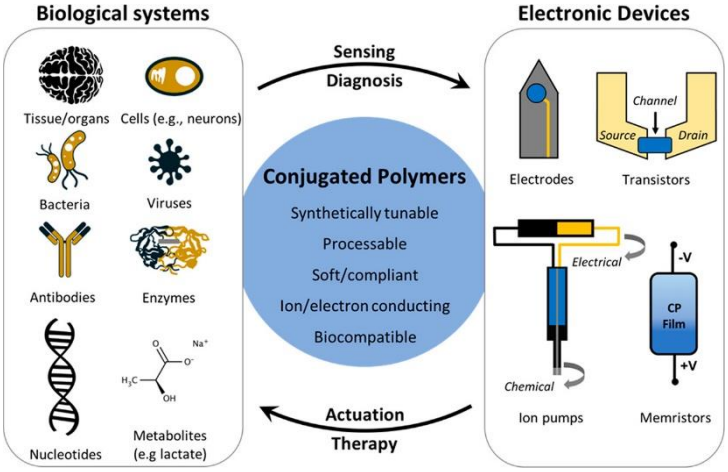

Figure 1.27: Scheme representing the bidirectional interaction between electronic devices and biological systems in bioelectronics. The gap between the two different worlds is bridged by conducting (conjugated polymers, whose unique features allow the development of state-of the-art devices used for sensing and actuation in biomedical, research and sanitary fields.[127]

A wide variety of device architectures has been developed to mediate bidirectional interactions with biology, ranging from electrodes,[149] scaffolds,[174] and actuators[169] to transistors[175] and ionic pumps.[18] The following chapters will examine the bioelectronic realizations explored in this thesis, studying both the material and device physics that govern their functionality, and the resulting applications. The overall emphasis will be put on how quantitative approaches can lead to a deeper comprehension on material operation and device functionality, leading to a rational optimization of bioelectronics interfaces for future biomedicine.

1.9 Neural recording and stimulating electrodes

Neurologic disorders account for 7% of total global burden of disease measured in disability-adjusted life years, with just under half of this sum attributed to neuropsychiatric disorders (including Alzheimer's disease, Parkinson's disease, and epilepsy), and the rest to cerebrovascular diseases.[176] The social and economic burden of these diseases has motivated and continues to motivate technological advance and development in neuroengineering, medicine, and fundamental science.[172] To date, these tools, combined with pharmacology, have been the workhorse of interventional and observational neuroscience research. The past decade, in particular, has seen an explosion in neuroscience research, driven by improved methods and devices, and by the development, distribution, and creative application of novel neuromodulatory and observational tools that have allowed for cell type–specific manipulation in model organisms. The refined use of electricity in neuroscience, usually with electrodes, has furthered our knowledge of how the brain collects sensory input from the environment, processes this information in the context of experience, and controls the rest of the body in response. Therapeutically, there are established and safe interventions to interrupt or stimulate defined targets in patients with Parkinson's disease[177] or essential tremor,[178] and there are clinical trials for obsessive compulsive disorder[179] and major depressive disorder.[180] Moreover, electrodes and arrays have seen impressive closed-loop applications for patients with spinal cord injury.[181] Recent advancements demonstrate how the communication between the brain and spinal cord in individual with chronic tetraplegia can be restored with a bioelectronic digital bridge enabling the patient to stand and walk naturally in community settings for more than one year.[182] These remarkable achievements, as well as future progresses in the field, result from the development of devices and materials allowing the efficient modulation of electrophysiology signals. A short introduction on how such modulation is provided is discussed in the next paragraphs.

1.9.1 Recording neural activity

A recording electrode operating at neural interfaces typically experiences the superposition of electrical excitations arising from two biological signals: single cell action potentials, and local field potentials (LFPs).[183] The electric fields at the electrode surface can vary greatly depending upon the spatial arrangement relative to the neurons and synapses. Single cell ("unit") activity consists of trains of extracellular action potentials (APs), typically 100–200 μV in amplitude and a few milliseconds per spike (see **par. 1.8.1** and **Figure 1.23**). These processes create ionic currents and voltages both across the membrane as well as in the extracellular space outside the cell (**Figure 1.28a**). This extracellular potential decays rapidly away from the cell body (soma) or axon where it is generated, requiring electrodes to be quite close to the cell, typically within 50–100 μm.[143] Remarkably, very little ionic flux is needed to create a typical AP. Na^+ concentration increases of 0.05% in the cell body can create significant electric fields. In regions dense with neurons, electrodes can often pick up more than one active

neuron at once, requiring spike sorting algorithms to determine which AP "spike" belongs to which cell and revealing correlations between cells.[184]

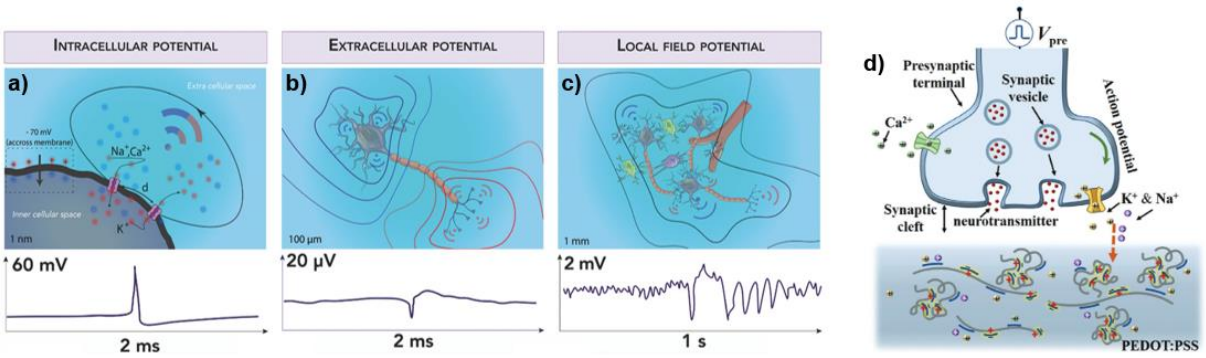

Figure 1.28: Recording of neural electrophysiology signals. **a)** Intracellular potential and corresponding electrical field. A dipole comprising two ion channels (source and sink) are represented with ions (anion in blue and cation in red). The equipotential field lines are represented in black. **b)** Extracellular potential and corresponding electrical field. The red and blue contour equipotential lines correspond to positive and negative values for the Local field potential (LFP) amplitude, respectively. The equipotential lines are the result of the summation of the fields generated by the multipole ion channel. **c)** LFP from a small population. Neurons, astrocytes (purple), microglia (green), and a blood vessel section are presented. The LFP is represented by black thin lined. **d)** Schematic of a biological synapse induced by an action potential arriving at the PEDOT:PSS terminal. The injection of cations in the organic film results in the de-doping of PEDOT (no shining yellow color). Adapted from [143, 134].

The concurrent activity of all the electrically active cell regions, including soma, axons, dendrites, and synapses, sum together to create the "local field potential," or LFP (**Figure 1.28c**).[185] Ionic imbalances due to the superposition of ion channel activity lead to electric fields throughout the brain tissue, and surface fields are often recorded with an electroencephalogram (EEG) on the scalp, or electrocorticography (ECoG) on the brain surface.[183] By using biocompatible, capacitive coupled, low-impedance OMIEC-based electrode coatings (see **par. 1.8.3**), such ionic imbalances induce the injection/removal of ions from the biological medium into the polymeric matrix. This process compensates intrinsic charges of the bulk polymer and affects its doping level and thus the electronic conduction (**Figure 1.28d**), producing a signal measurable with the supporting electronics.[134] Unlike APs, LFP signals are typically much larger amplitude (approximately millivolts), wider frequency range (≈5–1000 Hz), and have relatively homogeneous magnitudes over distances of ≈500 µm.[186] LFPs are not produced uniformly even within a single cell; typically individual cells create strongly dipolar fields (**Figure 1.28b**), with a predominantly negative potential near the cell body, and positive potentials near the dendritic arbors and synaptic connections.[185] LFPs have a critical role in coordinating the activity of different regions of the brain, and synchronizing the activity of individual neurons with that of a neural network, through phase locking to the global rhythm.[187] For example, theta- frequency (4–8 Hz) oscillations and phase-locked discharge of neurons to theta waves are found in the hippocampus and some cortical areas, providing potential mechanisms to synchronize neuronal assemblies involved in complex processes and functions of the brain, such as memory formation and neuroplasticity.[188] Recent

experimental and computational analysis have also shown that LFPs in the hippocampus can indicate animal position as accurately as single unit recordings of place cells,[189] demonstrating the signal is fundamentally connected to local neural behavior.

1.9.2 Stimulating neural activity

Electrodes can not only detect signals from nearby neurons but can also stimulate neuronal activity by injecting current into the surrounding extracellular region.[140] The resulting electric field gradients can induce APs, and influence the LFP.[190] Low-impedance electrodes (<100 kΩ) are highly desirable for stimulation electrodes, allowing more current to be passed at lower voltages and avoiding irreversible electrochemical reactions with possible toxic byproducts. The figure of merit of a stimulating electrode is the charge injection capacity (CIC), typically given in mC/cm^2, which measures the amount of charge the electrode is capable of passing per unit area at a voltage within the water window (e.g., without irreversible electrochemical reactions). **Table 1** reports an overview of the impedances per unit area at 1 kHz (e.g., specific impedance) and the CIC for a wide range of electrode materials. Since many of these materials are either highly porous (CNT structures) or volumetric capacitors (PEDOT), the total surface area within a given volume is necessary to accurately calculate specific impedance. Moreover, variations in processing conditions can greatly influence the actual surface area for the same material, or even from run-to-run, making comparisons between publications purely indicative.[143]

Material	Specific impedance at 1 kHz [MΩ μm²]	Charge injection capacity [mC cm⁻²]	Mechanism
PEDOT:PSS	2	15	Capacitive, volumetric
Carbon nanotube (CNT) fibers	20	6.52	Capacitive
Pt/lr	454	0.15	Faradaic
Liquid crystal graphene oxide (LCGO)	49	46	Capacitive, volumetric
Porous graphene	312.5	3.1	Capacitive
Tungsten coated with CNT	16	0.5	Capacitive
CNT/PoIypyrroIe	77	7.5	Capacitive
Iridium oxide (SIROF)	2	5	Faradaic
Platinum	314	0.26	Pseudocapacitive
Tungsten	474	–	faradaic
Au	160	–	Capacitive
TiN	40	0.87	Capacitive
Pt black	15	–	Capacitive

Table 1: Specific impedance and charge injection capacity (CSC) for a number of neural electrode materials. Among various candidates, PEDOT:PSS offers minimum specific impedance and large CSC due to its volumetric charging at biointerfaces. The full list of references is available at [143].

For electrical stimulation, a variable electrode impedance can change the distribution across the circuit of the voltage supplied by a stimulator between the working and counter electrode. When soft conductors of limited electrical conductivity are used as interconnects, the amount of voltage dropped before the electrode-tissue interface can be significant and comparable to the voltage required for charge injection at the interface.[191] This translates into a variation of the voltage required to access the electrode interface (referred to as access voltage). Practically, for a set stimulation voltage, different mechanical and electrochemical conditions change the number of charges that are injected at the electrode-tissue interface. This variation can be more or less significant depending on the gauge factor of the soft conductors and on the electrochemical and mechanical stability of the whole implant. To ensure reproducible stimulation effect, it is therefore important to deliver current-controlled stimulation protocols.[140]

In this case, a current pulse is injected between the working and counter electrode, delivering a fixed amount of charge given by the current amplitude times the pulse width. The current generator in the electronic system adjusts the voltage supply to deliver the selected pulse, ensuring that the amount of charge injected at the electrode interface is consistent. Typical pulse waveforms with pulse parameters are shown in **Figure 1.29a** and **b**.

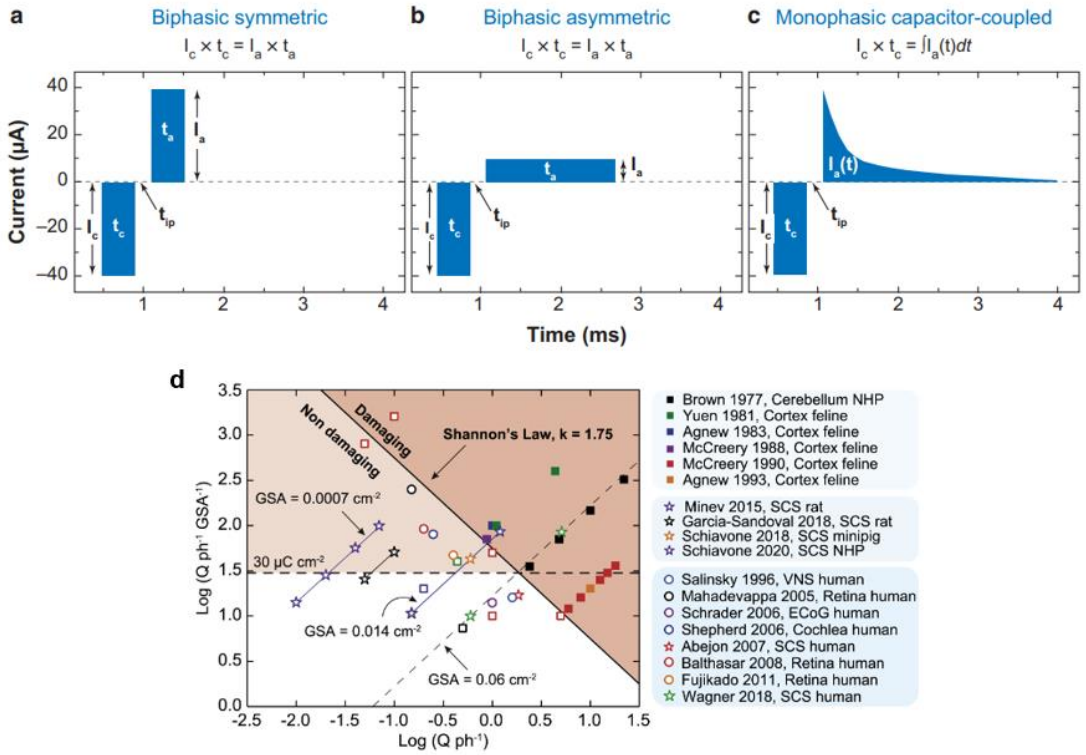

Figure 1.29: a,b,c) Typical charge-balanced, current waveforms used in neural stimulation. The parameters vary widely depending on the application and size of the electrode. Waveform parameters usually falling in the range of I_c (cathodic current), 1 μA − 10 mA; I_a (anodic current), 1 μA − 10 mA; t_c (cathodic half-phase period), 50 μs – 4 ms; t_{ip} (interphase dwell), 0 – 1 ms; and t_a (anodic half-phase period), 50 μs – 10 ms. **d)** Shannon's plot (k = 1.75) discriminating damaging and non-damaging stimulation protocols. Adapted from[143, 140].

Each pulse has cathodic (or cathodal) and anodic (or anodal) phases, with current amplitudes and durations that result in an overall zero net charge for the pulse (charge-balance). A cathodal current is reducing at the stimulation electrode, with the direction of electron flow being from the electrode to the tissue. As an example, when p-type OMIEC materials such as PEDOT:PSS are used as neural interfaces, this corresponds to the injection of holes from the underlying metallic electrode and ejection of cations from the polymeric matrix into the cellular environment. Anodal indicates an oxidizing current with electron flow in the opposite direction. The charge delivered is the time integral of the current, which is simply $i_c \cdot t_c$, for a cathodal constant-current pulse of magnitude i_c and pulse width t_c. Charge-balance with intramuscular electrodes and electrodes that interface with the peripheral nervous system is sometimes achieved by a capacitor discharge circuit, leading to a monophasic, capacitor-coupled waveform, which is also shown in **Figure 1.29c**. A number of variations on biphasic current waveforms are possible and have been described in several experiments.[192,193] For physiological reasons, the leading phase is usually cathodal, although anodal–first pulsing may more efficiently activate populations of some neural elements.[194] The importance of a charge-balanced waveform in avoiding damage to electrodes and surrounding tissue has been recognized for many years. Besides charge balance, stimulus waveforms must be limited to current and charge densities that allow charge injection by reversible processes, which inject cathodic or anodic charge at a finite rate. At the same time, an excessive current or charge density can induce irreversible tissue damage in in-vivo experiments.[195] Regarding this aspect, an empirical framework was introduced by Shannon, with an equation that defines a boundary between damaging and non-damaging levels of electrical neurostimulation:

$$log\left(\frac{Q}{A}\right) = k - log\,(Q) \qquad 1.26$$

where Q is the charge per phase (C) of the designed stimulation pulse, A is the electrode geometrical surface area (GSA, cm^2) and k is an adjustable parameter, typically chosen between 1.5 and 2.0.[196] Shannon's equation for $k = 1.75$ is plotted in **Figure 1.29d**, with the damaging and non-damaging regions highlighted. Shannon's equation is based on histological observations reported in several *in vivo* studies (square data points in **Figure 1.29d**), where stimulation protocols above the equation line (solid data points) proved to be damaging to the tissue, while those below the line did not cause damage (hollow data points). In practice, when an in-vivo experiment is performed, the electrode geometry is generally designed according to the intended application, so as to interface specific neural structures. Once the GSA is fixed, Shannon's plot provides safety guidelines to decide the maximum charge allowed per stimulation pulse

$$Q_{max} = \sqrt{10^k \cdot A} \qquad 1.27$$

It is important to point out that to date there is no agreed, mechanistic model for tissue damage due to electrical stimulation. Moreover, when implanting devices in the body, the surgical protocols, mechanical properties, and stabilization of the implant, its surface chemistry and

conditions of use, as well as inter-subject variability, are all factors that can influence the immune response and tissue damage in the host, as shown in the examples of **Figure 1.29d**. Isolating the damage caused exclusively by electrical stimulation is therefore not an easy endeavor.[191]

1.9.3 Novel electrode technologies for neural interfaces

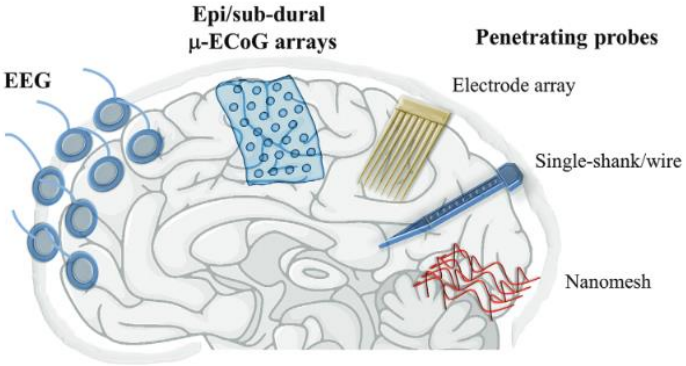

Figure 1.30: Neural devices for extracellular recording and stimulation. Different brain signals can be recorded through non-invasive or invasive approaches. EEG signals are recorded from the scalp; LFP signals can be recorded from μ-ECoG arrays placed on the cortex surface, while single-unit spikes are usually recorded with penetrating probes.[197]

Different methods are available for recording and stimulating neuronal activity, which differ in terms of spatial/temporal resolution of the signal and device invasiveness (see **Figure 1.30**).[197] Functionally relevant information can be obtained by means of large electrodes placed on the scalp, resulting in a non-invasive technique called electroencephalography (EEG). However, EEG (but the same applies to magneto-electroencephalography) provides rather weak and noisy electrical signals that generally encompass the activity of extended brain areas or reflect functional brain networks.[198] The detection with EEG of high frequency activity (>70 Hz) is also attenuated by the filtering phenomena produced by the scalp and the skull, interposed between the electrodes and the brain. Similar signals can be acquired using millimeter-sized macroelectrodes consisting of penetrating metallic wires.[199] Higher spatiotemporal resolution can be achieved using ultra-conformable electrocorticography (ECoG) and (micro) μ-ECoG arrays placed on the surface of the central nervous system (CNS).[200] Currently, μ-ECoG extracellular electrodes are the most viable interfaces to record LFPs at high spatial-temporal resolution and high signal-to-noise ratio,[201] but also action potentials (spikes) from a population of nearest neurons ("multi-unit" recording),[202] and in some instances also from single neurons.[203] Spikes are usually recorded by the means of penetrating probes, including dense arrays of penetrating conductive needles on silicon wafer platforms (so-called Utah arrays),[204] and linear sets of electrodes on narrow filaments (so-called Michigan probes). Penetrating structures offer powerful capabilities, but their lack of active semiconductor functionality in proximity to the biotissue interface and, in some cases, their non-ideal mechanical properties,

geometric layouts and/or integration approaches, limit the performance, scalability and ability to deploy into or onto biological systems of interest.

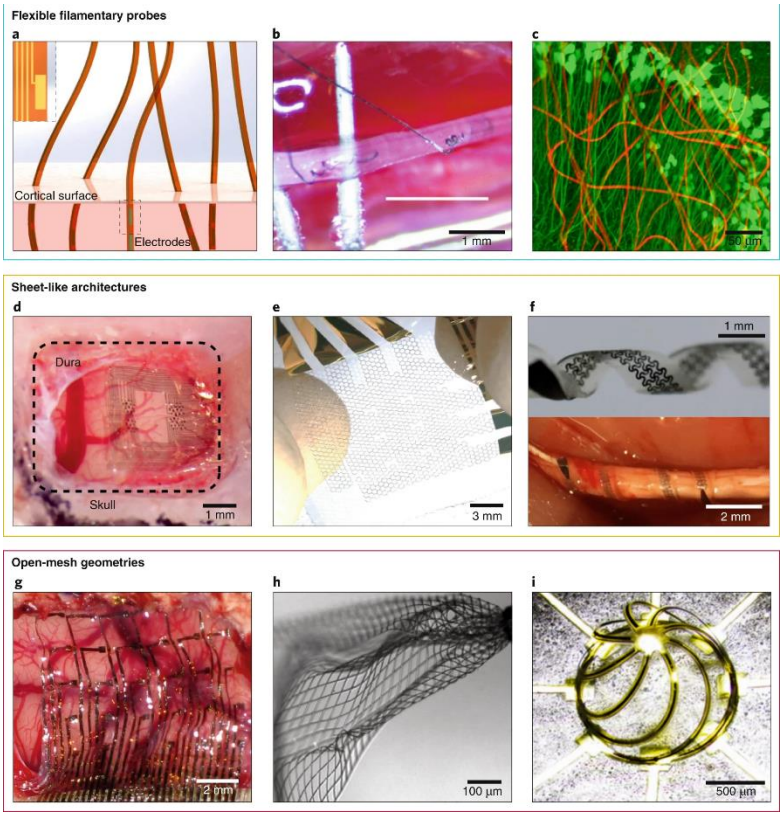

Figure 1.31: Novel electrodes for neural interfaces. **a**–**c)** Flexible filamentary probes. **a)** Schematic of the surface of rat cerebral cortex with implanted "Neuralink" filaments (polymer threads, 20 mm long, 5–50 µm wide, 4–6 µm thick), consisting of gold passive electrodes (area of 14 × 24 µm^2). **b)** Optical image of a carbon nanotube yarn (10–20 µm diameter) implanted in the rat vagus nerve. **c**)Three-dimensional image of flexible filaments (SU-8, 2–4 µm wide, 0.9 µm thick) that support collections of passive electrodes (platinum, circular area of ~2 × 10^2 µm^2) (red) and neurons (green) hosting the implant. **d**–**f)** Sheet-like architectures. **d)** Optical image of an array of sensing electrodes (PEDOT:PSS, area of 10 × 10 µm^2) embedded in a flexible parylene C sheet (4 µm thick) placed on the rat somatosensory cortex. [75] **e)** Stretchable PEDOT:PSS electrode array (area of 10 × 15 µm^2). **f)** Photographs of a soft, stimuli-responsive neural interface capable of conformally wrapping onto peripheral nerves based on narrow films of polyimide (2 µm thick) with serpentine gold electrodes (200 nm thick). **g**–**i)** Open-mesh geometries. **g)** Photograph of an implanted electrode arrays (gold, area of 500 × 500 µm^2, 150 nm thick) on ultrathin polyimide mesh (2.5 µm thick). **h)** Optical image of an open-mesh platform (SU-8, 5–20 µm wide, 1 µm thick) of platinum electrodes (each area of ~1.2 × 10^3 µm^2, 50 nm thick), injected into an aqueous bath through a syringe.[79] **i)** Optical image of a three-dimensional scaffold with eight gold electrodes (circular area of ~2 × 10^3 µm^2, 300 nm thick) for stimulation and recording, encapsulated by polyimide (~7 µm thick).[200]

Recent and conceptually distinct types of bioelectronic/optoelectronic devices take the form of functional thin-film membranes,[205] flexible filaments,[206] and open network meshes,[207] with powerful possibilities in levels of functional integration. Here, large-scale arrays of active components, sometimes with thousands of independent channels, establish direct biotissue/electronic contacts, demonstrating safe, chronic operation *in vivo* in freely moving and behaving animals.[208] The development of efficient implantable neural probes hinges on

several crucial factors, including biocompatible materials that allow for integration with the body, impenetrable barriers to prevent bodily fluids from interfering with device function, and flexible designs that adapt to the body's movements. These features are essential for creating hybrid, integrated platforms that minimize immune reactions and tissue damage while maintaining device performance comparable to conventional planar electronic/optoelectronic systems. Development efforts typically focus on high-fidelity biotic/abiotic interfaces, achieved through a combination of advanced materials, mechanical constructs, shapes and layouts, and surface coatings that ensure biocompatibility, low-impedance interfaces and stable operation. An important feature is the design of unique form factors with geometries and mechanics that are compatible with those of targeted biotissues for minimally invasive implantation and subsequent chronic use. As the overall device miniaturization can provide additional important benefits avoiding substantial biotissue damage during and after implantation, microfabrication techniques adapted from the semiconductor industry are used as the primary basis for the realization of devices.[209] **Figure 1.31** presents a collection of some recent examples, in layouts that range from flexible filamentary probes (**Figure 1.31a-c**) to sheet-like architectures (**Figure 1.31d-f**) and to open-mesh geometries (**Figure 1.31g-i**).[200] The growing number of device design and structure demonstrates how the biocompatibility of neural interfaces results from a collection of considerations in geometry, mechanics and biochemistry that match with targeted biotissues. A key frontier area is in the development of materials for implantable probes that offer not only these characteristics but also a combination of advanced form factors and distributed high-performance semiconductor functionality.[200] In this thesis work, we identify OMIECs as the most promising material platforms for highly stable, efficient and biocompatible neural interfaces, as demonstrated by a wide scientific literature.[93]

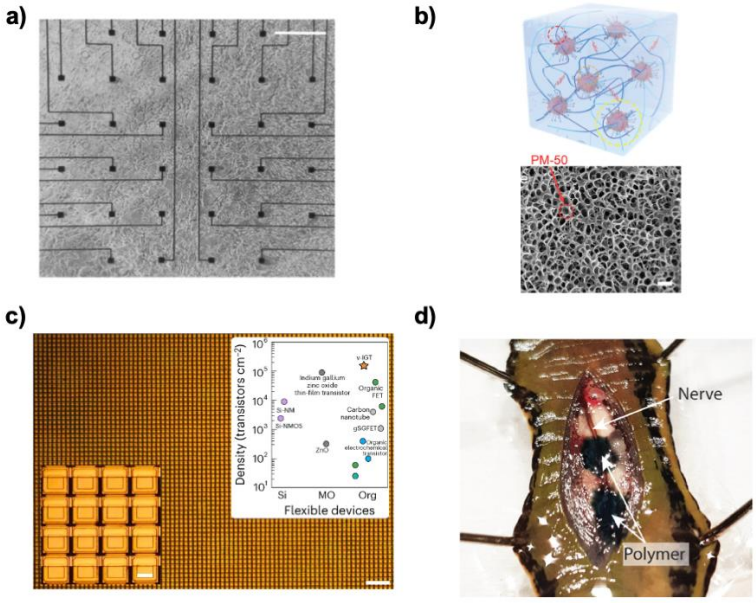

Figure 1.32: Recent advancements in OMIEC-based neural probes. **a)** Optical image showing induced pluripotent stem cells grown on a PEDOT:PSS biohybrid implant.[210] **b)** Polypyrrole-based hydrogel with enhanced electronic conductivity for ultrasoft neural interfaces.[211] **c)** Optical micrograph of a conformable wireless PEDOT:PSS transistor array with a density of 155586 transistors cm^{-2}.[212] **d)** Metabolite-induced *in vivo* fabrication of substrate-free OMIEC layers on a leech central nerve.[213]

Future developments on organic bioelectronics for neural interfaces (**Figure 1.32**) involve the integration of OMIECs with cultured cells in biohybrid implantable electrode arrays,[210] ultra-conformable devices based on hydrogel interfaces,[211] wireless and highly multiplexed active probes,[212] and substrate free OMIECs electrodes[213] among a wide variety of promising approaches.

1.10 Organic electrochemical transistors

Neurons and brain networks produce low-amplitude electrical signals that are difficult to isolate from background noise and require amplification before digitization. Conventional *in vivo* recording experiments using electrode structures employ ex-situ signal amplification, which unfortunately amplifies both signals from the biological environment and line noise, thereby reducing the signal-to-noise ratio (SNR) (see **Figure 1.33a**). Replacing simple electrodes with transistor structures holds immense potential for improved SNR thanks to the transistor localized amplification capabilities. Transistors act as voltage-controlled current amplifiers, effectively amplifying both the neurophysiological signal and biological noise directly at the recording site. In contrast, line noise remains unchanged, undergoing no amplification.[197] This arrangement results in a significantly enhanced SNR. Driven by this ultimate goal, research on inorganic semiconductor microelectronics has led to the development of electrolyte/oxide/silicon field-effect transistors (FETs), which were successfully used to measure *in vitro* signals from cell cultures and tissues slices.[214,215] In these devices, the transmembrane current from a neuron in the electrolyte alters the gate dielectric and induces a change in the conductance of the underlying silicon channel. Although silicon FETs have recently been integrated into *in vivo* probes as a means of enabling simultaneous addressing of hundreds of electrodes, neural recordings were carried out by "traditional" metallic microelectrodes, whereas the transistors themselves were carefully encapsulated to avoid direct contact with the brain due to the poor biocompatibility of the oxide layer.[216]

An alternative transistor architecture, termed the organic electrochemical transistor (OECT), was developed in the '80s[217], and makes use of an OMIEC layer as the device channel. In contrast to FETs, the channel of OECTs is in direct contact with extracellular fluids, and ions from the electrolyte penetrate the volume of the polymer film changing its conductance.[2] OECTs combine the biocompatibility and volumetric interaction with the surrounding biological milieu typical of mixed conductors with the intrinsic amplification of transistor structures. Thanks to these unique properties, OECTs were used to measure brain activity with a record-breaking signal-to-noise ratio (see **Figure 1.33b,c,d**), demonstrating the detection of low-level activity that was poorly recordable with low-impedance, OMIEC-based surface electrodes.[218] The use of electrolytes instead of MOS capacitors in OECTs also allows for large flexibility in device architecture and integration with a variety of substrates, employing a variety of form factors and a broad range of fabrication processes.[219] The inherent tunability of organic molecules further enables the optimization of ion and electron transport and facile biofunctionalization.[220] Because of these features, OECTs are being explored for a wealth of

applications, including chemical and biological sensors,[221] printed circuits,[222] neuromorphic devices,[81] and digital logic.[223] The promising performance of OECTs devices in these areas has motivated research about the device physics and has led to the publication of numerous models describing its operation.[224]

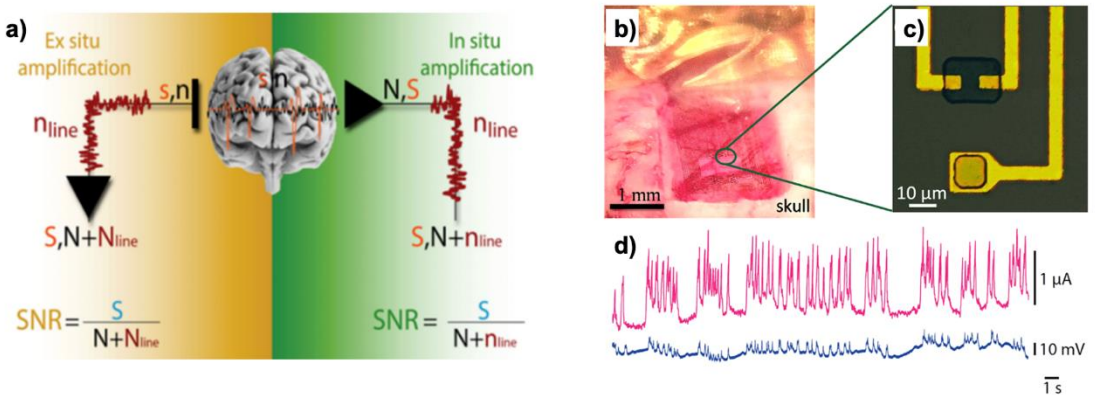

Figure 1.33: In-situ transistor amplification enables higher signal-to-noise ratio. **a)** In situ versus ex situ amplification by means of transistor-based neural interfaces. *n* is the biological noise, *s* is the neurophysiological signal, n_{line} is the line noise. Capital letters indicate the corresponding amplified signals.[197] **b)** Optical micrograph of an array carrying OECTs and electrodes, placed over the somatosensory cortex, and **(c)** detail of the transistor and electrode structures. **d)** Recordings from an OECT (pink) and an electrode (blue), showing the superior recording ability of the former.[228]

1.10.1 Structure of OECTs

The typical structure of an OECT consists of source, drain, and gate electrodes; an OMIEC layer; and an electrolyte between the channel and the gate (**Figure 1.34a**). Source and drain metal electrodes establish contact with the organic semiconductor film and define the channel through which holes or electrons flow from the source to the drain. The OECT operation is controlled by voltages applied to the gate (gate voltage, V_G) and to the drain (drain voltage, V_D), which are referenced with respect to the source electrode.[225] The gate voltage controls the injection of ions into the channel and therefore the doping level (or "redox state" in the language of electrochemistry) of the organic film. The drain voltage induces a current (drain current, I_D), which is proportional to the quantity of mobile electronic carriers in the channel, and therefore probes the doping state of the organic film. Like MOSFETs,[226] OECTs operate like a switch, in which the gate voltage (input) controls the drain current (output). OECTs based on type I OMIEC materials, such as PEDOT:PSS, typically work in depletion mode (**Figure 1.34b**).[33] In the absence of a gate voltage, a hole current flows in the channel (ON state), but once a positive gate bias is applied, cations from the electrolyte are injected into the channel and compensate fixed PSS^- acceptors. As a result, the number of holes in the channel decreases and the film is de-doped, leading to a drop in the drain current (OFF state).[225] By contrast, accumulation-mode OECTs are normally in the OFF state, but can be "switched on" by the application of a negative gate voltage which causes injection of anions into the channel and a corresponding accumulation of holes.[227] Due to the mixed conductivity of OMIEC

materials, doping processes in OECTs occur over the entire volume of the channel, as opposed to a thin interfacial region like in field-effect transistors (FETs). In a FET, an organic semiconductor film (the channel) is separated from a metal electrode (the gate) by a thin insulating layer (the gate dielectric) (**Figure 1.34c**). The application of a gate voltage polarizes the dipoles in the oxide, creating a field that causes an accumulation of electronic carriers in the semiconductor at the semiconductor/insulator interface. The charge in the channel is compensated by a sheet of charge at the gate electrode, forming the two plates of a parallel plate capacitor. The amount of charge that is induced in the channel can be estimated by $Q=C\cdot V_G$, where C is the capacitance of the dielectric and V_G is the gate voltage. As the capacitance is inversely proportional to the distance between the two plates, C is maximized when thin dielectric layers are used. In electrolyte-gated FETs, a double-layer capacitor is formed at the electrolyte–channel interface (**Figure 1.34c**), and a sheet of ionic charge in the electrolyte compensates the induced sheet of electronic charge in the channel. This configuration can be considered an extreme case of FET, because the thickness of the dielectric is reduced to dimensions comparable to the ionic radius, resulting in high capacitance.[228]

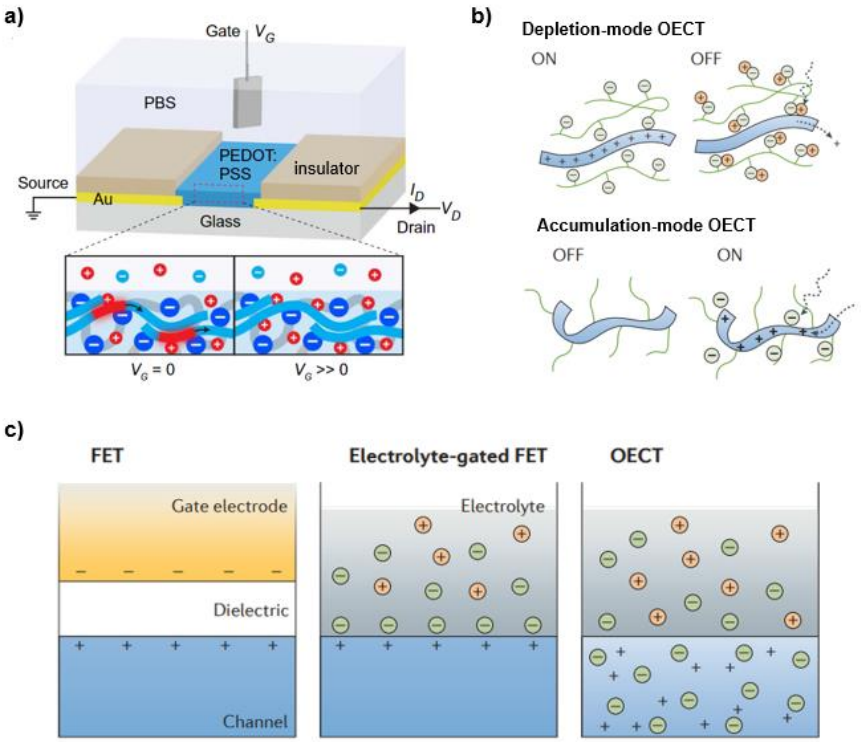

Figure 1.34: Structure of OECTs. **a)** The typical structure of an organic electrochemical transistor (OECT), showing the source, drain, PEDOT:PSS channel, electrolyte (PBS) and gate.[125] **b)** Depletion and accumulation-mode operation in OECTs. **c)** Comparison between FET, electrolyte-gated FET and OECTs.[229]

In an OECT, ions penetrate the OMIEC layer, leading to changes in the doping state throughout the channel (figure, part c). This configuration is described not by a parallel plate capacitance but by a volumetric capacitance, which can be many orders of magnitude larger. Compared with a FET of similar size, the same gate voltage induces more electronic charge in the channel

and thus a larger drain current in an OECT. The large gate-channel capacitive coupling allows OECTs to operate at low voltages (typically ~0.5 V) and results into impressive signal amplification properties exceeding most thin-film transistor technologies.[229]

1.10.2 Device physics of OECTs

Despite the significant differences between OECTs and MOSFETs, OECTs can be described by models for MOSFETs as long as the interfacial capacitance used to describe MOSFETs is replaced by a volumetric capacitance.[230] According to a pioneering work form Bernards and Malliaras,[225] the device is divided into two circuits: an electronic circuit, which describes the flow of electronic charge in the source–channel–drain structure according to Ohm's law, and an ionic circuit, which describes the flow of ions in the gate–electrolyte–channel structure (**Figure 1.35a**).

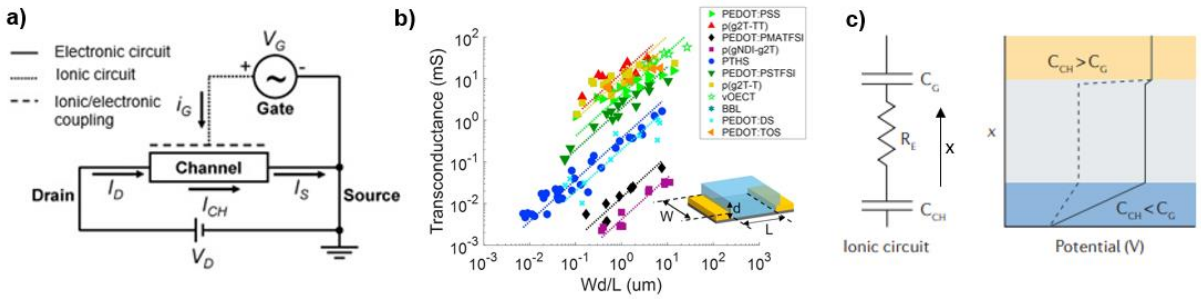

Figure 1.35: Steady state behavior of OECTs. **a)** Electronic and ionic circuit composing an OECT device. **b)** Geometry scaling of peak transconductance in OECTs based on different OMIEC materials. **c)** Ionic circuit and effective gate potential considering the effect of a finite gate capacitance. R_E indicates the electrolyte ionic resistance, while dashed and continuous lines in the potential profile refer to poor and efficient gating, respectively. Adapted from [229,233,75].

As the source/drain electrodes block ions and (ideally) do not allow direct faradaic charge transfer, the gate current is purely capacitive and vanishes at steady state. With these assumptions, electronic charge transport in a p-type OECT operating in depletion mode is described with the exact same set of equations used for long-channel MOSFETs,[231] yielding

$$I_{ch} = \begin{cases} \mu_p c_v \frac{W}{L} d \left(V_t - V_G + \frac{V_D}{2}\right) V_D, & for\ V_D > V_G - V_t \\ -\mu_p c_v \frac{W}{L} d \frac{(V_t - V_G)^2}{2}, & for\ V_D < V_G - V_t \end{cases} \quad 1.28$$

where I_{ch} is the channel current, μ_p is the hole mobility, c_v is the volumetric capacitance, V_G is the gate voltage, V_D is the drain voltage, V_t is the threshold voltage, and W, d, L are the channel width, thickness, and length. The two different expressions in **Eq. 1.28** distinguish between the linear and saturation regimes, respectively. OECTs transduce small voltage signals applied to the gate into large changes in the drain current. The efficiency of transduction is calculated by the first derivative of the transfer curve, namely, transconductance $g_m = \partial I_D / \partial V_G$, which is an

important figure of merit. High transconductance is highly wanted in applications like biosensing, digital logic, and neuromorphic engineering, where OECTs are configured such that an input voltage at the gate electrode is detected by measuring its effect on the output current flowing through the OECT channel.[92] By taking the derivative of **Eq. 1.28**, we obtain

$$g_m = \begin{cases} -\mu_p c_v \frac{W}{L} dV_D, & for\ V_D > V_G - V_t \\ \mu_p c_v \frac{W}{L} d(V_t - V_G), & for\ V_D < V_G - V_t \end{cases} \quad 1.29$$

Several authors have shown that OECT transconductance is directly proportional to the ratio *W*d/L*, as shown in **Eq. 1.29**.[232,227] The fact that transconductance scales with thickness, and not just *W/L*, distinguishes OECTs from FETs, where field-effect doping only modulates carrier density at the semiconductor-insulator interface.[231] The bulk doping effect in OECTs allows engineers to tune the OMIEC layer thickness and design high-transconductance OECTs without expanding the footprint (*W* or *L*) of devices.[229] Noteworthy, the expression for transconductance in **Eq. 1.29** contains the product of volumetric capacitance and electronic carrier mobility of the OMIEC material, and represents a figure of merit for mixed conduction. Therefore, one can benchmark material performance by designing OECTs of different geometries and characterizing transconductance as a function of *W*d/L* (**Figure 1.35b**).[79] The previous considerations hold only under the assumption that the channel capacitance is the only relevant capacitance in the OECT device. In real applications, the fraction of the applied gate voltage that drops across an OECT channel is also controlled by the nature and geometry of the gate electrode.[233] If a polarizable electrode, such as Pt or Au, is used as the gate, two capacitors are formed in the ionic circuit; one capacitor corresponds to the electrical double layer formed at the gate–electrolyte interface and the other corresponds to the volumetric capacitance of the channel. Because the capacitors are in series, the equivalent capacitance of the circuit is given by

$$C_{eq} = \left(\frac{1}{C_G} + \frac{1}{C_{ch}}\right)^{-1} \quad 1.30$$

and the applied gate voltage drops across the smaller capacitor, as reported in **Figure 1.35c**, showing the distribution of potential in the ionic circuit. The solid line corresponds to the case of efficient gating, in which most of the applied gate voltage drops at the electrolyte–channel interface, driving ions inside the channel. The dashed line corresponds to the case of poor gating, where most of the applied gate voltage drops at the gate–electrolyte interface. For efficient gating, the capacitance of the gate electrode must be more than ten times larger than the capacitance of the channel, otherwise a large fraction of the applied gate voltage will drop at the gate– electrolyte interface. Large gates can be technically difficult to implement for some applications; however, using thick PEDOT:PSS layers as gate electrodes can help achieve a large gate capacitance.[234] Alternatively, effective gating can be obtained by using a nonpolarizable gate electrode, such as Ag/AgCl, for which the voltage drop at the gate–

electrolyte interface is negligible.[144] However, a small gate electrode is preferable when a sensing reaction is meant to occur at the gate and the channel merely acts as the transducer. For instance, OECT-based enzymatic sensors detect analytes when enzymatic reactions are catalyzed at the gate electrode. These reactions cause a change in the voltage drop between the gate and the electrolyte, thus shifting the effective gate voltage and modulating channel conductivity.[235]

The high transconductance of OECTs comes at the cost of rather slow operation. Bernards and Malliaras modeled the OECT transient response describing how the transient gate current induced by a time-varying gate voltage contributes to the output current in an OECT device. Such result was obtained by making the quasi-static approximation. Under this assumption, the charge distribution in the channel is, at all times, given by the steady-state solution of **Eq. 1.29** for the instantaneous terminal voltages. Because the source and drain voltages are constant, the time dependence of the drain current is determined solely by the transient response of the ionic RC circuit, composed by the channel capacitance C_{ch} (the model assumes $C_G >> C_{ch}$, so the gate capacitance contributes negligibly to the ionic circuit) and the electrolyte resistance R_s (see **Figure 1.36b**). This time response yields the electrolyte voltage, $v_{G,sol}(t)$, determining both the ionic displacement current, $i_G(t)$ and the electronic transport current, $i_{ch}(t)$. Quantities that vary with time are indicated by using lower-case variable names. The displacement current $i_G(t)$ is related to doping (or de-doping) the OECT channel and is given by $i_G(t) = C_{ch}\frac{d}{dt}v_{G,sol}(t)$ for current flowing in the ionic circuit. The electronic transport current, $i_{ch}(t)$ results from the drift of electronic carriers between the source and drain and is given by **Eq. 1.29** where V_G is replaced by $v_{G,sol}(t)$. The drain current $i_d(t)$ is then a weighted sum of the displacement current and the channel current. When a square gate voltage step is applied, the resulting drain current takes the form

$$i_D(t) = I_{SS}(V_G) + \Delta I_{SS}\left|1 - f\frac{\tau_e}{\tau_i}\right| exp\left(-\frac{t}{\tau_i}\right) \qquad 1.31$$

where $i_d(t)$ is the drain current at time t, $I_{SS}(V_G)$ is the steady-state drain current when the gate voltage is V_G, ΔI_{SS} is the difference between the initial and final steady-state currents, f is a weighting factor, $\tau_e = \frac{L^2}{\mu_p V_D}$ is the electronic transit time along the channel; and $\tau_i = R_s C_{ch}$ is the ionic RC time constant.[225]

Two qualitatively different regimes of transient behavior emerge from **Eq. 1.31**. In the first regime, when electronic transport is faster than ionic charging, the drain current relaxes monotonically from the initial current to the final current, as shown in **Figure 1.36a**.[236] In the second regime, when ionic charging is faster than electronic transport, the drain current first spikes beyond and then exponentially recovers to the final current, as shown in see **Figure 1.36a**. These two regimes of behavior have been experimentally observed in several works.[236,237]

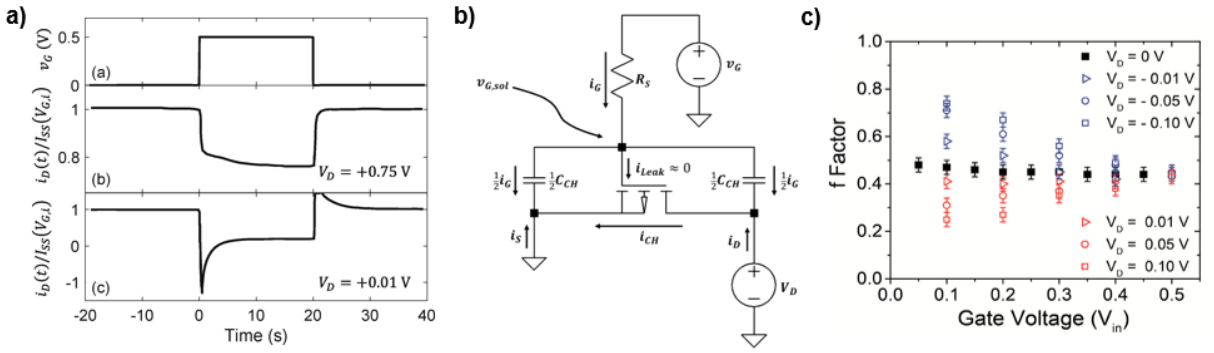

Figure 1.36: Transient behavior of OECTs. **a)** Measured transient behavior of an OECT in response to a square step of the gate voltage, showing both the monotonical relaxation and the "spike and recovery" response.[107] **b)** Friedlein model for OECT transport, assuming f=1/2.[121] **c)** Summary of extrapolated f factors for different drain and gate voltages using Faria's approach.[123]

Finally, **Eq. 1.31** contains is the unspecified factor f, which is equal to the fraction of the displacement (or gate) current that contributes to the drain current. The treatment of this weighting factor defines several variations on the Bernards model. In Friedlein's approach,[236] the weighting factor is simply assumed to be f=1/2, and the OECT transient response can be modeled by the circuit diagram shown in Fig, where, the drain current is given by $i_d(t) = i_{ch}(t) - \frac{1}{2}i_G(t)$, and, likewise, the source current is given by $i_d(t) = -i_{ch}(t) - \frac{1}{2}i_G(t)$. These expressions lend two important insights. First, in the transient regime the source and drain currents do not have equal amplitudes. Second, if the change in the channel current is exactly equal to one half of the maximum gate current, then the drain current will be a square step from its initial to its final value with no observable exponential relaxation. Although the Friedlein model provides fruitful insight about OECT behavior, it is valid only for $|V_G| \ll (V_t - V_G)$. Such limitation is overcome by Faria et al. by assuming that f is not a constant but depends on both the gate and drain voltages.[238] An empirical expression for this dependence is then provided by extracting f from a multi-parameter fit to experimental measurements (see **Figure 1.36c**). Such approach introduces a refinement of the f=1/2 assumption in the Friedlein model but lacks a satisfying theoretical foundation. Future developments on the determination of the weighting factor in **Eq. 1.31** could abandon the quasi-static approximation and to describe the OECT currents with either a transmission line model or a finite-element time-domain model. These distributed/finite-element models calculate the time varying voltages and currents at each location in the channel and therefore have no need of an explicit f factor. The transmission-line modeling approach has been used by Liu et al. and Drieschner et al. to describe electrolyte-gated field-effect transistors and could be adapted to describe the transient response of OECTs.[239] In contrast, finite-element time-dependent drift-diffusion calculation of both the electronic and the ionic charge in the OECT channel (such as Tybrandt's model) show that their results are qualitatively similar to those of quasi-static models.[122] However, further experimental data are needed to validate their model and show if it is accurate in the high-frequency regime where the quasi-static model is expected to fail.[224]

1.10.3 Measuring charge carrier mobility in OMIEC materials with OECTs

The characterization of mixed charge transport properties of OMIECs is crucial to develop novel and optimized materials for bioelectronic devices. Anyway, the mixed conductivity renders the experimental determination of individual ionic or electronic carrier mobilities difficult as both processes are intrinsically entangled and both can lead to the screening of electric fields or introduce local contact resistances.[170,120] Progress on all fronts is predicated on an advance in understanding the interrelations between ionic transport, electronic transport and ionic–electronic coupling and their dependence on processing, synthetic structure, microstructure/morphology, and electrolyte choice.[240] The extraction of the charge carrier mobility is a fundamental step for the analysis of the transport properties of OMIECs. High-mobility values allow fast device operation and amplified transduction as needed in many applications.[241] Due to their peculiar structure, OECTs provide an electrochemical test bed to characterize the electronic conductivity and at the same time control the ionic composition in OMIEC materials.[75] The source–drain current captures electronic transport, while the gate current captures ionic transport during device operation.

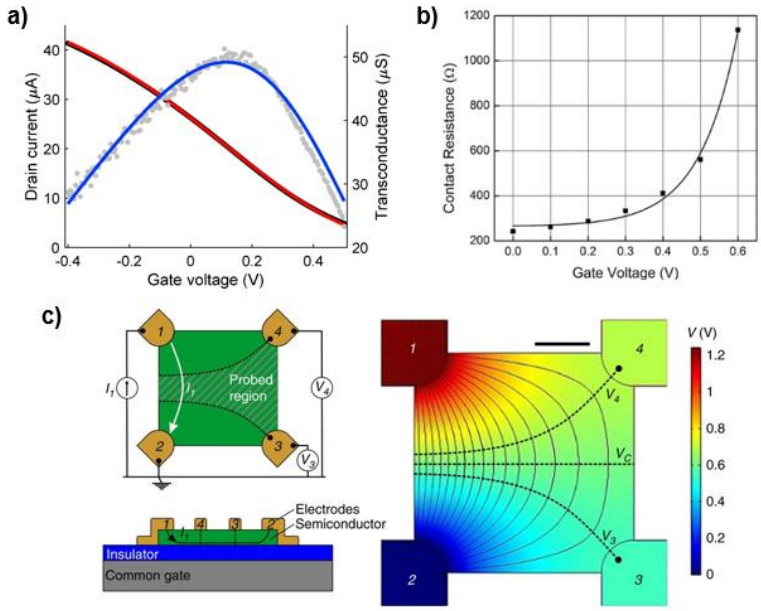

Figure 1.37: Contact resistance effect in OECTs and measurements of electronic mobility. **a)** Non monotonic transconductance in PEDOT:PSS-based OECTs, complicating the extraction of carrier mobility.[130] **b)** Exponential dependence of contact resistance with respect to gate voltage in OECT devices.[134] **c)** Gated-van der Pauw method, using a four point probe, contact independent, technique to measure thin film transistor mobility.[241]

Despite OECTs are studied in a wide range of applications, the interpretation of their characteristic curves and the extraction of the figures of merit still represent a difficult challenge, as their experimental behavior systematically differs from MOSFET interpretation. Experiments show that OECT transconductance has a nonmonotonic dependence on gate

voltage, decreasing at both high and low gate voltages (see **Figure 1.37a**).[242] Thereby, the extraction of OMIEC electronic mobility and volumetric capacitance is only restricted to a small potential window where a peak transconductance is reached (**Figure 1.35b**).[79] This behavior is an ubiquitous property of OECTs, reported in devices exploiting different organic semiconductors[230,38] having various electrode geometries[243] and realized using a wide range of fabrication technologies.[92] However, existing OECT models do not predict this effect. For example, Bernards' model (see **Eq. 1.29**) predicts that transconductance is constant in the linear regime and decreases linearly with gate voltage in the saturation regime. Both disorder-limited transport and contact resistance effects can be a possible cause of this behavior. Paterson et al. measured a contact resistance dependency on the gate voltage in n-type OECTs via transmission line measurements.[244] A similar result was obtained by Kaphle et al. for PEDOT:PSS-based OECTs working in depletion mode (**Figure 1.37b**).[245] This effect was interpreted as the consequence of ion accumulation at the drain contact caused by lateral ion currents in the OECT channel, which were included in a finite element simulation.[120] Gate-dependent contact effects are typically observed also in normal thin film transistors (TFTs) based on organic semiconductors.[246] A contact-independent technique was developed by Rolin et al. for a more accurate characterization of organic field-effect transistors (OFETs) and was called the gated van der Pauw (gVDP) method.[241] gVDP method is based on the normal van der Pauw (VDP) method that is a geometry-independent four-contact electrical measurement widely used to evaluate the sheet conductance σ_s of thin continuous films.[247] In gVDP characterization, a common gate is used to modulate the charge density in VDP devices (see **Figure 1.37c**). gVDP characteristics can be interpreted with a simple model, allowing for the extraction of charge carrier mobility and threshold voltage on several materials.[241] Afterward, Jiang et al. generalized the gVDP method to probe Coulomb interactions on charge transport in few-layer organic crystalline semiconductors,[248] while gating of conjugated polymers immersed in an aqueous electrolyte was observed by Wang et al. in P3HT-based van der Pauw structures.[249]
The contact-independent characterization of electronic transport in OMIEC materials during operation is one of the objectives of this thesis work. With the introduction of the electrolyte-gated van der Pauw (EgVDP) method, we measured the electronic mobility of PEDOT:PSS, revealing that gate voltage dependent contact resistance effects lead to systematic errors in OECT-based transport characterization. Details about this work are reported in the Results section **4.1**, and in ref [105].

1.10.4 Application of OECTs in Bioelectronics

Relying on the large transconductance combined with the biocompatible material properties, many research works propose OECTs as amplifying transistor to be integrated in electrochemical and bioelectronic sensors for healthcare applications.[250] The main bioelectronic applications of OECTs are i) electrophysiology and neural signal recordings, ii) analyte detection with a functionalized gate electrode, and iii) impedance sensing (**Figure 1.38**).

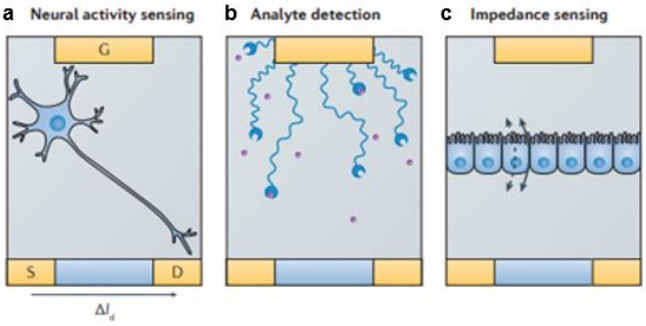

Figure 1.38: Applications of OECTs in bioelectronics. **a)** OECTs are used in electrophysiology to record the electrical activity of cells, such as neurons, in the electrolyte between the channel and the gate. They are also used for the detection of analytes (red circles) that interact with receptors placed at the gate or channel **(b)**, and as impedance sensors that record changes in ion permeability of cell layers placed between the channel and gate **(c).** In all these cases, the detection of an event is signaled by a change in the drain current ΔI_d.[219]

In the first case, the electrical circuit involving the OECT must operate ultimately as a voltage amplifier (see the introduction of **par. 1.10**), that produces an amplified output voltage ready for digitization. Gain is then expressed as the ratio between the original potentiometric signal and the output voltage. Depending on the circuit design, DC amplification gains reaching 30 V/V have been demonstrated in OECT based potentiometric sensors.[175] Given this large amplification properties, OECTs have been explored for a wealth of *in vivo* bioelectronic applications, ranging from brain interfaces[251] to wearable devices[252] and plant bioelectronics.[253] Established examples of OECT-driven analyte detection regard biosensors used to quantify the concentration of ionic or redox active molecules.[19] In such devices, selectivity towards specific analytes such as DNA or RNA biomarkers,[254] enzymes,[255] or immunoglobulins was demonstrated by device functionalization with biorecognition elements.[256] Finally, an emerging class of biosensors that takes advantage of OECT amplification regards impedance based sensors for monitoring cellular adhesion and cell layer barrier properties.[257] These are discussed with more detail in the next paragraph.

1.10.5 OECTs as impedance biosensors: towards single cell resolution

Cell adhesion is an essential process in cell communication and regulation and becomes of fundamental importance in the development and maintenance of tissues.[258] Changes in cell adhesion can be the defining event in a wide range of diseases, including arthritis,[259] cancer,[260] osteoporosis,[261] and atherosclerosis.[262] A considerable potential impact in bioelectronics can be achieved by studying single cell adhesion processes. Over the years, numerous studies have shown the use of different techniques for the analysis of single-cell adhesion. Both the traction force microscopy (TFM)[263] and micropillar-array technique measure the cell adhesion force by monitoring the deformation induced on an elastic substrate.[264] Other methods include the use of atomic force microscopy[265] and optical tweezers[266] to assess the impact of cellular shape, size, and deformability during adhesion.[267] Despite their success in different demonstrations,

these techniques rely on expensive equipment, are typically time consuming and potentially can alter the cell behavior.[268] An alternative non-invasive approach that combines scalability and real-time monitoring, is offered by electrical measurements that probe the electric cell–substrate impedance.[269] In this technique, the cells are allowed to adhere directly onto the conductive surface of a sensor. A small AC voltage is applied and the ionic current that passes through the layer of adhering cells to the sensor is measured (**Figure 1.39a**).[270] Changes in cellular adhesion or intercellular barrier properties change the measured current signal thus providing a simple means for real-time monitoring.[271] By replacing the metallic working electrode of a traditional impedance sensor with a electrolyte gated OECT, amplification of the current signal is achieved thus increasing sensitivity and reducing possible noise pickup (**Figure 1.39b**).[272] Current amplification becomes particularly important in high impedance applications as encountered when the sensor size is scaled down to micrometric scales matching cellular dimensions. Such downscaling opens the opportunity to translate impedance based cellular monitoring to the single-cell level.[273] This ultimate sensor resolution is highly desired in biomedical research as the importance of single-cell phenotyping is increasingly recognized for the study of cell development and physiology, as well as for research on cellular pathologies such as cancer.[274] An important step in this direction was recently achieved by Hempel et al. by demonstrating single-cell sensitivity in an OECT enabled impedance sensor. The authors found that significant differences in the sensors transfer function are caused by cells adhering to the transistor surface (**Figure 1.39c**). Such changes in transfer function are usually quantified as the transistor bandwidth (or response time) and equivalent circuit models were developed to explain the observed frequency response and its relation to impedances at the cell/PEDOT:PSS interface.[275] The rational optimization of OECT-based single cell sensors based on the quantitative understanding of their AC amplification properties is a main achievement of this thesis, ad it is discussed in detail in **sect. 4.5**.

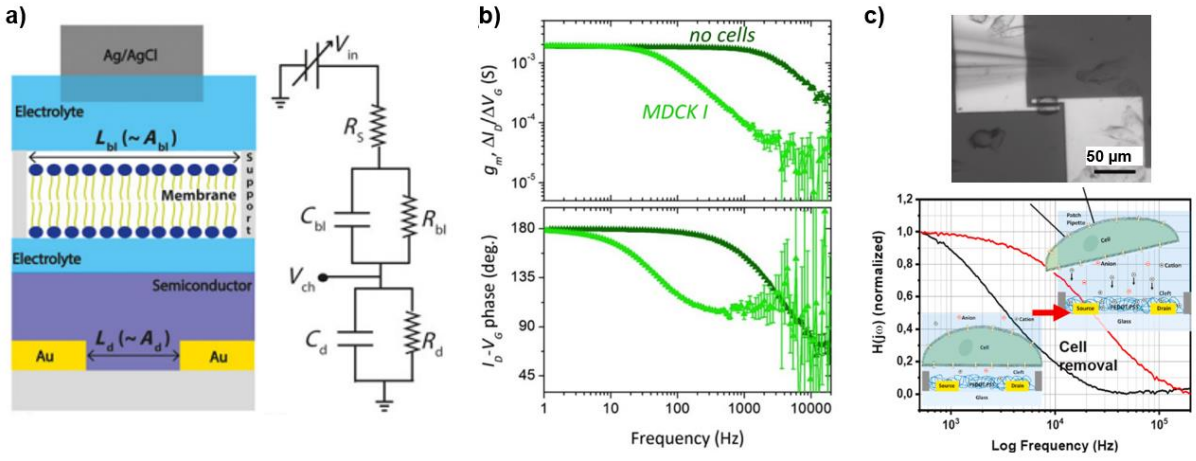

Figure 1.39: OECT as cell impedance sensors. **a)** Schematic of a barrier layer-functionalized OECT and the equivalent circuit used for modeling the electrical response.[270] **b)** Frequency dependence of transconductance of an OECT with (light colors) and without (dark colors) MDCK I cells cultured on the channel of the transistor.[272] **c)** Single cell adhesion on a PEDOT:PSS gate, and corresponding variation of the OECT bandwidth.[275]

1.11 Electrochemical actuators

Due to ion and solvent transport processes involving the entire material volume, OMIECs can convert electrical energy to mechanical deformation, and have received considerable attention in the last years due to their potential applications in soft robots operating at biointerfaces.[276] The volumetric electrically-induced swelling (electroswelling) of mixed conductors can be favorably exploited in devices able to mimic the functionalities of biological muscles (artificial muscles), with the OMIEC specific advantages of biocompatibility, low-voltage drive, nanoscale precision, miniaturization, and operation in liquid environments, including body fluids.[277] Such unique material properties combination has led to the development of soft actuators and drug delivery devices, but also motivated fundamental research on the physicochemical mechanisms responsible for actuation.

1.11.1 Electroswelling in OMIEC materials

Electrochemical actuation processes have been extensively studied for a large number of OMIEC formulations based on conducting polymers such as polyaniline (PANI),[278] poly (3,4-propylenedioxythiophene) (PProDOT),[168] and poly (3,4-ethylenedioxythiophene) (PEDOT).[279] Among them, polypyrrole (Ppy) has stood out due to its record-breaking actuation strain,[280] especially when it is blended with large dopant counterions such as dodecylbenzene sulfonate (DBS^-), forming the type I OMIEC Ppy:DBS.[281] Ppy:DBS electroactivity has been interpreted through several theoretical models based on different assumptions.[282] Starting from migration and diffusional models treating Ppy films as porous electrodes,[283] scientists developed alternative descriptions based on the capacitive charging of the internal polymer/electrolyte interface[118] or on electrochemically stimulated conformational relaxation (ESCR) model, attributing the electrochemical responses of a Ppy film to its conformational change.[284] From these studies, only one main conclusion is widely accepted: the strain and stress from a Ppy:DBS electroactuator are primarily driven by ion exchanges between the electroactive polymer and a supporting electrolyte (see **Figure 1.40a**).[285] When an electrochemical potential is applied, the electronic conductor in the OMIEC thin film (Ppy) is oxidized or reduced, and the overall charge neutrality is maintained through charge compensation in the ionically conducting phase[286] composed by nano-scaled DBS-rich grains. Such process involves the exchange of cations or anions and solvent between the ionically conducting phase and the electrolyte bath causing the swelling/deswelling of the film.[287] As DBS^- counterions are immobilized in the polymer matrix due to their large size, Ppy reduction can consistently draw hydrated cations from the electrolyte into the polymer matrix, resulting in a significant electroswelling, while a subsequent oxidation process restores the polymer both mechanically and electrochemically.[288] An analogue process takes place in PEDOT:PSS actuators, showing reduced actuation strain and stress,[169] but larger flexibility, higher ionic and electronic conductivity, and improved electrochemical cycling stability.[289]

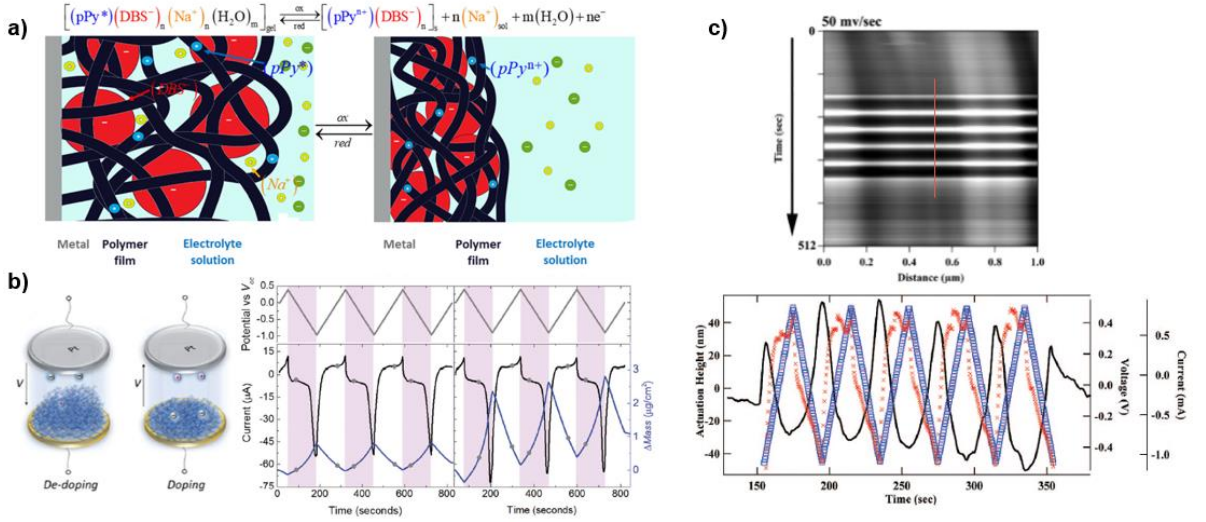

Figure 1.40: Electroswelling in OMIEC materials. **a)** Reversible electrochemical oxidation/reduction of Ppy:DBS, leading to a volume increase when the conjugated polymer (polypyrrole) is oxidized.[285] **b)** EC-QMC-D measurements of electroswelling in PEDOT:PSS for thin and thick layers. The setup monitors mass changes and the electrochemical current flowing in the OMIEC material during cyclovoltammetries.[291] **c)** EC-AFM height image of a Ppy:DBS thin film during a cyclovoltammetry measurement. Lighter (higher regions) and darker (lower regions) bands in the image correspond to the cyclic displacement, or actuation of the film in response to the CV. The cross-sectional height profile (black line) taken through the vertical line shown below as a function of the CV time (s). The height profile shows a cyclic increase and decrease in height, and out-of-phase response with the corresponding applied voltage (blue square) and current (red hatch) signals.[301]

The electrochemical mechanism responsible for OMIEC electroswelling has been explored by several experimental studies,[290] including quartz crystal microbalance measurements with dissipation monitoring (EC-QCM-D) during cyclic voltammetry (CV).[287] Through EC-QMC-D it is possible to monitor mass exchange between an electrically active film and an electrolyte as CV induces electrochemical doping/de-doping of the film (see **Figure 1.40b**).[291] EC-QMC-D was successfully used to study the electrochemical actuation of ferrocyanide-containing polyelectrolyte multilayers,[287] but also the ionic-to-electronic coupling efficiency in PEDOT:PSS [291], or the charge carrier dynamics in organic electrochemical transistors.[292] Moving reduction front experiments demonstrated how the slow ion transport is the rate-limiting step in the Ppy:DBS de-doping process responsible for electroactuation.[293] The impact of the supporting electrolyte composition, the amount and type of solvate cations, and the presence of further OMIEC dopants were studied with in-situ X-ray diffraction to reveal the microstructure variation during electrochemical processes,[294] or in situ X-ray scattering [295] and NMR[296] to probe the changes in ion coordination.[297,298] Also electrochemical atomic force microscopy (EC-AFM)[299,300] was used to follow changes in thickness in Ppy[301] and PEDOT:PSS[302] films, probing possible morphological changes induced by swelling (**Figure 1.40c**). However, these methods all required macroscopic electroactive thin films and could only reveal slow actuation processes occurring on the timescale of seconds and the monitoring of fast local ionic exchange processes remains elusive. As a faster and more local technique, electrochemical strain microscopy was introduced to study ion-exchange processes in P3HT,

but as only the tip generates the local electric field, results are of qualitative nature.[303] For these reason, the development of a quantitative characterization technique to study volume changes and interface forces related to dynamical electroactuation effects in OMIECs is an important objective of this thesis work, discussed in detail in **sect. 4.2** and **sect. 4.3.**

1.11.2 OMIECs electroactuators for soft robotics and drug delivery

Due to their biocompatibility and low-voltage operation, and given the possibility to apply electrochemical stimuli locally and in a controlled way, ionic electroactive thin films show a strong potential for applications.[290,304] By engineering the device structure and design, the reversible volume change of OMIECs can be used as the active part in an actuator leading to different motions such as bulk, linear, bending, or out of plane.[290] At the same time, electroactive OMIEC layers can actively use the surrounding physiological media as the ion source resulting in a simpler device geometry for application. Starting from the pioneering work of Baughman,[305] and Pei and Inganas[306], different OMIECs soft-actuators were developed, ranging from motile catheters[307] to cochlear electrode arrays or steering wires that can be electroactively bent using Ppy:DBS structures.[290] Despite the promising applications, the actuation performance of electroactive polymers is limited by the slow transport of ion and solvent in the OMEC matrix. The actuation speed can be increased either enhancing the ionic conductivity of the polymer or reducing the size of the electroactive layer. The large strains that these materials display as well as their ability to operate at low actuation potentials make them good candidates as actuators in microelectromechanical systems (MEMS). Microfabricated conjugated polymer actuators were first demonstrated at Linköping University by Smela et al.,[308] and then refined using differential adhesion fabrication methods.[309] Starting from that, several polymeric microactuators for bioelectronics were developed, including, for example, individually addressable chip for mechanical stimulation of single cells able to induce variations in the Ca^{2+} activity (**Figure 1.41a**).[310] In a similar approach, Ppy:DBS was used to actuate a multiplexed and switchable microneedle platform,[311] to control the motion of microrobots (**Figure 1.41b**),[312] or to generate high pressure in lab-on-chip systems.[310]
Another relevant application of a electroactive OMIEC layers is the controlled release of drugs or biomolecules based on the hypothesis that compounds, entrapped in the polymer during synthesis or fabrication, are released by repeated or continuous electrochemical swelling.[313] The drug loading capacity of a conductive polymer is not only dependent on the doping level, but can also be increased by introduction of cavities into the material.[314] As an example, micro- and nano-gaps that separate electrochemically prepared network of Ppy nanowires were act as drug storage reservoirs for dexamethasone (**Figure 1.41c**).[315] In this system, drug-loading capacity depends on the volume of the micro- and nano-vacancies, and not the doping level. Both hydrophilic and lipophilic drugs were loaded into the micro- and nano-gaps due to the amphilicity of the PPy nanowire network. In a similar way, Valdés-Ramírez et al. fabricated microneedle-based multi-drug reservoirs in conjunction with a PPy actuator, which can selectively switch between redox states to release each drug.[316] Together, patterned conducting

polymer actuators have been employed to control drug release from the reservoirs upon application of an electrical stimulus. The future goal of microactuators in drug delivery will be the development of a controlled release of drugs in response to certain physiological cues, such as abnormal brain signaling or unusual hormone/protein levels. Thus, careful integration of bioelectronics-based sensing and actuation will be essential for future closed-loop drug delivery devices.[317]

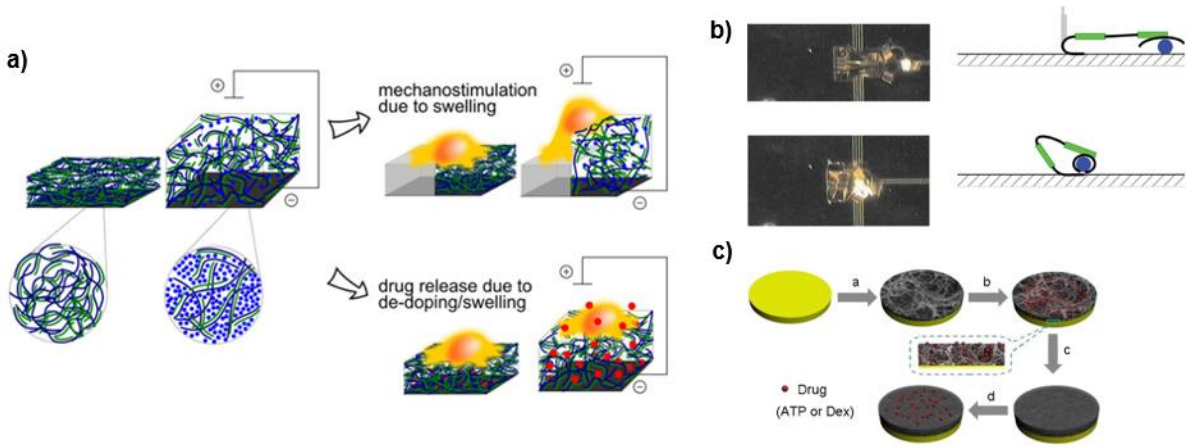

Figure 1.41: OMIEC electroactuators for soft robotics and drug delivery. **a)** The electroswelling properties of conducting polymers can be used in organic bioelectronic devices for mechanostimulation of cells of controlled drug release.[310] **b)** Ppy-based micro-robot able to grab and lift a 100 µm glass bead.[312] **c)** Fabrication of a Ppy nanowire network for electrically controlled drug release.[315]

2 Research objectives

The overview on the physicochemical properties of organic mixed ionic and electronic conductors reported in **sect. 1.1** demonstrate how OMIECs provide a unique material platform to enhance the efficiency and long-term stability of future bioelectronics interfaces. Inspired by the great potential of organic bioelectronics, numerous research teams worldwide are actively pursuing the development of novel devices tailored to a wide spectrum of applications. As discussed in the comprehensive review presented in **sect. 1.8** this ongoing research endeavor holds the promise of revolutionizing various fields, including healthcare, biomedicine, biosensing, and neuroscience. Despite the promising results, faster and significative developments in the field can only be achieved through a quantitative comprehension of the charge transport properties of OMIEC materials and their relation to device operation. The aim of this thesis work is to provide a contribution in this direction. To achieve this overall goal, the following specific objectives were identified during the thesis work:

1. **Operando characterization of electronic transport in OMIEC materials:**

As introduced in **sec. 1.3**, electronic transport is a fundamental process in OMIECs determining the operation speed of bioelectronic devices. However, mixed conduction complicates reliable measurements of electronic mobility, inducing contact resistance effects in organic electrochemical transistors (**sec. 1.10.3**). To address the problem, we develop the electrolyte-gated van der Pauw (EgVDP) method for the simple, accurate, and contact-independent determination of the electrical characteristics of OMIEC thin films. By comparing EgVDP measurements on PEDOT:PSS with OECTs observations, we demonstrate that a contact-independent technique is crucial for the proper determination of electronic mobility in OMIECs. The results of this research are discussed in **sect. 4.1**.

2. **Operando characterization of ionic transport in OMIEC materials:**

Ionic transport is another fundamental process in OMIECs which is particularly relevant when materials operate in hydrated conditions (**sec. 1.4**). Ion-driven electrochemical processes in mixed conductors induce mechanical deformation enabling artificial muscle-like actuators (**sec. 1.11.2**) but also lead to degradation processes affecting OMIEC based devices. Despite its relevance in different fields of material research, fundamental knowledge on the intrinsic mechanism of electroswelling is still lacking, and monitoring fast local ionic exchange processes in OMIECs remains elusive (**sec. 1.11.1**). To provide a microscopic understanding of electroactuation, we introduced the modulated electrochemical atomic force microscopy (mEC-AFM) as a novel characterization method for electroactive materials. In this technique, AFM is exploited as a local probe for volume changes and interface forces that provides transient data on dynamical effects related to electroactuation in OMIECs. The combination of the electroswelling data with electrochemical impedance spectroscopy in OMIEC microstructures

yields a multidimensional spectroscopy revealing the dominant timescales for ion migration and electroswelling.
Multidimensional spectroscopy experiments on PEDOT:PSS allowed us to implement multichannel mEC-AFM imaging, providing maps of local electroswelling amplitude and phase as well as surface morphology. The resulting knowledge provides a quantitative insight on ion transport in OMIEC materials, demonstrating the major role of ion drift in swelling processes. Results are presented in **sect. 4.2**.
At the same time, some electroactive materials show a more complex electroactuation dynamics which require in-depth investigations for its comprehension. For this reason, we extended mEC-AFM as a depth-sensitive technique to measure subsurface profiles of ion migration and swelling in Ppy:DBS electroactive layers. The interpretation of experimental data with a quantitative model demonstrates that electroactuation is not uniform in the Ppy:DBS layer but depends both on the film morphology and redox state, suggesting that the efficient actuation performance is caused by rearrangements of the polymer microstructure. Results are presented in **sec. 4.3**.

3. Recording and stimulating biosystems with OMIEC-based neural probes

Flexible microelectrode arrays placed on the surface of the brain cortex are promising tools for treating neurological deficits and restoring lost functionalities, as well as investigating unexplored aspects of neuroscientific research (see **sect. 1.9**). Further progresses in this direction require the development of biocompatible bioelectronics platforms enabling the long-term recording and stimulation of neural activity. In this thesis, we face this challenge by developing and characterizing microelectrode arrays (MEAs) based on PEDOT:PSS for electrocorticography (ECoG) experiments. We take advantage of microfabrication techniques onto flexible substrates to realize low-impedance devices both conformable with the brain surface and with high spatial and temporal resolution. We test the electrode arrays in an in-vitro setup combining electrochemical impedance spectroscopy (EIS), analysis of the voltage transients during simulated stimulation protocols, and atomic force microscopy (AFM) characterization of the PEDOT:PSS coating on the electrode surface. The combination of these techniques allows the optimization of an implantable neural probe prototype able to sense and stimulate the brain activity in chronic in-vivo experiments aiming to study induced-torpor states in animal models. Results are presented in **sect. 4.4**.

4. Amplifying biosignals with OMIEC-based active devices for single cell sensing

Research on organic electrochemical transistor (OECT) architectures is motivated by the prospect of a highly biocompatible interface capable of amplifying bioelectronic signals at the site of detection. Despite advancements in the field have led to the development of *in vitro* sensors reaching single cell resolution, a quantitative study on the transistor amplification gain in cellular impedance sensing is still lacking. A clear understanding of gain is also desired to define when OECT amplification has significant advantages over one-terminal, low-impedance microelectrode-based sensors offering simpler fabrication and electrical operation. To

overcome the issue, we introduce in this work a model experiment that allows a quantitative study of AC amplification in OECT impedance sensors. As cellular *in vitro* experiments are inherently difficult to control, we substitute the cell by a dielectric microparticle of similar dimensions. We control the position of the microparticle on top of the microscale impedance sensors with an AFM and achieve highly reproducible measurements that enable to compare the current output of OECT-based sensors with equivalent microelectrode sensors. To rationalize the findings, we develop an analytical model that describes the gain as a function of the applied frequency, the device geometry and PEDOT:PSS materials properties. Relying on this model, we design an optimized device and demonstrate its efficiency by measuring the transients of single-cell adhesion and detachment in *in vitro* experiments. Results are presented in **sect. 4.5**.

3 Methods

3.1 Device microfabrication

The realization of the OMIEC-based structures studied in this thesis requires microfabrication techniques. An overview of the process used to pattern and encapsulate metallic microstructures serving as electrodes for the final devices is reported in **Figure 3.1**. The fabrication techniques involved in the process are briefly described in the next paragraphs.

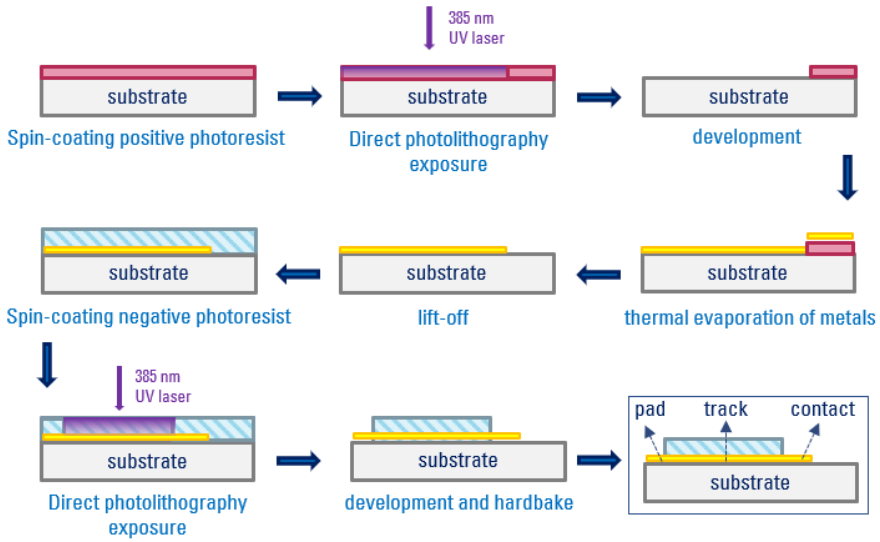

Figure 3.1: Microfabrication procedure for metallic microelectrodes used in OMIEC-based devices. The final structure includes pads to connect the device to the experimental setup and contacts to establish an electrical interface with OMIEC layers. Photolithography is used to pattern the microelectrodes and to encapsulate tracks (or feedlines) connecting pads and contacts. The encapsulation insulates the tracks from the surrounding electrolyte when OMIEC devices are used in liquid environment.

3.1.1 Spin-coating

Spin-coating is a procedure used to deposit uniform thin films onto flat substrates. Usually, a small amount of coating material dissolved in a volatile solvent is applied on the center of the substrate, which can be stationary or already spinning. A constant rotational speed (up to 10000 rpm) is then maintained for a defined time interval to spread the coating material by centrifugal force (as illustrated in **Figure 3.2**). The machine used for spin-coating is called a spin-coater. Rotation is continued until a flat surface is achieved through the complete evaporation of the solvent. The higher the angular speed ω of spinning, the smaller the thickness t of the film, being $t \propto \omega^{-1/2}$.[318] The thickness of the film also depends on the viscosity and concentration of the solution, and spin-coating curves of commercial solutions are typically provided by the manufacturer. The main advantage of spin-coating is the uniformity of the film

thickness. If the substrate is sufficiently small compared to the viscosity of the solution to spin, owing to self-leveling, thicknesses vary less than 1% throughout the film.

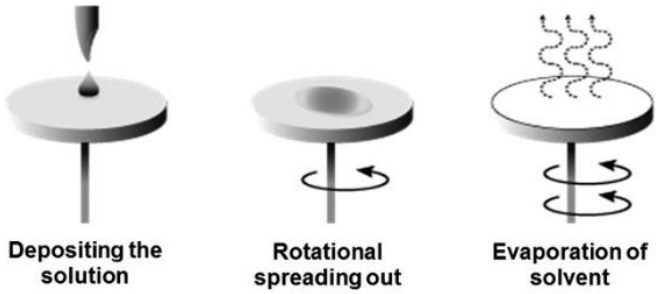

Figure 3.2: Thin film deposition using the spin-coating technique.[318]

3.1.2 Photolithography

The word photolithography identifies processes using light to transfer specific pattern with small features onto films, substrates, or wafers. Photolithography employs photons, usually UV photons, and a shaped mask to expose thin films of photoresist in some specific areas.[319] Photoresists are materials sensitive to UV radiation which change their chemical properties. These are divided into positive and negative resist. When exposed to UV photons, positive photoresists become soluble in a specific chemical agent call developer. On the contrary, negative photoresists become insoluble in the developer after UV absorption. Photolithography (see **Figure 3.3a**) begins with the preparation of the substrate, where a photoresist layer of a few microns is deposited through spin-coating. A baking (annealing) step on a hotplate is usually required to fully solidify the photoresist after its deposition. The sample is then exposed to UV light through a mask that blocks UV photons from going into unwanted regions of the photoresist. After exposure, the sample is immersed in the developer, and the photoresist layers exposed to UV light are dissolved or preserved depending on the type of photoresist used.

In this work I used the MicroWriter ML3 from Durham Magneto Optics to perform direct photolithography (see **Figure 3.3b**). This system uses a digital mask created via software for the photoresist exposure instead of a physical mask. The digital mask guides the machine to irradiate the sample with UV light only in specified regions. The MicroWriter is equipped with a precise sample positioning system in the x-y plane and a z stage hosting both the UV laser source and an interferometer for focus control. The MicroWriter provides extreme flexibility since the mask can be easily created with a CAD software. I used the Microposit S1818 positive photoresist to pattern metallic microelectrodes. The photoresist was spin-coated on dried glass or flexible polyethylene naphthalate (PEN) substrates with a rotating speed of 4000 rpm for 60 s. Samples were annealed at 110 °C for 1 minute and then exposed to the 385 nm laser source of the MicroWriter with exposure dose of 230 mJ/cm^2. The photoresist was finally developed with Microposit MF-319 developer. Metallic tracks were encapsulated with the mr-DWL 5 negative photoresist (from Micro Resist Technology). The resin was spin coated at 3000 rpm

for 30 s and annealed at 100 °C for 2 min. After laser exposure, samples were soft-baked at 100 °C for 2 min and relaxed for 1 h at room temperature. Development was performed with mr-Dev 600 developer (Micro Resist Technology), and the resist was finally hard-baked at 120 °C for 30 min.

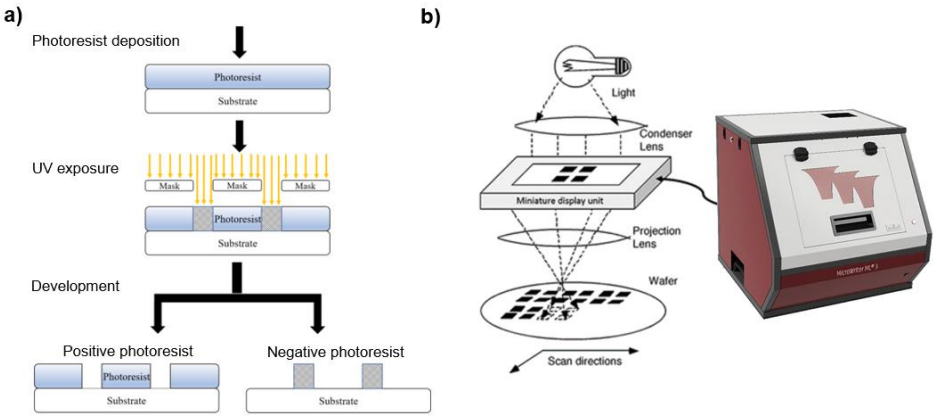

Figure 3.3: Photolithography. **a)** Deposition, exposure, and development of positive and negative photoresists. **b)** Direct photolithography process enabled by the MicroWriter ML3 from Durham Magneto Optics.

3.1.3 Thermal evaporation

Metallic thin films composing the device microelectrodes were produced using physical vapor deposition. Such process consists in the evaporation or sublimation of the material to deposit and the subsequent deposition onto a substrate. A schematic of the vacuum chamber hosting the setup for thermal evaporation is reported in **Figure 3.4**. Small pieces of metallic wires are placed in tungsten crucibles (called "sources") connected to an external power supply providing electrical current. The current heats up the source and the material inside, which first melts and then slowly evaporates on the substrate (placed about 50 cm above the source). The hot metallic atoms from the sources lose their kinetic energy when hitting the cold substrate and the film formation starts. A shutter is used to control the begin and end of the evaporation procedure. Both the layer thickness and the evaporation rate are measured by a quartz crystal balance, properly calibrated, placed near the substrate. The evaporation rate is controlled by varying the current across the crucible. The vacuum chamber containing the system is kept under ultra-high vacuum conditions ($< 5 \times 10^{-6}$ mbar) using a turbomolecular pump. Ultra-high vacuum (UHV) is needed to increase the mean free path of the evaportated atoms and to reduce the oxidation of the deposited layers.

In this work, after (positive) photoresist development (see **Figure 3.1**), I sequentially deposited 5 nm of chromium (evaporation rate 0.3 Å/s) and 40 nm of gold (evaporation rate 0.6 Å/s) on the sample substrate. The chromium layer acts as adhesion promoter for the gold thin films, used as conductor in the final device.

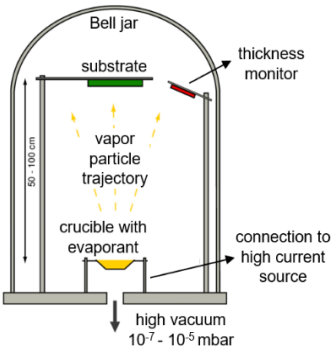

Figure 3.4: Setup for thermal evaporation. Samples are placed on a sample holder facing the evaporation source inside a glass bell jar in high vacuum conditions. The metal to be evaporated is placed inside a crucible (usually made of tungsten) heated by a flowing electric current. A quartz-crystal balance is placed near the sample holder and monitors the thickness of the metal being evaporated.

3.1.4 Lift-off

The lift-off process involves the removal of the residual photoresist after the deposition of metals. This procedure was performed by dissolving the positive photoresist in acetone for 4 h. Samples were finally rinsed by sonication in acetone/isopropanol and distilled water baths.

3.1.5 Micropatterning OMIEC layers

Micro-structured OMIEC layers were patterned onto encapsulated metallic electrodes using two different techniques. The PEDOT:PSS active layers used in neural probes, van der Pauw structures, and OECTs for single cell detection were deposited through spin coating (**Figure 3.5**). A double layer of positive photoresist was deposited and exposed to define the device regions to be covered by PEDOT:PSS.[320] The thicker photoresist structure inhibits crosslinking processes between PEDOT:PSS molecular chains deposited between the developed and not developed regions of the sample surface. In this way, OMIEC patterns had neater profiles after photoresist lift-off. The OMIEC formulation was prepared by mixing the PEDOT:PSS dispersion Clevios PH1000 (Heraeus) (94% v/v) with ethylene glycol (5% v/v) and 4-dodecylbenzenesulfonic acid (DBSA) (0.25% v/v/) to improve the film conductivity and adhesion on the glass substrates (or gold contacts), respectively. 3-glycidoxypropyltriimethoxysilane (GOPS) (1% v/v) was added in the solution as cross-linking agent. The realized suspension was sonicated for 10 minutes and then filtered using 1.2 µm cellulose acetate filters (Sartorius) before spin coating (3000 rpm for 9 s) on substrates treated with air plasma (15 W for 4 min). Samples were then annealed at 120°C for 1h hour to remove the residual water and excess secondary dopants. Finally, the photoresist was lifted-off by chemical dissolution in isopropanol for 4 hours. The resulting PEDOT:PSS thickness was 150±10 nm.

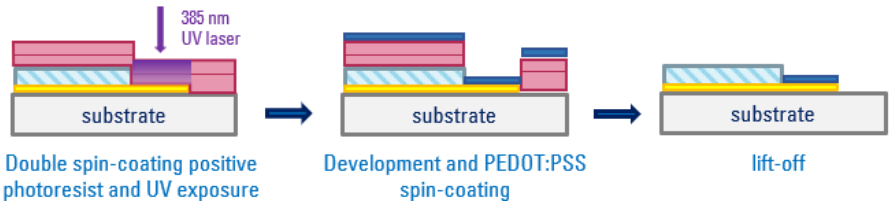

Figure 3.5: Micropatterning of PEDOT:PSS thin films using photolithography and spin-coating. A double layer of positive photoresist (S1818) provides a higher vertical separation between the undeveloped and developed S1818 regions, resulting in a better definition for the OMIEC micropattern.

The second technique used to fabricate microstructured OMIEC layers is the electrochemical deposition.[98] In this approach, a potentiostat (see **3.2.1**) is used to electropolymerize polymeric layers on a conductive substrate immersed in an electrolyte containing both the monomers and dopant counterions. The geometry of the OMIEC coating can be controlled by micropatterning and encapsulating the underlying metallic electrode. Further details are given in **3.2.2**.

3.2 Electrochemical methods

3.2.1 Potentiostat

The electrochemical properties of a material immersed in an electrolyte can be studied in an electrochemical cell. This must include an electrode based on the material under investigation and an electrode which can close the circuit through a redox reaction with any of the species present in the electrolyte. The former is named Working Electrode (WE) and the latter Counter Electrode (CE). The CE must have a known potential serving as a reference point to measure the WE potential and compensate for the charge introduced or extracted by the working electrode. Anyway, it is extremely difficult for an electrode to maintain a constant potential while passing current to counterbalance charge flow at the working electrode. The problem is solved by dividing between two separate electrodes the roles of supplying electrons and providing a reference potential. In this scheme, the Reference Electrode (RE) is a half cell with a known reduction potential.[144] A standard RE is given by the silver/silver chloride (Ag/AgCl) electrode based on the redox equilibrium between the solid silver metal and its solid salt silver chloride in a chloride solution of a given concentration. The Ag/AgCl reduction potential in a 3M KCl solution is +210 mV vs Normal Hydrogen Electrode (NHE). The electronic setup needed to control a three-electrodes cell is called potentiostat (see **Figure 3.6**). This features an operational amplifier to control the electrochemical potential *E* between the working and reference electrode, and measure the current sourced by the counter electrode to maintain such potential. It follows that the CE must be made of a material with facile reduction and oxidation kinetics so that a low resistance path with the electrolyte is established independently from the potential in which we are working. In aqueous environment, such

condition can be obtained using Platinum electrodes which are good catalyzers both for the water reduction and oxidation reactions.
Finally, the setup in **Figure 3.6** can be easily adapted to realize a galvanostat circuit which can measure the electrochemical potential between the WE and RE while controlling the current flowing between the WE and CE.

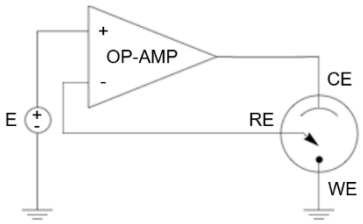

Figure 3.6: Schematic of the potentiostat circuit. An operational amplifier controls the potential *E* between the working and reference electrode, which is maintained by the counter electrode which supplies the current *I* flowing in the cell.

3.2.2 Electrochemical deposition of OMIEC thin films

I used electrochemical deposition to deposit OMIEC thin films on gold microelectrodes for AFM measurements of electroactuation. PEDOT:PSS was electropolymerized from an aqueous solution containing 10 mM 3,4-Ethylenedioxythiophene (EDOT) and 0.1 mM Poly(sodium 4-styrenesulfonate) (NaPSS) (both from Merck). Polypyrrole doped with dodecylbenzenesulfonate (Ppy:DBS) was electropolymerized from an aqueous solution 0.1 M in pyrrole and 0.1 M in sodium-dodecylbenzene sulfonate (NaDBS) (both from Merck). OMIEC layers of controlled thicknesses were obtained through a two-electrodes galvanostatic procedure, where the current density flowing between the (working) microelectrode and a Ag/AgCl wire counter/reference electrode was kept constant to 2 mA/cm^2. The use of a two-electrodes cell is justified by the fact that the impedance of the microstructured working electrodes was order of magnitude larger than the one of the Ag/AgCl wire, with the potential drop in solution being relevant only at the WE/electrolyte interface.[321] The electrochemical potential *E* (vs Ag/AgCl) measured during the galvanostatic deposition procedure of Ppy:DBS is shown in **Figure 3.7a**. The highly stable voltage profiles allowed for a linear control of the polymeric coating thickness by setting a proper deposition time. The deposition rate resulting from the linear fit in **Figure 3.7b** is 17±2 nm/s. Similar results were obtained for the electropolymerization of PEDOT:PSS, with a deposition rate of 11.2±1.4 nm/s.

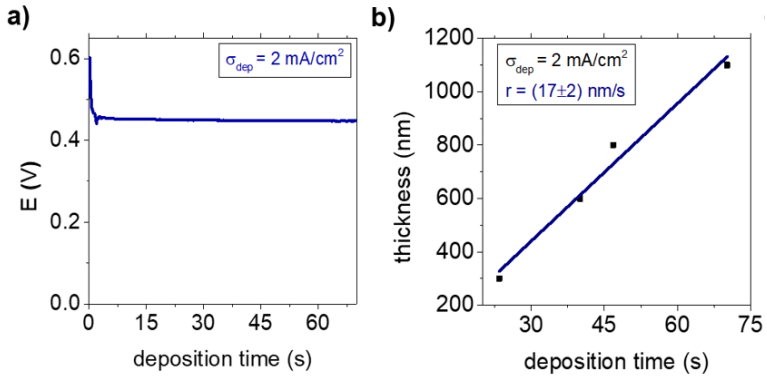

Figure 3.7: a) Galvanostatic electrodeposition of a Ppy:DBS coating on a gold microelectrode with a diameter of 30 µm. **b)** Control of the Ppy:DBS coating thickness through the deposition time.

3.2.3 Electrochemical impedance spectroscopy

Electrochemical reactions at an electrode–electrolyte interface can be decomposed into a series of multistep processes (mass transport, charge transfer, adsorption, capacitance charging), each occurring at distinct rates. The individual steps are time dependent and may occur at different timescales. The study of electrochemical systems is facilitated by the use of the transient techniques enabling the analysis of time dependent processes occurring at selected frequencies.[322] Electrochemical impedance spectroscopy (EIS) uses a small amplitude potential periodic perturbation V to excite the electrochemical system at different frequencies, as illustrated in **Figure 3.8**. By measuring the response of the system to this perturbation (the electrochemical current I), it is possible to calculate the electrochemical impedance transfer function of the system as

$$Z(\omega) = \frac{V(\omega)}{I(\omega)} = \left|\frac{V(\omega)}{I(\omega)}\right| \left[cos\big(\phi(\omega)\big) + i\, sin(\phi(\omega))\right] = Z_R + iZ_I \qquad 3.1$$

where ω is the angular frequency, ϕ is the phase angle between the input and output signals, and i (or j) is the imaginary unit. The electrochemical impedance, as defined by **Eq. 1.1**, is a frequency dependent complex number, whose real part, Z_R, is a frequency dependent resistance and imaginary part Z_I is a frequency dependent reactance. EIS measurements should be designed to conform to the Kramers-Kronig relations, which are derived under the assumptions that the system under investigation is linear, stable, and causal (**Figure 3.8c**). Such a condition is typically achieved when the amplitude of the potentiostatic modulation V ranges from 10 to 100 mV. The frequency range of EIS experiments should be set to match the dynamic range of the system under study, which is typically 100 kHz–100mHz for electrochemical processes. Usually, seven to ten points per frequency decade equally spaced logarithmically are required for measuring an impedance spectrum with sufficient accuracy for a detailed data analysis. It is preferable to start the measurement from the high frequency limit sweeping

towards the low frequency limit (**Figure 3.8b**). This because at high frequency capacitive currents and charge transfer inside the WE are predominant, while at low frequency faradaic processes with the electrolyte become significative and the generation of new chemical species at the interface might interfere with subsequent measurements. The first step towards data analysis is the use of graphical methods to visualize and interpret the impedance data (**Figure 3.8d**). To emphasize a specific feature or behavior, impedance can be presented in different formats including the Nyquist representation for mass transfer and kinetic behavior and the Bode representation for frequency dependent behavior. By fitting these data with equivalent circuits (**Figure 3.8e**), it is possible to correlate the frequency response of the system with specific interfaces and processes modeled by equivalent circuit elements.
In this thesis, EIS was widely used to study charge transport and accumulation processes at OMIECs/electrolyte interfaces both in fundamental studies and devices for applications. The quantitative interpretation of the obtained results is discussed in detail in **chapter 4**.

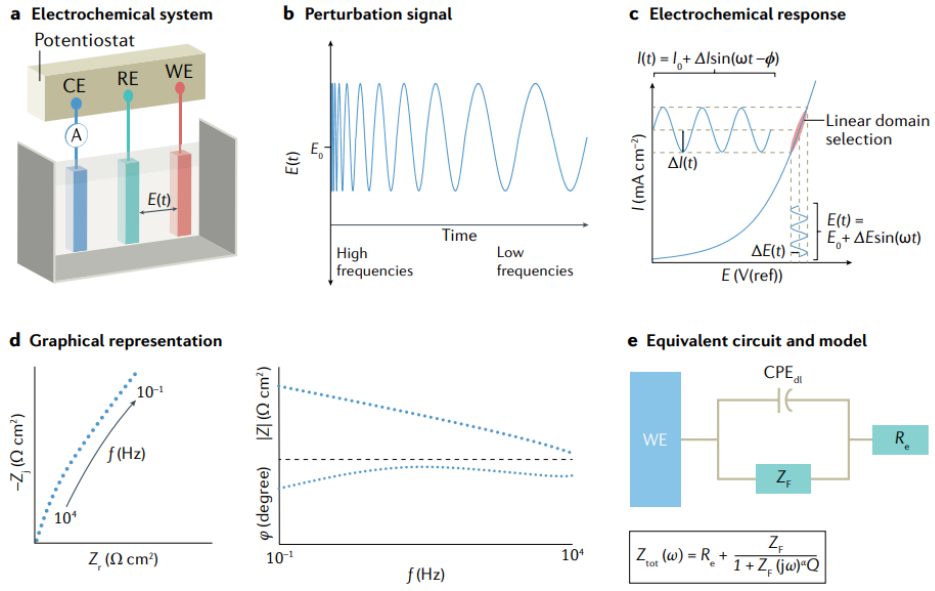

Figure 3.8: Electrochemical impedance spectroscopy. **a)** Electrochemical cell where a small amplitude voltage modulation is applied between the working and reference electrode. **b)** The frequency of the voltage modulation is swept in a wide frequency range, from the high frequency limit towards the low frequency limit. **c)** The response of the electrochemical system (the current *I*) is measured in the linear regime. **d)** Graphical representation of the acquired data, featuring the Nyquist (left) and Bode (right) plots. Data are analyzed using equivalent circuit descriptions (**e**).[322]

3.3 Atomic force microscopy

Atomic Force Microscopy (AFM) is a high-resolution non-optical imaging technique, allowing accurate and non-destructive measurements of the topographical, electrical, magnetic, chemical, optical, and mechanical properties of a sample surface in air, liquids or ultrahigh vacuum.[323] The basic operation principle of a standard AFM system with optical feedback involves scanning an AFM probe with a sharp AFM tip over a sample surface in a raster pattern (see **Figure 3.9a**). The AFM tip is usually made of silicon or silicon nitride and is integrated near the free end of a flexible AFM cantilever. A piezoelectric ceramic scanner controls the lateral and the vertical position of the AFM probe relative to the surface. When the tip is approached to the sample at distances down to 0.1-20 nm, information on the sample properties can be studied from the interactions between the tip and the sample surface, inducing the deflection of the AFM cantilever. Such a process is tracked by a laser beam reflected from the back site of the cantilever and directed into a position sensitive photodetector (PSPD). A PSPD is a photodiode divided into four quadrants: from the measurement of the laser intensity variations on the different sections it is possible to extract the amount of vertical and lateral deflection of the cantilever. As the AFM tip moves over features of different height, the deflection of the AFM cantilever changes according to the different local interactions. A feedback loop controls the vertical extension of the vertical scanner to maintain near-constant constant interaction force. The coordinates that the AFM tip tracks during the scan are combined to generate a three-dimensional topographic image of the surface.

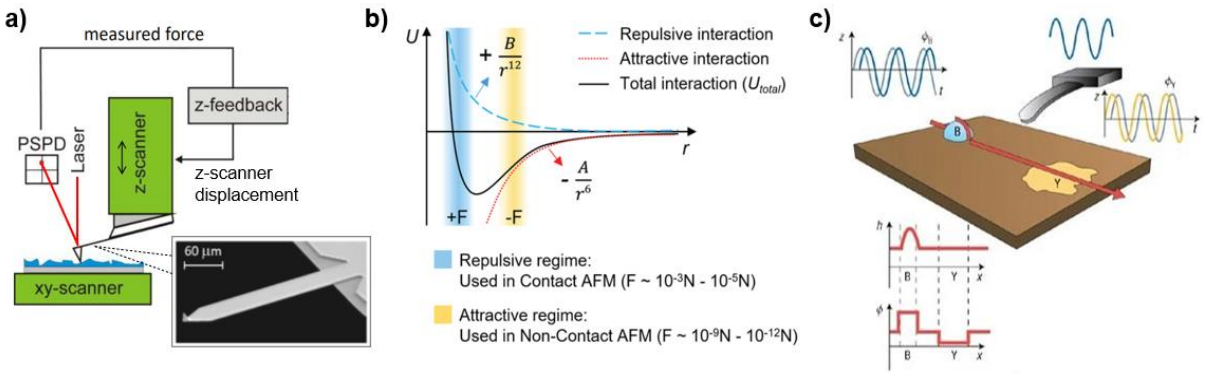

Figure 3.9: Atomic force microscopy. **a)** Schematic representation of the AFM components. The scanning electron microscope image of an AFM probe is reported as inset, showing the AFM cantilever and tip. **b)** Lennard-Jones potential approximating the tip-sample interaction energy. According to the tip-sample distance, AFM can be operated in contact or non-contact mode.[324] **c)** Non-contact AFM operation. Variations in the sample topography (blue region) are measured by changes in both the cantilever oscillation amplitude and phase, while only phase traces are sensitive to compositional changes (yellow region).[325]

As the dimension of the edge of the tip is one order of magnitude higher than the atomic dimension, the potential energy of the tip can be approximated with the van der Waals energy of two atoms (also known as the Lennard-Jones potential):[324]

$$U_{LJ}(r) = U_0\left[-2\left(\frac{r_0}{r}\right)^6 + \left(\frac{r_0}{r}\right)^{12}\right] \quad 3.2$$

where r_0 is the equilibrium distance between the atoms. According to the tip-sample distance r, the interaction between the tip and the sample can be either repulsive or attractive, enabling two different AFM operation modes (see **Figure 3.9b**). In contact mode, the AFM probe tip is scanned across the sample surface while maintaining constant contact with it. The feedback system aims to maintain constant AFM cantilever deflection and consequently a constant interaction force. The forces between the AFM tip and the surface are repulsive. Soft AFM cantilevers with force constants $\leq$ 1N/m are usually used to minimize AFM tip wear and surface damage and to increase sensitivity. Among the main drawbacks of contact mode operation are the susceptibility of AFM tips on soft AFM cantilevers to both lateral forces and sticking to the surface contamination layers. These result in image distortions. In addition, lateral forces can be damaging to the AFM probe tip and to soft samples. For these reasons, non-contact (or dynamic) AFM was introduced. In non-contact mode, the AFM probe cantilever is oscillated by a piezoelectric actuator at or near its fundamental resonance frequency, usually several tens to several hundred kilohertz. The AFM probe is then lowered towards the sample keeping a distance of several nanometers away from the surface. The resulting attractive interaction forces damp the cantilever oscillation amplitude and modify its phase. The feedback loop acts to maintain a constant AFM cantilever oscillation amplitude and hence a constant interaction force. The advantage of non-contact mode is that it offers the lowest possible interaction between the tip and the sample surface. Small interaction forces help preserve AFM tip sharpness and achieve high resolution. The oscillation phase is affected by variation in the dissipated energy on the sample surface, thus non-contact mode AFM is sensitive to the sample composition (see **Figure 3.9c**).[325] The disadvantage is that it is challenging to keep at the AFM tip in the attractive regime. For small tip-surface distances, high performance feedback controls are needed.

In this thesis, I used the Park NX10 AFM system operating in non-contact mode to image the surface topography of the samples under study. At the same time, in-liquid AFM experiments under potentiostatic control (electrochemical atomic force microscopy, EC-AFM) have a major importance in this work.

3.3.1 Electrochemical atomic force microscopy

Atomic force microscopes can measure nanometer-scale-resolution images of samples submerged in a liquid, facilitating applications in physical as well as life sciences.[326] In these experiments, the sample is held in a small vessel (or cell) with a small amount of liquid. The probe is on a special holder with a glass window directly above the probe. In operation, the probe is submerged in the liquid while scanning (**Figure 3.10a**). Electrochemical atomic force microscopy (EC-AFM) combines high-resolution imaging of surfaces with electrochemical characterization (**Figure 3.10b**). EC-AFM is operated in a liquid

environment containing electrochemical reactive species. A set of electrodes allows the application of an electrochemical potential to the sample inducing electrochemical processes. At the same time, an AFM setup measures the surface morphology and changes induced by the chemical reactions. Such measurements are realized with an electrochemical cell that is designed to simultaneously control processes of interest while providing a suitable medium to image the topography of the sample surface. This cell is like the setup used for standard measurements in liquid environments with the main difference that the electrochemical cell is also equipped with working, counter, and reference electrodes. An optical image of the setup I used for EC-AFM experiments is reported in **Figure 3.10c**. A polyether ether ketone (PEEK) substrate supports a sample microfabricated on a glass slide. The electrolyte is confined on the sample by a PEEK well sealed with screws and an underlying polydimethylsiloxane (PDMS) O-ring. A Ag/AgCl wire and a platinum wire are placed on the right and left side of the well, respectively; with the former acting as (pseudo)reference electrode and the latter as counter electrode. The microstructured OMIEC devices acting as working electrodes are aligned with the center of the well and individually addressable though the metallic contact pads patterned outside the liquid well.

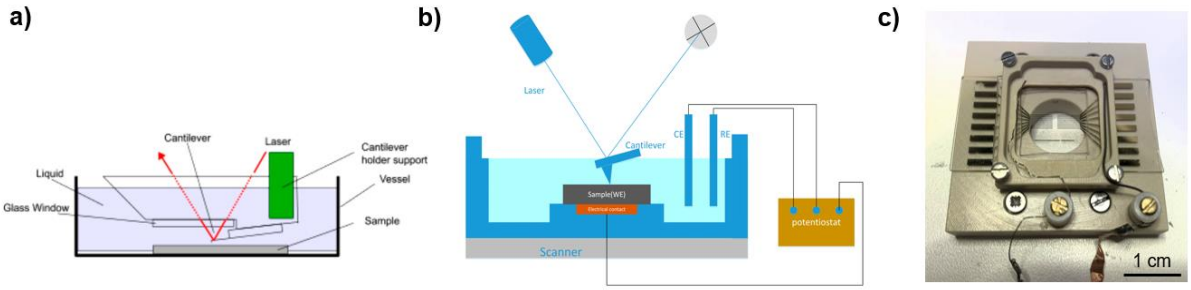

Figure 3.10: Electrochemical atomic force microscopy. **a)** Schematic of an open cell to perform in-liquid AFM experiments. **b)** Schematic of an EC-AFM setup with potentiostatic control. **c)** EC-AFM cell used for in-liquid experiments in this thesis, featuring a Ag/AgCl wire as reference electrode, a Pt wire as counter electrode and a set of microstructured OMIEC devices patterned at the center of the cell. These are individually addressable through the contact pads fabricated at the left and right sides of the liquid cell.

3.4 Electrical characterization of OECTs

OECT electrical measurements were used both to investigate their characteristic behavior and to evaluate their performances as sensors. Experiments were carried out in ambient conditions, using a Ag/AglCl wire as gate to have a nonpolarizable electrode for which the voltage drop at the electrolyte interface is negligible (see **sect. 1.10.2**). Both the gate and the microstructured PEDOT:PSS OECT channels (resulting from the microfabrication process in **Figure 3.5**) were immersed in a phosphate-buffered saline (PBS) solution (1×), ensuring a pH-neutral and water-based experimental environment.[327]

3.4.1 DC measurements

DC measurements were performed to study the steady state behavior of the OECTs and extract the related figures of merit. Measurements were performed with a 2-channels Keysight B2912A source-measure unit (SMU) using the setup in **Figure 3.11a**. DC electrical measurements on OECTs can be divided into characteristic (or output) curves and transcharacteristic (or transfer) curves. Output measurements involve the sweep of the source-drain voltage $V_{D,DC}$ over a defined range, while the gate potential $V_{G,DC}$ is maintained at a fixed value, and the current at the drain electrode $I_{D,DC}$ is recorded as a function of $V_{D,DC}$. Then, the potential on the gate is changed and another curve is recorded to study the transistor characteristic behavior for different gate potentials. Output curves measured for a PEDOT:PSS OECT with channel width and length WxL = 100x100 µm and thickness 100±10 nm are reported as an example in **Figure 3.11b**.

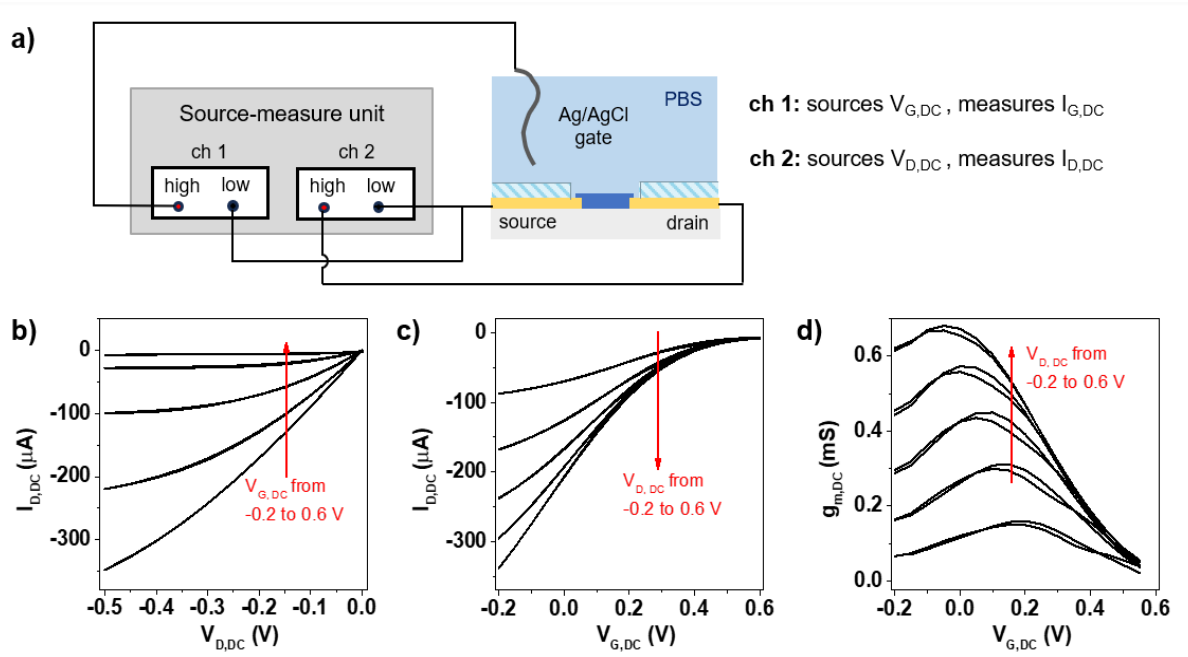

Figure 3.11: DC characterization of organic electrochemical transistors. **a)** Experimental setup, involving a microstructurated PEDOT:PSS channel and a Ag/AgCl gate to constitute the OECT device. Measurements are performed with a 2-channel SMU, with the source electrode operating as low reference point for voltages for both channels. Output **(a)**, transfer **(b)**, and transconductance **(c)** curves measured for a PEDOT:PSS OECT with channel width and length WxL = 100x100 µm and thickness 100±10 nm.

Transcharacteristic curves require a fixed drain voltage $V_{D,DC}$, while sweeping the potential on the gate $V_{G,DC}$ and recording the current at the drain electrode $I_{D,DC}$ (**Figure 3.11c**). Transfer curves monitor how the channel doping and de-doping process (mediated by $V_{G,DC}$) influences the OECT current, studying the device amplification properties. Thereby, an important figure of merit of the devices - the transconductance, defined as $g_{m,DC} = \partial I_{D,DC}/\partial V_{G,DC}$ - can directly calculated from the transistor transfer curves at different applied potentials (**Figure 3.11d**).

3.4.2 AC measurements

AC measurements were performed to study the transient behavior (or frequency response) of the OECTs extract the related figures of merit. Experiments were performed with the MFLI lock-in amplifier (from Zurich Instruments) using the setup in **Figure 3.12a**. A constant DC offset voltage $V_{G,DC}$ and a sinusoidal AC modulation $V_{G,AC}$ (with amplitude 10 mV and desired frequency) were applied to the gate terminal using the internal reference signal generated by the instrument. The resulting AC current flowing from OECT source ($I_{S,AC}$) was demodulated to acquire its amplitude and phase. A constant DC voltage $V_{D,DC}$ was applied between the source and the drain electrodes using a MFLI auxiliary output. The source electrode was used as a low reference point for the applied voltages.

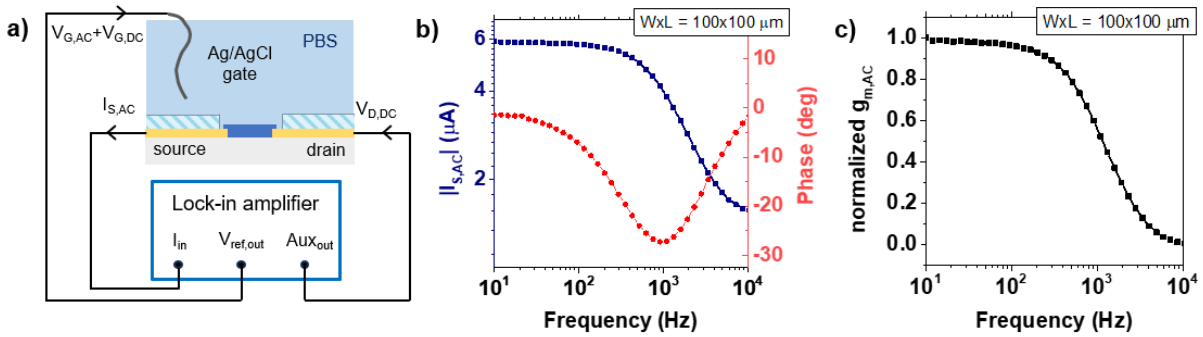

Figure 3.12: AC characterization of organic electrochemical transistors. **a)** Experimental setup, involving a microstructurated PEDOT:PSS channel and a Ag/AgCl gate to constitute the OECT device. Measurements are performed with a lock-in amplifier, with the source electrode operating as low reference point for applied voltages. Source current spectrum **(b)** and AC transconductance **(c)** measured for a PEDOT:PSS OECT with channel width and length *W*x*L* = 100x100 µm and thickness 100±10 nm.

The OECT frequency response was measured by sweeping the frequency of $V_{G,AC}$ from 10 to 10^4 Hz. A source current spectrum acquired in a PEDOT:PSS OECT with channel width and length *W*x*L* = 100x100 µm and thickness 100±10 nm is reported in **Figure 3.12b**. Data show both the measured current amplitude and phase, and allow to calculate the AC transconductance as $g_{m,AC} = \partial I_{D,AC}/\partial V_{G,AC}$, which determines the OECT bandwidth (**Figure 3.12c**).

4 Results

In this chapter, I present the main results of my thesis work. The first three sections deal with studies on fundamental transport processes in OMIEC materials, while both the fourth and the fifth section are focused on applications. The findings reported in this chapter led to the publication of four scientific papers, and to the preparation of one manuscript submitted to a scientific journal.

4.1 Charge carrier mobility in organic mixed ionic-electronic conductors by the electrolyte-gated van der Pauw method

Electronic transport is a fundamental process in OMIECs determining the operation speed of bioelectronic devices, but mixed conduction complicates reliable measurements of electronic mobility. For this reason, we introduced the electrolyte-gated van der Pauw method to characterize electronic carrier transport in OMIECs. PEDOT:PSS thin films are used as a widely applied model system for OMIECs. We control the electrolyte gate potential by a potentiostat and measure the sheet conductance in a four-point probe geometry as a function of gate potential. We show then for the electrolyte gated van der Pauw method (EgVDP) a straightforward analysis to extract the threshold voltage V_t and the hole mobility μ_p. Results are compared with 2-point probe measurements done in OECT devices, where a simple model is discussed for the quantification of contact resistance effects. The reproducibility of the EgVDP method, combined with its intrinsic independence from contact resistance effects and the straightforward data analysis, validate this technique as an effective strategy for the accurate characterization of electronic mobility in OMIEC thin films.
Results presented in this chapter were published in August 2021 on the *Advanced Electronic Materials* journal.[105] I collaborated on this work with Francesco Decataldo, Beatrice Fraboni, and Tobias Cramer from the Department of Physics and Astronomy of the University of Bologna.

4.1.1 The electrolyte-gated van der Pauw method

EgVDP experiments required micro-structured PEDOT:PSS thin film devices fabricated according to the procedure in **sect. 3.1**. The optical micrographs in **Figure 4.1a** demonstrate the well-defined gold contacts serving as electrodes for the measurements. The area covered by PEDOT:PSS gets visible by its slightly blue color. Four symmetric gold electrodes are placed at the edges of the PEDOT:PSS thin film for EgVDP measurements. As required by van der Pauw's (VDP) method, the dimensions of the metallic contacts are maintained as small as possible with respect to the film size. The PEDOT:PSS film is patterned with a square shape (with side 500 µm) to reduce contact displacement errors in VDP

measurements.[328] The PEDOT:PSS layer is designed with the same dimensions in two-contacts OECTs (**Figure 4.1b**). Here, the metallic contacts are patterned with the same width of the PEDOT:PSS film to provide well defined dimensions to the semiconducting channel undergoing electrical measurements. A schematic of the experimental setup realized for EgVDP characterization is finally reported in **Figure 4.1c**. The PEDOT:PSS active layer is immersed in an electrolyte (PBS 0.1 M). A current is injected between the high-force and the low-force contacts of the device (contacts 1 and 2 in **Figure 4.1c**, respectively) and the corresponding voltage drop is measured between the other two (the high and low-sense, contacts 4 and 3, respectively). Simultaneously, a potentiostat (Metrohm Autolab PGSTAT204) is employed to generate an electrical potential (the gating voltage V_G) between a Ag/AgCl reference electrode (Amelchem 373/SSG/12) and the low-sense contact. A platinum wire was used as counter electrode.

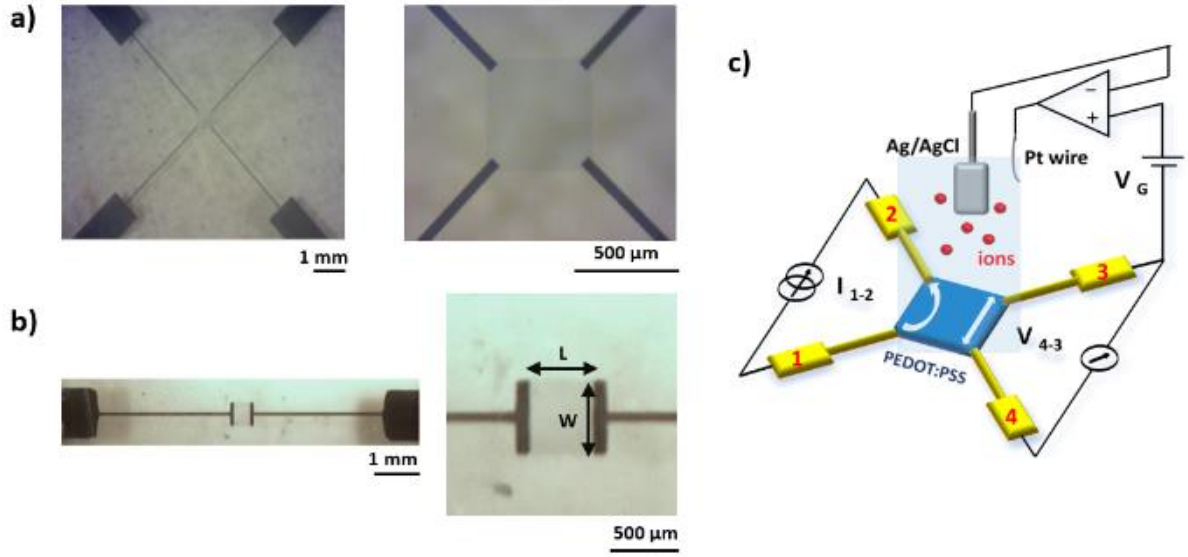

Figure 4.1: Experimental setup for electrolyte gated van der Pauw measurements to characterize electronic transport in PEDOT:PSS thin films. **a)** Optical micrographs of a four-contact measurement structure with the PEDOT:PSS active layer patterned at the center of the device. **b)** Optical micrographs of an organic electrochemical transistor. **c)** Schematic of the experimental setup for EgVDP characterization.

4.1.2 Electrical characterization of electrolyte-gated PEDOT:PSS thin films

We measured the channel capacitance of the fabricated thin films by characterizing the PEDOT:PSS-electrolyte interface with electrochemical impedance spectroscopy. Results for EgVDP devices and OECTs are presented, respectively, in **Figure 4.2a** and **b**. The acquired Bode plots were fitted with the equivalent circuit shown in the inset. Both interfaces can be modeled with a simple RC circuit, representing the electrolyte resistance R_{el} and the channel capacitance C of the device.[329] As expected, the frequency response of EgVDP devices reproduces the one of OECTs, since the PEDOT:PSS layers under investigation have the same

dimensions. The resulting average volumetric capacitance of PEDOT:PSS is (29±2) F/cm^3, which is consistent with literature values.[330] The channel capacitance was measured as a function of the gate voltage (**Figure 4.2 c**) for two different macroscopic EgVDP devices, with an active PEDOT:PSS film area of 35 mm^2. C resulted to be independent from V_G and approximately constant in the voltage range in which the EgVDP characterizations were performed (-0.2 V < V_G < 0.6 V). Therefore, measurements were fitted with a constant line, and the resulting mean capacitances are compatible to each other.

Next, we investigate the timescales at which gating is effective in electrolyte-gated van der Pauw structures. **Figure 4.2d** and **e** show the behavior of two EgVDP structures with different dimensions when gate voltage steps are applied. The time response of a larger, macroscopic device (**Figure 4.2d**), with an active PEDOT:PSS film area of 35 mm^2, is compared with the one of a microscopic EgVDP structure (**Figure 4.2e**), with film area 0.25 mm^2 (see **Figure 4.1a**). During each step, V_G is kept constant for 10 s, and then increased by 0.04 V (scan rate 4 mV/s). In both cases, the voltage drop on the sample between the sensing contacts 4 and 3 reaches a stationary state after a transient RC response. The time duration of the transitory state depends on the time constant of the device (τ), which is proportional to its capacitance. Many studies demonstrate that the electrical capacitance of a PEDOT:PSS film depends on its volume.[331] As the polymeric layers present the same film thickness in macroscopic and microscopic devices, the difference in capacitance is only related to the different film area.

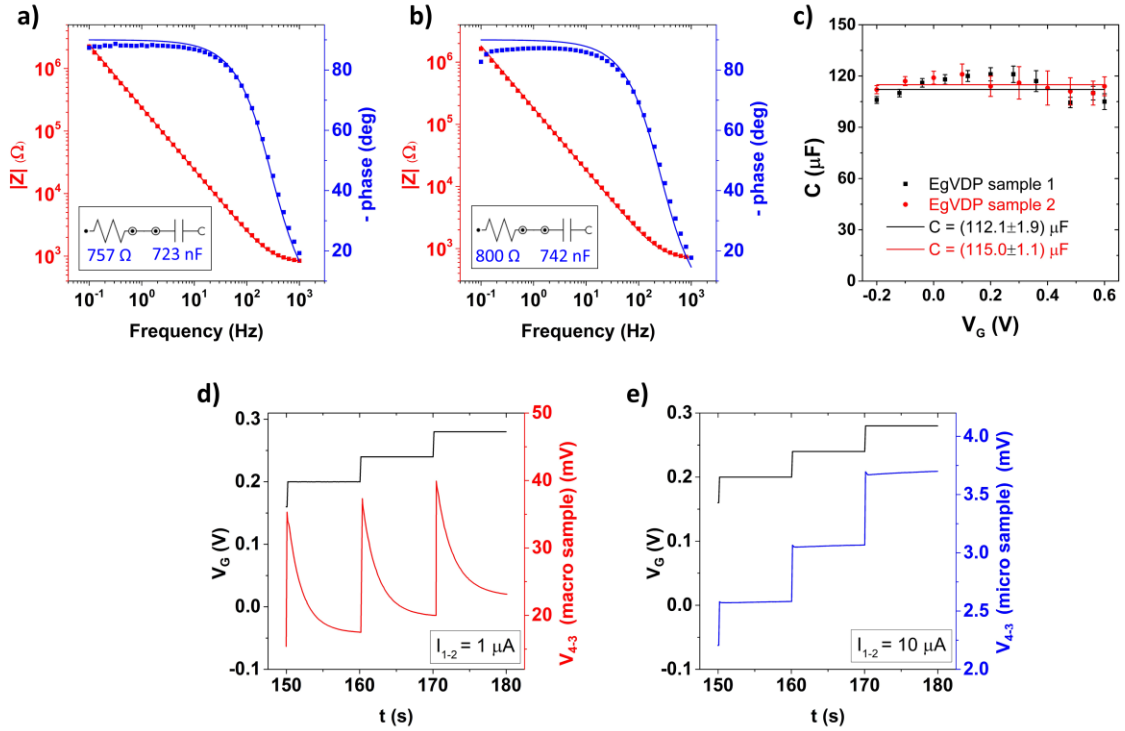

Figure 4.2: Electrical characterization of electrolyte-gated PEDOT:PSS thin films. Electrochemical impedance spectroscopy of four contact **(a)** and two contact OECT **(b)** structures. The Bode plot was fitted with the circuit shown in the inset. Time response of macroscopic **(d)** and microscopic **(e)** four contact structures during electrolyte gated van der Pauw measurements. The voltage drop on the sample between the sensing contacts 4 and 3 is measured in time while varying the applied gate voltage V_G.

Figure 4.2d demonstrates that the large capacitance of macroscopic EgVDP samples poses a strong limitation during the EgVDP characterization. In particular, when the carrier concentration in PEDOT:PSS is small (high channel resistance), the charge/discharge processes are too slow for a reasonable scan rate on V_G and the circuit fails to reach the stationary behavior. For this reason, during the characterization of macroscopic sized samples we could not apply gating voltages above 0.4 V, and only a limited range of carrier concentration was studied. Miniaturization is therefore crucial to study low carrier concentration regimes.

4.1.3 Electronic transport in van der Pauw and OECT devices

Results of the electrolyte gated transport measurements are reported in **Figure 4.3a** and **b**. The gate voltage is scanned between -0.2 and 0.6 V (forward and backward scans), while a constant current $I_{1\text{-}2}$ = 10 μA is injected between the High and Low force contacts 1 and 2. The gate potential range of the experiment was selected to avoid material degradation and water splitting processes. The measured sheet conductance of the thin film (**Figure 4.3a**) is plotted as a function of the difference between V_G and V_C, with V_C being defined as half the voltage drop measured on the sample ($V_C = V_{4\text{-}3}/2$). For comparison, the transfer curve of a two contact OECT measured in linear regime (V_{DS} = 0.05 V) is presented in **Figure 4.3b**. In both cases, the behavior of the samples are reproducible during the gate voltage scan, and measurements show only a small hysteresis. Both EgVDP devices and OECTs reach a linear operation regime below a threshold voltage V_t. The linear behavior of an OECT is commonly described by the Bernard's model [329]

$$I_{DS} = \mu_p C \frac{W}{L}\left(V_t - V_{GS} + \frac{V_{DS}}{2}\right)V_{DS} \qquad (4.1)$$

where C indicates the capacitance per unit area of the PEDOT:PSS-electrolyte interface, and W, L are respectively the channel width and length. Equation 4.1 can also be used to describe EgVDP operation. The probed region between the sensing contacts 4 and 3 in EgVDP structures can be treated as a semiconducting channel with source and drain at potentials V_3 and V_4, respectively. The geometrical dimensions of the channel are related by $L/W = \ln(2)/\pi$, as demonstrated by van der Pauw for square VDP structures.[332] The injected current $I_{1\text{-}2}$ can be expressed in terms of the sheet conductance σ_s as

$$\frac{ln(2)}{\pi} I_{1-2} = \sigma_s |V_{4-3}| \qquad (4.2)$$

with

$$\sigma_s = \mu_p C |V_t - V_G + V_C| \qquad (4.3)$$

The space charge density accumulated in the PEDOT:PSS layer is $\delta = C|V_t\text{-}V_G\text{+}V_C|$, where $V_C = V_{4\text{-}3}/2$ approximates the potential in the probed region of the EgVDP structures.

Figure 4.3a and **b** were fitted with **Eq. 4.1** and **Eq. 4.3** respectively to extract the charge carrier mobility and the threshold voltage of the devices. Quantitative results obtained from different samples are reported in **Table 4.1**. Mobilities measured in OECT devices are in good

comparison with findings described in literature. Typical values measured in OECTs are on the order of 1-10 $cm^2V^{-1}s^{-1}$.[333-334] In general, high mobilities for transport in OECT are reasonable, as the mobility is extracted in the high carrier density regime, were carrier trapping at band-edge states has only limited importance. At the same time, the accumulation does not exceed a critical limit at which energetic and structural disorder set-in due to PEDOT overoxidation.[335] **Table 4.1** also confirms that the EgVDP method allows for a very reproducible parameter extraction on the three different samples. Mobilities measured with the contact-independent EgVDP characterization are systematically higher than the ones measured with OECTs. A similar value for mobility was determined in contact independent measurements based on terahertz and infrared spectroscopy.[336]

Sample	μ_p [$cm^2V^{-1}s^{-1}$]	V_t [V]
EgVDP 1	12.0±0.5	0.436±0.011
EgVDP 2	11.7±0.4	0.44±0.02
EgVDP 3	11.3±0.4	0.45±0.02
OECT 1	5.9±0.3	0.57±0.02
OECT 2	6.7±0.2	0.520±0.012
OECT 3	4.2±0.2	0.530±0.010

Table 4.1: PEDOT:PSS mobilities and threshold voltages measured from EgVDP and OECT characterization.

To study in detail the difference between the OECT and EgVDP measurement techniques, we compare both the calculated sheet conductances in **Figure 4.3c**. At high gate voltages (low carrier concentrations) both curves are superimposed. Instead at low V_G, the EgVDP measurement shows the linear increase in conductance due to accumulation of carriers, while the two contact OECT measurement flattens and shows a significantly limited conductance. The difference between the two measurements can only be attributed to contact resistance effects. The presence of a contact resistance R_C generates an additional potential drop along the semiconducting channel of an OECT: $I_{DS} = V_{DS} / (R_{ch} + R_C)$, where R_{ch} indicates the channel resistance

$$R_{ch} = \frac{1}{\mu_p c \frac{W}{L}\left(V_t - V_{GS} + \frac{V_{DS}}{2}\right)} \qquad (4.4)$$

By substituting in the transfer curve equation the contact-independent mobility $\langle\mu_p\rangle$ = (11.7±0.3) $cm^2V^{-1}s^{-1}$ (obtained by averaging the EgVDP mobilities), the following equation can be solved to calculate R_C as a function of the gate voltage:

$$I_{DS} = \frac{\langle\mu_p\rangle c \frac{W}{L}\left(V_t - V_{GS} + \frac{V_{DS}}{2}\right)}{\langle\mu_p\rangle c \frac{W}{L}\left(V_t - V_{GS} + \frac{V_{DS}}{2}\right) R_c + 1} V_{DS} \qquad (4.5)$$

Results of this analysis are reported in **Figure 4.3d**. We thus obtain that, in linear regime, the contact resistance of an OECT is exponentially dependent on the gate voltage, and the equation

$$R_c\,(V_{GS}) \;=\; a * exp(b * V_{GS}) + c \qquad (4.6)$$

is fitted to the data, obtaining a = 0.0351±0.0012 V, b = 8.76±0.07 V^{-1} and c = 0.483±0.005 V. Hence carrier injection from the contact into the semiconductor channel is strongly mediated by the gate voltage in OECTs. This aspect is clearly visible in **Figure 4.3e**, which compares the OECT channel resistance with the contact resistance, both as a function of the gate potential. From this plot it is possible to observe that the gate-dependent contact resistance dominates on the channel resistance at low gate voltages. Consequently, contact resistance effects strongly affect the modulation of the PEDOT:PSS conductivity when the electronic carrier density in the material is high, causing the conductivity saturation typically observed in OECTs.

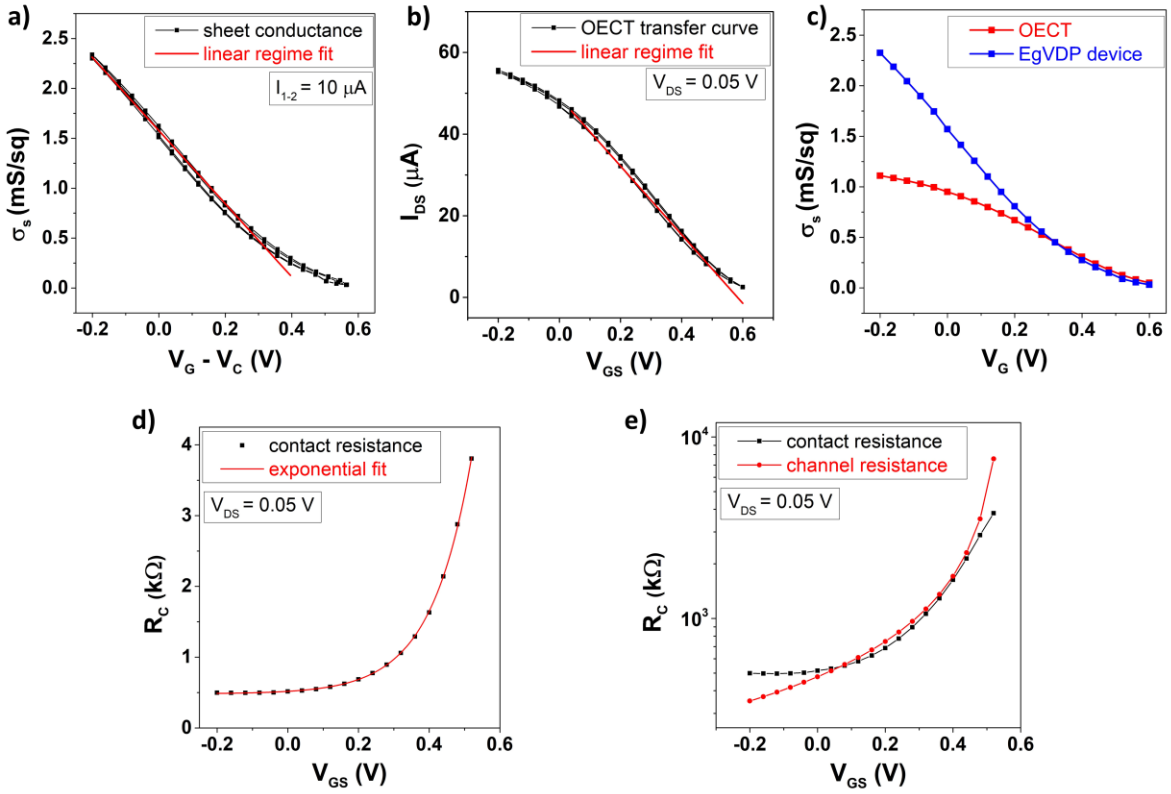

Figure 4.3: Analysis of the van der Pauw and OECT transport characterizations. **a)** Sheet conductance of an electrolyte gated van der Pauw structure plotted as a function of V_G -V_C (with V_C = $V_{4\text{-}3}$/2). A constant current $I_{1\text{-}2}$ = 10 µA is injected between the forcing contacts. **b)** Transfer curve of an OECT. The drain voltage is fixed at 0.05 V. The linear regime of the EgVDP and OECT characteristics is fitted to extract the mobility and the threshold voltage. **c)** Comparison between the sheet conductance of an EgVDP (red line) and an OECT (blue line). **d)** Evaluation and exponential fit of the contact resistance as a function of the gate voltage in an OECT. **e)** Comparison between the contact resistance and the channel resistance of an OECT device at different gate voltages.

4.1.4 Discussion

Previous works demonstrate gate-dependent effects can lead to mobility underestimations,[337-338] consistent with the results of our experiment. In contact-resistance free

measurements this effect is not observed and the conductivity of van der Pauw structures increases linearly with negative gate voltages in the potential range of measurements. A contact resistance exponentially dependent on the gate voltage was already found in OECTs by Kaphle et al.[339] This observation was interpreted as the consequence of ion accumulation at the drain contact, caused by lateral ion currents in the OECT channel.[340] Lateral ion transport can also be responsible for the threshold voltage overestimation in OECT characteristics. According to Kaphle's simulation[340], the application of a positive drain-to-source voltage (V_{DS} = 0.05 V) generates an equilibrium ion distribution in the channel which partially depletes from cations the region nearby the drain contact. Consequently, the electronic conductivity of PEDOT:PSS is locally increased, as the concentration of ionic de-dopants is reduced.[341] This effect can shift the threshold voltage of an OECT working in depletion mode towards higher gate voltages. In the EgVDP such a systematic error in threshold voltage determination cannot occur. A pair of high impedance electrodes measures the electric field strength relevant for carrier acceleration and is thus not affected by local ion-accumulation. We remark that in our experiment, we used a potentiostat and a well-defined reference electrode (Ag/AgCl 3M KCl) to have a precise control of the electrochemical potential in both van-der-Pauw and OECT characteristics. Under such conditions, the threshold voltage is reproducible and can be related to the materials properties. Therefore, it is possible to compare the threshold voltages extracted with both techniques. In doing so, we observe that contact resistance affects the linearity of the OECT transfer curves and renders the extraction of V_t difficult. On the other hand, the transfer curves acquired with EgVDP measurements are perfectly linear at high carrier densities, allowing for an accurate determination of the contact-independent threshold voltage. For such an ideal case, one can refer to more advanced models on carrier transport that relate V_t to the energy levels of the semiconductor and work function of the gate terminal. The energy diagram of a PEDOT:PSS-based OECT/van der Pauw structure immersed in PBS is reported in **Figure 4.4**.

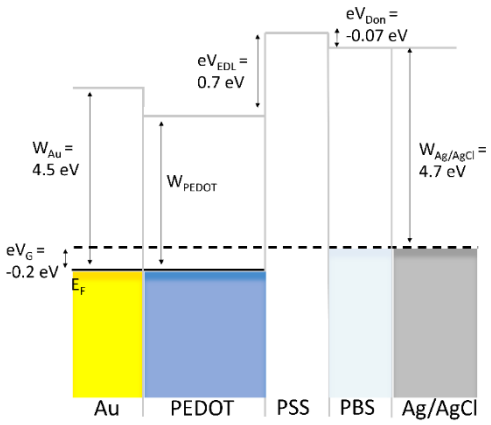

Figure 4.4: Energy diagram of an OECT/van der Pauw structure when a gate voltage of 0.2 V is applied, allowing for a fundamental interpretation of the threshold voltage in van der Pauw structures.

A gate voltage of 0.2 V is applied to the Ag/AgCl with respect to the gold electrode. The electrostatic coupling between the electronic phase (PEDOT) and the ionic phase (PSS) in the

intermixed PEDOT:PSS blend generates an electric double layer at all interfaces present in the phase separated material, whose potential is indicated with V_{EDL}. An additional potential drop must be considered at the interface between the PSS phase and the PBS electrolyte that is called Donnan potential, V_{Do}. The Donnan potential is caused by different ionic concentrations in the PSS-phase with respect to the free electrolyte, and was measured to be $V_{Do} = -0.072$ V.[122] The work function of the Ag/AgCl reference electrode is set to W_{AgCl} = 4.7 eV,[342] while W_{PEDOT} indicates the valence band edge of PEDOT (the work function of PEDOT:PSS is $W_{PEDOT:PSS} = W_{PEDOT} + eV_{EDL}$). The holes concentration in the PEDOT phase can be calculated from the product between the volumetric capacitance of the material and the double layer potential, that is $p = C_V V_{EDL}$, while the electrochemical equilibrium at the interfaces is expressed by

$$eV_G + W_{PEDOT} + eV_{EDL} - eV_{Do} - W_{Ag} = 0 \qquad (4.7)$$

From these equations, it's possible to find an equation for the linear transport regime of the device and a relation between the threshold voltage and the PEDOT work function:

$$V_t = \frac{W_{Ag}}{e} + V_{Do} - \frac{W_{PEDOT}}{e} \qquad (4.8)$$

V_t results to be dependent on the position of the valence band edge of PEDOT in its pristine state, which electrochemical measurements indicate to be W_{PEDOT} = 4.5 eV.[343] The contact independent threshold voltage extracted from EgVDP characterizations allows for a better estimate of this value ($W_{PEDOT,\ EgVDP}$ = (4.36±0.04) eV) with respect to OECT measurements ($W_{PEDOT,\ OECT}$ = (4.25±0.03) eV).

Finally, we note that alternative contact-independent techniques such as four-point probe (FPP)[344] and transmission line method (TLM)[339] can be used to extract the charge carrier mobility in the high-charge density regime of OMIECs. However, we think that the EgVDP method has many advantages over them:[345] TLM requires multiple devices with different channel length and mobility extraction is weakened by the problematic determination of the threshold voltage.[346] As shown in **Figure 4.3c**, transfer curves of OECT are not linear and therefore threshold voltage depends strongly on the mathematical extraction procedure. On the other hand, gated Four Point-Probe (gFPP) devices require the precise alignment of the voltage probes along the very edge of the semiconductor channel, and mobility extraction is typically compromised by small variations in device geometry.[347] In contrast, measuring the EgVDP device is of the same complexity as the gFPP device measurement (both require five contacts). However, the data obtained are more precise than in gFPP thanks to the averaging over different sides and the independence from geometric dimensions.

4.1.5 Conclusions

In this section, I introduced a four-point probe characterization technique for OMIEC materials, the electrolyte-gated van der Pauw's method. This technique is applied for the first time to PEDOT:PSS thin-film devices for an accurate extraction of the mobility and the threshold voltage, that are representative of the transport properties of the blend. The EgVDP

method combines many advantages: (1) the device structure and fabrication constraints are the same as for standard OECTs, allowing easy device integration and comparison; (2) the method is independent from contact effects that are detrimental to transistor characteristics; (3) a straightforward data analysis allows precise parameter extraction owing to the inherent averaging and independence from geometrical dimensions. We tested this method on three different EgVDP devices, obtaining highly reproducible results. The average PEDOT:PSS mobility and threshold voltage obtained from measurements are $<\mu_p>$ = (11.7±0.3) $cm^2V^{-1}s^{-1}$ and $<V_t>$ = (0.44±0.02) V . By comparing this result with 2-point-probe measurements, we found that contact resistance effects complicate the extraction of both the mobility and the threshold voltage, leading to an underestimation and an overestimation for the former and the latter, respectively. These observations indicate that a contact-independent technique is crucial for the proper characterization of PEDOT:PSS, and the EgVDP method is revealed to be a simple, elegant but effective technique for this scope. Given its general applicability and good accuracy, the EgVDP method can be a promising and useful tool to characterize electronic transport in new OMIEC formulations.

4.2 Ionic solvent shell drives electroactuation in organic mixed ionic-electronic conductors

Ionic transport is another fundamental process in OMIECs which is particularly relevant when materials operate in hydrated conditions. Ion-driven electrochemical processes in organic mixed conductors induce mechanical deformation enabling artificial muscle-like actuators, but also lead to degradation processes affecting OMIEC based devices. Despite its relevance in different fields of material research, fundamental knowledge on the intrinsic mechanism of electroswelling is still lacking, and monitoring fast local ionic exchange processes in OMIECs remains elusive. In this chapter, I address this issue introducing the modulated electrochemical force microscopy (mEC-AFM) as novel operando characterization method for electrochemical actuation, combining both microscopy and spectroscopy of electroswelling. AFM is used as a local probe for volume changes and interface forces that provides transient data on dynamical effects related to electroactuation in OMIECs. Combination of the electroswelling data with impedance spectroscopy in PEDOT:PSS microelectrodes yields a multidimensional spectroscopy revealing the dominant timescales for ion migration and electroswelling. The resulting knowledge allows us to implement multichannel mEC-AFM imaging, providing maps of local electroswelling amplitude and phase as well as surface morphology. Results demonstrate that the amplitude and timescales of electroswelling are governed by the drift motion of hydrated ions. Accordingly, slower water diffusion processes are not limiting and microactuators can operate at frequencies exceeding several kHz.

The findings presented in this chapter were published in *Advanced Science* journal in March 2024.[348] I collaborated on this work with Francesco Decataldo, Tobias Cramer, and Beatrice Fraboni from the Department of Physics and Astronomy of the University of Bologna.

4.2.1 The modulated electrochemical atomic force microscopy

mEC-AFM experiments require micro-structured devices based on electroactive OMIEC materials. For this reason, we fabricated PEDOT:PSS microelectrodes according to the procedure in **sect. 3.1**. An optical image of the final devices is reported in **Figure 4.5a**. Two rows of 8 gold microelectrodes are symmetrically patterned onto a glass substrate, allowing for each electrode the electrodeposition of a PEDOT:PSS layer with controlled thickness. Multiple electrodes are designed on the same substrate to vary systematically the thickness of the electroactive polymer layer. Also, a higher magnification image of a single electrode with 50 µm-diameter is shown featuring a PEDOT:PSS layer of 1 µm thickness. A thick negative photoresist layer (3 µm) electrically insulates the gold feedline from the surrounding electrolyte.

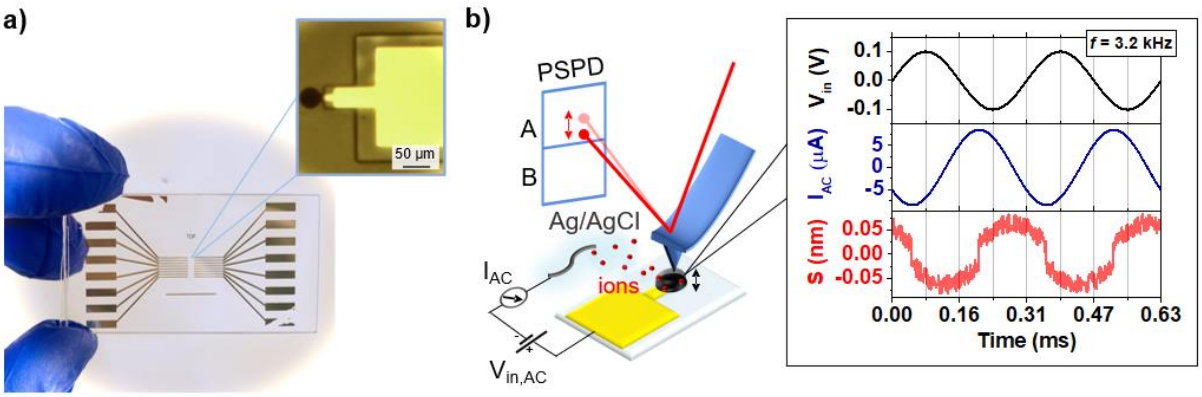

Figure 4.5: Experimental setup. **a)** Optical image of a PEDOT:PSS microelectrode array used for the AFM experiment. The structure of a single electrode is provided by the magnified image shown as an inset. **b)** Schematic of the experimental setup for mEC-AFM, showing the AFM operating in contact mode on a microelectrode when an AC voltage is applied. The signals measured during the experiment are plotted as a function of time. The frequency of the input voltage V_{in} is f = 3.2 kHz

Figure 4.5b shows a schematic of the experimental setup used for the modulated electrochemical atomic force microscopy (mEC-AFM) measurements. In this technique, we used a frequency modulation to induce electrochemical doping/de-doping of an OMIEC material and we acquire the local thickness variations induced by the process. Samples are immersed in a 0.1 M PBS solution, using a Ag/AgCl wire as reference electrode, and the AFM probe is brought into contact with the surface of the PEDOT:PSS layer (force set point 10 nN, using NSC36 probes of the Park NX10 AFM). The application of a sinusoidal modulation V_{in} (with amplitude $|V_{in}|$ =100 mV and angular frequency ω) to the microelectrode drives the reversible oxidation and reduction processes of the PEDOT:PSS layer. Concurrently, the exchange of ions between the electrolyte and the PEDOT:PSS film assures charge neutrality and gives rise to the AC current signal.[7] The continuous injection and extraction of ions into and out of the PEDOT:PSS leads to the swelling and deswelling of the soft polymeric matrix at the same frequency as the drive signal. The resulting thickness oscillation is measured by

acquiring the vertical deflection of the AFM cantilever in contact with the film surface. Fast adjustments of tip height are avoided as the oscillation frequencies are kept above the bandwidth of the z-scanner feedback-loop control. This condition was achieved by setting the z-servo gain parameter to 0.01. Typical data traces obtained by this procedure are shown in **Figure 4.5b** as a function of time: they include the input voltage applied by the AC voltage source, the resulting AC microelectrode current and the AFM height changes. All signals are observed here at the fundamental frequency of f=3.2 kHz as provided by the AC signal source.

4.2.2 mEC-AFM multidimensional spectroscopy

To perform spectroscopic measurements, a multichannel lock-in amplifier is introduced to demodulate the AC signals, measuring the voltage, current and swelling phasors $\bar{V}(\omega)$, $\bar{I}(\omega)$ and $\bar{S}(\omega)$(see **sect. 4.2.6**). The last is obtained by measuring the phasor corresponding to the vertical deflection of the AFM cantilever and dividing its amplitude by the cantilever sensitivity (see **sect. 4.2.7**).

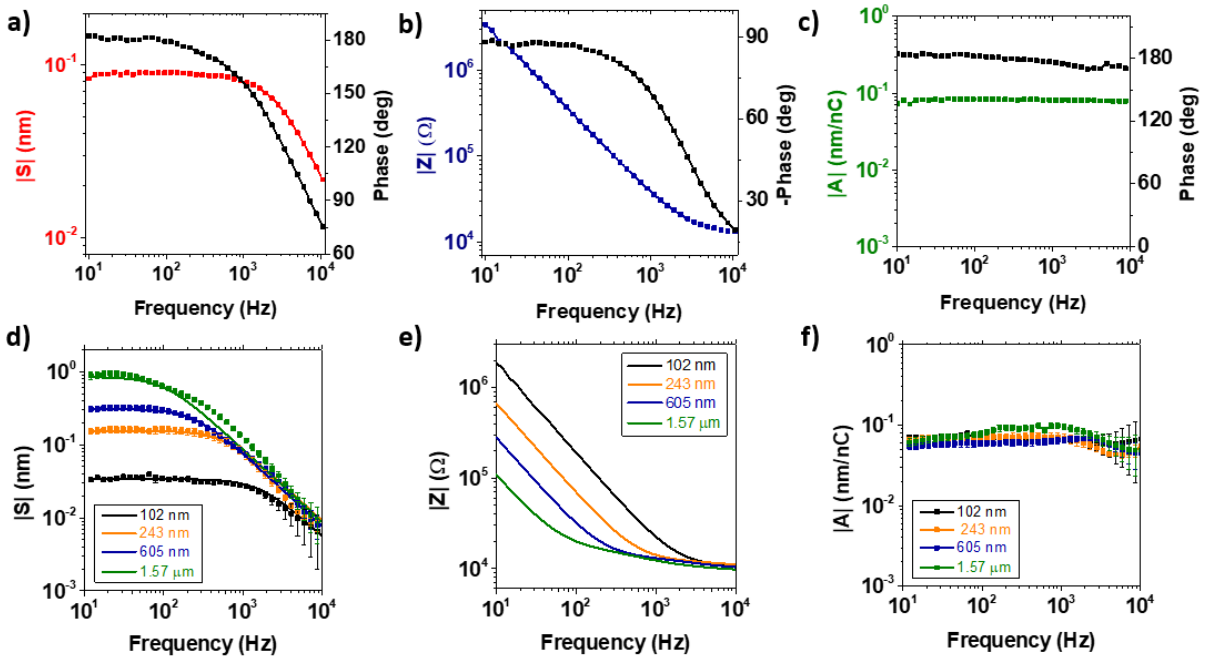

Figure 4.6: Multidimensional electroswelling spectroscopy. **a)** Electroswelling spectrum obtained by sweeping the frequency of the AC input voltage in a wide range. Spectra of the **(b)** electrochemical impedance and **(c)** actuation transfer functions relating charge uptake and swelling in the polymer matrix. Electroswelling **(d)**, impedance **(e)**, and actuation function **(f)** amplitudes measured on PEDOT:PSS layers with different thicknesses. The electrode diameter is 50 µm. Error bars indicate the average between measurements performed in 5 different positions on the electrode surface. Experimental data in **(d)** (indicated with squares) are fitted assuming a constant value a for the actuation function for each thickness. Fitting results are reported in Table 4.2.

The resulting spectrum (**Figure 4.6a**) shows how the swelling amplitude has a plateau in the low frequency regime with a stable phase of 180°. In this condition, the local height of the

PEDOT:PSS layer increases by |*S*| when the AC voltage reaches its minimum value (-100 mV). Then, after a critical frequency, the phase shift reduces, and the swelling amplitude decreases with increasing frequency. This behavior can be better understood considering the transfer functions relating the three measured phasors. The electrochemical impedance transfer function $Z = \bar{V}/\bar{I}$ reveals how the electrolyte limits charge entering the polymer film. The resulting Bode plot (**Figure 4.6b**) shows how the impedance amplitude is limited by the electrolyte resistance at high frequency but increases in the low frequency range where the swelling plateau is measured. In such a regime, the phase of the corresponding current reaches 90°, indicating capacitive charge accumulation in the PEDOT:PSS layer. The second relevant transfer function is the actuation function $A = \bar{S}/\bar{Q}$, where $\bar{Q} = \int_0^t \bar{I}(s)ds$ is the phasor defining the charge accumulated in the polymer film (see **sect. 4.2.9**). The actuation function *A* reveals how the morphology of the soft polymer matrix changes through the injection of charge. The spectrum of *A* is reported in **Figure 4.6c** and illustrates how its amplitude remains constant across all frequencies, with a phase of 180°. We remark that the electroswelling measurements are local, while AC current measurements involve the entire electrode area. To assure reproducibility we performed electroswelling spectroscopies on 5 different points on the polymer surface and find experimental variations in the transfer functions that are smaller than 5% (**Figure 4.6a** and **c**, see also **Figure 4.7** and **Figure 4.8** for the mapping of the amplitude and phase of *S*). In the spectroscopy experiments we also varied systematically the drive amplitude up to V_{in}=200 mV and found a linear response of the current and swelling signal (**sect. 4.2.8**). This finding is in agreement with the absence of faradaic reactions in PEDOT:PSS over a broad electrochemical potential window.[105]

From this evidence, we can formulate an interpretation for electroswelling in PEDOT:PSS. When a positive voltage is applied to the microelectrode, the PEDOT phase gets oxidized and positive hole charges enter the film. To maintain charge neutrality, the ionic PSS phase is depleted from cations, leading to a decrease in the film volume. Instead upon reduction (negative voltage) hole carriers are removed from the PEDOT phase and cations must enter the film to counterbalance the negative charge present in the PSS phase. As a consequence, the film increases in local height by |*S*|, when a negative voltage is applied, explaining the antiparallel response of *A* (180°) with respect to the voltage signal. Our observations are confirmed performing experiments on electrodes with different PEDOT:PSS thicknesses (**Figure 4.6d**, **e**, **f**). Analysis of the two transfer functions reveals that electroswelling is only limited by the impedance of the PEDOT:PSS/electrolyte interface. Consequently, the amplitude of *A* (**Figure 4.6f**) has a constant value *a* independently on both, the film thickness as well as frequency. Following this observation, we can model the impedance spectra in **Figure 4.6e** with an equivalent RC circuit to calculate the charge accumulated in the film, and then fit the swelling spectra keeping the "actuation coefficient" *a*, as the only adjustable parameter (see **sect. 4.2.10**). Results (continuous lines in **Figure 4.6d**) show an excellent agreement with the experimental points. The related fit parameters are reported in Table 1 and show values for *a* compatible within the experimental errors.

Two important conclusions arise from the multidimensional spectroscopy: (i) fast electroswelling can be obtained if sufficient charge can be injected. The timescale of actuation

is provided by the characteristic time of the RC circuit $\tau = RC$. (ii) The actuation function has a constant value a for the PEDOT:PSS formulation independent of both the frequency and the amount of injected charge. This identifies a as an intrinsic metric of the actuation extent and allows for a microscopic interpretation which will be discussed in the final paragraph.

Thickness	R (kΩ)	C (nF)	a (nm nC^{-1})
102±6 nm	10.4±0.8	9.2±0.8	0.063±0.008
243±8 nm	11.4±1.2	24±2	0.076±0.002
605±10 nm	11.3±1.4	57±3	0.080±0.006
1.6±0.5 µm	10.1±1.8	147±8	0.075±0.007

Table 4.2: Quantitative analysis of impedance and electroswelling spectroscopies on PEDOT:PSS electrodes with diameter of 50 µm, resulting from the fits in Figure 4.6d and 4.6e.

4.2.3 mEC-AFM imaging experiments

Next, we aim to investigate the impact of the local morphology on electroswelling properties. Like piezoelectric force microscopy, mEC-AFM maps transient electroactuation on the polymer surface by acquiring the amplitude and phase of the surface height oscillations induced by an AC voltage modulation. Such a mEC-AFM imaging experiment can be implemented on microelectrode surfaces with sufficiently small RC constant to allow for electroswelling at frequencies extending into the kHz range. Achieving fast electroswelling operation is essential to perform stable mEC-AFM image acquisitions with a reasonable scan time. **Figure 4.7a** shows the electroswelling spectrum for a 30-µm diameter electrode. For imaging experiments on this electrode, we used a modulation frequency of f_{im} = 3.2 kHz that is in the frequency roll-off region but still offers a good signal to noise ratio, indicating that a significant amount of charge is capacitively accumulated in the bulk of the PEDOT:PSS layer and contributes to the swelling process. For the soft polymer surface, we use fast approach and retract curves to avoid shear forces and potential tip or sample damage during scanning. As shown in **Figure 4.7b**, for each pixel of the image, the tip is approached until a threshold force of F_{max} =16.7 nN is reached. During the same approach, the surface oscillation amplitude and phase are recorded (**Figure 4.7c**). Both signals increase only after the AFM tip gets into contact with the PEDOT:PSS layer (indicated with z=0). Upon increased force, the swelling amplitude and phase become stable and remain constant, indicating that the threshold force F_{max} applied on the sample during the spectroscopy does not hinder the oscillation of the electroactive polymer surface. It also allows us to exclude other distant dependent forces such as electrostatic interactions between tip and sample as origin of the observed oscillations. Once above threshold force, the amplitude and phase signals are averaged for t_{hold} =1 ms. Then the AFM probe is lifted from the contact position, and the operation is repeated for the following pixel. Images obtained by the mEC-AFM technique on the entire microelectrode region (50x50 µm) are shown in **Figure 4.7d**, **e**, **f** and represent the surface height, the swelling amplitude

and the swelling phase. A constant electroswelling and stable phase are only measured on the PEDOT:PSS covered microelectrode. The encapsulation layer and the substrate show changes in surface morphology, but no electroswelling signal (**Figure 4.7e** and **f**).

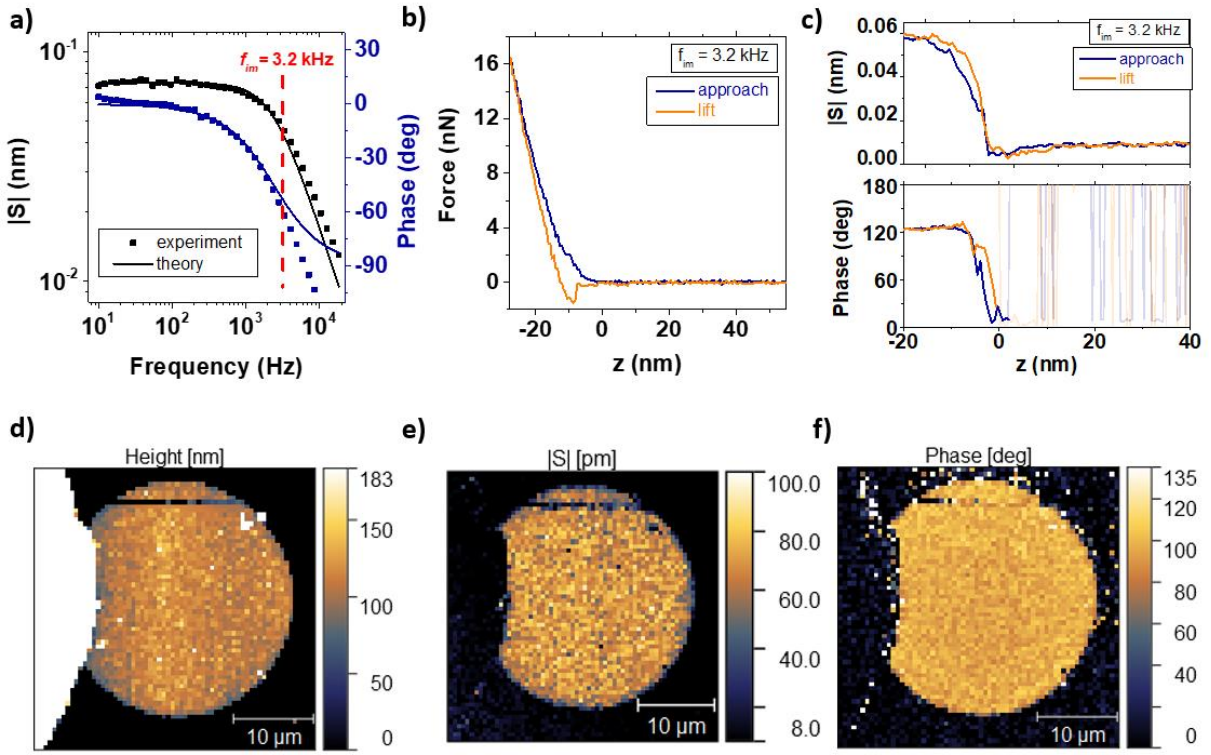

Figure 4.7: mEC-AFM imaging of electroswelling amplitude and phase on a PEDOT:PSS covered microelectrode. **a)** Electroswelling spectrum of the 30-µm electrode, the frequency f_{im} applied to the input voltage V_{in} during the image acquisition is indicated. **b,c)** Simultaneous measurement of force-distance spectroscopy **(b)** and electroswelling amplitude and phase **(c)** on a single pixel. The repetition of this process allows for the imaging of the electrode height **(d)**, electroswelling amplitude **(e)** and phase **(f)** on the entire electrode region.

Next, we acquire a multichannel mEC-AFM image with increased resolution imposing 128x128 pixels on a region of 3x3 µm in the center of the microelectrode (**Figure 4.8**). The height (**Figure 4.8a**) and electroswelling amplitude (**Figure 4.8b**) show a strong correspondence in the image. The combined line profiles in **Figure 4.8d** demonstrate that increased electroswelling is measured in regions of the film surface where the PEDOT:PSS layer is thicker. Instead, the signal phase (**Figure 4.8c**) is not affected by the local morphology and maintains a constant value. The quantitative analysis of the correlations is depicted in **Figure 4.8f** that relies on a statistical analysis of all pixels of the image. A linear correspondence between the PEDOT:PSS film height and the electroswelling amplitude is observed. The finding is rationalized by considering the intrinsic volumetric capacitance of PEDOT:PSS. By considering $c_v = 28 \pm 2$ Fcm^{-3},[39] and the electrode area A_{el}, we can calculate the actuation coefficient from the slope k of the correlation line as $a = \frac{k}{A_{el}|V_{in}|c_v} = 0.09 \pm 0.01$ nm nC^{-1}, obtaining results consistent with the spectroscopy experiments.

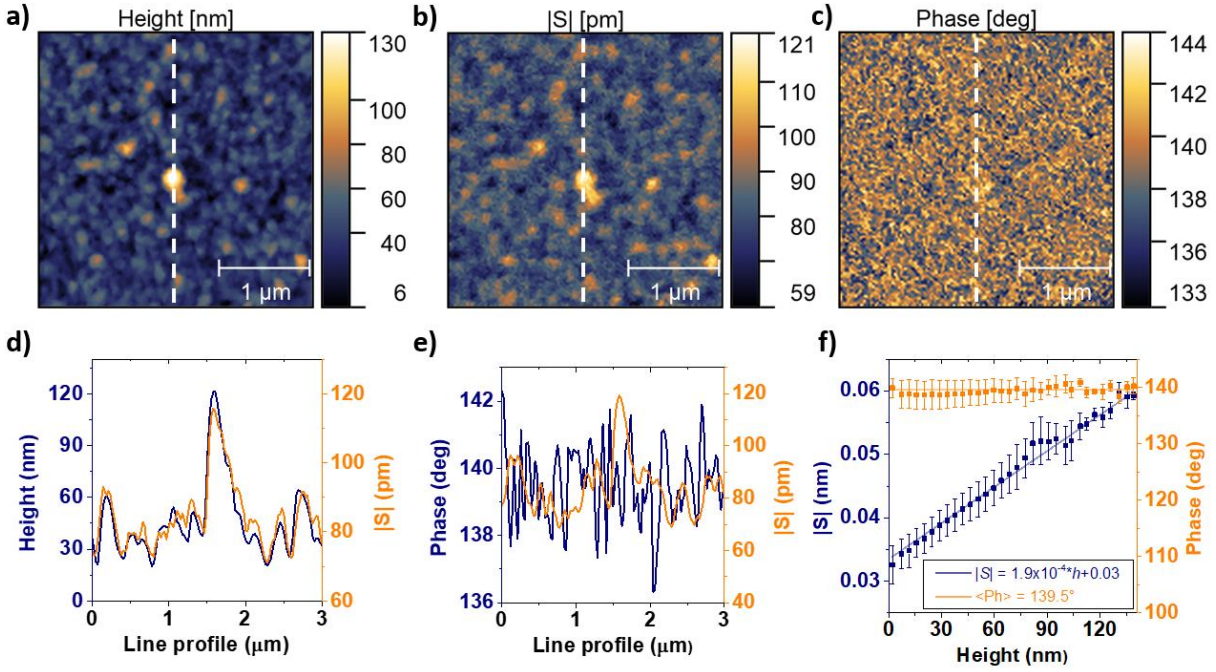

Figure 4.8: Nanoscale mEC-AFM imaging of the electroswelling effect. Multichannel AFM acquisition of the topography **(a)**, electroswelling amplitude **(b)**, and phase **(c)** on a PEDOT:PSS microelectrode. The imaging frequency f_{im} was set to 3.2 kHz. **d)**, **e)** Line profiles extracted on the vertical axis of the images comparing the acquired data. **f)** Correlation between the local thickness, electroswelling amplitude and phase. Error bars are obtained dividing the height distribution in 32 bins and calculating the standard deviation of each histogram bar.

4.2.4 Discussion

Our experimental observations demonstrate that charge accumulation is intrinsically related to volume change in PEDOT:PSS. Two different hypotheses can be initially formulated to account for the dynamics of the swelling behavior. The first hypothesis (that we can define "energetic") predicts that hydrated ions are driven with their water shell inside PEDOT:PSS by the external electrical potential V_{in}. The second hypothesis (that we can define "entropic") assumes that "bare" ions are injected into the electroactive material and water uptake is caused by a subsequent osmotic process. Despite the possibility to model the PEDOT:PSS layer as a semi-permeable membrane due to the presence of the fixed PSS^- acceptors,[134] our spectroscopy measurements highlight how osmosis plays only a minor role in the electroswelling mechanism. In the entropic interpretation, the actuation timescale would be limited by the diffusive transport of water at the polymer/electrolyte interface. Modeling experiments of water uptake in PEDOT:PSS allow for the quantification of the water diffusion coefficient in the material as $D_w \approx 10^{-12}\ m^2s^{-1}$.[349] Using this value and assuming the complete hydration of the polymeric layer on the vertical axis, we can estimate the diffusion time as $t_d = \frac{t^2}{4D_w}$, where t is the thickness of the PEDOT:PSS film. Typical timescales for the 300 nm thick films of 22.5 ms (see **sect. 4.2.11**) clearly illustrate that water diffusion is a relatively "slow" process with respect to electroswelling and validate the "energetic" interpretation. In this view, we can directly

associate the actuation coefficient a to the dimension of the hydrated radius in the PEDOT:PSS layer. If we assume that each injected ion is responsible for the electronic doping/de-doping of the material, we can calculate the volume of hydrated ions as $v_{ion} = A_{el}*e*a$ (see **sect. 4.2.12**), and correlate the hydration radius r_{ion} to the actuation coefficient:

$$r_{ion} = \left(\frac{3aA_{el}e}{4\pi}\right)^{1/3} \qquad (4.9)$$

where e is the elementary charge. By replacing the average actuation coefficient $\langle a \rangle$ = 0.075±0.007 nm nC^{-1} from Table 1, we obtain $\langle r_{ion} \rangle$ = 0.18±0.02 nm, which corresponds to half the value typically measured for Na^+ cation in water ($r_{Na,w}$ = 0.36 nm).[350] This result can be interpreted by alternative descriptions: i) when cations enter inside the polymeric matrix, a considerable fraction of anions is ejected, reducing the swelling extent (**Figure 4.9a**), or ii) only cations are responsible for the electroswelling, but their water shell inside PEDOT:PSS gets smaller (**Figure 4.9a**). A final, third hypothesis is provided by a combination of the two.

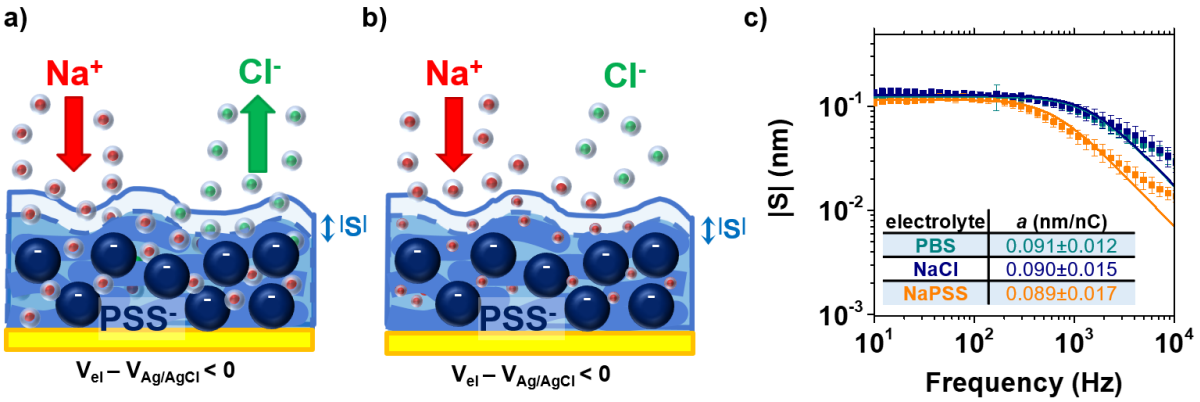

Figure 4.9: Interpretation of electroswelling in PEDOT:PSS. **a)** Ion transport involves both cations and anions inside their water shell, with a smaller fraction of anions leaving the material when a negative potential is applied to the electrode. **b)** Ion transport involves only cations, and their water shell gets smaller inside the material. **c)** Electroswelling spectroscopies performed in different electrolytes. Results are a strong support for the hypothesis in **(b)**. Error bars indicate the average between measurements performed in 5 different positions on the electrode surface.

To properly identify which one of the three scenarios best fits with the ion dynamic inside the material, we performed electroswelling spectroscopies in three different electrolytes (0.1 m PBS, 0.14 m NaCl and 0.4 mm NaPSS). These differ by pH (being 7.38±0.02, 6.24±0.02, and 3.94±0.02 for the 0.1 M PBS, 0.14 M NaCl and 0.4 mM NaPSS, respectively), sodium cation concentration, and anion composition. Results are reported in **Figure 4.9c** and demonstrate equal actuation coefficients for the three different electrolytes. As a consequence, measurements exclude a significant role for the PSS protonation/deprotonation in the active swelling, despite its major importance in the passive water uptake causing material hydration.[150] The findings in NaPSS solution, allow us to exclude the transport of anions as PSS^- are too large to enter the polymer films. Still, the swelling coefficient does not differ from the one measured in PBS and NaCl solutions, proving that chloride anions do not substantially contribute to the electroswelling, and ion uptake is limited only to sodium cations. This observation strongly

supports the swelling mechanism illustrated in **Figure 4.9b**. Fixed PSS^- acceptors limit the uptake of mobile anions from the surrounding electrolyte by electrostatic repulsion, while coordination to sulfate groups causes smaller hydrodynamic radius $\langle r_{ion} \rangle = 0.18 \pm 0.02$ nm for cations. Similar results are expected to be obtained in solutions containing (mixtures of) different monovalent cations, as their free water hydration radii do not substantially differ. [350] The experimental $\langle r_{ion} \rangle$ value is consistent with previous analyses performed using an electrochemical quartz crystal microbalance (EQCM), estimating an uptake of 1-2 water molecules for every injected ion.[291]

4.2.5 Conclusions

Results obtained in this chapter demonstrate how modulated electrochemical force microscopy (mEC-AFM) can be successfully applied to reveal the intrinsic dynamics of electrochemical actuation in OMIEC materials. We prove that the amplitude and timescales of electroswelling are governed by the drift motion of hydrated ions and not limited by slower water diffusion processes. Accordingly, we demonstrate how fast ionic charging of the PEDOT:PSS volumetric capacitance leads to high frequency operation in microactuators, and how the swelling extent is intrinsically limited by the size of the ionic solvent shell. The resulting knowledge can serve as a guideline for the development of OMIEC-based actuators with maximized performance. This research also shows how mEC-AFM offers novel means to interrogate materials with mixed ionic-electronic conductivity at the nanoscale during operation providing information on the local ionic distribution and the ion-to-electron coupling. This capability will be critical to understand more complex OMIEC-based realizations such as organic electronic ion pumps[351] or organic electrochemical transistors.[219]

4.2.6 Appendix 1: detailed schematic of the experimental setup used for mEC-AFM experiments

A complete schematic of the experimental setup used for mEC-AFM experiments is reported in **Figure 4.10a**. A function generator connected to the PEDOT:PSS microelectrode provides the AC input voltage and DC offset (vs Ag/AgCl) leading to swelling/deswelling of the OMIEC layer. The same signal is given as a reference to the lock-in amplifier. Both the AFM cantilever deflection resulting from the PEDOT:PSS surface oscillations and the AC current flowing in the electrochemical cell are acquired by the lock-in amplifier. This demodulates the provided signals measuring the amplitude and phase of the voltage, current, and swelling phasors. The amplitude of the latter is calculated as $|S| = D/s_c$ according to **sect. 4.2.7**. An optical image of the liquid cell containing both the samples and the AFM probe during mEC-AFM experiments is reported in **Figure 4.10a** (see also **sect. 3.3.1**). A Ag/AgCl wire is placed on the right side of the well acting as reference electrode. The microstructured PEDOT:PSS structures acting as working electrodes are aligned with the center of the well and

individually addressable though the metallic contact pads patterned at the left and right sides of the well.

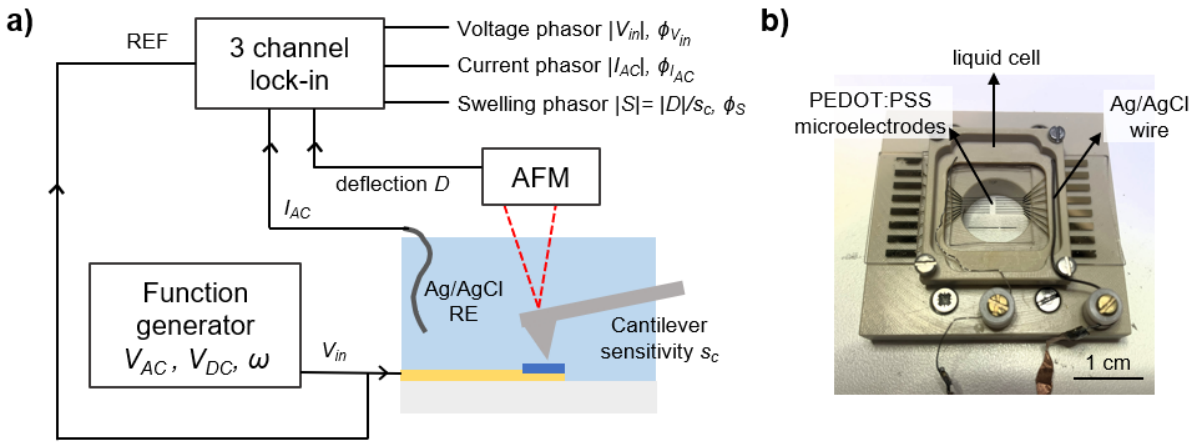

Figure 4.10: **a)** Detailed schematic of the experimental setup used for mEC-AFM experiments. **b)** Liquid cell used for in-liquid mEC-AFM experiments, featuring a Ag/AgCl wire as reference electrode on the right and microstructured PEDOT:PSS electrodes fabricated on a glass slide and aligned with the center of the cell.

4.2.7 Appendix 2: measurement of the cantilever sensitivity and calculation of the swelling amplitude in mEC-AFM

We measured the cantilever sensitivity s_c of NSC36 probes in liquid through force-distance spectroscopies on the rigid glass substrate of the samples (**Figure 4.11a**). The probe was lifted to the vertical coordinate z_0 = 0.1 µm from the contact position, then gradually approached to the sample surface (scan speed 0.3 µm/s) down to z_1 = -0.2 µm and finally retracted again to z_0. The resulting force is calculated by dividing the acquired vertical deflection D (A-B voltage in the AFM position-sensitive photodiode (PSPD)) by the cantilever elastic constant (**Figure 4.11b**). s_c = dD/dz was extracted from the slope of the linear cantilever deflection signal measured in contact regime (**Figure 4.11c**). During electroswelling measurements, the force set point for contact mode operation was set to 10 nN to have a significative interaction between the probe and the sample. After applying the V_{in} signal, we calculated the swelling amplitude as $|S| = |D|/s_c$, where $|D|$ is the amplitude of the vertical deflection of the AFM cantilever caused by the sample oscillation.

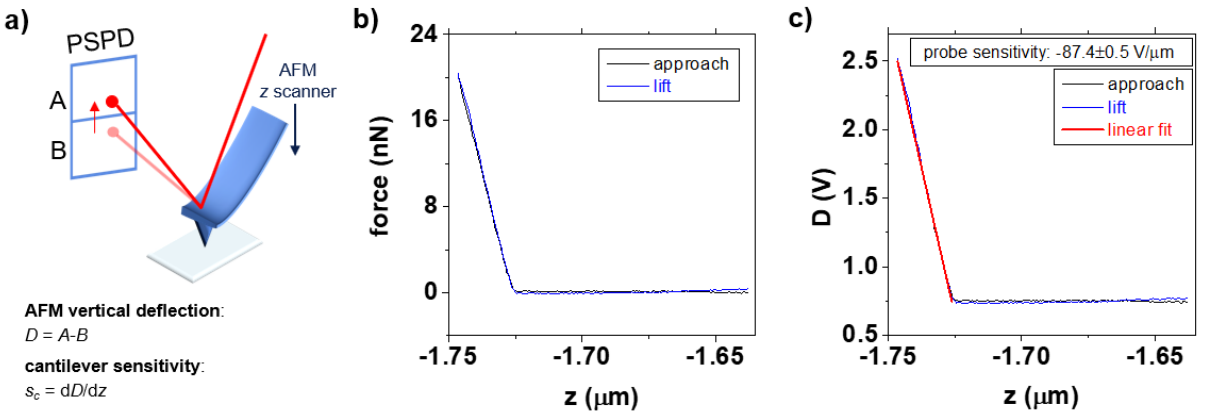

Figure 4.11: a) Experimental setup used to measure the NSC36 cantilever sensitivity. **b)** Force-distance spectroscopy on the glass substrates of the sample. **c)** Determination of the cantilever sensitivity.

4.2.8 Appendix 3: linearity of the electrochemical response of PEDOT:PSS microactuators

We ensure the linearity of the mEC-AFM characterization method by measuring the electroswelling amplitude for different amplitudes of the applied AC voltage modulation. Experimental data reported in **Figure 4.12** confirm a linear electroactuation response from PEDOT:PSS, and the actuation coefficient resulting from the fitting line slope results to be compatible with experimental results reported in Table 1. This finding also furtherly confirms the frequency dependent model of the swelling phasor (**sect. 4.2.10**). **Eq. 4.19** predicts that when the frequency is fixed, the actuation amplitude can be linearly controlled through different amplitudes of the input voltage determining the amount of charge injected in the polymeric matrix.

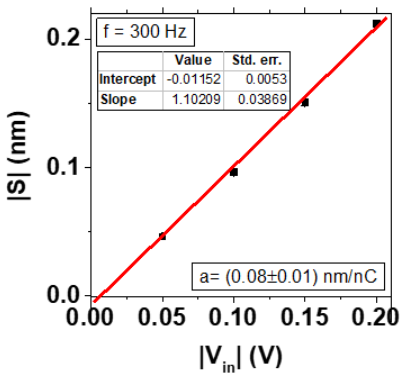

Figure 4.12: linear electrochemical response of PEDOT:PSS microactuators. The actuation coefficient can be calculated from the slope of the fitting line using Eq. 4.19.

4.2.9 Appendix 4: derivation of the charge phasor

In an AC circuit, we can define the charge phasor as the time integral of the current phasor:

$$\bar{Q} = \int \bar{I} dt \qquad (4.10)$$

$$\bar{Q} = \int |I| e^{j(\omega t + \phi_I)} dt \; = \frac{|I| e^{j(\omega t + \phi_I)}}{j\omega} = \frac{\bar{I}}{j\omega} \qquad (4.11)$$

thereby, we obtain

$$\bar{Q}(t) = \frac{|I|}{\omega} e^{j(\omega t + \phi_I - \frac{\pi}{2})} = |Q| e^{j(\omega t + \phi_Q)} \qquad (4.12)$$

with

$$|Q| = \frac{|I|}{\omega}; \qquad \phi_Q = \phi_I - \frac{\pi}{2} \qquad (4.13)$$

4.2.10 Appendix 5: frequency dependence model of the swelling phasor

The PEDOT:PSS/electrolyte interface can be modeled with an equivalent RC series circuit, composed by the ionic resistance of the electrolyte *R* and the capacitance *C* of the electric double layer in the polymeric layer. The input voltage phasor $\overline{V_{in}}(t) = |V_{in}| e^{j\omega t}$ and the current phasor $I(t) = |I| e^{j(\omega t + \phi_I)}$ are related through the electrochemical impedance transfer function:

$$Z = \frac{1}{j\omega C} + R \qquad (4.14)$$

Using the impedance, we can express the charge phasor as a function of the input voltage phasor:

$$\bar{Q}(t) = \int \bar{I} dt = \int \frac{|V_{in}|}{\frac{1}{j\omega C} + R} e^{j\omega s} ds \qquad (4.15)$$

we obtain

$$\bar{Q}(t) = \frac{C|V_{in}|}{\sqrt{1 + (\omega RC)^2}} e^{j[\omega t + \mathrm{atan}\,(-\omega RC)]} \qquad (4.16)$$

with amplitude and phase

$$|\bar{Q}| = \frac{C|V_{in}|}{\sqrt{1 + (\omega RC)^2}}; \qquad \phi_Q = atan(-\omega RC) \qquad (4.17)$$

We can finally relate charge and swelling phasors through the actuation function:

$$A = \frac{\bar{S}}{\bar{Q}} \qquad (4.18)$$

The experimental spectroscopy data shows that A has a constant value $A(\omega) = a$ over the experimental frequency range. Accordingly, we can write the mathematical expressions for the swelling amplitude and phase:

$$|\bar{S}| = \frac{aC|V_{in}|}{\sqrt{1 + (\omega RC)^2}}; \qquad \phi_S = atan(-\omega RC) \qquad (4.19)$$

obtaining a good agreement with experimental results in **Figure 4.6d**.

4.2.11 Appendix 6: water diffusion and osmosis in electroactuation of conductive polymers

Electroswelling spectroscopy measurements highlight how osmosis plays a minor role in the electroactuation mechanism. Using $D_w \approx 10^{-12}$ m^2/s as the water diffusion coefficient in PEDOT:PSS[349] and assuming the complete hydration of the polymeric layer on the vertical axis, we can estimate the diffusion time as $t_d = \frac{t^2}{4D_w}$, where t is the thickness of the PEDOT:PSS film. Results obtained for our experiment are reported in **Table 4.3**. These clearly illustrate that water diffusion is a relatively "slow" process with respect to electroswelling. Assuming osmosis as responsible for the latter implies a substantial discrepancy between the charge injected in the material and its volume change for frequencies higher than $f_d = 1/t_d$, which is not observed in the experiments (**Figure 4.6b** and **c**). Moreover, no significative increases in the actuation width are measured when $f < f_d$. The actuation timescale is not limited by the diffusive transport of water at the polymer/electrolyte interface caused by an increase of the osmotic pressure, but by the transport of hydrated cations.

thickness (nm)	t_d (s)	f_d (Hz)
102	0.002601	384.4675125
243	0.01476225	67.74035123
605	0.09150625	10.92821529
1570	0.616225	1.622783886

Table 4.3: Estimation of the timescale (t_d) and characteristic frequency (f_d) of water diffusion in PEDOT:PSS

4.2.12 Appendix 7: calculation of the ion hydration radius

If we assume that each injected ion is responsible for the electronic doping/de-doping of the material, we can express the swelling amplitude as a function of the number of ions as

$$S = aN_{ion}e \qquad (4.20)$$

where a is the actuation coefficient (expressed in nm/nC), N_{ion} the total number of ions, and e the elementary charge. Spectroscopy data combined with the imaging experiment demonstrate that the charge uptake in the polymeric matrix is uniformly distributed within the film volume. Thereby, the volume change V_s induced by ionic injection is $V_s = A_{el}S = N_{ion}(aA_{el}e)$, where A_{el} is the electrode area. This identifies the volume of a single ion as

$$v_{ion} = aA_{el}e \qquad (4.21)$$

and its radius will be

$$r_{ion} = \left(\frac{3v_{ion}}{4\pi}\right)^{1/3} = \left(\frac{3aA_{el}e}{4\pi}\right)^{1/3} \qquad (4.22)$$

4.3 Subsurface Profiling of Ion Migration and Swelling in OMIEC Actuators with mEC-AFM

Results presented in **sect. 4.2** introduce the mEC-AFM as a novel operando characterization method to study electroactuation in OMIEC materials. For this reason, mEC-AFM can be particularly relevant when focusing organic mixed conductors optimized for actuation, such as polypyrrole doped with dodecylbenzenesulfonate (Ppy:DBS). Anyway, Ppy:DBS shows a more complex electroactuation dynamics which requires in-depth investigations for its comprehension. Therefore, we extended mEC-AFM as a depth-sensitive technique to measure subsurface profiles of ion migration and swelling in Ppy:DBS electroactive layers. We performed multidimensional spectroscopy experiments combining electroswelling and electrochemical impedance measurements on micro-structured Ppy:DBS electrodes. We developed a quantitative description for the charging properties of Ppy:DBS able to reproduce the experimental data both for different electrode thicknesses and at different applied electrochemical potentials. Using the actuation transfer function, we correlated electrochemical and actuation properties of the material by revealing the distribution of electroswelling and charge in the electroactive polymer layer region. The resulting depth profiles demonstrate that electroactuation is not uniform in the Ppy:DBS layer but depends both on the film morphology and redox state, which determine the size and transport dynamics of hydrated ions. Our findings suggest that the efficient actuation performance is caused by rearrangements of the polymer microstructure induced by charge accumulation in the soft polymeric matrix. Such process causes the influx of water from the surrounding electrolyte increasing the effective ionic volume in the electroactive layer up to two times the value measured in free water.

Results presented in this chapter are organized in a manuscript draft intended for submission to the *Advanced Functional Materials* journal. I collaborated on this work with Tobias Cramer and Beatrice Fraboni from the Department of Physics and Astronomy of the University of Bologna, and with Chaoqun Dong and George Malliaras from the Department of Electrical Engineering of the University of Cambridge (UK).

4.3.1 mEC-AFM analysis of electrochemical actuation in Ppy:DBS

Figure 4.13a shows the experimental setup used to study ion-migration in micro-structured Ppy:DBS thin films with mEC-AFM. Samples were prepared by coating a Ppy:DBS thin film onto a 30 µm-diameter gold microelectrode on a glass substrate using galvanostatic electro-polymerization (current density J_{dep} = 2 mA/cm^2). A negative photoresist layer (3 µm of mrDWL 5 photoresist) electrically insulates the gold feedline from the surrounding electrolyte. Ppy:DBS microelectrodes were electrochemically activated through cyclovoltammetry (CV) experiments in 0.1 m NaDBS solution, leading to ion injection and complete hydration of the electroactive films (see **sect. 4.3.5**).

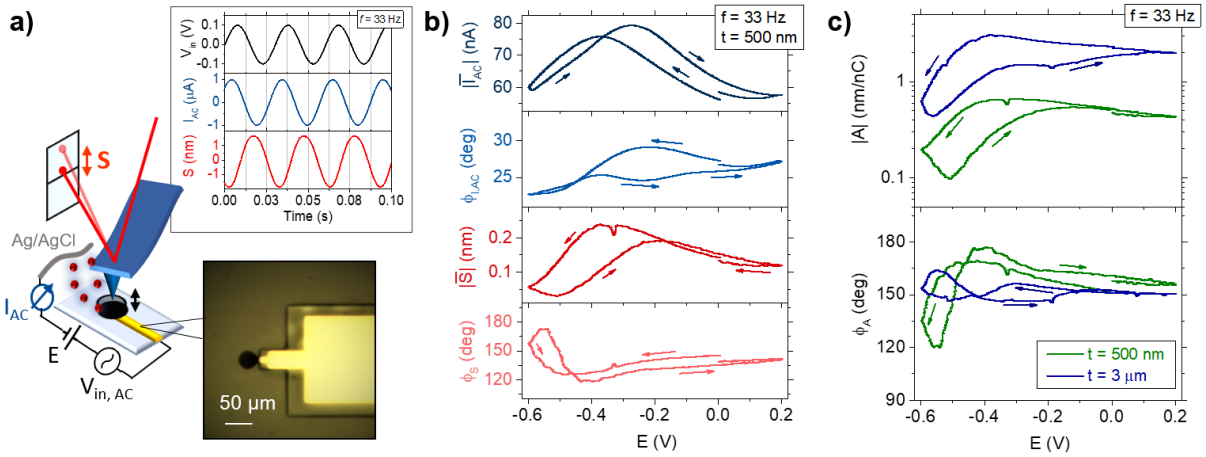

Figure 4.13: mEC-AFM analysis of electrochemical actuation in Ppy:DBS. **a)** Schematic of the experimental setup for mEC-AFM spectroscopies of electroswelling. The AFM operates in contact mode on a microelectrode while an AC voltage V_{in} (f = 33 Hz) is superimposed to the electrochemical potential E. **b)** Amplitude and phase of the AC current and the swelling signal measured in a 500 nm-thick microelectrode by varying the applied electrochemical potential E (scan rate 0.01 V/s). **c)** Amplitude and phase of the actuation function, defined as the transfer function between swelling and charge measured in microelectrodes with different Ppy:DBS coating thickness.

Ion migration and swelling where investigated with mEC-AFM measurements conducted in 0.1 M NaDBS solution, using a Ag/AgCl wire as reference electrode. A small sinusoidal modulation V_{in} (with amplitude $|V_{in}|$ =100 mV and angular frequency ω) is superimposed to the DC electrochemical potential E (vs Ag/AgCl) applied to the microelectrode. V_{in} leads to the generation of an ionic AC current in the Ppy:DBS layer (I_{AC}) and consequent swelling/deswelling S of the soft polymeric matrix at the same frequency. The thickness variation resulting from this process is measured by acquiring the vertical deflection of the AFM cantilever operating in contact mode (as illustrated in **sect. 4.2.7**). An example of the data traces obtained by this procedure are shown as inset in **Figure 4.13a** as a function of time, including the applied AC input voltage, the resulting AC microelectrode current and the AFM height changes (corresponding to the swelling S). All signals are observed at the frequency of f=33 Hz as provided by the AC voltage source. The simultaneous acquisition of such signals allows for a multidimensional analysis aiming to study how charge accumulation in the polymeric film occurs. As the electrode area A_{el} is fixed, ion injection in the film bulk is

only reflected by a change in the electrode thickness, which is measured acquiring the swelling signal *S*.

A multichannel lock-in amplifier is used to determine the phasors of the voltage, current and swelling signals $\overline{V_{in}}$, $\overline{I_{AC}}$ and $\bar{S}$. The phasors contain the information about the amplitude and phase of the driving voltage, the ionic current entering the OMIEC film and the swelling of the OMIEC film. The setup allows to measure the phasors while frequency or electrode potential *E* are varied. As an example, we show a sweep of the potential *E* (scan rate of 0.01 V/s) in **Figure 4.13b** obtained with a constant frequency of 33 Hz. When *E* is scanned towards negative potentials, both the amplitude of $\overline{I_{AC}}$ and $\bar{S}$ increase up to a maximum and then decrease. When the scan direction is reversed, again a maximum is observed in both traces, but slightly shifted towards positive voltages due to hysteresis. The phase values of the current and swelling signal show less variation and only the phase of the swelling signal increases significantly to values around 180° when the most negative potentials are reached.

We perform a first quantitative analysis on the actuation data by computing the average actuation transfer function $A = \bar{S}/\bar{Q}$, linking the input charge $\bar{Q} = \int \overline{I_{AC}} dt$ and the resulting polymer swelling $\bar{S}$. The plot of *A* as a function of the electrochemical potential is represented in **Figure 4.13c** for two Ppy:DBS films of different thickness (495±15 nm and 3.1±0.2 mm). The two plots show similar shape with a maximum value of *A* at around -0.3 V to -0.4 V and strong hysteresis. The thicker film is shifted to higher values of the transfer function revealing a more efficient actuation mechanism. In both experiments, the transfer function phase has a value close to 180°, confirming that, independent on thickness, electroactuation is driven by the removal of positive hole charges and consequent injection of cations from the surrounding electrolyte.[293]

From the previous observations we derive two main conclusions: first, electroactuation in Ppy:DBS reaches a maximum at a well-defined electrochemical potential. At larger positive or negative potentials swelling is hindered. Second, electroactuation depends on film thickness. Both findings contrast with observations made in **sect. 4.2** on PEDOT:PSS not optimized for actuation. In PEDOT:PSS the transfer function *A* has smaller values (|*A*|= 0.1 nm/nC) and is independent on film thickness and electrochemical potential.[348] To explain the more complex electroswelling behavior of Ppy:DBS, we hypothesize that ionic and electronic transport are limiting and cause a non-uniform distribution of charge and swelling in the polymeric layer. To test this hypothesis, we introduce an advanced analysis scheme of the multidimensional spectroscopy dataset $\{\overline{I_{AC}}(\omega,E)$ and $\bar{S}(\omega,E)\}$ provided by mEC-AFM experiments. The aim is to extract the depth profile of charge accumulation and of the actuation transfer function from the experimental data allowing to reconstruct the spatiotemporal electroactuation dynamics in Ppy:DBS. To this end, we proceed in two steps. First, we analyze the impedance data contained in the phasors $\overline{V_{in}}$ and $\overline{I_{AC}}$ measured as a function of frequency. Second, we will relate the obtained insights to the swelling phasor $\bar{S}$.

4.3.2 Analysis of charge accumulation in Ppy:DBS

We acquired the electrochemical impedance spectroscopies of Ppy:DBS microelectrodes by systematically varying the frequency of the AC input voltage while recording amplitude and phase of the I_{AC} signal ($|Z| = |V_{in}|/|I_{AC}|$). Results obtained at different electrochemical potential for electrodes with thickness 500 nm and 3 µm are presented in **Figure 4.14a** and **b**, respectively.

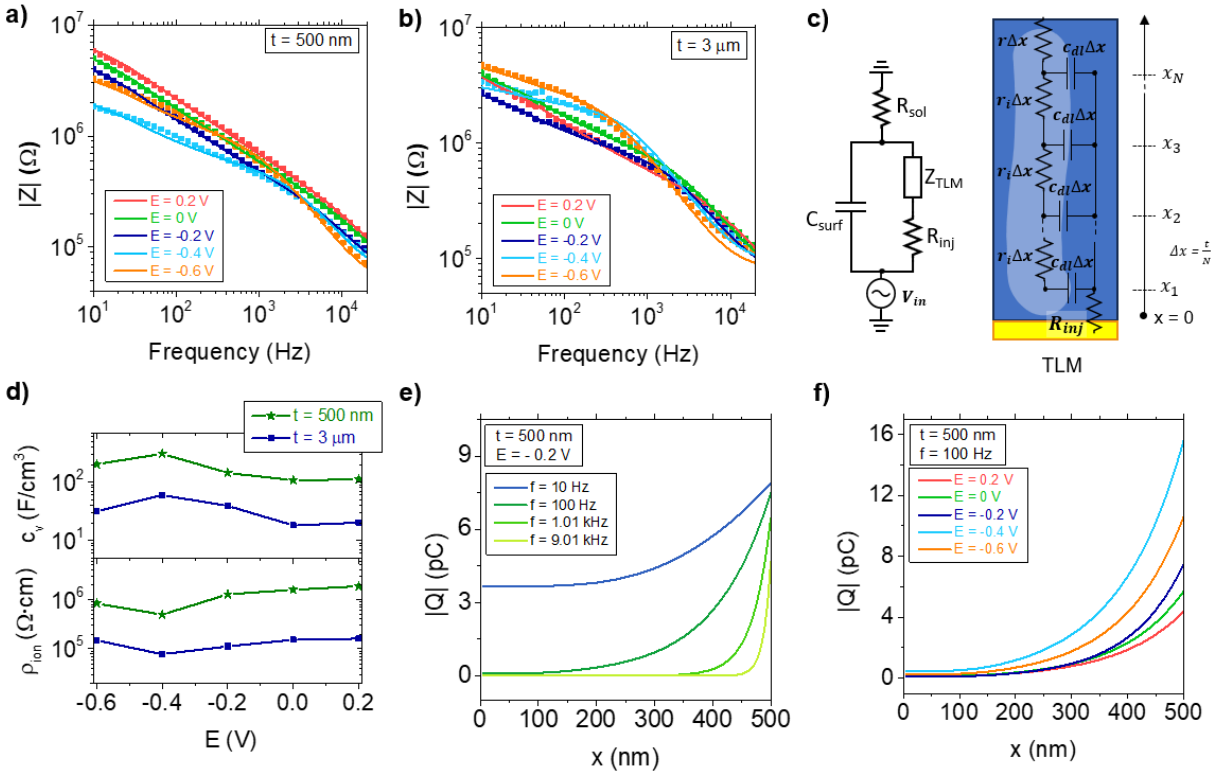

Figure 4.14: Analysis of charge accumulation in Ppy:DBS. Electrochemical impedance spectroscopies of a 500 nm-thick **(a)** and a 3 µm-thick **(b)** Ppy:DBS microelectrodes at different electrochemical potentials E. Experimental points (squares) are fitted with the equivalent circuit (continuous lines) in **c)**, showing an insight on the transmission line model (TLM) for charge accumulation in the polymer bulk and the corresponding morphological interpretation (the ionic phase containing DBS^- acceptors is drawn in light blue). Under the assumption of uniform volumetric capacitance and ionic resistivity, the line elements result to be $r_i = \rho_{ion}/A_{el}$ and $c_{dl} = c_v A_{el}$. **d)** Volumetric capacitance and ionic resistivity of Ppy:DBS extracted from the fit. Subsurface profiles of charge accumulation in Ppy:DBS at different frequencies **(e)** and applied electrochemical potential **(f)**.

We developed an equivalent circuit description (**Figure 4.14c**) able to interpret impedance data in every experimental condition. Fitting results are represented with continuous lines in **Figure 4.14a** and **b** and show excellent agreement with the experimental data (indicated with squares). In the depicted equivalent circuit scheme, R_{el} represents the electrolyte resistance, C_{surf} the capacitance of the polymer surface, R_{inj} the electron/hole injection resistance, and Z_{TLM} the impedance of the polymer bulk. In our interpretation, we describe conjugated polymer/polyelectrolyte blends such as Ppy:DBS through a two-phase model,[122] an ionic conductive and hydrophilic phase containing DBS^- anions and an electronic conducting phase

constituted by Ppy grains.[7] After polymer hydration ("passive" swelling) the electroactive layer assumes the structure of a porous film, where inner voids in the electronic phase are bathed with the electrolyte solution permeating the ionic phase.[23] A graphical scheme of this model is reported in Figure 2c, showing in a lighter blue color the hydrated DBS phase mixed with the electronic conductive Ppy phase (dark blue). The application of a negative electrochemical potential at the electrode site leads to the injection of cations in the ionic phase. These electrostatically compensate the fixed DBS^- acceptors, de-dope the electronic phase through the extraction of holes and give rise to double layer capacitance at the interphase interfaces. The charging process of the electroactive layer is limited by the rate of ionic transport within the pore.[352] Consequently, a possible way to describe electrical properties of bulk Ppy:DBS is using a transmission line model (TLM - **Figure 4.14c**), where a series of *N* resistors *R* (describing ionic transport along the vertical axis of the polymeric layer) is used to connect a net of *N* capacitors *C* (indicating charge accumulation in the pores). Under the assumption of a constant volumetric capacitance c_v for Ppy:DBS [353] and an uniform ionic resistivity ρ_{ion} on the vertical axis of the polymer, we calculate $R = \frac{\rho_{ion}}{A_{el}}\Delta x$ and $C = c_v A_{el}\Delta x$, where A_{el} is the electrode area and $\Delta x = t/N$ the length increment along the vertical profile of the Ppy:DBS layer with thickness *t.* The electrical potential distribution $\phi_i = \phi(x_i, \omega, E)$ (with i=1, 2, ...*N*) along the line can be obtained by solving the matrix equation

$$\boldsymbol{A^t K A \phi = b} \qquad (4.23)$$

where the diagonal matrix $\boldsymbol{K}$ contains the reciprocal of the impedances along the line, and $\boldsymbol{A}$ and $\boldsymbol{b}$ are defined according to **sect. 4.3.6**. The resulting total impedance of the transmission line (**sect. 4.3.7**) is fully convergent to the continuous limit (given by the De Levie equation[354]) when the number of nodes *N* is sufficiently large, and can be used to extract bulk parameters from spectroscopy data.

Fitting the model to the experimental data yields values for the volumetric capacitance and the ionic resistivity of the Ppy:DBS films as reported in **Figure 4.14d**. The thick Ppy:DBS film has a significantly lower volumetric capacitance and lower ionic resistivity. Such evidence suggests that the thicker film has a "looser" microstructure containing relatively more volumetric percentage filled with electrolyte.[301] Accordingly ionic transport is facilitated and less charged organic semiconductor is present to counterbalance ionic charges reducing the capacitance per volume. The dependence of the fitting parameters on the external electrochemical potential *E* is similar for both electrode thicknesses. When *E* is pushed towards negative values, an increasing number of hydrated cations is injected inside the material. Such process leads to morphological changes in the polymeric matrix, increasing the volumetric capacitance and facilitating ionic transport in the film (thus, decreasing ρ_{ion}). Nanomechanical AFM indentation experiments (**sect. 4.3.8**) further confirm this hypothesis measuring a reduction in the elastic modulus of the film for negative electrochemical potentials. At the same time, the resistivity of the electronic phase is gradually increased until complete de-doping of the polymer (E < -0.4 V), and injection of electronic carriers from the gold substrate (modeled by the injection resistance R_{inj} in **Figure 4.14c** – see **sect. 4.3.9**) is largely suppressed. In such a condition, the DBS^- acceptors are entirely compensated and cations cannot permeate anymore

in the electroactive layer bulk. Consequently, the ionic resistivity increases again at very negative potentials and the volumetric capacitance decreases.
The completed fitting procedure provides us according to **Eq. 4.23** the potential profile inside the polymer $\phi(x_i, \omega, E)$. This knowledge enables us to determine the spatial distribution of charge for the different applied electrochemical potentials and frequencies:

$$|Q(x_i, \omega, E)| = |c_v(E) A_{el} \Delta x \cdot \phi(x_i, \omega, E)| \qquad (4.24)$$

The resulting charging profiles obtained for the 500 nm-thick microelectrode are reported in **Figure 4.14e** and **f**, where the position *x*=0 corresponds to the gold/OMIEC contact. The corresponding extended colormaps are reported in **sect. 4.3.11**. Charge accumulation throughout the film occurs only at very low frequencies due to the limited mobility of the injected ions. Increasing the applied frequency reduces the amount of injected charge and pushes the charging front towards the polymer/electrolyte interface. Data obtained at constant frequency but varying potential (*f*=100 Hz - **Figure 4.14f**) demonstrates that charging increases by sweeping the applied electrochemical potential towards negative values (from 0.2 to -0.4 V). Then, when the polymer is fully de-doped (*E* = -0.6 V), charge injection is again limited by the reduced electronic conductivity of the OMIEC material. Qualitatively similar findings are obtained for the 3 µm-thick Ppy:DBS layer as reported in **sect.** Error! Reference s ource not found..

4.3.3 Analysis of electroswelling in Ppy:DBS

In the second part of our analysis, we relate the charging profiles obtained from the discrete transmission line model to the electroswelling data $\bar{S}(\omega,E)$ (**Figure 4.15a** and **b**). Clearly, the overall swelling results as a sum of contributions *s* generated at different thicknesses x_i of the polymer film. Each contribution is expressed as the product of the amount of local charging Q and local actuation function $A(x_i, E)$:

$$\bar{S}(\omega, E) = \sum_{i=1}^{N} \bar{s}(x_i, \omega, E) = \sum_{i=1}^{N} \bar{Q}(x_i, \omega, E) \cdot A(x_i, E) \qquad (4.25)$$

where the charging is calculated from **Eq. 4.24**. The local actuation function is related to the effective volume occupied by the entering ions $|A| = \frac{V_{ion}}{e\, A_{el}}$. It is reasonable to assume that this effective volume is not dependent on frequency but only a function of the position x_i and *E*. Furthermore, we assume that the function describing the volume is monotonous and has only one local maximum or minimum within the film. Accordingly, we simplify the fitting procedure by defining the profile of the local actuation function as:

$$|A(x_i)| = A_0 exp\left[-\frac{\left(x_i - x_{i,0}\right)^2}{2\sigma^2}\right] + B \qquad (4.26)$$

With this definition we fit **Eq. 4.25** to the electroswelling spectroscopy data (**Figure 4.15a** and **b**), obtaining an excellent agreement with experimental results. Fitting parameters for Eq.

Eq. 4.26 are reported in **sect. 4.3.12**. The parametrized model provides explanations for the different observations made on the Ppy:DBS actuators. Most importantly, it allows to compute the swelling depth profile $\bar{s}(x_i, \omega, E)$ occurring at different electrochemical potentials and frequencies as represented in **Figure 4.15c** and **d** (see also **sect. 4.3.13** for the 2D representations). The depth profiles $|\bar{s}|$ peak in a spatial region close to the electrolyte bath, and the position, the amplitude, and the width of such peaks reflect the local charge profiles in the electroactive material. Maximum peak heights are observed at low frequencies. At increased frequencies the swelling amplitude decreases due to the slow transport of hydrated cations in the OMIEC bulk reducing the amount of charge that is injected into the polymer. Sweeping the applied electrochemical potential from 0.2 V towards negative values increases further the amount and the spatial extent of the local swelling $\bar{s}$. However, when the polymer is fully de-doped (E = -0.6 V), the local swelling is again strongly reduced, which is explained by the limitations in electronic transport through the OMIEC material.

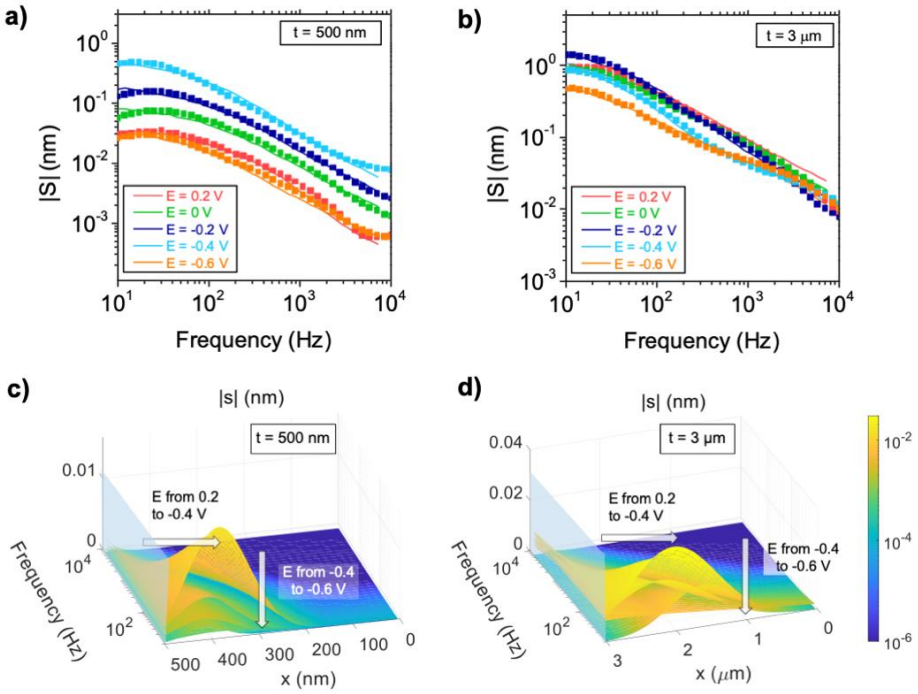

Figure 4.15: Analysis of electroswelling in Ppy:DBS. Results on the right and the left columns are referred to Ppy:DBS layers with thickness 3 µm and 500 nm, respectively. **a)** and **b)** Electroswelling spectroscopies of Ppy:DBS. Experimental data (squares) are fitted by the discrete model in Eq. 3.25 (continuous line). **c)** and **d)** Spatiotemporal subsurface profiles of the local swelling amplitude in Ppy:DBS.

At the same time, the subsurface profiles of the local actuation function (**Eq. 3.26** highlight how the effective ionic volume V_{ion} varies as a function the vertical coordinate of the polymer film. The distributions obtained for different Ppy:DBS layer thicknesses are reported in **Figure 4.16 a** and **b**. Data are normalized to the "free water" volume of hydrated sodium cations $V_0 = 0.19$ nm^3.[355] Consistently with local swelling profiles, the amplitude and the central position of the volume traces are strongly dependent on the applied electrochemical potential

controlling the amount and the spatial distribution of the injected charge. Noteworthy, the effective ionic volume measured in **Figure 4.16 b** exceeds the free water volume by a factor of >2. Such a finding can only be explained by assuming morphological rearrangements of the polymer microstructure induced by charge accumulation (**Figure 4.16 c**). We hypothesize that the electrostatic compensation of fixed DBS^- acceptors with mobile cations in the OMIEC ionic phase causes electrostatic repulsion between charged molecular domains in the electronic phase. The resulting repulsive stress favors the influx of additional water from the surrounding electrolyte increasing the effective ionic volume of the injected cations. The process is strongly localized in the regions of the polymer layer where charge accumulation is large, but the interdomains spacings are sufficiently small to allow for effective electrostatic interactions. Thereby, the central position of the ionic volume distribution moves according to the charging front and does not coincide with the polymer/electrolyte interface, where the interphase separation is expected to be wider. Moreover, larger effective ionic volumes are measured when the percentage of the polymeric matrix filled with electrolyte rises. This is evident from the progressive increase of the V_{ion} peak amplitude in the 500 nm thick Ppy:DBS layer (**Figure 4.16 a**), and by the large values assumed in the less compact microstructure of the thicker film (**Figure 4.16 b**), doubling the free water volume V_0. Finally, once the OMIEC blend is completely de-doped, ionic charge accumulation in the polymer bulk is suppressed, leading to a structural relaxation and a decrease of the effective ionic volume. Additional studies with complementary techniques are necessary to further investigate this preliminary phenomenological description.

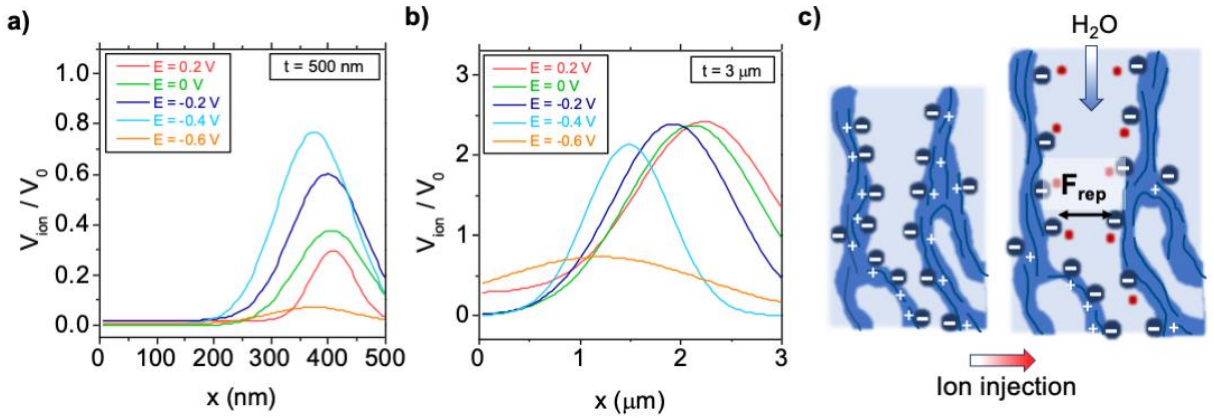

Figure 4.16: Effective volume of hydrated ions in Ppy:DBS**.** Spatial distribution of the effective volume of injected cations for Ppy:DBS layers with thickness 500 nm **(a)** and 3 µm **(b)**. Data are normalized to the ionic volume in free water V_0. **c)** Phenomenological model for Ppy:DBS electroswelling including morphological changes of the OMIEC microstructure induced by charge accumulation and influx of water from the surrounding electrolyte.

4.3.4 Conclusions

In this chapter, we develop a depth-sensitive characterization technique to study the subsurface dynamics of ion migration and swelling in electroactive materials operating at liquid interfaces. We use modulated electrochemical atomic force microscopy (mEC-AFM) as a local

probe to study volume changes and interface forces resulting from dynamical electroactuation effects in Ppy:DBS. By combining electroswelling data with electrochemical impedance spectroscopy we achieve a multidimensional analysis revealing the dominant spatial and temporal scales for ion migration and electroactuation. We interpret the charging properties of Ppy:DBS with a discrete transmission line model able to reconstruct the spatiotemporal dynamics of charge accumulation both for different electrode thicknesses and at different applied electrochemical potentials. Using the actuation transfer function, we correlate electrochemical and actuation properties of the material obtaining subsurface distributions of ion migration and swelling in Ppy:DBS microstructures with different thicknesses. We demonstrate that both the doping level and the film morphology impact on the electroswelling distribution in the polymer layer, which is not uniform, but reflects the distribution of the ionic effective volume in the material. The resulting data suggest morphological rearrangements of the polymer microstructure induced by charge accumulation, leading to the influx of water from the surrounding electrolyte. Such a process increases the actuation efficiency of thicker OMIEC coatings, where the looser microstructure favors larger effective ionic volumes, but at the same time limits the OMIEC volumetric capacitance determining the amount of accumulated charge. Maximized electroactuation can be obtained in material formulations with an optimized balance between these fundamental parameters.

This work demonstrates the successful application of quantitative mEC-AFM profiling of ion migration and swelling on electroactive OMIECs. Similar characterization approaches can benefit material research on solid/liquid interfaces where ion transport plays a major role in device functionality and stability. Notable mentions for this case are energy storage devices operating in electrolytes like batteries [356] and supercapacitors,[357] or low-impedance coatings for bioelectronics electrodes.[358] An in-depth analysis of the distribution of ionic charge and electroswelling is expected to clarify mechanisms responsible for poor electrochemical cycling of devices, leading to an extension of their application lifetime.

4.3.5 Appendix 1: electrodeposition and electrochemical activation of Ppy:DBS thin films

Ppy:DBS was electropolymerized on gold microelectrodes (see **Figure 4.13a**) from an aqueous solution 0.1 M in pyrrole and 0.1 M in sodium-dodecylbenzene sulfonate (NaDBS) (both from Merck). **Figure 4.17a** shows the electrochemical potential E (vs Ag/AgCl) measured during the galvanostatic deposition procedure (with current density σ_{dep} = 2 mA/cm^2). The highly stable voltage profiles allow for a linear control of the polymeric coating thickness by setting a proper deposition time. The deposition rate resulting from the linear fit in **Figure 4.17b** is 17±2 nm/s. The electrochemical activation of Ppy:DBS layer was performed in a 0.1 M NaDBS solution sweeping the applied electrochemical potential from 0.2 to -0.8 V vs Ag/AgCl with a scan rate of 0.01 V/s. Cyclovoltammetries were repeated three times for each electroactive polymer layer During this process, the applied electrochemical potential E (with scan rate 0.01 V/s) drives the injection (and extraction) of ions in the polymeric matrix leading

to the complete hydration of the electroactive film. Results obtained for Ppy:DBS layers with two different thicknesses (500 nm and 3 µm) are presented in **Figure 4.17c**, indicating redox peaks correspondent to ion injection and a compete stabilization of the material properties after the third CV cycle.

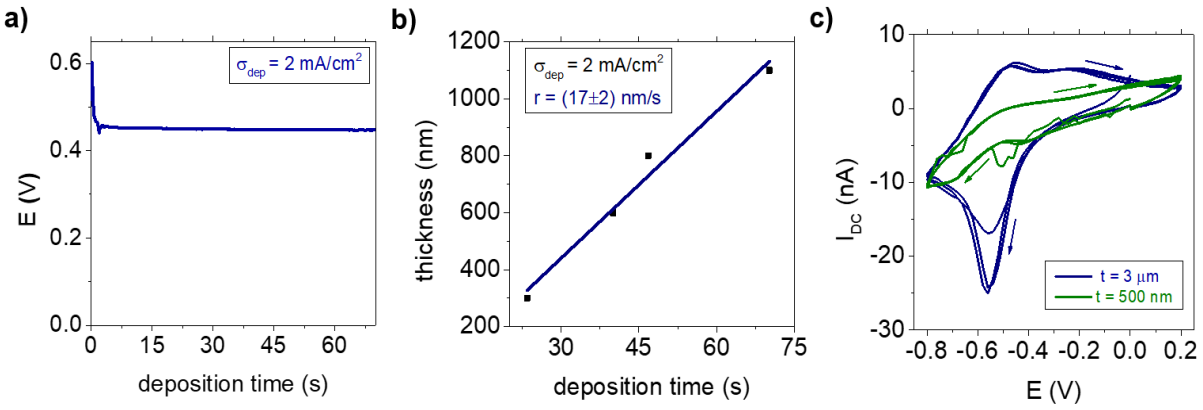

Figure 4.17: a) Galvanostatic electrodeposition of a Ppy:DBS coating on a gold microelectrode with a diameter of 30 µm. **b)** Control of the Ppy:DBS coating thickness through the deposition time. **c)** Electrochemical activation of the actuating microelectrodes in a 0.1 M NaDBS solution. The electrochemical potential E is measured vs Ag/AgCl.

4.3.6 Appendix 2: the discrete transmission line model

If we consider a transmission line composed by *2N* elements, we can calculate the voltage drop e_j (with $j = 1, 2, \dots 2N$) associated to each element composing the net.

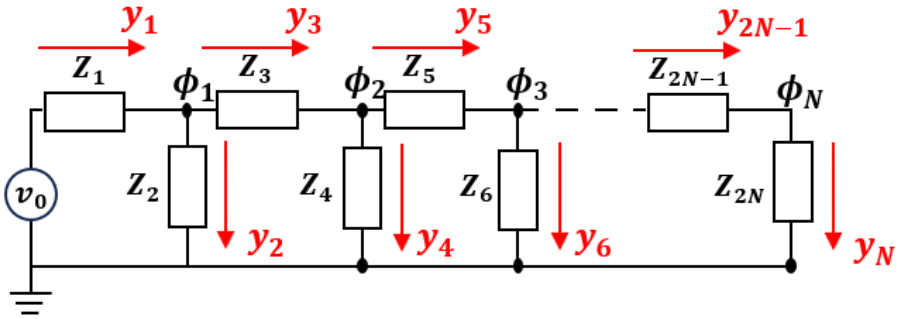

Figure 4.18: Transmission line model with *N* nodes and *2N* elements

If v_0 is the amplitude of the voltage source, and ϕ_i the electrical potential on the *i*-th node we get $e_1 = v_0 - \phi_1$, $e_2 = \phi_1$, $e_3 = \phi_1 - \phi_2$, $e_4 = \phi_2$, … , which can be written in a more compact matrix form as

$$\begin{bmatrix} e_1 \\ e_2 \\ e_3 \\ e_4 \\ e_5 \\ e_6 \\ \vdots \end{bmatrix} = \begin{bmatrix} v_0 \\ 0 \\ 0 \\ 0 \\ 0 \\ 0 \\ \vdots \end{bmatrix} - \begin{bmatrix} 1 & 0 & 0 \\ -1 & 0 & 0 \\ -1 & 1 & 0 \\ 0 & -1 & 0 \\ 0 & -1 & 1 \\ 0 & 0 & -1 \\ & \vdots & \end{bmatrix} \cdot \begin{bmatrix} \phi_1 \\ \phi_2 \\ \phi_3 \\ \vdots \end{bmatrix} \qquad (4.27)$$

or

$$\boldsymbol{e} = \boldsymbol{v} - \boldsymbol{A\phi} \qquad (4.28)$$

The current y_i flowing across each TLM element will be

$$\begin{bmatrix} y_1 \\ y_2 \\ y_3 \\ y_4 \\ y_5 \\ y_6 \\ \vdots \end{bmatrix} = \begin{bmatrix} 1/Z_1 & 0 & 0 & 0 & 0 & 0 \\ 0 & 1/Z_2 & 0 & 0 & 0 & 0 \\ 0 & 0 & 1/Z_3 & 0 & 0 & 0 \\ 0 & 0 & 0 & 1/Z_4 & 0 & 0 \\ 0 & 0 & 0 & 0 & 1/Z_5 & 0 \\ 0 & 0 & 0 & 0 & 0 & 1/Z_6 \end{bmatrix} \cdot \begin{bmatrix} e_1 \\ e_2 \\ e_3 \\ e_4 \\ e_5 \\ e_6 \\ \vdots \end{bmatrix} \qquad (4.29)$$

or

$$\boldsymbol{y} = \boldsymbol{Ke} \qquad (4.30)$$

Kirchoff's current law takes the form

$$\begin{bmatrix} 1 & -1 & -1 & 0 & 0 & 0 \\ 0 & 0 & 1 & -1 & -1 & 0 \\ 0 & 0 & 0 & 0 & 1 & -1 \end{bmatrix} \cdot \begin{bmatrix} y_1 \\ y_2 \\ y_3 \\ y_4 \\ y_5 \\ y_6 \\ \vdots \end{bmatrix} = \begin{bmatrix} 0 \\ 0 \\ 0 \\ \vdots \end{bmatrix} \qquad (4.31)$$

or

$$\boldsymbol{A^t y} = \boldsymbol{0} \qquad (4.32)$$

By replacing **Eq. 4.28** in **Eq. 4.30**, and then **Eq. 4.30** in **Eq. 4.32**, we obtain the solving equation for the potentials along the line $\boldsymbol{\phi}$

$$\boldsymbol{A^t K A \phi} = \boldsymbol{b} \qquad (4.33)$$

where $\boldsymbol{b}$ is identified as $\boldsymbol{b}=\boldsymbol{A^t K v}$. We can apply this general model to describe charging properties of the Ppy:DBS film bulk. Following our interpretation of charge accumulation in **Figure 4.14c** and under the assumption of a constant volumetric capacitance c_v for Ppy:DBS and a uniform ionic resistivity ρ_{ion} on the vertical axis of the polymer, we get

$$Z_1 = Z_3 = Z_5 = \ldots = Z_{2N-1} = \frac{\rho_{ion}}{A_{el}} \Delta x \qquad (4.34)$$

and

$$Z_2 = Z_4 = Z_6 = \ldots = Z_{2N} = \frac{1}{j\omega c_v A_{el} \Delta x} \qquad (4.35)$$

where $\Delta x = t/N$ is the length increment along the vertical profile of the polymer. By substituting these elements in the circuit model in **Figure 4.18**, we can solve **Eq. 4.33** and map the potential (and charge) distributions in the polymer. The total impedance of the line can finally be calculated as

$$Z_{TOT} = \frac{v_0}{v_0 - \phi_1} Z_1 \quad (4.36)$$

4.3.7 Appendix 3: continuous limit for the transmission line model impedance

Electric field-driven transport through a porous capacitive electrode can be described using a transmission line consisting of resistors along the length and capacitors in parallel (**Figure 4.14c**). Let r_i be the ionic resistance and c_{dl} the double layer capacitance for one-unit thick electrode (with units of Ωcm^{-1} and Fcm^{-1}, respectively). At a distance x from the electrode/gold interface, the potential is $u(x)$ and the current crossing a resistance $r_i\,dx$ is $i(x)$. The difference of potential at the edges of the resistance is

$$u(x) = r_i \cdot i(x)dx \quad (4.37)$$

while the (infinitesimal) current flowing through the capacitance $c_{dl}\,dx$ is given by

$$di(x) = \frac{u(x)}{j\omega c_{dl} dx} = \frac{u(x)}{z_{dl}} dx \quad (4.38)$$

where z_{dl} is the impedance of the double layer capacitance for a unit thick electrode (with unit Ωcm). By solving the differential equation

$$\frac{d^2u}{dx^2} = \frac{r_i}{z_{dl}} u(x) \quad (4.39)$$

with boundary condition $i(x=0)=0$, where t is the electrode thickness, we obtain the De Levie impedance[359]

$$Z_{TLM} = \sqrt{r_i \cdot z_{dl}} \coth\left(\sqrt{\frac{r_i}{z_{dl}}} \cdot t\right) \quad (4.40)$$

By assuming uniform ionic conductivity and volumetric capacitance in the polymeric matrix, we can identify the ionic resistivity and the volumetric capacitance of the Ppy:DBS bulk as $\rho_{ion} = r_i/A_{el}$ and $c_v = c_{dl} * A_{el}$, obtaining

$$Z_{TLM} = \sqrt{\frac{\rho_{ion}}{j\omega c_v {A_{el}}^2}} \coth\left(\sqrt{j\omega c_v \rho_{ion} t^2}\right) \quad (4.41)$$

By comparing **Eq. 4.41** result with **Eq. 4.36**, we demonstrate in **Figure 4.19** that the discrete approximation converges to the continuous limit when we consider N=100 elements composing the line.

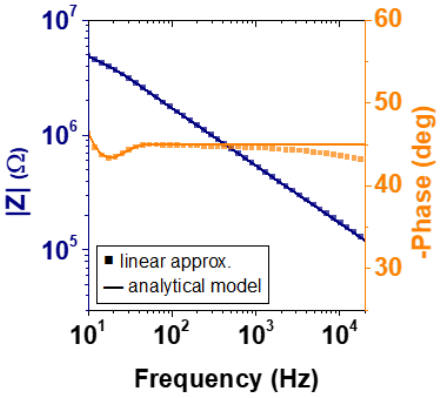

Figure 4.19: Comparison between the discrete linear approximation with *N*=100 elements and the continuous TLM impedance

4.3.8 Appendix 4: nanomechanical indentation experiments on Ppy:DBS

We used AFM nanoindentation experiments to measure the elastic modulus of Ppy:DBS at different oxidation states. The cantilever sensitivity s_c = 47.2±0.8 V/µm of NCHR probes (force constant *K*=42 N/m) was measured according to the procedure described in **sect. 4.2.7**. We then performed in liquid force-distance spectroscopies (force limit 900 nN, approach/retract speed 0.3 µm/s) on the soft polymer matrix (thickness 3 µm) for the nanomechanical characterization. During the process (**Figure 4.20a**), the probe-sample interaction causes both the indentation *I* of the tip on the polymer layer and the deflection *d* of the cantilever. The latter can be calculated from the vertical deflection voltage as $d=V_{PSPD}/s_c$. Thereby, the indentation is easily found as $I = z - d$. **Figure 4.20b** shows the force $F=K*d$ acquired repeating the experiment on 9 different points on the polymer surface. The corresponding indentation plot (**Figure 4.20c**) can be fitted with a polynomial in the form $F = a \cdot |I - b|^{3/2} + c$ (Hertzian model),[360] and the elastic modulus E_{el} can be calculated from the coefficient $a = \frac{4}{3}\sqrt{R_c}\frac{E_{el}}{1-\nu^2}$, where ν=0.3 is the Poisson's ratio, and R_c=20 nm the tip radius. Results obtained at different electrochemical potential *E* (**Figure 4.20d**) provide values consistent with literature[361] and demonstrate changes in the mechanical properties caused by the injection of hydrated cations. This evidence further confirms the hypothesis of morphological changes in the polymer matrix during electrochemical de-doping.

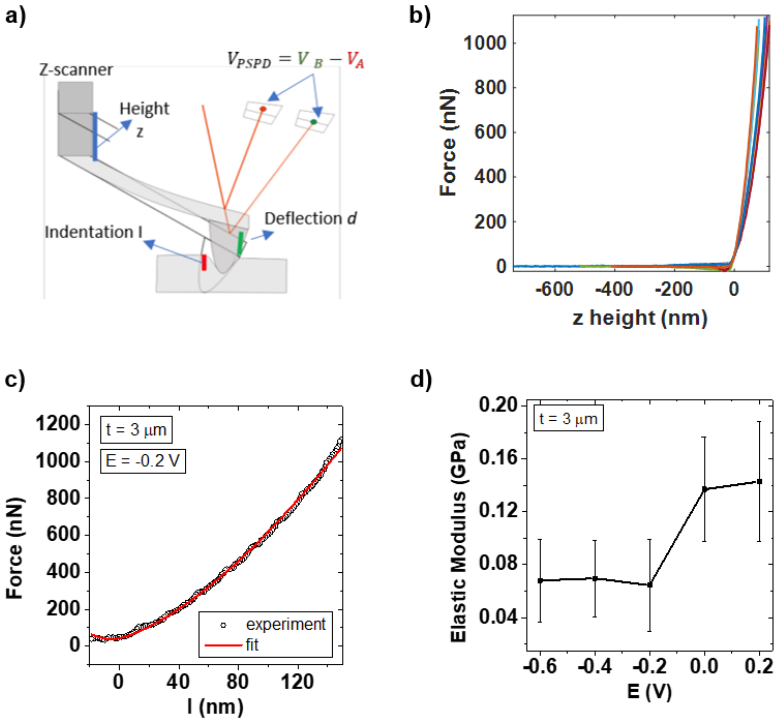

Figure 4.20: a) Probe-sample interaction during a force distance spectroscopy, showing the tip indentation *I* and the cantilever deflection *d*. **b)** Force distance spectroscopies on a 3 µm-thick Ppy:DBS layer. Measurements are repeated on 9 different points of the electrode surface. **c)** Indentation plot. This can be fitted with the Hertzian model to measure the elastic modulus **(d)** as a function of the applied electrochemical potential *E*.

4.3.9 Appendix 5: injection resistance and surface capacitance of Ppy:DBS microelectrodes

Pushing the applied electrochemical potential *E* towards negative values decreases the conductivity of the electronic phase in the Ppy:DBS blend reducing the amount of electronic charge injected from the gold substrate (modeled by the injection resistance R_{inj} in **Figure 4.21a**).

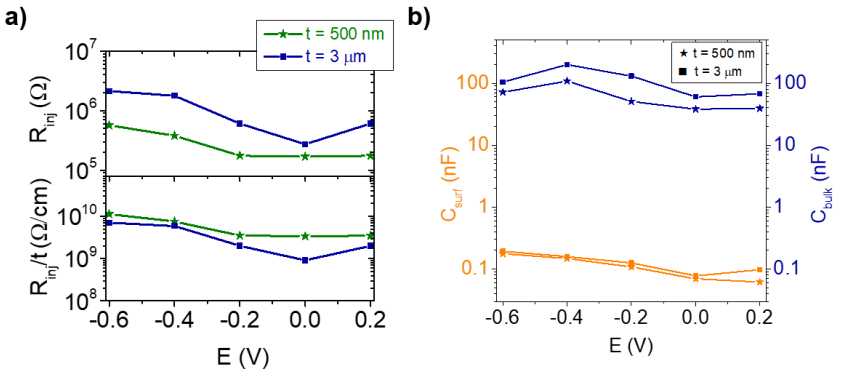

Figure 4.21: a) Electronic injection resistance from the gold substrate in Ppy:DBS microelectrodes. Results in the bottom row are normalized by the polymer layer thickness. **b)** Comparison between the bulk and the surface capacitances of the Ppy:DBS thin films.

When Ppy is fully de-doped (E < -0.4 V), the DBS^- acceptors are entirely compensated, and the injection of cations from the electrolyte is largely suppressed. In this condition, ionic charge accumulation occurs only on the polymer surface, but given its small capacitance C_{surf} (see **Figure 4.21b**), such effect plays only a minor role in the electroactuation process.

4.3.10 Appendix 6: subsurface profiles of charge accumulation in the 3 µm-thick Ppy:DBS microelectrode

Charging profiles obtained for the 3 µm-thick Ppy:DBS layer are reported in as a function of frequency (**Figure 4.22a**) and electrochemical potential (**Figure 4.22b**). Results are fully analogue to the ones obtained for the 500 nm-thick microelectrode, confirming the interpretation given to Fig. 2e and 2f in the main text.

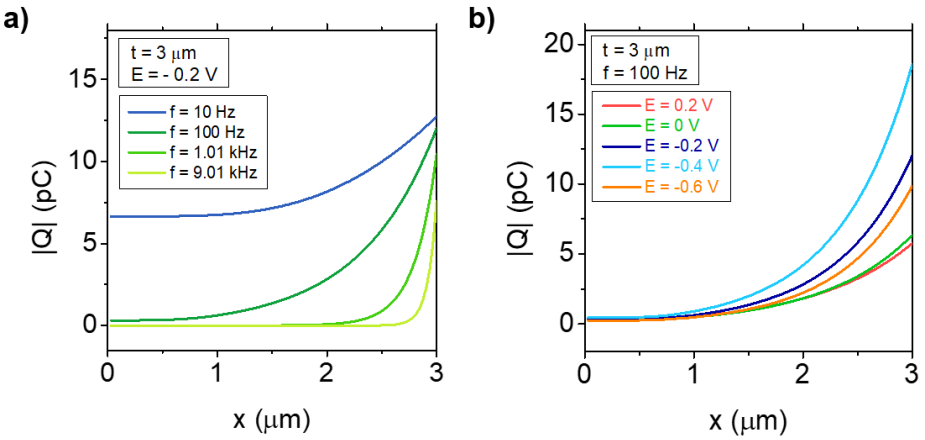

Figure 4.22: Subsurface profiles of charge accumulation in the 3 µm-thick Ppy:DBS layer at different frequencies **(a)** and applied electrochemical potential **(b)**.

4.3.11 Appendix 7: colormap evolution of charging in Ppy:DBS

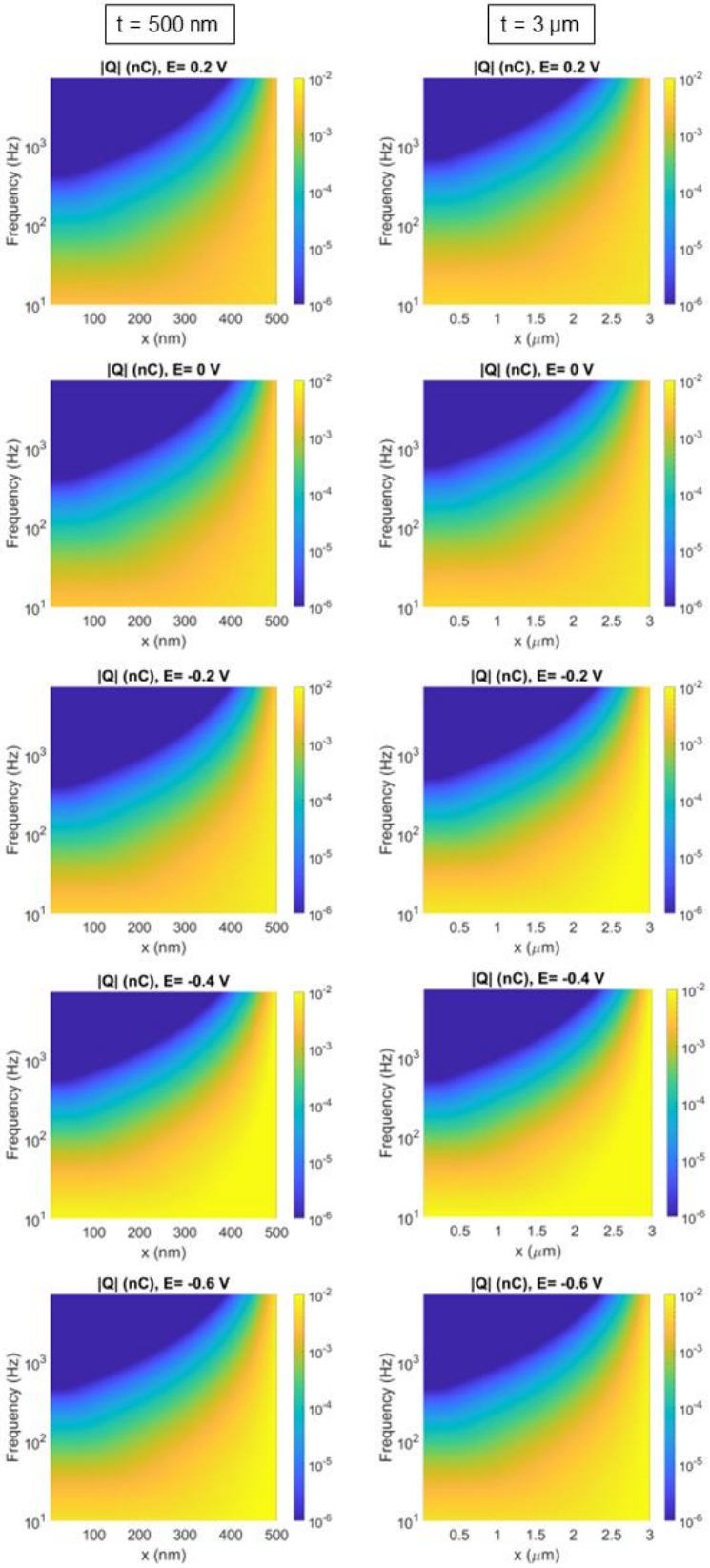

Figure 4.23: Spatiotemporal evolution of charge amplitudes in a 500 nm and a 3 µm-thick Ppy:DBS layer calculated from Eq. 4.24.

4.3.12 Appendix 8: fitting parameters for the actuation function spatial distribution

thickness	E (V)	A_0 (nm/nC)	x_0	σ	B (nm/nC)
500 nm	0.2	0.48	403.1 nm	38.1 nm	0.031
500 nm	0	0.65	400.1 nm	62.5 nm	0.001
500 nm	-0.2	1.01	393.5 nm	64.1 nm	0.033
500 nm	-0.4	1.31	370.05 nm	65.3 nm	0.01
500 nm	-0.6	0.11	368 nm	75.4 nm	0.008
3 µm	0.2	3.90	2.19 µm	0.65 µm	0.52
3 µm	0	3.70	2.08 µm	0.65 µm	0.006
3 µm	-0.2	3.62	1.89 µm	0.59 µm	-0.002
3 µm	-0.4	3.57	1.53 µm	0.45 µm	0.52
3 µm	-0.6	1.26	1.72 µm	1.35 µm	0.11

Table 4.4: Fitting parameters used in equation 3.26 to reproduce the experimental electroswelling spectroscopies in **Figure 4.15a** and **b**.

4.3.13 Appendix 9: colormap evolution of swelling in Ppy:DBS

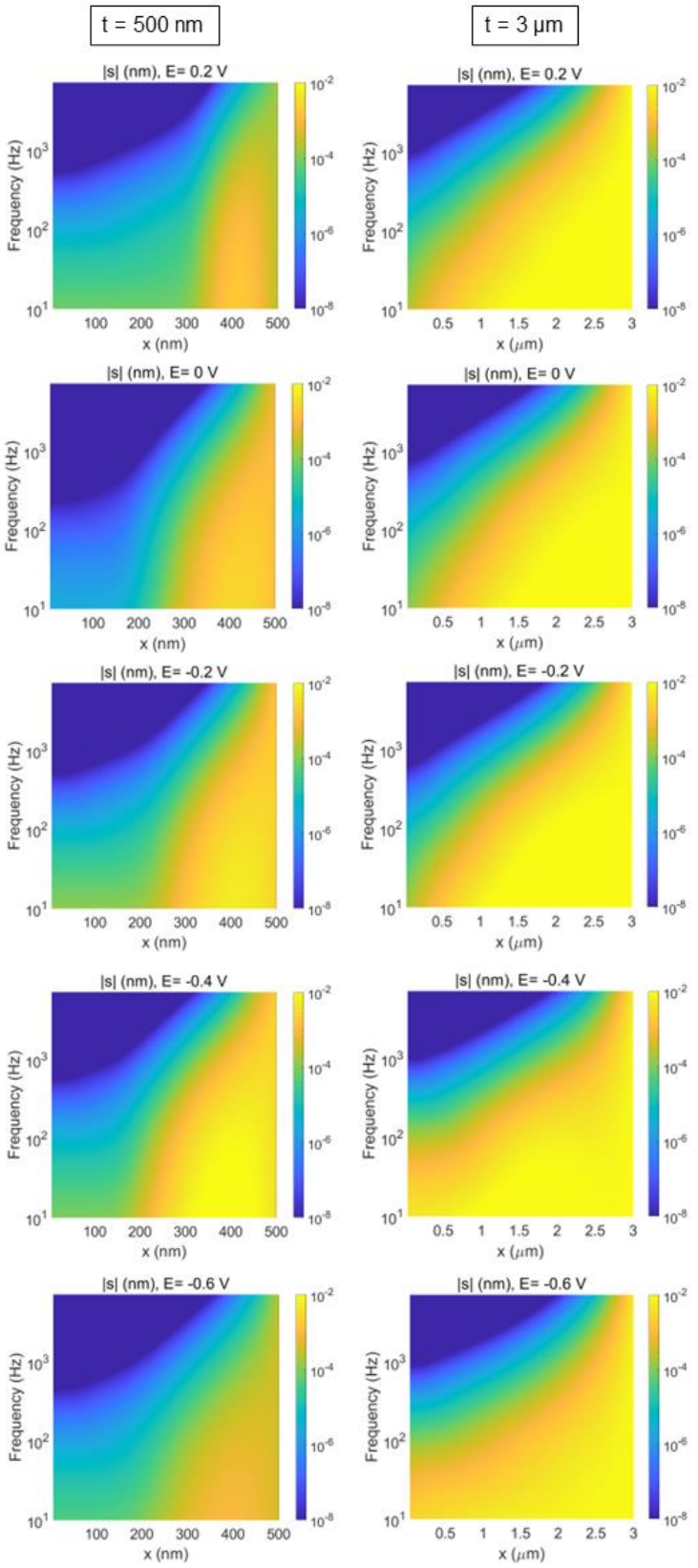

Figure 4.24: Spatiotemporal evolution of swelling amplitudes in a 500 nm and a 3 µm-thick Ppy:DBS layer calculated from Eq. 4.25.

4.4 Flexible microelectrode arrays based on PEDOT:PSS for Neural Recording and Stimulation

Flexible microelectrode arrays placed on the surface of the brain cortex are promising tools for treating neurological deficits and restoring lost functionalities, as well as investigating unexplored aspects of neuroscientific research. Further progress in this direction requires the development of biocompatible bioelectronics platforms enabling the long-term recording and stimulation of neural activity. In this chapter, we face this challenge by developing and characterizing microelectrode arrays (MEAs) based on PEDOT:PSS for electrocorticography (ECoG) experiments. We extended the microfabrication techniques presented in **sect. 3.1** to flexible substrates to realize low-impedance devices conformable with the brain surface and with high spatial and temporal resolution. We test the electrode arrays in an in-vitro setup combining electrochemical impedance spectroscopy (EIS), analysis of the electrode polarization during simulated stimulation protocols, and atomic force microscopy (AFM) characterization of the PEDOT:PSS coating on the electrode surface. The combination of these techniques allows the optimization of an implantable neural probe prototype able to sense and stimulate the brain activity in *in-vivo* experiments studying induced-torpor states in animal models. Preliminary results of *in-vivo* acute ECoG recordings on anesthetized laboratory rats are presented in the last section of this chapter.
Results regarding the microfabrication of the neural probes were published in August 2022 on the *Il Nuovo Cimento* journal.[80] I collaborated on this work with Francesco Decataldo, Tobias Cramer and Beatrice Fraboni from the Department of Physics and Astronomy of the University of Bologna. *In-vivo* experiments were performed at the Department of Biomedical and Neuromotor Sciences of the University of Bologna in the research group of Roberto Amici and Matteo Cerri, collaborating with Emiliana Piscitiello and Timna Hitrec.

4.4.1 Microfabrication of PEDOT:PSS flexible microelectrode arrays

An optical image of the MEA resulting from the microfabrication procedure described in **sect. 3.1** is presented in **Figure 4.25a**. The flexible neural probe is composed by 32 independent recording and stimulating channels, allowing for conformability with the brain cortex and high spatial resolution in a small active area (4.5 mm^2). An optical image and the detailed structure of a single electrode are reported in **Figure 4.25b** and **c**, respectively. Gold metallic tracks are patterned onto a flexible polyethylene naphthalate (PEN) plastic substrate (thickness 12.5 μm), and insulated from the biological environment using a 5 μm thick negative photoresist. Glass slides were used as rigid carriers for flexible plastic foils during the photolithography process. For every channel, a circular electrode with diameter of 200 μm is left as the active region to be placed in direct contact with the brain surface. A 1 μm thick PEDOT:PSS layer is deposited onto the electrode surface to reduce the recording impedance and improve the device biocompatibility. AFM measurements on the electrode site (**Figure 4.25d**) provide the topography of the electrode border and the morphology of the PEDOT:PSS

polymeric matrix. The OMIEC film was obtained using electrodeposition (**sect. 3.2.2)**, but micropatterned PEDOT:PSS electrodes can be fabricated also using photolithography methods and spin-coating (**sect. 3.1.5**). The second approach was preferred for devices used in *in-vivo* experiments. Despite the spin-coating procedure provides thinner PEDOT:PSS structures (150 ± 10 nm) with smaller electrical capacitance, secondary dopants can be added to the OMIEC formulation to enhance its stability during prolonged recording and stimulation procedures.

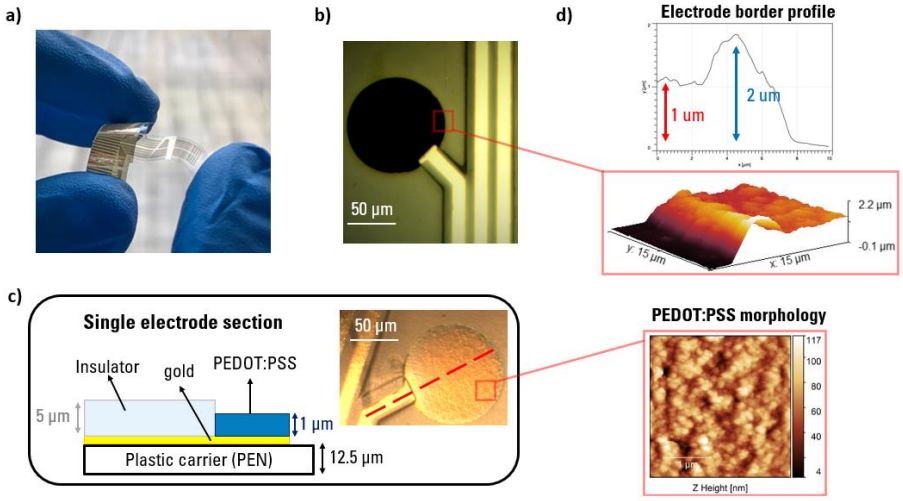

Figure 4.25: Microfabrication of the flexible microelectrode array. **a)** Optical image of the neural probe. Picture **(b)** and structure **(c)** of a single electrode. **d)** AFM topography of the PEDOT: PSS electrode coating, showing the electrode border profile and the morphology of the polymeric film.

4.4.2 In vitro characterization of the flexible MEA

Results from the *in-vitro* characterization of the MEA are presented in fig. 2. The electrochemical impedance spectroscopy (EIS) (**Figure 4.26a**) of a single electrode was acquired in 0.1 M PBS solution, using an Ag/AgCl wire as the reference electrode. The acquired data can be modeled with an equivalent RC circuit description. In the high frequency regime, the electrode impedance is dominated by the electrolyte resistance R_{el}, while the large volumetric capacitance of PEDOT:PSS (c_v = (45 ± 5) F/cm3)) limits the linear capacitive impedance increase in the low-frequency range. The electrode impedance at 1 kHz results to be 1.7±0.8 kΩ, indicating the low-impedance recording properties of the MEA. **Figure 4.26b** shows the electrode polarization during a typical neural stimulation protocol. Two current pulses (*phases*) with amplitude 40 μA and opposite sign are applied for t_p = 1 ms, with an interphase delay of *td* = 500 μs. The linear polarization transients indicate a capacitive charge injection from the electrode, and are accurately reproduced by an equivalent RC circuit simulation. Finally, we performed a bending test to study the impact of the mechanical deformation of the plastic substrate during practical use (**Figure 4.26c**). The MEA was bent at different curvature radii while measuring the electrical resistance of a single electrode with a micromanipulator needle (**Figure 4.26c**). Results highlight the large mechanical stability

of the device, indicating how these two quantities are not directly correlated, with an average resistance change of 0.4% during the process.

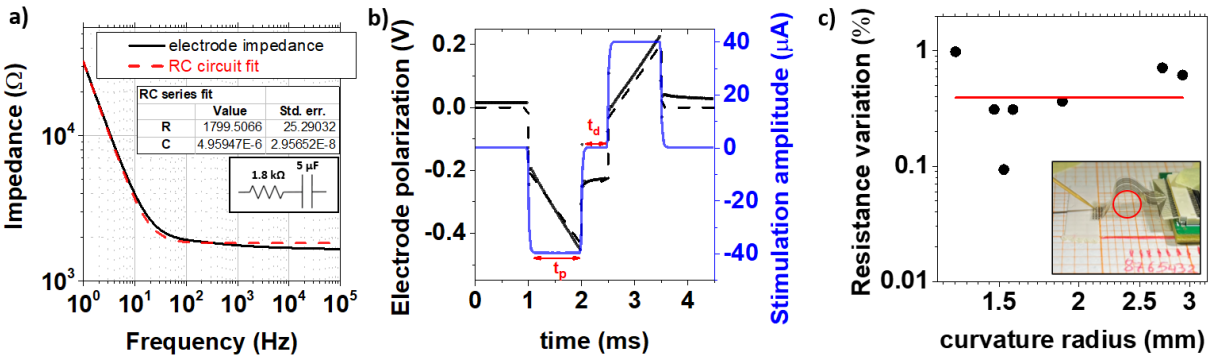

Figure 4.26: In vitro characterization of the flexible microelectrode array. **a)** Electrochemical impedance spectroscopy of a single electrode, and fit with an equivalent RC circuit. **b)** Electrode polarization during a stimulation procedure, and RC simulation of the voltage transients (dashed line). **c)** Bending test on the neural probe, showing the variation of the resistance of a single electrode when the device is bent at different curvature radii.

4.4.3 *In-vivo* electrocorticography experiments

The low-impedance, linear charge injection and mechanical stability of the neural probe were exploited in *in-vivo* experiments aiming to record and stimulate the neural activity of an anesthetized animal model at different temperatures. A schematic of the experimental setup is reported in **Figure 4.27**.

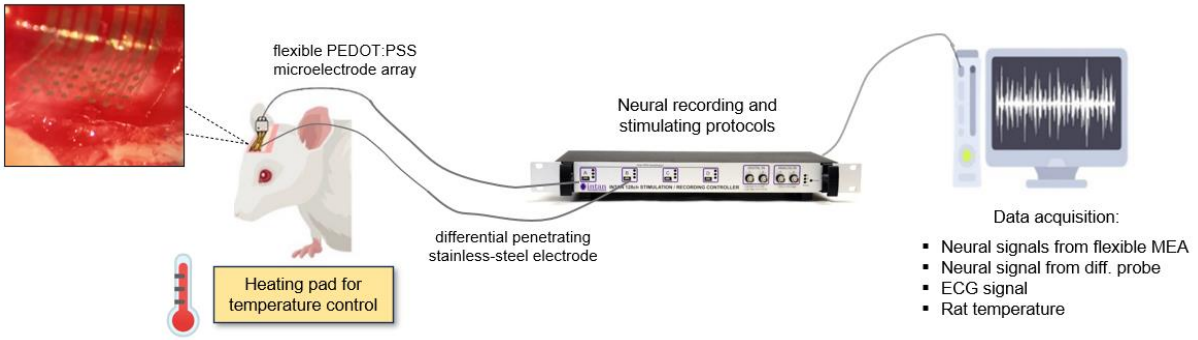

Figure 4.27: Experimental setup for *in-vivo* neural recording and stimulation experiments.

Laboratory rats were pre-anesthetized with Diazepam (Valium Roche, 5 mg/Kg intramuscular) and, after sedation was obtained, they underwent a general anesthesia with an intraperitoneal injection of Ketavet (Ketamine - HCl, Parke-Davis, 100 mg/Kg). After confirming the surgical plane of anesthesia by the absence of blink and toe-pinch reflexes, rats were subjected to tracheotomy and intubation and mechanically ventilated (isoflurane). Then, each animal was positioned on a stereotaxic apparatus (David Kopf Instruments) to firmly block the head with the aid of a transverse support bar for the jaw (muzzle blocking bar, 4 mm) and two ear bars

inserted gently in the external auditory meatus. The exposed skin was incised, the periosteum was removed, and the cranium surface was cleaned. Using a drill tip, the right parietal bone was removed, paying attention not to damage the dura mater, and the PEDOT:PSS MEA was placed on the cerebral cortex (see the inset in **Figure 4.27**) to perform epidural electrocorticography (ECoG) recording and stimulation protocols. Two stainless-steel wires acting as differential penetrating electrode (with penetration depth of about 2 mm and diameter 0.3 mm) were also implanted for the recording of the frontal–parietal electroencephalogram (EEG). Rats' rectal temperature was monitored and regulated by means of either a heating pad (or blanket) or a cold environment, according to experimental requirements. Electrical recording and stimulation procedures were performed using the Intan RHS system, featuring specialized integrated circuits for electrophysiology. We developed custom electronics including a printed circuit board to interface the flexible MEA with the data acquisition system. A stainless-steel screw placed on the rat skull was used as reference electrode for ECoG electrical protocols.

Figure 4.28 compares the EEG signal recorded with the differential penetrating stainless steel electrode to the ECoG signal simultaneously measured with a PEDOT:PSS microelectrode. Electrical traces are acquired with sampling frequency of 30 kHz and plotted as a function of time for 15 sec. Despite different features emerge due to the different placement and geometry of the probes, the acquired signals show an analogue trend. The power spectral analysis performed on a 10 minutes acquisition shows how ECoG signals concentrate their power spectral density (PSD) at low frequency (0-5 Hz), consistently with the recording of slow delta waves typically measured during sleep.[183]

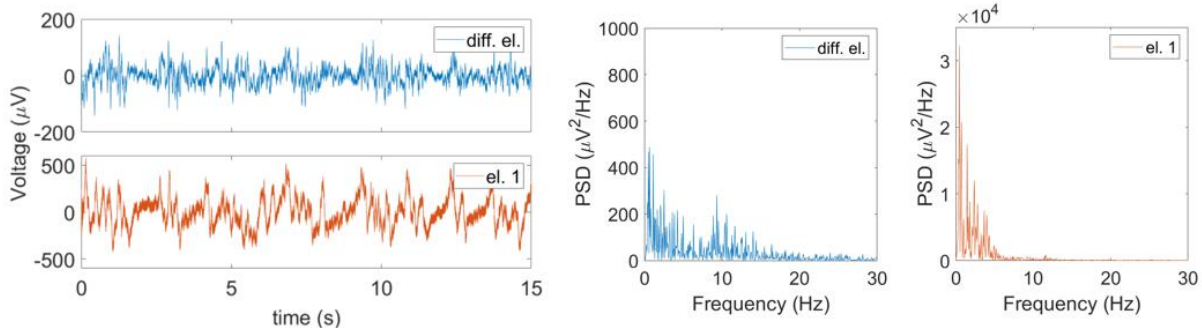

Figure 4.28: Comparison between an EEG signal recorded with a differential penetrating stainless steel electrode and an ECoG signal measured with a PEDOT:PSS microelectrode. Electrical traces show analogue features and concentrate their power spectral density (PSD) at low frequency.

Similar considerations can be extended to ECoG data simultaneously acquired with PEDOT:PSS microelectrodes placed at different sites on the cortex surface (**Figure 4.30**). Given the spatial separation of 1.5 mm between the first and second, and the second and third recording units, slight differences appear both in the time traces and in the PSD.

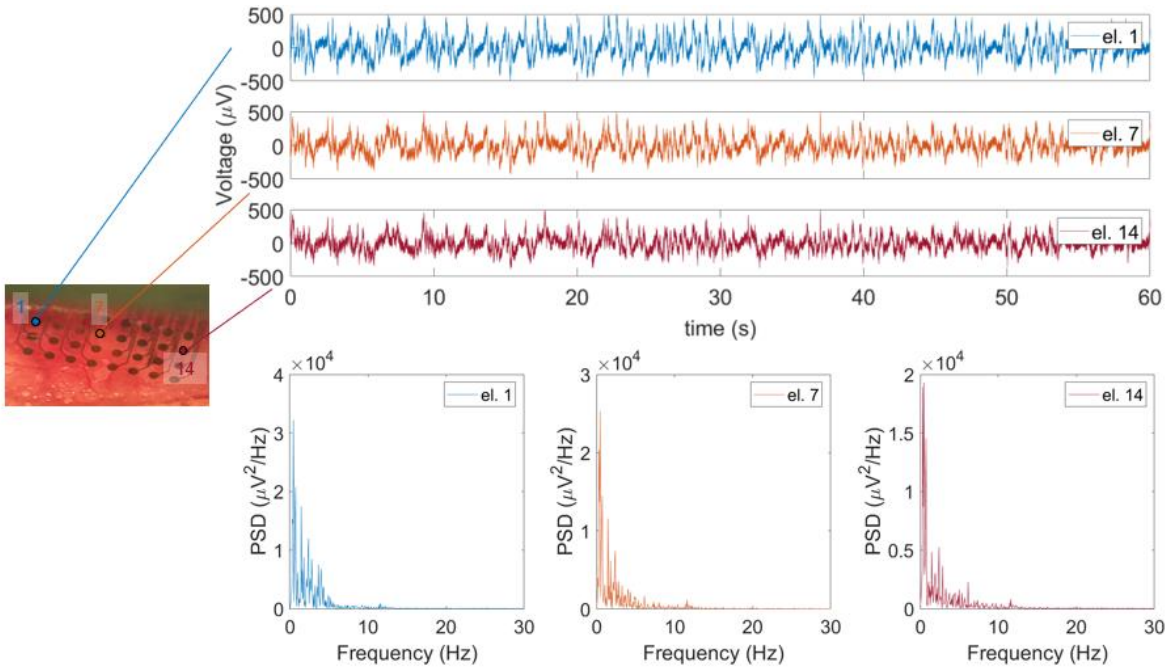

Figure 4.30: Simultaneous ECoG recordings with three PEDOT:PSS microelectrodes with spatial separation of 1.5 mm on the cerebral cortex.

A preliminary demonstration on the effect of rat temperature changes on neural activity is reported in **Figure 4.29**. Spectrograms of the ECoG signals (showing the corresponding electrical traces in overlay) acquired with one PEDOT:PSS microelectrode at T= 37°C and T= 30°C show how higher frequency components are measured more frequently at higher temperature.

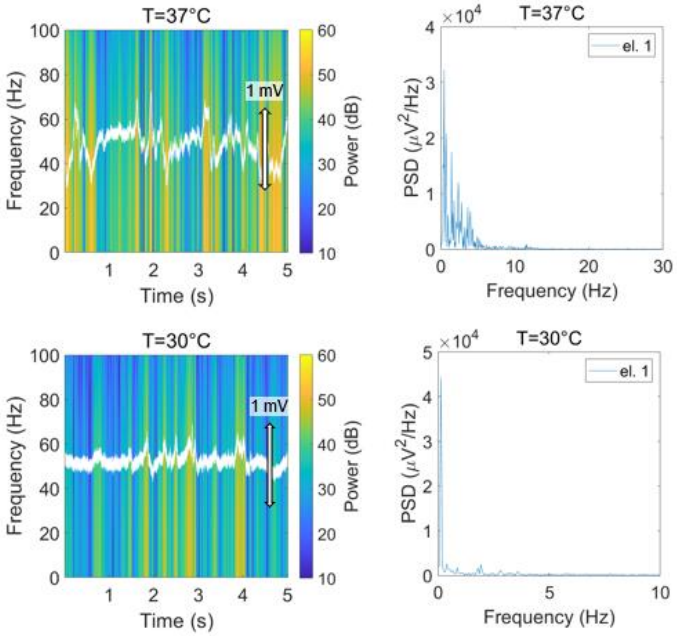

Figure 4.29: Spectrograms and power spectral analysis of ECoG signals measured with the same PEDOT:PSS microelectrode at different temperatures of the animal.

Consistently, PDS data show how signals acquired at T=37°C distribute most of their power in the 0-5 Hz range where the power spectral density reaches a plateau around 40 dB. At 30°C,

these oscillations are slower, and the PSD decreases with frequency. Anyway, further experiments supported by stimulation protocols are required to experimentally confirm these first observations.

4.4.4 Conclusions

In this chapter, we developed and characterize a microelectrode array based on the conductive polymer PEDOT:PSS for neural recording and stimulation. We realized a flexible neural probe with 32 independent recording and stimulating channels. Electrochemical impedance spectroscopy measurements and the analysis of the voltage transients during simulated stimulation protocols demonstrate the low-impedance recording properties and the linear charge injection of the neural probe. The characterization of the bending properties of the electrode array highlights the device stability against mechanical deformation. These promising device properties originate from both the application of microfabrication techniques onto flexible substrates and from the use of OMIECs as active materials. *In-vivo* recording and stimulation experiments are currently ongoing in our group to investigate the neural activity of animal models at different temperatures. The resulting knowledge is expected to contribute to the study of neural connectivity in torpor and hibernation states.

4.5 AC amplification gain in organic electrochemical transistors for impedance-based single cell sensors

In-vitro experiments studying cellular adhesion and cell-cell interactions constitute a field of application of OMIEC materials of primary importance. Recent advancements in organic electrochemical transistor (OECT) research have led to impedance sensors reaching single cell resolution, but a quantitative study on the transistor amplification gain is still lacking. A clear understanding of gain is also desired to define when OECT amplification has significant advantages over one-terminal, low-impedance microelectrode-based sensors offering simpler fabrication and electrical operation. To overcome the issue, we introduce in this work a model experiment that allows a quantitative study of AC amplification in OECT impedance sensors. As cellular *in vitro* experiments are inherently difficult to control, we substitute the cell by a dielectric microparticle of similar dimensions. We control the position of the microparticle on top of the microscale impedance sensors with an AFM and achieve highly reproducible measurements that enable to compare the current output of OECT-based sensors with equivalent microelectrode sensors. To rationalize the findings, we develop an analytical model that describes the gain as a function of the applied frequency, the device geometry and PEDOT:PSS materials properties. Relying on this model, we design an optimized device and demonstrate its efficiency by measuring the transients of single cell adhesion and detachment in *in-vitro* experiments. Noteworthy, we observe a significant AC gain reaching values of

(20.2±0.9) dB for the transistor structure, thereby demonstrating the advantages arising from the OECT amplification in single-cell impedance sensing experiments.
Results presented in this chapter were published in September 2022 on the *Nature Communications* journal.[39] I collaborated on this work with Francesco Decataldo, Isabella Zironi, Daniel Remondini, Tobias Cramer, and Beatrice Fraboni from the Department of Physics and Astronomy of the University of Bologna.

4.5.1 Impedance sensing of a dielectric microparticle

The first objective of our work is to introduce a novel experiment to quantify the sensitivity of electrochemical impedance sensors operated in OECT or microelectrode configuration. To this end we realized the experimental setup shown in **Figure 4.31a** and **b**. The setup contains a dielectric microparticle (with diameter of 50 μm) attached to the bottom part of an AFM cantilever to have micrometric control of its position in the 3 spatial directions (**Figure 4.31c**). Further details on probe fabrication are given in **sect. 4.5.5**. Once the microparticle is finely aligned with the *x*-y coordinates on the center of the sensor surface, we use the *z*-stage of the microscope to control the particle-sample distance *d*. Contact of the microparticle with the sensor surface is determined by the onset of a repulsive force acting on the AFM cantilever. OECT sensors were fabricated according to **sect. 3.1.5**. The electric circuit to operate the OECT impedance sensor contains an Ag/AgCl wire that is used as the gate electrode, controlling the electrical potential of the aqueous electrolyte solution (0.1 M PBS). A DC voltage $V_{D,DC}$ is applied between the source (S) and drain (D) electrodes of the OECT to drive the electronic current $I_{D,DC}$ in the PEDOT:PSS channel. The measured transfer and output characteristics of a typical OECT (**Figure 4.31d**), demonstrate that the gate voltage effectively modulates the channel current (the entire set of transfer curves of the devices with different channel dimensions used in the experiments is reported in **sect. 4.5.6**). For impedance sensing we superimpose a small sinusoidal oscillation signal $V_{G,AC}$ (with amplitude 10 mV and angular frequency ω) on the gate bias $V_{G,DC}$. This leads to an AC current in the PEDOT:PSS layer,[362] which is measured by a lock-in amplifier connected to the source contact ($I_{S,AC}$).
In the microelectrode configuration (**Figure 4.31b**) the circuit is simplified, as source and drain electrodes are in short circuit and are jointly connected to the lock-in amplifier. Therefore, no OECT channel current is present, and all the electric current measured during impedance sensing is the gate current $I_{G,AC}$, flowing from the electrolyte into the PEDOT:PSS layer. All other components are identical to the OECT configuration to permit a direct comparison here conducted at 5 different frequencies (0.12, 0.33, 1.17, 3.33 and 11.7 kHz) .
In **Figure 4.31e** we show the results of a typical microparticle distance - AC current experiment. conducted at 1.17 kHz excitation frequency, which was chosen as an example. The amplitudes of the AC currents in OECT and microelectrode configuration are plotted as a function of time. During the experiment, the microparticle is approached and retracted from the device channel for three consecutive times. For both configurations, the current amplitude follows the motion of the microparticle in a highly reproducible manner over consecutive

cycles, highlighting the stability of the characterization method. In **Figure 4.31f**, the same data is plotted as a function of the distance between microparticle and sensor surface (normalized data are reported in **sect. 4.5.9**). Both types of devices produce a reversible, linear response in which the approach leads to a reduction in AC amplitude. Qualitatively, this response is expected, as the microsphere represents a barrier for the ionic current in the electrolyte: when it is close to the sensor surface, the half space through which ions can approach the active layer is reduced, thus increasing the effective impedance of the electrolyte Z_{el}. Consequently, upon approach, the interfacial impedance measured with the sensor increases and the AC current amplitude drops. We note that in first order approximation a similar response is expected when a biological cell adheres to the sensor surface.

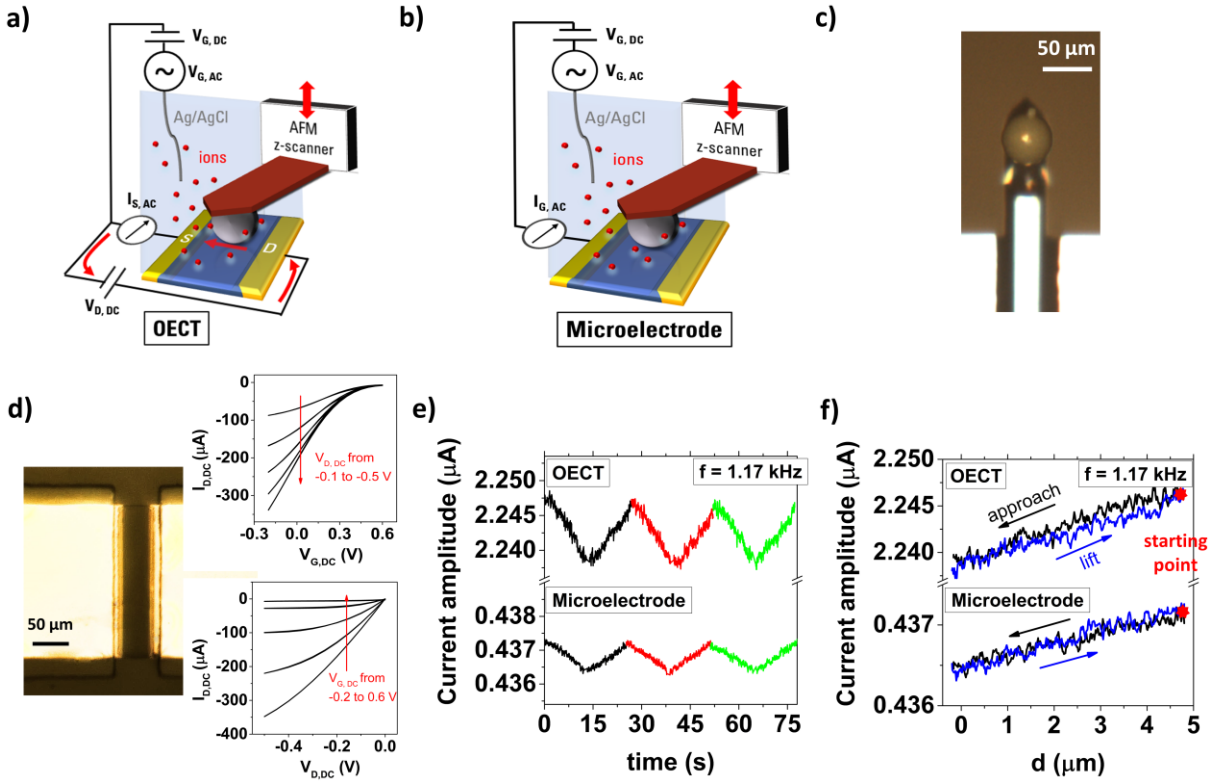

Figure 4.31: Impedance sensing of a dielectric microparticle. **a,b)** Schematic of the experimental setup in OECT and microelectrode configuration. **c)** Optical microscopy image of the microparticle attached to the AFM cantilever. **d)** Optical image of the active PEDOT:PSS channel (WxL = 200x50 µm) in an OECT device, whose DC transfer and output characteristics using a Ag/AgCl gate are shown in the inset. **e)** Variation of the AC current amplitude in OECT and microelectrode configuration during repeated microparticle approach and retract. Consecutive measurements are indicated with different colors. **f)** Detail on a single microparticle distance - AC current measurement acquired with an OECT and a microelectrode device. Different colors are used to indicate the microparticle approach and lift. The slope of the curves yields the sensitivity s of the impedance sensor.

These results are crucial for our goal as they permit the quantitative assessment of the sensitivity of the impedance sensor. For the case of a high sensitivity, small changes in the impedance Z_{el} cause large variation in AC current amplitude. Therefore, we define the sensitivity as s =

$\partial I_{AC}/\partial Z_{el}$. In our experiment, ∂Z_{el} is directly related to the microparticle displacement $\partial Z_{el} = p \cdot \partial d$. The proportionality constant p quantifies how much the electrolyte impedance changes when the microparticle-channel distance d is modified. Therefore, p is independent on the sensor configuration (OECT vs microelectrode) but is only a measure of the variation of the electrolyte impedance when the geometry of the ionic current barrier is modified. We obtain its numerical value for each channel geometry by fitting the microelectrode impedance spectrum (see **sect. 4.5.10**). Accordingly, the sensitivity is given by the slope of the approach curves shown in **Figure 4.31f**. For the channel geometry of WxL = 100x100 µm we obtain values of s_{OECT} = 0.059±0.002 nA/Ω and $s_{\mu E}$ = 0.023±0.006 nA/Ω. The values show a greater sensitivity in the OECT device with respect to the microelectrode, due to the contribution of OECT channel current to the AC response.

4.5.2 Quantitative model for PEDOT:PSS-based impedance sensors

We developed an analytical model to express the impedance sensitivity s as a function of the sensor operation conditions, material properties and geometry. Objective is a quantitative understanding of the factors that increase sensitivity in OECT configuration with respect to PEDOT:PSS microelectrodes. Many studies decouple charge transport in OECTs in an electronic and an ionic circuit.[219] A schematic of this representation is reported in **Figure 4.32a**, where the components of the electronic and the ionic circuit are indicated in blue and orange, respectively. Electronic charge carriers (holes) are driven by the drain voltage $V_{D,DC}$ and carry the channel current in an OECT, while ionic charge carriers are driven by the gate voltage $V_G = V_{G,DC} + V_{G,AC}$ and modulate the concentration of holes and, consequently, the electronic conductivity of the transistor channel. The limited conductivity of the electrolyte as well as the presence of dielectric objects close to the sensor surface generate an impedance Z_{el} which causes a potential drop in the electrolyte, and the voltage at the electrolyte/channel interface $V_{G*,AC}$ that acts on the channel and determines the drain current.[270] For the impedance sensing we are interested in the AC response of the transistor and we express the AC current flowing in the OECT channel as $I_{ch,AC} = g_m \cdot V_{G*,AC}$. Following Bernards model,[225] g_m can be expressed as $g_m^{lin} = -\frac{W}{L}\mu c_v t V_{D,DC}$ and $g_m^{sat} = -\frac{W}{L}\mu c_v t (V_{G,DC} - V_t)$ in linear or saturation conditions. In these expressions, W, L and t indicate the width, length and thickness of the sensor channel, μ_p the holes mobility, c_v the volumetric capacitance of PEDOT:PSS and V_t the OECT threshold voltage.

To derive the overall AC current, it is important to note that in AC transport conditions the source (and drain) current signals are composed of two contributions:

$$I_{S,AC} = I_{ch,AC} + f_{OECT} \cdot I_{G,AC} \qquad (4.42)$$

The first ($I_{ch,AC}$) originates from the channel current, whereas the second ($I_{G,AC}$) is due to the gate current and regards the capacitive current that has increasing importance at higher frequencies. Its value is given by $I_{G,AC} = V_{G,AC}/Z_G$ in which $Z_G = Z_{el} + Z_{ch}$ is the overall impedance of the sensor given by the series combination of the electrolyte impedance Z_{el} and the impedance

related to the PEDOT:PSS channel capacitance $Z_{ch}=1/(i\omega C_{ch})$. The channel capacitance can further be related to the geometry and the volumetric capacitance of the PEDOT:PSS layer: $C_{ch}=c_v*t*W*L$. Possible contributions due to parasitic capacitances are neglected for simplicity. The factor f_{OECT} in **Eq. 4.42** determines how the gate current is distributed between the source and the drain terminal.[224] In general, the factor f_{OECT} depends on the bias conditions ($V_{D,DC}$ and $V_{G,DC}$), on channel geometry and on AC or DC measurement conditions.[363] In our case, we consider the AC transport regime where the gate current is a pure capacitive current without faradaic contributions. Further, in our biasing conditions ($V_{G,DC}$ = 0.1 V and $V_{D,DC}$ = -0.4 V) a significant negative potential is applied to the drain electrode leading to a depletion of holes from the channel region nearby the drain contact.[364] As a result, the capacitive gate current encounters a resistive barrier at the drain electrode and instead enters into the source electrode. For this reason, we set f_{OECT} =1 in our data analysis for each sensor geometry. The value is supported by numerical fitting procedures of our frequency dependent data leading to values close to one (see **sect. 4.5.11**).

The figure of merit of the OECT impedance sensor (the sensitivity s_{OECT}) quantifies its capability to transduce a variation of Z_{el} into a current output. This can be calculated from the model by differentiating **Eq. 4.42**:

$$s_{OECT} = \left|\frac{\partial(I_{ch,AC} + f_{OECT} I_{G,AC})}{\partial Z_{el}}\right| = \left|s_{ch} + f_{OECT} \cdot s_{\mu E}\right| \qquad (4.43)$$

After inserting the expressions for the two AC current contributions and differentiation we obtain for the channel sensitivity

$$s_{ch} = \frac{g_m}{Z_G}\left(1 - \frac{Z_{el}}{Z_G}\right) V_{G,AC} \qquad (4.44)$$

and the sensitivity of the microelectrode

$$s_{\mu E} = \frac{1}{Z_G^2} V_{G,AC} \qquad (4.45)$$

The explicit mathematical expressions relating the devices' sensitivity to the applied frequency are reported in **sect. 4.5.12**. The suitability of this simple approach to model the AC response of an OECT is demonstrated in **Figure 4.32b** and **c**. **Figure 4.32b** compares the frequency response of an OECT and of a microelectrode with the model predictions. The PEDOT:PSS channel width and length are W = 100 mm and L = 100 mm, respectively. The channel capacitance and the electrolyte resistance R_{el} were extracted for each device geometry by fitting the microelectrode impedance spectrum with an equivalent RC circuit. The average volumetric capacitance of PEDOT:PSS resulted to be c_v = 28 ± 2 F/cm^3 , obtaining a result consistent with literature findings.[23] The OECT device shows a significantly higher current in the low frequency domain. Here the electronic channel current I_{ch} prevails, and the transistor demonstrates clear amplifying properties. Then, above a cutoff frequency f_c = 625 Hz, the transistor response is limited by the slow ionic transport between the channel and the electrolyte.[365] At the same time the microelectrode's response increases with frequency until a current limitation is reached due to the electrolyte impedance. Therefore, in the high frequency limit both impedance sensor configurations yield the same current response. Importantly, the

cutoff frequency that determines the OECT amplification is determined by the channel geometry as demonstrated in **Figure 4.32c**. The plot of the current amplitude versus frequency for OECTs with different channel sizes clearly shows that with increasing channel area and length, a strong reduction in f_c is observed.

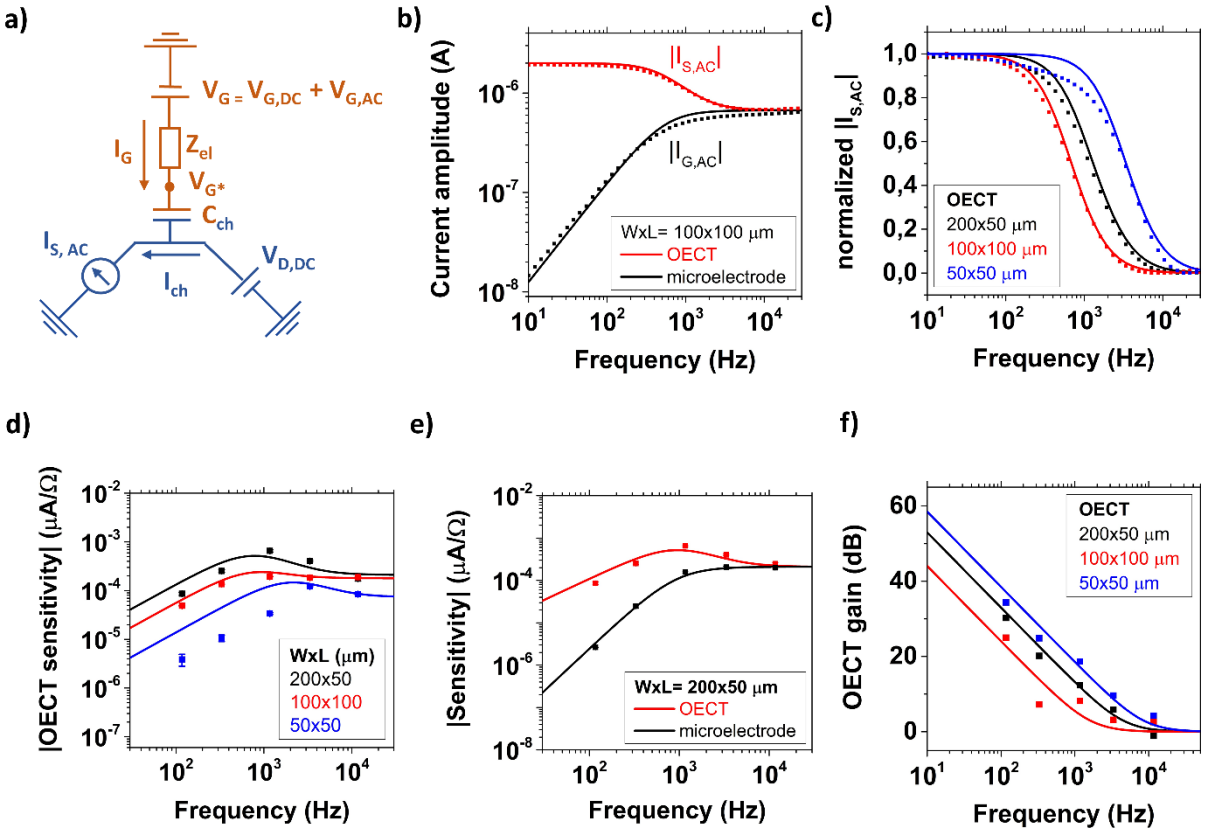

Figure 4.32: Quantitative model for PEDOT:PSS-based impedance sensors. **a)** Equivalent circuit of an OECT during impedance sensing. Orange and blue colors indicate ionic and electronic parts of the circuit, respectively. **b)** Modeling of the current frequency spectra of an OECT and a PEDOT:PSS microelectrode. **c)** Normalized OECT source current amplitudes as a function of the applied frequency for different channel geometries. **d)** OECT sensitivity during the microparticle impedance sensing experiment. The error bars are obtained by averaging between the approach and lift curves of the AFM experiment. **e)** Comparison between the sensitivity of an OECT and a microelectrode having the same dimensions. **f)** OECT gain for different channel geometries.

Finally, we systematically study the OECTs sensitivity towards electrolyte impedance changes with the microsphere experiment introduced above. **Figure 4.32d** shows the measured values for s_{OECT} obtained for three different channel geometries at different AC frequencies. **Eq. 4.43** is in excellent agreement with the frequency dependence of the measured data, allowing to resume the main findings of the model with the following statements. **(i)** In the low frequency regime, the OECT sensitivity shows a linear increase with frequency until it reaches a sensitivity maximum $s_{OECTmax}$. In this frequency range the sensitivity increases strongly with the channel aspect ratio W/L as it is highly controlled by the OECT transconductance. **(ii)** In the intermediate regime, OECT impedance-based sensors have a maximum sensitivity at a defined operation frequency, which corresponds to their low-pass cutoff f_c. The spectral

position of f_c (see **sect. 4.5.13**) is mainly determined by the channel area, which defines the channel capacitance C_{ch} and the electrolyte resistance R_{el}. Changes in the aspect ratio W/L modify the OECT transconductance and have a direct impact on the value of $s_{OECTmax}$. Accordingly, the frequency cutoffs of the 100x100 μm and the 200x50 μm structures are almost coincident, but the latter shows a higher sensitivity maximum. The smaller dimensions of the 50x50 μm device shift its f_c towards higher frequency, while $s_{OECTmax}$ is limited by the square aspect ratio. **(iii)** In the high frequency limit the OECT sensitivity results from the capacitive gate current and is mostly controlled by the area of the channel. This is also evident from **Figure 4.32e**, where we compare the sensitivity of a microelectrode and an OECT with the same dimensions (WxL = 200x50 μm). The transistor amplification, which is significant at low frequencies, has a relevant impact on the sensitivity. However, at high frequencies the response of both devices is limited by the electrolyte resistance and no significant differences are present. Such an observation is reflected by a frequency dependent OECT gain, which can be directly calculated with our model from **Eq. 4.43** and **Eq. 4.44**:

$$gain_{\,OECT} = 20 \cdot \log_{10}\left(\left|\frac{s_{OECT}}{s_{\mu E}}\right|\right) = 20 \cdot \log_{10}\left(\frac{g_m}{\omega C_{ch}} + f_{OECT}\right) \qquad (4.46)$$

The OECT gain is highest in the low-frequency regime, but is still significant in the 0.1-10 kHz range, where the impedance of the cell layers is typically measured.[272] This justifies the use of a transistor structure for high precision bioelectronic impedance sensing experiments.[275] **Figure 4.32f** demonstrates that the OECT gain is a geometry-dependent parameter. The smallest device (WxL = 50x50 μm) shows the highest gain, while a rectangular channel geometry is preferable for OECTs with the same area, since the transconductance increases with the W/L ratio while the channel capacitance remains constant.

4.5.3 Single cell impedance sensor experiment

We demonstrated the value of the mathematical model here proposed for the optimization of a PEDOT:PSS-based single cell impedance sensor by monitoring single cell adhesion and detachment in an *in-vitro* experiment, simultaneously measuring the impedance changes with both an OECT and a microelectrode. According to the model prediction and the AFM experiment, we patterned the device channels with a 200x50 μm rectangular geometry, which provides the best performances in terms of sensitivity. The T98G cell line cultured in Minimum Essential Medium was diluted to have a final density of 1 x 10^3 cells/cm^3 and poured on the surface of the impedance sensors (see **sect. 4.5.5** for full details). After seeding, the cells reached the underlying substrate by gravity. We microfabricated a linear array of 10 PEDOT:PSS channels (see **sect. 4.5.14**) to largely increase the probability of a single cell settling onto a sensor. An optical image of the final experimental configuration is reported in **Figure 4.33a**, showing a single T98G cell positioned at the center of the PEDOT:PSS channel. The encapsulation of the metallic electrodes with negative photoresist insulates the device from all the remaining cells which are not lying in the PEDOT:PSS active layer. We

acquired the current spectra of both the OECT and the microelectrode at consecutive time intervals to make a real-time detection of the cell adhesion process. To stress the full consistency of the measurements acquired with the OECT and the microelectrode, we plot in **Figure 4.33b** the current amplitudes measured at 625 Hz as a function of time. The sensing frequency was selected in correspondence to the OECT cutoff (measured at time t=0), where the model indicates the maximum sensitivity. The signals acquired at the beginning of the experiment are stable around a maximum value. Afterwards, at time t=20 min the current starts to decrease, indicating the beginning of the cell adhesion process. This produces a rapidly varying response until t=60 min, when the decrease becomes slower, and the current stabilizes around a minimum value. At t=200 min, we used a cell dissociation agent (trypsin) to completely remove the cell from the sample surface, and devices recovered their original current amplitude.

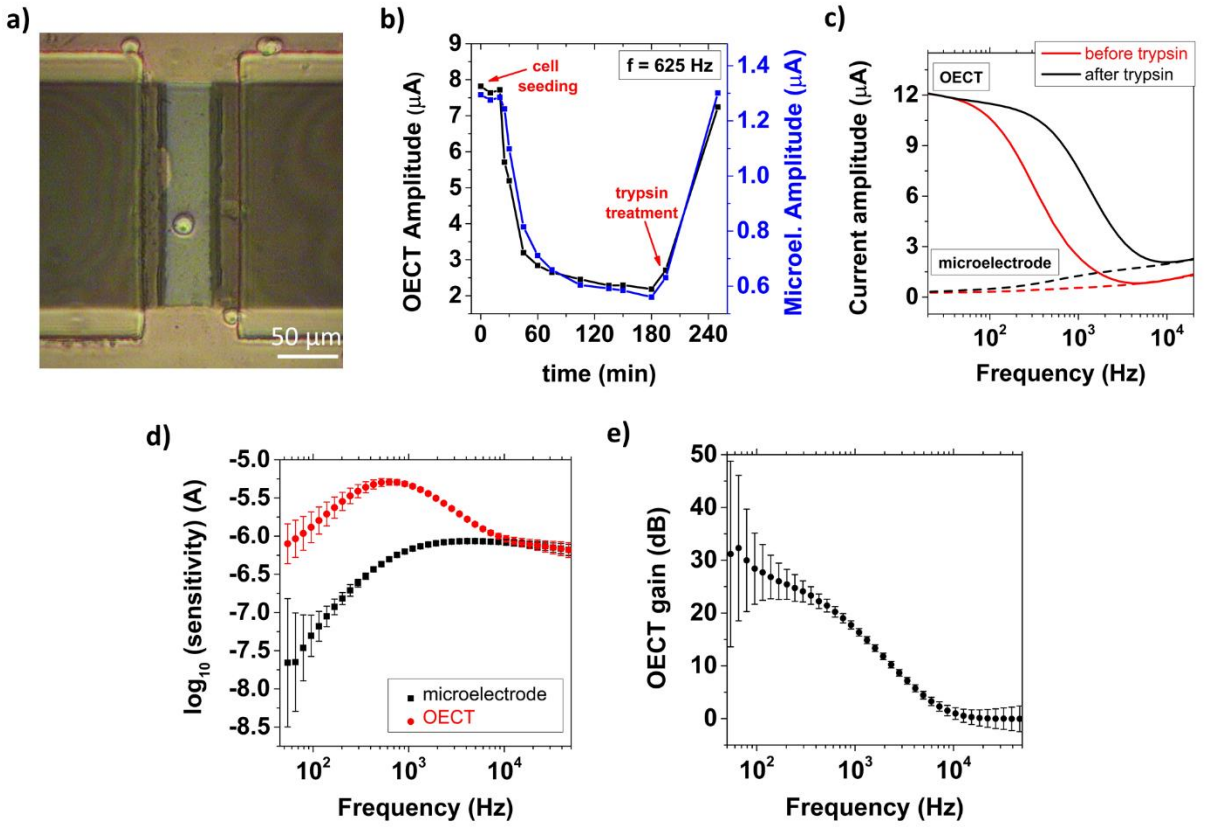

Figure 4.33: Single cell impedance sensor experiment. **a)** Optical image acquired after seeding a single cell at the center of a PEDOT:PSS sensing channel. **b)** Time evolution of the cell adhesion monitored with an OECT and a microelectrode. **c)** Current spectra acquired in the OECT (straight line) and microelectrode (dashed line) configuration before and after trypsinization. **d)** Experimental OECT and microelectrode sensitivity. Error bars are obtained by averaging between n=4 measurements acquired at different time. **e)** Experimental OECT gain. Error bars are calculated from the experimental sensitivities by applying Eq. 1.46.

We report in **Figure 4.33c** the full current spectra acquired before and after the treatment with trypsin (t=180 min and t=240 min, respectively). The cell adhesion produced a large shift of the OECT low-pass cutoff towards smaller frequency. In parallel, the current spectrum of a

control device placed in the same reservoir, but with no cell seeded on the PEDOT:PSS layer, remained unaltered (see **sect. 4.5.15**). After trypsinization, the initial cutoff frequency is fully recovered. These combined observations clearly demonstrate that the cutoff shift is only caused by the single cell adhesion on the PEDOT:PSS layer. The same considerations can be extended to the PEDOT:PSS microelectrode. Here, the cell adhesion process is revealed by a decrease in the gate current amplitude, which reaches its minimum at t=180 min, coherently with the OECT measurements. After the cell detachment (t=240 min), the current increases to its original values.

To provide a direct comparison between the sensing performances, we averaged the current amplitudes acquired when the cell is detached (t<30 min and t=240 min) and attached (120<t<180 min), and we subtracted the resulting values to calculate the experimental sensitivity for both devices. Repeating this analysis in the whole frequency spectrum, we obtained the curves reported in **Figure 4.33d**, that confirm the results of the quantitative AFM experiments (**Figure 4.32e**). The transistor amplification has a significative impact on the device sensitivity in the frequency range between 10^2 and 10^4 Hz, with a peak at 625 Hz, corresponding to the OECT cutoff. On the other hand, when the modulation frequency is high, the OECT transconductance becomes negligible, and the transistor structure does not offer substantial advantages with respect to a microelectrode. The OECT gain (**Figure 4.33e**) was calculated by applying **Eq. 4.46** and reaches a value of 20.2±0.9 dB at the highest sensitivity point (625 Hz).

The frequency response of the OECT gain is well described by our model for both experiments, the single cell as well as the dielectric particle detection. However, the OECT current amplitude reduction is much larger for the case of the single cell even though the cell body has a diameter that is smaller than the dielectric particle. The effect is attributed to the much larger impedance increase caused by the cell adhering to the sensor surface. Glioblastoma tumor cells such as T98G secrete large amounts of laminin and glycoproteins to self-assemble the basement membrane below their cellular body.[366] We hypothesize that the basement membrane spreads below the cell body on top of the PEDOT:PSS channel and acts as a barrier increasing significantly the impedance. Trypsin treatment removes the cell body and dissolves also the basement membrane, making the effect reversible.

4.5.4 Discussion and conclusions

In this chapter, I introduced a quantitative analysis of the performance of OECTs as single cell impedance sensors. We developed a model experiment where we simulate the detection of a single cell by the impedance sensing of a dielectric microparticle. The microparticle is attached to an AFM cantilever to have a refined control of its positioning on the sensor surface. By approaching and retracting the microparticle from the sensor surface, we ensure a controlled impedance change that permits to quantify the sensitivity of the impedance sensor. With the model experiment we can compare in a reproducible manner the sensitivity of different OECT or microelectrode-based sensors. To rationalize the experimentally determined

sensitivities, we develop a mathematical model. The model correctly predicts the dependence of the sensitivity on frequency, sensor geometry and semiconductor materials properties such as carrier mobility and volumetric capacitance. From these findings, we derive two major conclusions for OECT based impedance sensors**: i)** depending on geometry and semiconductor materials properties, the sensitivity has a maximum at a defined operation frequency; **ii)** the OECT based sensor has a significant gain with respect to a simpler microelectrode-based sensor. The gain increases towards lower frequencies due to the increased contribution of the transistor channel current. Instead, towards very high frequencies the microelectrode approaches the OECT performance as the overall current is dominated by the ionic gate current. Smaller OECT channel geometries shift this transition to higher frequencies, thus achieving larger gain.

Based on the model findings, we develop optimized sensors to perform *in-vitro* single cell detection experiment. We find that both the PEDOT:PSS microelectrode and the OECT can monitor the cell adhesion process and recover their original performances after the cell detachment with trypsin. However, in the OECT the single cell adhesion transient is measured with a current signal gain of (20.2±0.9) dB at 625 Hz, in close agreement with the model prediction. Such an improvement is significant and facilitates measurement conditions regarding noise pickup and digitization, making OECT amplified impedance sensors a powerful tool for a new era of cell-substrate adhesion experiments with a single cell resolution.[275]

Importantly, our quantitative approach to compare bioelectronic impedance sensors is not limited to PEDOT:PSS based OECTs but can easily be extended to different electrolyte gated transistor architectures. The crucial parameter that describes the different material properties in our model is the channel transconductance. Large transconductances have been demonstrated for different channel materials and device architectures. They result from high capacitive couplings, as observed in organic mixed ionic and electronic conductors (e. g. PEDOT:PSS) or high carrier mobilities as found for example in graphene or carbon nanotubes.[367,368] Current research in the material properties of such water stable semiconductors warrants further improvements in mobility or volumetric capacitance and will also augment the sensitivity of bioelectronic impedance sensors.[270] Our quantitative approach can serve as a guideline for the development of impedance sensors with maximized sensitivity and establishes a metric to compare future devices.

4.5.5 Appendix 1: details on experimental methods

Microparticle sensing experiment: To fabricate the AFM probe supporting the dielectric microparticle, we dispersed a powder of pyrophosphate microspheres (from Polymat) on a glass slide. A PPP-NCHR cantilever of the Park NX10 AFM (force constant 34.55 N/m) was approached onto a drop of glue, and then put in contact with the upper part of a microsphere (with diameter of about 50 µm) until complete adhesion.

AFM measurements were performed in liquid, using 0.1 m PBS as electrolyte and an Ag/AgCl wire as gate electrode. To measure the current-distance spectroscopies, we placed the

microparticle in the center of the PEDOT:PSS channel of the impedance sensor and we performed an AFM force-distance spectroscopy. The probe was lifted to the vertical coordinate z_0, distant 5µm from the contact position, then gradually approached to the sample surface (scan speed 0.3 µm/s), and finally retracted again to z_0. During this process, we applied a constant modulation frequency to the gate terminal, and we measured the current amplitude flowing in the PEDOT:PSS layer (using the setup in **sect. 3.4.2**), obtaining a current-distance spectroscopy curve. The experiment was repeated at 5 different frequencies (117, 330, 1170, 3330, and 11700 Hz) both in the OECT and in the microelectrode configurations.

Single cell detection experiment: The human malignant glioma cell line, T98G (CRL-1690™), derived from a glioblastoma multiform tumor, was selected for the single cell detection experiment. This is characterized by indefinite lifespan and adherence properties previously reported also on PEDOT:PSS layers.[369] It was purchased from ATCC (Manassas, VA, USA) and cultured in Minimum Essential Medium (MEM) (Gibco™ 51200046, ThermoFisher scientific), supplemented with 10% fetal bovine serum, 1% L-glutamine, 10% sodium pyruvate and antibiotics (1% penicillin and 1% streptomycin) at 37 °C in 5% CO_2 incubator. All chemicals were from Merck. The experimental day, the sub-confluent (70-80%) cells population was detached by 0.25 % trypsin in 0.02 % EDTA (both from Merck) solution, re-suspended in fresh supplemented MEM and counted by the hemocytometric chamber. An aliquot, calculated to have a final density of 1 x 10^3 cells/cm^3 was diluted in 600 µL of supplemented MEM and poured on the surface of the impedance sensors, previously sterilized by 20 min of UV exposure. A polydimethylsiloxane (PDMS) well was attached onto the sample substrate to host both the solution containing the cells and the Ag/AgCl gate electrode. After seeding, the cells reached the underlying substrate by gravity. For the experiment, we microfabricated a linear array of 10 PEDOT:PSS channels with dimensions WxL=200x50 µm (an optical image is reported in **sect. 4.5.14**). In this way, the probability of a single cell falling onto a device channel after seeding was largely increased. Once this configuration was achieved, the sample was connected for the electrical measurements. The current spectra of the impedance sensor were acquired both in the OECT and the microelectrode configurations every 10 minutes after cell seeding. During each acquisition, the modulation frequency applied at the gate terminal was swept between 10 and 10^5 Hz. At time t = 200 min, trypsin was used to completely remove the cells from the sample surface. Biological residuals were rinsed with PBS, and a final current spectrum was acquired in MEM to measure the sensor response after the cell detachment.

4.5.6 Appendix 2: DC transfer characteristics of OECTs with different channel geometries

We acquired the OECT transfer characteristics of the three channel geometries studied in the microparticle sensing experiment. Both the DC drain and gate (leakage) currents were monitored. An Ag/AgCl wire was used as gate electrode in PBS solution.

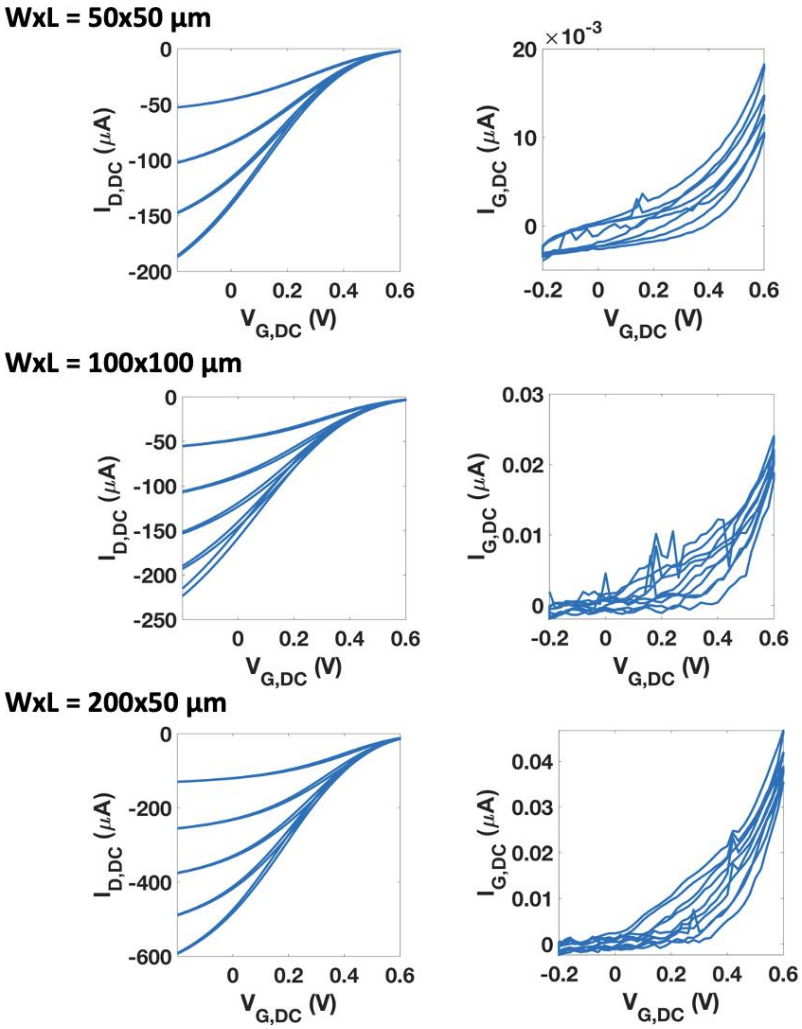

Figure 4.34: DC transfer characteristics of OECTs with different channel geometries. The gate voltage was scanned between -0.2 and 0.6 V during each acquisition. The drain voltage was varied from -0.1 to -0.5 V, with steps of -0.1 V between two consecutive acquisitions.

4.5.7 Appendix 3: setting the OECT working point for impedance sensing

During impedance sensing measurements, the OECTs were biased with the DC gate and drain voltages at which their transconductance $g_{m,DC}$ takes its maximum value (the *working point*). We plot in **Figure 4.35** the DC trans-characteristic and transconductance curves of a WxL= 100x100 µm sensor. The latter were obtained by direct differentiation of the former and show a transconductance peak which increases with the absolute value of the applied DC drain voltage. The working point was set in correspondence of one of these maxima, choosing a configuration with both a reasonably high transconductance and low potential operation to limit material degradation and power consumption.

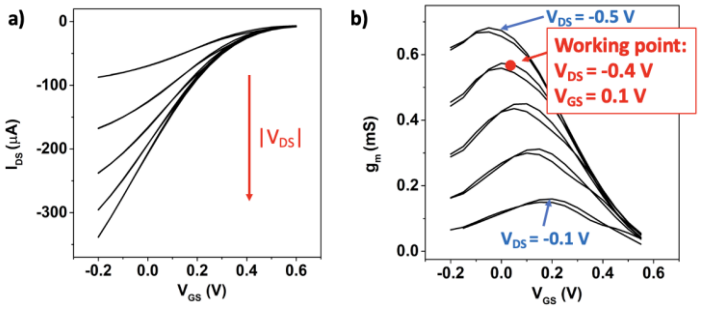

Figure 4.35: setting the OECT working point for impedance sensing. **a)** Transfer characteristic of an OECT sensor and **b)** DC transconductance curves indicating the working point set for impedance sensing.

4.5.8 Appendix 4: measuring the microparticle displacement

The presence of the dielectric microparticle in close contact to the sensor surface hinders the ionic flow from the electrolyte into the sensing channel and thus increases the electrolyte impedance. This is widely observed in our experiment and reproduces in first approximation the basic working principle of impedance-based cell sensors. A qualitative demonstration of this observation is furtherly provided in the reported experiment (**Figure 4.36a**), where we measured the source current amplitude while gradually increasing the microparticle-channel distance *d* starting from the contact position.

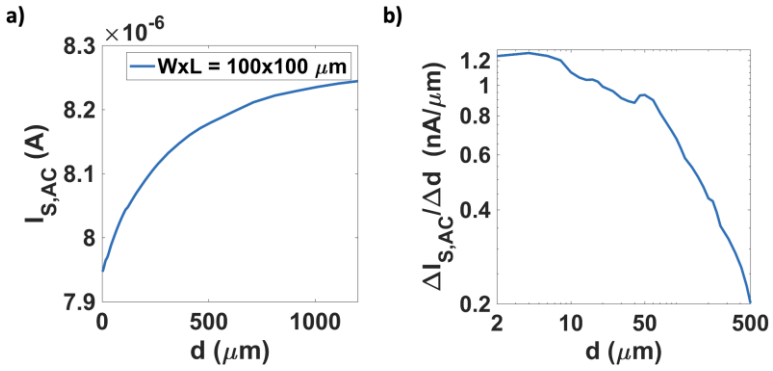

Figure 4.36: Measuring the microparticle displacement. **a)** Current amplitude variation in an OECT sensor (biased at its working point) when the microparticle is lifted from the contact position. The modulation frequency applied to the gate electrode is 1.17 kHz. **b)** OECT current variation per 1 μm-step as a function of the microparticle-channel distance d.

The microparticle displacement produces larger effect on the sensor response when the AFM probe is retracted for short distances from the contact position. At the same time, both the cantilever and the AFM stage changes the geometry of the liquid electrolyte and reasonably modify the electrolyte resistance R_{el}. Anyway, given the large diameter of the dielectric microparticle (50 μm) and the small displacement of the z-stage during the sensing experiment (5 μm), we expect that only the bottom part of the dielectric microparticle has an active role in

modifying the ionic current flow, simulating in first order approximation a biological cell which adheres to the sensor surface. This is highlighted in **Figure 4.36b**, where we report the OECT current variation per 1 μm-step as a function of *d*. We observe that larger effects are produced when the AFM probe is retracted for short distances from the contact position, indicating that the microparticle hindrance has a primary role in blocking the ionic flow from the electrolyte to the sensor channel.

4.5.9 Appendix 5: normalized microparticle distance - AC current measurements

We report in **Figure 4.37** the normalized microparticle distance-AC current measurement shown in absolute value in **Figure 4.31f**. The steepest line acquired with the OECT configuration results from its amplification gain, that increases the level of the measured signal. Naturally, also noise present in the signal will be amplified. Such intrinsic noise sources include thermal noise effects and shot noise effect due to the impedance of the measured system and noise effects due to the living activities of the cell. Accordingly, the OECT cannot improve on the signal to noise ratio when the noise level is only determined by these intrinsic factors. The role of gain in improving signal to noise ratio becomes important when noise is introduced by the data acquisition system. In our case such noise is minimized in both cases (microelectrode and OECT) due to the use of very sophisticated signal conditioning circuits. For this reason, both signal traces in **Figure 4.31f** have a comparable signal to noise ratio. We note that in a realistic application scenario, microelectrode impedance recordings would be deteriorated due to a limited digital resolution.

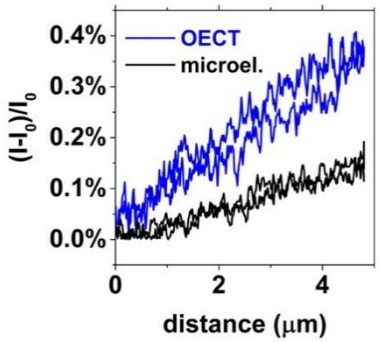

Figure 4.37: normalized microparticle distance - AC current measurements. Comparison between normalized microparticle distance - AC current measurements acquired in the OECT and microelectrode configurations. The absolute data are shown in **Figure 4.31f**.

4.5.10 Appendix 6: impedance analysis of the sensors and extraction of the $R_{el}(d)$ curve in the microparticle sensing experiment

We report in **Figure 4.38a** and **b** the impedance and the phase spectra of the PEDOT:PSS channels used in the experiments (acquired in the microelectrode configuration). Measurements were fitted with an equivalent RC circuit to extract the electrolyte resistance and the channel capacitance. Fit results are shown in **sect. 4.5.11**, where we report the whole set of parameters used in the quantitative model. By neglecting polarization effects on the microparticle surface, a change in the relative position between the microparticle and the sensing channel in the AFM experiment only causes a change in the electrolyte resistance. Therefore, $Z_{el}(d) = R_{el}(d)$. The experimental current-distance spectroscopies (**Figure 4.31f**) can be fitted with a linear model to extract the slope $\alpha = \partial I_{AC}/\partial d$. This can be related to the device sensitivity as $\partial I/\partial R_{el} = \partial I/\partial d \times \partial d/\partial R$. The coefficient $p = \partial R/\partial d$ is universal and does not change as a function of frequency or transistor or microelectrode parameters for each channel geometry. To determine its value, we measured the gate impedance $Z_G(d)$ in the microelectrode configuration at high modulation frequency (11.7 kHz). In such a condition, the impedance of the channel capacitance $Z_{ch}=1/(i\omega C_{ch})$ is negligible, and only the $R_{el}(d)$ curve is consequently measured. This is confirmed by the phase of the acquired signals (see inset in **Figure 4.38b**), which assumes values close to zero in that frequency regime. We report in **Figure 4.38c** the $R_{el}(d)$ curve obtained for the 50x50 µm structure. Measurements indicate a linear relation between the two quantities ($R_{el}(d) = d \times p + R_0$) for all channel geometries , allowing for a straightforward extraction of the p parameter. The obtained results are p =19.4±0.1 Ω/µm for the 50x50 µm geometry, p =14.4±0.1 Ω/µm for the 100x100 µm geometry, and p= 44.3±0.1 Ω/µm for the 200x50 µm geometry.

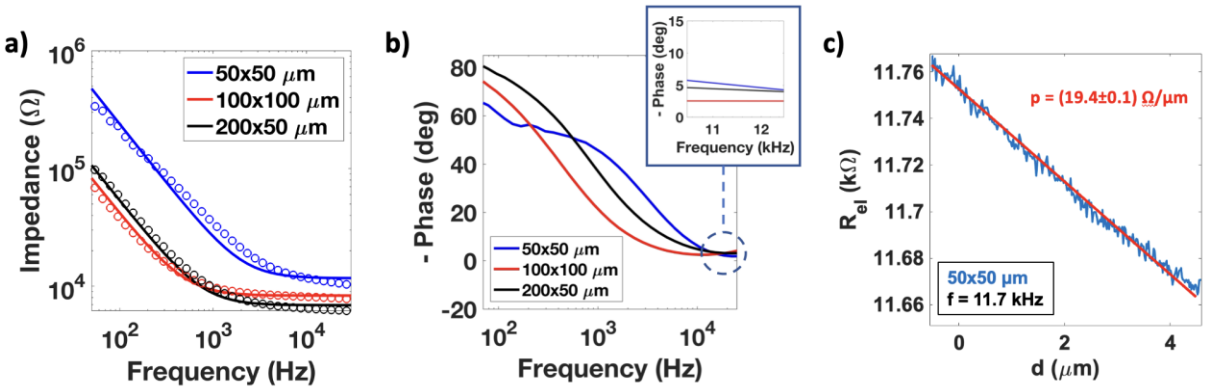

Figure 4.38: Impedance analysis of the sensors and extraction of the $R_{el}(d)$ curve in the microparticle sensing experiment. Impedance (a) and phase (b) spectra acquired for the different channel geometries. c) $R_{el}(d)$ curve extracted from an AFM current-distance experiment. The linear fit (R^2 = 0.996) allows for the extraction of the slope p.

4.5.11 Appendix 7: parameters used in the quantitative model for PEDOT:PSS-based impedance sensors

We report in the following table the full set of parameters used to best fit the experimental data with the quantitative model for PEDOT:PSS-based impedance sensors. The channel capacitance C_{ch} and the electrolyte resistance R_{el} were extracted by fitting the electrochemical impedance spectroscopies with a RC series circuit model. The OECT transconductance g_m was calculated from the DC transfer characteristics.

Channel aspect ratio WxL (µm)	C_{ch} (nF)	R_{el} (kΩ)	g_m (mS)
50x50	6.69	12.3	0.33
100x100	27.5	7.47	0.33
200x50	30.5	6.90	0.70

Table 4.5: Full list of parameters used in the model for PEDOT:PSS-based impedance sensors.

4.5.12 Appendix 8: mathematical treatment for the OECT impedance sensor

As expressed by **Eq. 4.43**, the OECT sensitivity is obtained by the sum of the microelectrode and the channel sensitivity, s_{ch} and $s_{\mu E}$, respectively. The sensitivities are defined as the derivative of the AC current with respect to the cell induced changes in electrolyte impedance: $s_{ch} = \frac{\partial I_{ch,AC}}{\partial Z_{el}}$ and $s_{\mu E} = \frac{\partial I_{G,AC}}{\partial Z_{el}}$. We first consider the AC current contribution generated in the OECT channel.

$$I_{ch,AC} = g_m V^*_{G,AC} \qquad (4.47)$$

Following the equivalent circuit in **Figure 4.32a** we can substitute the effective gate voltage $V^*_{G,AC}$ by

$$V^*_{G,AC} = V_{G,AC} - I_{G,AC} Z_{el} \qquad (4.48)$$

and

$$I_{G,AC} = \frac{V_{G,AC}}{Z_{el} + Z_{ch}} \qquad (4.49)$$

Combining **Eq. 4.47**, **Eq. 4.48**, and **Eq. 4.49** and taking the derivative yields **Eq. 4.43**.
Similar for $s_{\mu E}$ we use **Eq. 4.49** and take the derivative to obtain **Eq. 4.44**.
Next, we introduce the explicit frequency dependence of **Eq. 4.43** and **Eq. 4.44**. To do so, we must introduce the explicit expression for the impedance $Z_G = Z_{el} + Z_{ch}$ with $Z_{ch} = \frac{1}{i\omega C_{ch}}$. The channel transconductance g_m and the electrolyte impedance Z_{el} do not depend on frequency.

$$s_{\mu E} = \frac{V_{G,AC}}{{Z_G}^2} = \frac{V_{G,AC}}{(Z_{el} + Z_{ch})^2} = \frac{V_{G,AC}}{\left(Z_{el} + \frac{1}{i\omega C_{ch}}\right)^2} \qquad (4.50)$$

$$s_{ch} = \frac{g_{m,AC}}{Z_G}\left(1 - \frac{Z_{el}}{Z_G}\right)V_{G,AC} = \frac{g_{m,AC}}{Z_{ch}\left(\frac{Z_{el}}{Z_{ch}} + 1\right)^2}V_{G,AC} = \frac{i\omega C_{ch} g_{m,AC} V_{G,AC}}{(i\omega C_{ch} Z_{el} + 1)^2} \qquad (4.51)$$

We note that **Eq. 4.50** and **Eq. 4.51** can be fully expressed in terms of device geometry (channel width *W*, channel length *L* and film thickness *t*) and materials parameters (mobility μ, threshold voltage V_{th} and volumetric capacitance c_v). To achieve a direct dependence on these parameters we introduce (i) the equation for the transconductance g_m in linear or saturation regime as written in the main manuscript and (ii) we express the channel capacitance by $C_{ch} = c_v tWL$. Also, for the electrolyte impedance one can derive an analytical expression that contains the channel area and the electrolyte resistance by assuming that the perturbation due to the cell is small. For example, for a square micro-channel one obtains: $Z_{ch} = \frac{\rho \cdot \ln 4}{\pi \cdot L}$ with being the electrolyte resistivity.[370]

Similar we can derive the explicit frequency dependence of the gain of the OECT impedance sensor:

$$gain_{\,OECT} = 20 \cdot \log_{10}\left(\left|\frac{s_{OECT}}{s_{\mu E}}\right|\right) = 20 \cdot \log_{10}\left(\frac{g_m}{\omega C_{ch}} + f_{OECT}\right) \qquad (4.52)$$

4.5.13 Appendix 9: OECT cutoff and maximum sensitivity

OECTs working in AC operation exhibit low pass filtering properties, thereby the cutoff frequency f_c can be calculated from $\left|\frac{I_{S,AC}(f_c)}{I_0}\right| = \frac{\sqrt{2}}{2} \approx 70\%$. From **Eq. 4.42**, $I_{S,AC} = g_m \cdot V_{G,AC}\left(1 - \frac{Z_{el}}{Z_G}\right) + f_{OECT} \cdot \frac{V_{G,AC}}{Z_G}$, while I_0 can be obtained from the low-frequency limit as $I_0 = g_m * V_{G,AC}$.

In the microparticle sensing experiment, the electrolyte impedance $Z_{el} \approx R_{el}$ is a real number, allowing for a straightforward expression for the cutoff frequency:

$$f_c = \frac{1}{2\pi C_{ch}} \frac{g_m}{\sqrt{{g_m}^2 \cdot {R_{el}}^2 - 2 \cdot {f_{OECT}}^2}} \qquad (4.53)$$

It is worth highlighting that f_c corresponds to the frequency at which an OECT-based impedance sensor reaches its maximum sensitivity. This can be demonstrated by considering **Eq. 4.43** and setting stationary point conditions: $\frac{\partial s_{OECT}}{\partial f} = \frac{\partial}{\partial f}\left|\frac{g_m}{Z_G} \cdot \left(1 - \frac{Z_{el}}{Z_G}\right)V_{G,AC} + \frac{f_{OECT} \cdot V_{G,AC}}{{Z_G}^2}\right| = 0$

The resulting expression for ${s_{OECT}}^{max}$ is

$${s_{OECT}}^{max} = \frac{V_{G,AC} \cdot {g_m}^2}{2 \cdot {g_m}^2 {R_{el}}^2 - 2} \sqrt{{g_m}^2 \cdot {R_{el}}^2 - 2 + {f_{OECT}}^2} \qquad (4.54)$$

4.5.14 Appendix 10: device for single cell detection experiment

For the single cell detection experiment we microfabricated a linear array of 10 PEDOT:PSS channels with dimensions WxL=200x50 µm. In this way, we largely increased the probability that a single cell reached a single PEDOT:PSS channel by gravity after seeding. We report in **Figure 4.39a** an optical image of the device. A PDMS well is attached onto the sample substrate to host both the solution containing the cells and the Ag/AgCl gate electrode. Magnified images of the channel array and of a single channel are provided in Supplementary **Figure 4.39b** and **Figure 4.39c**, respectively.

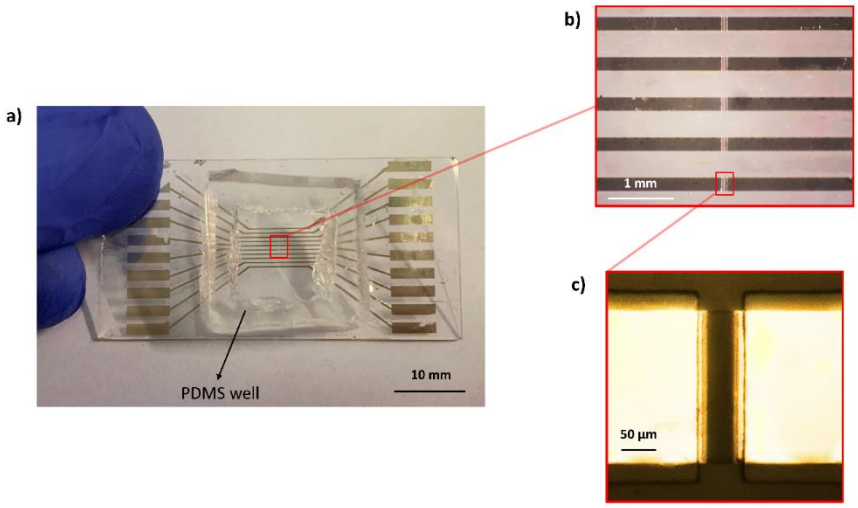

Figure 4.39: Device for single cell detection experiment. **a)** Optical image of the device used in the single cell detection experiment. 10 PEDOT:PSS channels are vertically aligned to increase the probability to find a single cell placed on a single channel after seeding. **b)** Insight on 5 PEDOT:PSS channels composing the linear array. Each one was patterned with a WxL = 200x50 µm geometry **(c)**.

4.5.15 Appendix 11: control of the single cell detection experiment

During the single-cell detection experiment, the OECT-based impedance sensors showed a significative shift in the low-pass cutoff, which was recovered only after the treatment with trypsin. To demonstrate that such effect was caused by the cell adhesion process and not by other effects in the experimental setup (sensor degradation/contamination of the cell culture medium), we acquired the current spectrum of a control device (with the same dimensions and operating parameters) placed in the same reservoir, but with no cell seeded on the sensing channel. Results are reported in **Figure 4.40a**, showing that the current spectrum of the control device remains unaltered during the experiment. After treatment with trypsin sensors recover their original current spectrum (see **Figure 4.33b** and **c**), and a final DC transfer acquired after the removal of the biological residuals with PBS demonstrates the correct working behavior of the OECT (**Figure 4.40b**).

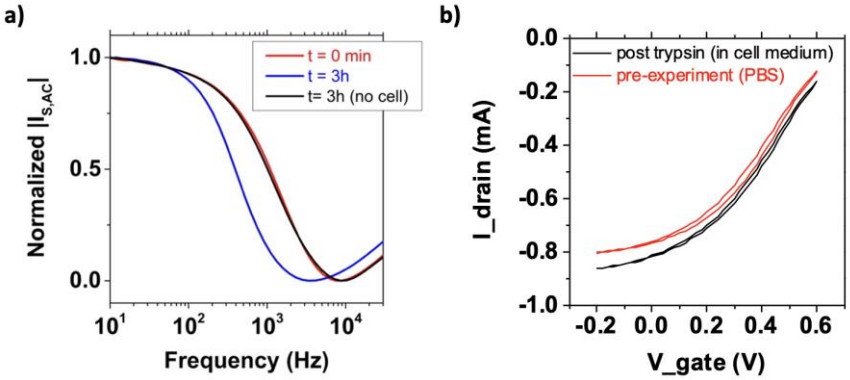

Figure 4.40: Control of the single cell detection experiment. **a)** the adhesion of a single cell produces a visible shift in the low pass cutoff of the OECT sensor (red and blue lines), while the frequency response of a control device (black line) remains unaltered. **b)** OECT DC transfer characteristics acquired before the experiment (red line) and after trypsinization (black line). Measurements are acquired in different electrolytes but confirm the correct behavior of the device after removal of the cell residuals.

5 Conclusions

This thesis work focused on the study of organic mixed ionic-electronic conductors (OMIECs) for bioelectronic interfaces. The research project is divided into two main parts overall. In the first part, I investigated fundamental processes in OMIECs, aiming to a quantitative understanding of the charge transport properties and their correlation with material functionality. In the second part, I studied applications of OMIEC materials in bioelectronic devices, including low-impedance electrodes for *in-vivo* neural interfaces and *in-vitro* biosensors reaching the single-cell resolution limit. This work required different experimental activities, ranging from the design and microfabrication of micro-structured devices to electrical and electrochemical analyses, including the development of novel operando characterization techniques for organic mixed conductors. These activities were carried out at the Department of Physics and Astronomy of the University of Bologna, at the Department of Biomedical and Neuromotor Sciences of the University of Bologna, and at the Electrical Engineering Department of the University of Cambridge (UK).

Research interest in OMIEC materials is motivated by the possibility to combine electronic semiconductor functionality with ionic conductivity, biocompatibility, and electrochemical stability in water. Progress on all fronts is predicated on an advance in understanding fundamental material processes, but the mixed conductivity renders the experimental characterization of individual ionic or electronic carrier transport difficult as both are intrinsically entangled and can lead to the screening of electric fields or introduce local contact resistances. To address the problem, I introduced in this work the electrolyte-gated van der Pauw (EgVDP) method for the determination of the electrical characteristics of OMIEC thin films, independent of contact effects. This technique is applied for the first time to the most widespread OMIEC formulation, poly(3,4-ethylenedioxythiophene) doped with poly(styrenesulfonic acid) (PEDOT:PSS) for the simple and accurate extraction of the hole mobility and threshold voltage, representing important figures of merit for electronic transport in the blend. Measurements repeated on three different EgVDP devices obtained highly reproducible results. The average PEDOT:PSS mobility and threshold voltage were found to be $\langle \mu_p \rangle$ = (11.7±0.3) $cm^2V^{-1}s^{-1}$ and $\langle V_t \rangle$ = (0.44±0.02) V. By comparing with organic electrochemical transistor (OECT) measurements, we found that gate voltage dependent contact resistance effects lead to systematic mobility underestimation in OECT based transport characterization. These observations confirmed that a contact-independent technique is crucial for the proper characterization of OMIECs, and the EgVDP method reveals to be a simple, elegant, but effective technique for this scope. Given its general applicability and good accuracy, our experimental approach can be a useful tool to characterize electronic transport in novel OMIEC formulations.

Ionic transport in OMIEC layers operating at liquid interfaces was studied investigating the mechanical deformations resulting from charge injection. The electrically-driven swelling of the soft polymeric matrix induces mechanical deformation enabling artificial muscle-like

actuators, but also leads to degradation processes affecting OMIEC based devices. Despite its relevance in different fields of material research, fundamental knowledge on the intrinsic mechanism of electroswelling is still lacking, and monitoring fast local ionic exchange processes in OMIECs remains elusive. To provide a microscopic understanding of electroactuation, I introduced in this thesis the modulated electrochemical atomic force microscopy (mEC-AFM) as a novel characterization method for electroactive materials. The combination of the electroswelling data with electrochemical impedance spectroscopy in PEDOT:PSS microelectrodes yielded a multidimensional spectroscopy revealing the dominant timescales for ion migration and electroswelling. The resulting knowledge allowed us to implement multichannel mEC-AFM imaging, providing maps of local electroswelling amplitude and phase as well as surface morphology. Results proved that the amplitude and timescales of electroswelling are governed by the drift motion of hydrated ions. Accordingly, we demonstrated how fast ionic charging of the PEDOT:PSS volumetric capacitance leads to high frequency operation in microactuators, and how the swelling extent is intrinsically limited by the radius $<r_{ion}>$ = 0.18±0.02 nm of the cation solvent shell.

mEC-AFM experiments were then performed to characterize organic mixed conductors optimized for actuation, such as polypyrrole doped with dodecylbenzenesulfonate (Ppy:DBS). This material showed a more complex electroactuation dynamics which required subsurface investigations for its comprehension. For this reason, we extended mEC-AFM as a depth-sensitive technique to measure subsurface profiles of ion migration and swelling in Ppy:DBS electroactive layers. We interpreted charge accumulation in the polymeric matrix with a quantitative model, giving access to both the spatiotemporal dynamics of ion migration and the distribution of electroswelling in the electroactive polymer layer region. The resulting subsurface maps demonstrated a non-uniform distribution of the effective ionic volume in the Ppy:DBS layer depending on the film morphology and redox state. Our findings indicated that the highly efficient actuation performance of Ppy:DBS is caused by rearrangements of the polymer microstructure induced by charge accumulation in the soft polymeric matrix, increasing the effective ionic volume in the electroactive film bulk up to two times the value measured in free water. The obtained results also how mEC-AFM offers novel means to interrogate materials with mixed ionic-electronic conductivity at the nanoscale during operation, providing information on the local ionic distribution and the ion-to-electron coupling. This capability will be critical to understand more complex OMIEC-based realizations such as organic electronic ion pumps or organic electrochemical transistors. At the same time, subsurface mEC-AFM characterizations are expected to clarify mechanisms responsible for poor electrochemical cycling of energy storage devices operating in electrolytes like batteries and supercapacitors, leading to an extension of their application lifetime.

The knowledge resulting from OMIEC transport characterization constituted a conceptual basis to develop OMIEC applications. In this contest, I realized and characterized microelectrode arrays (MEAs) based on PEDOT:PSS for *in-vivo* electrocorticography (ECoG) experiments. Microfabrication techniques were extended to flexible substrates to realize miniaturized devices conformable with the brain surface and with high spatial and temporal resolution. We tested the electrode arrays in an *in-vitro* setup combining electrochemical impedance spectroscopy (EIS),

analysis of the electrode polarization during simulated stimulation protocols, and atomic force microscopy (AFM) characterization of the PEDOT:PSS coating on the electrode surface. Results demonstrate the low-impedance recording properties (Z = 1.7±0.8 kΩ at 1 kHz, with electrode diameter 200 µm) and the linear charge injection of the neural probe. Both properties are a consequence of the large capacitance of PEDOT:PSS electrode coatings resulting from the volumetric mixed conduction. The characterization of the bending properties of the electrode array highlights the device stability against mechanical deformation. These promising device properties are currently exploited in *in-vivo* recording and stimulation experiments ongoing in our group. Such experiments aim to investigate the neural activity of animal models at different temperatures. The resulting findings are expected to contribute to the study of neural connectivity and consciousness in torpor and hibernation states.

OMIEC materials were finally studied *in-vitro* experiments measuring cellular adhesion properties. Recent advancements in organic electrochemical transistor (OECT) research have led to impedance sensors reaching single cell resolution, but a quantitative study on the transistor amplification gain is still lacking. To overcome the issue, I introduced a model experiment where a single cell was simulated by a dielectric microparticle of similar dimensions. We controlled the position of the microparticle on top of the microscale impedance sensors with an AFM and achieved highly reproducible measurements comparing the current output of OECT-based sensors with equivalent microelectrode sensors. Experimental data were interpreted with a mathematical model which correctly predicts the dependence of the sensitivity on frequency, sensor geometry and semiconductor materials properties such as carrier mobility and volumetric capacitance. From these findings, we derived two major conclusions for OECT based impedance sensors**: i)** depending on geometry and semiconductor materials properties, the sensitivity has a maximum at a defined operation frequency; **ii)** the OECT based sensor has a significant gain with respect to a simpler microelectrode-based sensor. Following these predictions, we designed an optimized device to measure the transients of single cell adhesion and detachment in *in-vitro* experiments, observing a significant AC gain reaching values of (20.2±0.9) dB for the transistor structure. Our quantitative approach to compare bioelectronic impedance sensors is not limited to PEDOT:PSS based OECTs but can easily be extended to different electrolyte gated transistor architectures. Results can serve as a guideline for the development of impedance sensors with maximized sensitivity and establish a metric to compare future devices.

This thesis provides a further step forward in the ongoing research of organic mixed ionic-electronic conductors for bioelectronics interfaces. The experimental work was motivated by the belief that substantial advancements in the field can be achieved only through a quantitative understanding of the charge transport properties of OMIEC materials and their interplay with device operation. For this reason, we introduced novel characterization techniques to investigate mixed transport and material functionalities during operation. Experimental results were interpreted though the development of mathematical models offering clear guidelines for the rational optimization of devices. The resulting bioelectronics applications, including OMIEC-based microelectrodes and electrochemical transistors, underwent successful testing in both *in-vivo* and *in-vitro* experiments. The quantitative findings

obtained in his work contribute to the development of enhanced organic bioelectronics interfaces, holding the promise to revolutionize future healthcare, biomedicine, biosensing, and neuroscience.

Bibliography

1. Zeglio, E., Rutz, A. L., Winkler, T. E., Malliaras, G. G. & Herland, A. Conjugated Polymers for Assessing and Controlling Biological Functions. *Advanced Materials* **31**, 1806712 (2019).
2. Rivnay, J. & Malliaras, G. G. The Rise of Organic Bioelectronics. (2014) doi:10.1021/cm4022003.
3. Berggren, M. & Richter-Dahlfors, A. Organic bioelectronics. *Advanced Materials* (2007) doi:10.1002/adma.200700419.
4. Owens, R. M. & Malliaras, G. G. Organic Electronics at the Interface with Biology. *MRS Bulletin* **35**, 449–456 (2010).
5. Minett, M. G. & Owen, J. R. Polymeric insertion electrodes. *Solid State Ionics* **28–30**, 1192–1196 (1988).
6. Tan, S. T. M. *et al.* Mixed Ionic–Electronic Conduction, a Multifunctional Property in Organic Conductors. *Advanced Materials* **34**, 2110406 (2022).
7. Paulsen, B. D., Tybrandt, K., Stavrinidou, E. & Rivnay, J. Organic mixed ionic–electronic conductors. *Nature Materials* (2020) doi:10.1038/s41563-019-0435-z.
8. Bolto, B., McNeill, R. & Weiss, D. Electronic Conduction in Polymers. III. Electronic Properties of Polypyrrole. *Aust. J. Chem.* **16**, 1090 (1963).
9. Shirakawa, H., Louis, E. J., MacDiarmid, A. G., Chiang, C. K. & Heeger, A. J. Synthesis of electrically conducting organic polymers: halogen derivatives of polyacetylene, (CH)x. *J. Chem. Soc., Chem. Commun.* 578–580 (1977) doi:10.1039/C39770000578.
10. Wright, P. V. Electrical conductivity in ionic complexes of poly(ethylene oxide). *British Polymer Journal* **7**, 319–327 (1975).
11. Elschner, A., Kirchmeyer, S., Lövenich, W., Merker, U. & Reuter, K. *PEDOT: Principles and Applications of an Intrinsically Conductive Polyme*. (2010). doi:10.1201/b10318.
12. Huang, F., Wu, H. & Cao, Y. Water/alcohol soluble conjugated polymers as highly efficient electron transporting/injection layer in optoelectronic devices. *Chem. Soc. Rev.* **39**, 2500 (2010).
13. Smela, E. Conjugated Polymer Actuators for Biomedical Applications. *Advanced Materials* **15**, 481–494 (2003).

14. Kushida, S. *et al.* Light-Emitting Electrochemical Cells Based on Conjugated Ion Gels. *ACS Appl. Mater. Interfaces* **12**, 38483–38489 (2020).
15. Meng, Q., Cai, K., Chen, Y. & Chen, L. Research progress on conducting polymer based supercapacitor electrode materials. *Nano Energy* **36**, 268–285 (2017).
16. Serafini, M. *et al.* A Wearable Electrochemical Gas Sensor for Ammonia Detection. *Sensors* **21**, 7905 (2021).
17. Khodagholy, D. *et al.* NeuroGrid: Recording action potentials from the surface of the brain. *Nature Neuroscience* (2015) doi:10.1038/nn.3905.
18. Strakosas, X., Seitanidou, M., Tybrandt, K., Berggren, M. & Simon, D. T. An electronic proton-trapping ion pump for selective drug delivery. *Sci Adv* **7**, eabd8738 (2021).
19. Decataldo, F. *et al.* Oxygen Gas Sensing Using a Hydrogel-Based Organic Electrochemical Transistor for Work Safety Applications. *Polymers* **14**, 1022 (2022).
20. van de Burgt, Y. *et al.* A non-volatile organic electrochemical device as a low-voltage artificial synapse for neuromorphic computing. *Nat Mater* **16**, 414–418 (2017).
21. Paulsen, B. D., Fabiano, S. & Rivnay, J. Mixed Ionic-Electronic Transport in Polymers. *Annual Review of Materials Research* **51**, 73–99 (2021).
22. Liu, Y., Duzhko, V. V., Page, Z. A., Emrick, T. & Russell, T. P. Conjugated Polymer Zwitterions: Efficient Interlayer Materials in Organic Electronics. *Acc. Chem. Res.* **49**, 2478–2488 (2016).
23. Volkov, A. V. *et al.* Understanding the Capacitance of PEDOT:PSS. *Advanced Functional Materials* **27**, (2017).
24. Fenoy, G. E., von Bilderling, C., Knoll, W., Azzaroni, O. & Marmisollé, W. A. PEDOT:Tosylate-Polyamine-Based Organic Electrochemical Transistors for High-Performance Bioelectronics. *Advanced Electronic Materials* **7**, 2100059 (2021).
25. Harman, D. G. *et al.* Poly(3,4-ethylenedioxythiophene):dextran sulfate (PEDOT:DS) – A highly processable conductive organic biopolymer. *Acta Biomaterialia* **14**, 33–42 (2015).
26. Andreoli, E., Liao, K.-S., Haldar, A., Alley, N. J. & Curran, S. A. PPy:PSS as alternative to PEDOT:PSS in organic photovoltaics. *Synthetic Metals* **185–186**, 71–78 (2013).
27. Cao, Y., Yu, G., Heeger, A. J. & Yang, C. Y. Efficient, fast response light-emitting electrochemical cells: Electroluminescent and solid electrolyte polymers with interpenetrating network morphology. *Applied Physics Letters* **68**, 3218–3220 (1996).
28. Patel, S. N. *et al.* Morphology and Thermodynamic Properties of a Copolymer with an Electronically Conducting Block: Poly(3-ethylhexylthiophene)-block-poly(ethylene oxide). *Nano Lett.* **12**, 4901–4906 (2012).

29. Moon, H. C. & Kim, J. K. Phase segregation of poly(3-dodecylthiophene)-block-poly(methyl methacrylate) copolymers. *Polymer* **54**, 5437–5442 (2013).
30. Inal, S. *et al.* A High Transconductance Accumulation Mode Electrochemical Transistor. *Advanced Materials* **26**, 7450–7455 (2014).
31. Karlsson, R. H. *et al.* Iron-Catalyzed Polymerization of Alkoxysulfonate-Functionalized 3,4-Ethylenedioxythiophene Gives Water-Soluble Poly(3,4-ethylenedioxythiophene) of High Conductivity. *Chem. Mater.* **21**, 1815–1821 (2009).
32. Savagian, L. R. *et al.* Balancing Charge Storage and Mobility in an Oligo(Ether) Functionalized Dioxythiophene Copolymer for Organic- and Aqueous- Based Electrochemical Devices and Transistors. *Advanced Materials* **30**, 1804647 (2018).
33. Giovannitti, A. *et al.* N-type organic electrochemical transistors with stability in water. *Nat Commun* **7**, 13066 (2016).
34. Javier, A. E., Patel, S. N., Hallinan Jr., D. T., Srinivasan, V. & Balsara, N. P. Simultaneous Electronic and Ionic Conduction in a Block Copolymer: Application in Lithium Battery Electrodes. *Angewandte Chemie International Edition* **50**, 9848–9851 (2011).
35. Wang, Z. & Liu, R. PEDOT:PSS-based electrochromic materials for flexible and stretchable devices. *Materials Today Electronics* **4**, 100036 (2023).
36. Jager, E. W., Smela, E. & Inganas, O. Microfabricating conjugated polymer actuators. *Science* **290**, 1540–1545 (2000).
37. Ling, H. *et al.* Electrolyte-gated transistors for synaptic electronics, neuromorphic computing, and adaptable biointerfacing. *Applied Physics Reviews* (2020) doi:10.1063/1.5122249.
38. Keene, S. T. *et al.* Hole-limited electrochemical doping in conjugated polymers. *Nat. Mater.* 1–7 (2023) doi:10.1038/s41563-023-01601-5.
39. Bonafè, F. *et al.* AC amplification gain in organic electrochemical transistors for impedance-based single cell sensors. *Nat Commun* **13**, 5423 (2022).
40. Zeglio, E. Self-doped Conjugated Polyelectrolytes for Bioelectronics Applications. (2016).
41. Pauling, Linus. THE NATURE OF THE CHEMICAL BOND. APPLICATION OF RESULTS OBTAINED FROM THE QUANTUM MECHANICS AND FROM A THEORY OF PARAMAGNETIC SUSCEPTIBILITY TO THE STRUCTURE OF MOLECULES. *J. Am. Chem. Soc.* **53**, 1367–1400 (1931).
42. Lidberg, R. Time-of-Flight Investigation of Charge Carrier Mobilities in Oligoacene Single Crystals. (2017).

43. Pauling, L. & Brockway, L. O. Carbon—Carbon Bond Distances. The Electron Diffraction Investigation of Ethane, Propane, Isobutane, Neopentane, Cyclopropane, Cyclopentane, Cyclohexane, Allene, Ethylene, Isobutene, Tetramethylethylene, Mesitylene, and Hexamethylbenzene. Revised Values of Covalent Radii. *J. Am. Chem. Soc.* **59**, 1223–1236 (1937).
44. Davies, J. H. *The Physics of Low-Dimensional Semiconductors: An Introduction*. (Cambridge University Press, Cambridge, 1997). doi:10.1017/CBO9780511819070.
45. Peierls, R. E. *Quantum Theory of Solids*. (2007). doi:10.1093/acprof:oso/9780198507819.001.0001.
46. Heydari Gharahcheshmeh, M. & Gleason, K. K. Texture and nanostructural engineering of conjugated conducting and semiconducting polymers. *Materials Today Advances* **8**, 100086 (2020).
47. Maddalena, F., De Falco, C., Caironi, M. & Natali, D. Assessing the width of Gaussian density of states in organic semiconductors. *Organic Electronics* **17**, 304–318 (2015).
48. Heeger, A. J. Nobel lecture: Semiconducting and metallic polymers: The fourth generation of polymeric materials. *Reviews of Modern Physics* **73**, 681–700 (2001).
49. Grundmann, M. *The Physics of Semiconductors: An Introduction Including Nanophysics and Applications*. (Springer International Publishing, Cham, 2016). doi:10.1007/978-3-319-23880-7.
50. Bredas, J. L. & Street, G. B. Polarons, bipolarons, and solitons in conducting polymers. *Acc. Chem. Res.* **18**, 309–315 (1985).
51. Reddinger, J. L. & Reynolds, J. R. Molecular Engineering of π-Conjugated Polymers. in *Radical Polymerisation Polyelectrolytes* (eds. Capek, I. et al.) vol. 145 57–122 (Springer Berlin Heidelberg, Berlin, Heidelberg, 1999).
52. *Handbook of Oligo- and Polythiophenes*. (John Wiley & Sons, Ltd, 1998). doi:10.1002/9783527611713.
53. Salaneck, W. R., Friend, R. H. & Brédas, J. L. Electronic structure of conjugated polymers: consequences of electron–lattice coupling. *Physics Reports* **319**, 231–251 (1999).
54. Heeger, A. J., Kivelson, S., Schrieffer, J. R. & Su, W.-P. Solitons in conducting polymers. *Rev. Mod. Phys.* **60**, 781–850 (1988).
55. Wijeratne, K. Conducting Polymer Electrodes for Thermogalvanic Cells. (2018).
56. Petrucci, R. H., Herring, F. G., Madura, J. D. & Bissonnette, C. General Chemistry: Principles and Modern Applications, 11e.

57. Bardeen, J., Cooper, L. N. & Schrieffer, J. R. Theory of Superconductivity. *Phys. Rev.* **108**, 1175–1204 (1957).
58. Anderson, P. W. Model for the Electronic Structure of Amorphous Semiconductors. *Phys. Rev. Lett.* **34**, 953–955 (1975).
59. Gleason, K. K. *CVD Polymers: Fabrication of Organic Surfaces and Devices*. (John Wiley & Sons, 2015).
60. Muñoz, W. A., Crispin, X., Fahlman, M. & Zozoulenko, I. V. Understanding the Impact of Film Disorder and Local Surface Potential in Ultraviolet Photoelectron Spectroscopy of PEDOT. *Macromolecular Rapid Communications* **39**, 1700533 (2018).
61. Rolland, N., Franco-Gonzalez, J. F., Volpi, R., Linares, M. & Zozoulenko, I. V. Understanding morphology-mobility dependence in PEDOT:Tos. *Phys. Rev. Mater.* **2**, 045605 (2018).
62. Heydari Gharahcheshmeh, M. *et al.* Tuning, optimization, and perovskite solar cell device integration of ultrathin poly(3,4-ethylene dioxythiophene) films via a single-step all-dry process. *Science Advances* **5**, eaay0414 (2019).
63. Collini, E. & Scholes, G. D. Coherent Intrachain Energy Migration in a Conjugated Polymer at Room Temperature. *Science* **323**, 369–373 (2009).
64. Kim, N. *et al.* Role of Interchain Coupling in the Metallic State of Conducting Polymers. *Phys. Rev. Lett.* **109**, 106405 (2012).
65. Wang, S., Ha, M., Manno, M., Daniel Frisbie, C. & Leighton, C. Hopping transport and the Hall effect near the insulator-metal transition in electrochemically gated poly(3-hexylthiophene) transistors. *Nature Communications* (2012) doi:10.1038/ncomms2213.
66. Kunugi, Y., Harima, Y., Yamashita, K., Ohta, N. & Ito, S. Charge transport in a regioregular poly(3-octylthiophene)film. *J. Mater. Chem.* **10**, 2673–2677 (2000).
67. Fratini, S., Nikolka, M., Salleo, A., Schweicher, G. & Sirringhaus, H. Charge transport in high-mobility conjugated polymers and molecular semiconductors. *Nat. Mater.* **19**, 491–502 (2020).
68. Paulsen, B. D. & Frisbie, C. D. Dependence of Conductivity on Charge Density and Electrochemical Potential in Polymer Semiconductors Gated with Ionic Liquids. *J. Phys. Chem. C* **116**, 3132–3141 (2012).
69. Kiefer, D. *et al.* Double doping of conjugated polymers with monomer molecular dopants. *Nature Mater* **18**, 149–155 (2019).
70. Collins, S. D. *et al.* Observing Ion Motion in Conjugated Polyelectrolytes with Kelvin Probe Force Microscopy. *Advanced Electronic Materials* **3**, 1700005 (2017).

71. van Reenen, S., Janssen, R. A. J. & Kemerink, M. Dynamic Processes in Sandwich Polymer Light-Emitting Electrochemical Cells. *Advanced Functional Materials* **22**, 4547–4556 (2012).
72. Matta, M. *et al.* Ion Coordination and Chelation in a Glycolated Polymer Semiconductor: Molecular Dynamics and X-ray Fluorescence Study. *Chem. Mater.* **32**, 7301–7308 (2020).
73. Wieland, M., Dingler, C., Merkle, R., Maier, J. & Ludwigs, S. Humidity-Controlled Water Uptake and Conductivities in Ion and Electron Mixed Conducting Polythiophene Films. *ACS Appl. Mater. Interfaces* **12**, 6742–6751 (2020).
74. Amdursky, N., Głowacki, E. D. & Meredith, P. Macroscale Biomolecular Electronics and Ionics. *Advanced Materials* **31**, 1802221 (2019).
75. Wu, R., Matta, M., Paulsen, B. D. & Rivnay, J. Operando Characterization of Organic Mixed Ionic/Electronic Conducting Materials. *Chem. Rev.* **122**, 4493–4551 (2022).
76. Savva, A. *et al.* Influence of Water on the Performance of Organic Electrochemical Transistors. *Chem. Mater.* **31**, 927–937 (2019).
77. Stavrinidou, E. *et al.* Direct Measurement of Ion Mobility in a Conducting Polymer. *Advanced Materials* **25**, 4488–4493 (2013).
78. Yao, B. *et al.* Ultrahigh-Conductivity Polymer Hydrogels with Arbitrary Structures. *Advanced Materials* **29**, 1700974 (2017).
79. Inal, S., Malliaras, G. G. & Rivnay, J. Benchmarking organic mixed conductors for transistors. *Nat Commun* **8**, 1767 (2017).
80. Bonafè, F. Flexible microelectrode array based on PEDOT:PSS for neural recording and stimulation. *IL NUOVO CIMENTO C* **45**, 1–4 (2022).
81. Mariani, F. *et al.* High-Endurance Long-Term Potentiation in Neuromorphic Organic Electrochemical Transistors by PEDOT:PSS Electrochemical Polymerization on the Gate Electrode. *ACS Appl. Mater. Interfaces* (2023) doi:10.1021/acsami.3c10576.
82. Conjugated Polyelectrolytes: Underexplored Materials for Pseudocapacitive Energy Storage - Quek - 2022 - Advanced Materials - Wiley Online Library. https://onlinelibrary.wiley.com/doi/full/10.1002/adma.202104206.
83. *The IUPAC Compendium of Chemical Terminology: The Gold Book*. (International Union of Pure and Applied Chemistry (IUPAC), Research Triangle Park, NC, 2019). doi:10.1351/goldbook.
84. Trefz, D. *et al.* Electrochemical Investigations of the N-Type Semiconducting Polymer P(NDI2OD-T2) and Its Monomer: New Insights in the Reduction Behavior. *J. Phys. Chem. C* **119**, 22760–22771 (2015).

85. Keene, S. T., Rao, A. & Malliaras, G. G. The relationship between ionic-electronic coupling and transport in organic mixed conductors. *Science Advances* **9**, eadi3536 (2023).
86. Groenendaal, L., Jonas, F., Freitag, D., Pielartzik, H. & Reynolds, J. R. Poly(3,4-ethylenedioxythiophene) and its derivatives: past, present, and future. *Advanced Materials* (2000) doi:10.1002/(SICI)1521-4095(200004)12:7<481::AID-ADMA481>3.0.CO;2-C.
87. Rivnay, J. *et al.* Structural control of mixed ionic and electronic transport in conducting polymers. *Nature Communications* (2016) doi:10.1038/ncomms11287.
88. Martin, D. C. *et al.* The Morphology of Poly(3,4-Ethylenedioxythiophene). *Polymer Reviews* **50**, 340–384 (2010).
89. Cheng, T., Zhang, Y.-Z., Zhang, J.-D., Lai, W.-Y. & Huang, W. High-performance free-standing PEDOT:PSS electrodes for flexible and transparent all-solid-state supercapacitors. *J. Mater. Chem. A* **4**, 10493–10499 (2016).
90. Decataldo, F. *et al.* Organic Electrochemical Transistors as Versatile Tool for Real-Time and Automatized Viral Cytopathic Effect Evaluation. *Viruses* **14**, 1155 (2022).
91. Gualandi, I. *et al.* Organic Electrochemical Transistors as Versatile Analytical Potentiometric Sensors. *Frontiers in Bioengineering and Biotechnology* **7**, (2019).
92. Khodagholy, D. *et al.* High transconductance organic electrochemical transistors. *Nature Communications* **4**, 1–6 (2013).
93. Dimov, I. B., Moser, M., Malliaras, G. G. & McCulloch, I. Semiconducting Polymers for Neural Applications. *Chem. Rev.* **122**, 4356–4396 (2022).
94. Hohnholz, D. & MacDiarmid, A. G. Line patterning of conducting polymers: New horizons for inexpensive, disposable electronic devices. *Synthetic Metals* **121**, 1327–1328 (2001).
95. Krebs, F. C. Fabrication and processing of polymer solar cells: A review of printing and coating techniques. *Solar Energy Materials and Solar Cells* (2009) doi:10.1016/j.solmat.2008.10.004.
96. Valtakari, D. *et al.* Conductivity of PEDOT:PSS on Spin-Coated and Drop Cast Nanofibrillar Cellulose Thin Films. *Nanoscale Research Letters* **10**, 1–10 (2015).
97. Zhou, M., Pagels, M., Geschke, B. & Heinze, J. Electropolymerization of Pyrrole and Electrochemical Study of Polypyrrole. 5. Controlled Electrochemical Synthesis and Solid-State Transition of Well-Defined Polypyrrole Variants. *J. Phys. Chem. B* **106**, 10065–10073 (2002).
98. Cui, X. & Martin, D. C. Electrochemical deposition and characterization of poly(3,4-ethylenedioxythiophene) on neural microelectrode arrays. *Sensors and Actuators B: Chemical* **89**, 92–102 (2003).

99. Lang, U., Naujoks, N. & Dual, J. Mechanical characterization of PEDOT:PSS thin films. *Synthetic Metals* (2009) doi:10.1016/j.synthmet.2008.11.005.

100. Gustafsson, J. C., Liedberg, B. & Inganäs, O. In situ spectroscopic investigations of electrochromism and ion transport in a poly (3,4-ethylenedioxythiophene) electrode in a solid state electrochemical cell. *Solid State Ionics* (1994) doi:10.1016/0167-2738(94)90403-0.

101. Patil, A. O., Heeger, A. J. & Wudl, F. Optical properties of conducting polymers. *Chem. Rev.* **88**, 183–200 (1988).

102. Heuer, H. w., Wehrmann, R. & Kirchmeyer, S. Electrochromic Window Based on Conducting Poly(3,4-ethylenedioxythiophene)–Poly(styrene sulfonate). *Advanced Functional Materials* **12**, 89–94 (2002).

103. Elgrishi, N. *et al.* A Practical Beginner's Guide to Cyclic Voltammetry. *J. Chem. Educ.* **95**, 197–206 (2018).

104. Ghosh, S. & Inganäs, O. Electrochemical Characterization of Poly(3,4-ethylene dioxythiophene) Based Conducting Hydrogel Networks. *J. Electrochem. Soc.* **147**, 1872 (2000).

105. Bonafè, F., Decataldo, F., Fraboni, B. & Cramer, T. Charge Carrier Mobility in Organic Mixed Ionic–Electronic Conductors by the Electrolyte-Gated van der Pauw Method. *Advanced Electronic Materials* 2100086 (2021) doi:10.1002/aelm.202100086.

106. Kim, S.-M. *et al.* Influence of PEDOT:PSS crystallinity and composition on electrochemical transistor performance and long-term stability. *Nat Commun* **9**, 3858 (2018).

107. Ugur, A. *et al.* Low-Dimensional Conduction Mechanisms in Highly Conductive and Transparent Conjugated Polymers. *Advanced Materials* **27**, 4604–4610 (2015).

108. Palumbiny, C. M. *et al.* The Crystallization of PEDOT:PSS Polymeric Electrodes Probed In Situ during Printing. *Advanced Materials* **27**, 3391–3397 (2015).

109. Crispin, X. *et al.* The Origin of the High Conductivity of Poly(3,4-ethylenedioxythiophene)−Poly(styrenesulfonate) (PEDOT−PSS) Plastic Electrodes. *Chem. Mater.* **18**, 4354–4360 (2006).

110. MacDiarmid, A. G. & Epstein, A. J. The concept of secondary doping as applied to polyaniline. *Synthetic Metals* **65**, 103–116 (1994).

111. Zhang, S. *et al.* Solvent-induced changes in PEDOT:PSS films for organic electrochemical transistors. *APL Materials* **3**, 014911 (2014).

112. Ghosh, S. & Inganäs, O. Nano-structured conducting polymer network based on PEDOT-PSS. *Synthetic Metals* **121**, 1321–1322 (2001).

113. Nardes, A. M., Janssen, R. A. J. & Kemerink, M. A Morphological Model for the Solvent-Enhanced Conductivity of PEDOT:PSS Thin Films. *Advanced Functional Materials* **18**, 865–871 (2008).

114. Nardes, A. M. *et al.* Conductivity, work function, and environmental stability of PEDOT:PSS thin films treated with sorbitol. *Organic Electronics* **9**, 727–734 (2008).

115. Piehler, J., Brecht, A., Valiokas, R., Liedberg, B. & Gauglitz, G. A high-density poly(ethylene glycol) polymer brush for immobilization on glass-type surfaces. *Biosensors and Bioelectronics* **15**, 473–481 (2000).

116. Håkansson, A. *et al.* Effect of (3-glycidyloxypropyl)trimethoxysilane (GOPS) on the electrical properties of PEDOT:PSS films. *Journal of Polymer Science Part B: Polymer Physics* **55**, 814–820 (2017).

117. Dickinson, E. J. F. & Wain, A. J. The Butler-Volmer equation in electrochemical theory: Origins, value, and practical application. *Journal of Electroanalytical Chemistry* **872**, 114145 (2020).

118. Feldberg, S. W. Reinterpretation of polypyrrole electrochemistry. Consideration of capacitive currents in redox switching of conducting polymers. *J. Am. Chem. Soc.* **106**, 4671–4674 (1984).

119. Wang, X., Shapiro, B. & Smela, E. Development of a model for charge transport in conjugated polymers. *Journal of Physical Chemistry C* **113**, 382–401 (2009).

120. Kaphle, V., Paudel, P. R., Dahal, D., Radha Krishnan, R. K. & Lüssem, B. Finding the equilibrium of organic electrochemical transistors. *Nature Communications* (2020) doi:10.1038/s41467-020-16252-2.

121. Cucchi, M. *et al.* Thermodynamics of organic electrochemical transistors. *Nat Commun* **13**, 4514 (2022).

122. Tybrandt, K., Zozoulenko, I. V. & Berggren, M. Chemical potential-electric double layer coupling in conjugated polymer-polyelectrolyte blends. *Science Advances* **3**, 1–8 (2017).

123. Lundstrom, M. Fundamentals of Carrier Transport, 2nd edn. *Measurement Science and Technology* (2002) doi:10.1088/0957-0233/13/2/703.

124. Romele, P., Ghittorelli, M., Kovács-Vajna, Z. M. & Torricelli, F. Ion buffering and interface charge enable high performance electronics with organic electrochemical transistors. *Nature Communications* (2019) doi:10.1038/s41467-019-11073-4.

125. Zondaka, Z. *et al.* Optimal phosphotungstinate concentration for polypyrrole linear actuation and energy storage. *Multifunct. Mater.* **1**, 014003 (2018).

126. Huang, L.-M., Hu, C.-W., Peng, C.-Y., Su, C.-H. & Ho, K.-C. Integration of polyelectrolyte based electrochromic material in printable photovoltaic electrochromic module. *Solar Energy Materials and Solar Cells* **145**, 69–75 (2016).

127. Inal, S., Rivnay, J., Suiu, A.-O., Malliaras, G. G. & McCulloch, I. Conjugated Polymers in Bioelectronics. *Acc. Chem. Res.* **51**, 1368–1376 (2018).

128. Simon, D. T., Gabrielsson, E. O., Tybrandt, K. & Berggren, M. Organic Bioelectronics: Bridging the Signaling Gap between Biology and Technology. *Chemical Reviews* (2016) doi:10.1021/acs.chemrev.6b00146.

129. Brittinger, M. & Fromherz, P. Field-effect transistor with recombinant potassium channels: fast and slow response by electrical and chemical interactions. *Appl. Phys. A* **81**, 439–447 (2005).

130. Levin, M., Pezzulo, G. & Finkelstein, J. M. Endogenous Bioelectric Signaling Networks: Exploiting Voltage Gradients for Control of Growth and Form. *Annual Review of Biomedical Engineering* **19**, 353–387 (2017).

131. Prentki, M. *et al.* Rapid mobilization of Ca2+ from rat insulinoma microsomes by inositol-1,4,5-trisphosphate. *Nature* (1984) doi:10.1038/309562a0.

132. Karlsson, P., Farde, L., Halldin, C. & Sedvall, G. PET Study of D1 Dopamine Receptor Binding in Neuroleptic-Naive Patients With Schizophrenia. *AJP* **159**, 761–767 (2002).

133. Hodgkin, A. L. & Huxley, A. F. A quantitative description of membrane current and its application to conduction and excitation in nerve. *The Journal of Physiology* **117**, 500–544 (1952).

134. Liang, Y., Offenhäusser, A., Ingebrandt, S. & Mayer, D. PEDOT:PSS-Based Bioelectronic Devices for Recording and Modulation of Electrophysiological and Biochemical Cell Signals. *Advanced Healthcare Materials* **10**, 2100061 (2021).

135. Ahmari, S. E. & Smith, S. J. Knowing a Nascent Synapse When You See It. *Neuron* **34**, 333–336 (2002).

136. Moon, J.-M., Thapliyal, N., Hussain, K. K., Goyal, R. N. & Shim, Y.-B. Conducting polymer-based electrochemical biosensors for neurotransmitters: A review. *Biosensors and Bioelectronics* **102**, 540–552 (2018).

137. Kandel, E. R., Koester, J. D., Mack, S. H. & Siegelbaum, S. A. Principles of Neural Science, Sixth Edition.

138. Théry, M. *et al.* Anisotropy of cell adhesive microenvironment governs cell internal organization and orientation of polarity. *Proceedings of the National Academy of Sciences* **103**, 19771–19776 (2006).

139. Munesue, S. *et al.* The role of syndecan-2 in regulation of actin-cytoskeletal organization of Lewis lung carcinoma-derived metastatic clones. (2002).

140. Merrill, D. R., Bikson, M. & Jefferys, J. G. R. Electrical stimulation of excitable tissue: Design of efficacious and safe protocols. *Journal of Neuroscience Methods* **141**, 171–198 (2005).

141. Helmholtz, H. Ueber einige Gesetze der Vertheilung elektrischer Ströme in körperlichen Leitern, mit Anwendung auf die thierisch-elektrischen Versuche (Schluss.). *Annalen der Physik* **165**, 353–377 (1853).

142. Grahame, D. C. The Electrical Double Layer and the Theory of Electrocapillarity. *Chem. Rev.* **41**, 441–501 (1947).

143. Ferro, M. D. & Melosh, N. A. Electronic and Ionic Materials for Neurointerfaces. *Advanced Functional Materials* **28**, 1704335 (2018).

144. Bard, A. J., Faulkner, L. R. & White, H. S. *Electrochemical Methods: Fundamentals and Applications*. (John Wiley & Sons, 2022).

145. Conway, B. E. & Pell, W. G. Double-layer and pseudocapacitance types of electrochemical capacitors and their applications to the development of hybrid devices. *J Solid State Electrochem* **7**, 637–644 (2003).

146. Cogan, S. F. Neural Stimulation and Recording Electrodes. *Annual Review of Biomedical Engineering* **10**, 275–309 (2008).

147. Conway, B. E., Birss, V. & Wojtowicz, J. The role and utilization of pseudocapacitance for energy storage by supercapacitors. *Journal of Power Sources* **66**, 1–14 (1997).

148. Silbey, R. J., Alberty, R. A., Papadantonakis, G. A. & Bawendi, M. G. *Physical Chemistry*. (John Wiley & Sons, 2022).

149. Decataldo, F. *et al.* Stretchable Low Impedance Electrodes for Bioelectronic Recording from Small Peripheral Nerves. *Sci Rep* **9**, 10598 (2019).

150. Modarresi, M., Mehandzhiyski, A., Fahlman, M., Tybrandt, K. & Zozoulenko, I. Microscopic Understanding of the Granular Structure and the Swelling of PEDOT:PSS. *Macromolecules* **53**, 6267–6278 (2020).

151. Jones, P. D. *et al.* Low-Impedance 3D PEDOT:PSS Ultramicroelectrodes. *Frontiers in Neuroscience* **14**, (2020).

152. Giovannitti, A. *et al.* Energetic Control of Redox-Active Polymers toward Safe Organic Bioelectronic Materials. *Advanced Materials* **32**, 1–9 (2020).

153. Bettinger, C. J. Recent advances in materials and flexible electronics for peripheral nerve interfaces. *Bioelectronic Medicine* **4**, 6 (2018).

154. Anderson, J. M., Rodriguez, A. & Chang, D. T. Foreign body reaction to biomaterials. *Seminars in Immunology* **20**, 86–100 (2008).

155. Wellman, S. M. & Kozai, T. D. Y. Understanding the Inflammatory Tissue Reaction to Brain Implants To Improve Neurochemical Sensing Performance. *ACS Chem. Neurosci.* **8**, 2578–2582 (2017).

156. Root, S. E., Savagatrup, S., Printz, A. D., Rodriquez, D. & Lipomi, D. J. Mechanical Properties of Organic Semiconductors for Stretchable, Highly Flexible, and Mechanically Robust Electronics. *Chem. Rev.* **117**, 6467–6499 (2017).

157. Sommer, M. 2 - Development of conjugated polymers for organic flexible electronics. in *Organic Flexible Electronics* (eds. Cosseddu, P. & Caironi, M.) 27–70 (Woodhead Publishing, 2021). doi:10.1016/B978-0-12-818890-3.00002-3.

158. Wang, Y. *et al.* A highly stretchable, transparent, and conductive polymer. *Science Advances* (2017) doi:10.1126/sciadv.1602076.

159. von Erlach, T. C. *et al.* Cell-geometry-dependent changes in plasma membrane order direct stem cell signalling and fate. *Nature Mater* **17**, 237–242 (2018).

160. Kim, Y. *et al.* A strong regioregularity effect in self-organizing conjugated polymer films and high-efficiency polythiophene:fullerene solar cells. *Nature Mater* **5**, 197–203 (2006).

161. Tessarolo, M., Gualandi, I. & Fraboni, B. Recent Progress in Wearable Fully Textile Chemical Sensors. *Advanced Materials Technologies* **3**, 1700310 (2018).

162. Mandal, S. *et al.* Fully-printed, all-polymer, bendable and highly transparent complementary logic circuits. *Organic Electronics* **20**, 132–141 (2015).

163. Land, K. J., Boeras, D. I., Chen, X.-S., Ramsay, A. R. & Peeling, R. W. REASSURED diagnostics to inform disease control strategies, strengthen health systems and improve patient outcomes. *Nat Microbiol* **4**, 46–54 (2019).

164. Chortos, A. Extrusion 3D printing of conjugated polymers. *Journal of Polymer Science* **60**, 486–503 (2022).

165. Liu, Y. *et al.* Soft and elastic hydrogel-based microelectronics for localized low-voltage neuromodulation. *Nat Biomed Eng* **3**, 58–68 (2019).

166. Wang, W. *et al.* Inflight fiber printing toward array and 3D optoelectronic and sensing architectures. *Science Advances* **6**, eaba0931 (2020).

167. Li, Z. *et al.* Self-Healing Hydrogel Bioelectronics. *Advanced Materials* **n/a**, 2306350.

168. Gunbas, G. & Toppare, L. Electrochromic conjugated polyheterocycles and derivatives—highlights from the last decade towards realization of long lived aspirations. *Chem. Commun.* **48**, 1083–1101 (2012).

169. Zainudeen, U. L., Careem, M. A. & Skaarup, S. PEDOT and PPy conducting polymer bilayer and trilayer actuators. *Sensors and Actuators B: Chemical* **134**, 467–470 (2008).

170. Mariani, F. *et al.* Microscopic Determination of Carrier Density and Mobility in Working Organic Electrochemical Transistors. *Small* (2019) doi:10.1002/smll.201902534.

171. Berto, M. *et al.* EGOFET Peptide Aptasensor for Label-Free Detection of Inflammatory Cytokines in Complex Fluids. *Advanced Biosystems* **2**, 1700072 (2018).

172. Rivnay, J., Wang, H., Fenno, L., Deisseroth, K. & Malliaras, G. G. Next-generation probes, particles, and proteins for neural interfacing. *Sci. Adv.* **3**, e1601649 (2017).

173. Decataldo, F. <1992>. Semiconducting Polymers for Electronic Biosensors and Biological Interfaces. (Alma Mater Studiorum - Università di Bologna, 2020). doi:10.6092/unibo/amsdottorato/9344.

174. Cox-Pridmore, D. M., Castro, F. A., Silva, S. R. P., Camelliti, P. & Zhao, Y. Emerging Bioelectronic Strategies for Cardiovascular Tissue Engineering and Implantation. *Small* **18**, 2105281 (2022).

175. Braendlein, M., Lonjaret, T., Leleux, P., Badier, J.-M. & Malliaras, G. G. Voltage Amplifier Based on Organic Electrochemical Transistor. *Advanced Science* **4**, 1600247 (2017).

176. Neurological Disorders | Disease Control Priorities, Third Edition (Volume 4): Mental, Neurological, and Substance Use Disorders. *Disease Control Priorities* (2023) doi:10.1596/978-1-4648-0426-7_ch5.

177. Deep-Brain Stimulation of the Subthalamic Nucleus or the Pars Interna of the Globus Pallidus in Parkinson's Disease. *New England Journal of Medicine* **345**, 956–963 (2001).

178. Ondo, W., Jankovic, J., Schwartz, K., Almaguer, M. & Simpson, R. K. Unilateral thalamic deep brain stimulation for refractory essential tremor and Parkinson's disease tremor. *Neurology* **51**, 1063–1069 (1998).

179. Greenberg, B. D. *et al.* Three-year outcomes in deep brain stimulation for highly resistant obsessive-compulsive disorder. *Neuropsychopharmacology* **31**, 2384–2393 (2006).

180. Mayberg, H. S. *et al.* Deep Brain Stimulation for Treatment-Resistant Depression. *Neuron* **45**, 651–660 (2005).

181. Bouton, C. E. *et al.* Restoring cortical control of functional movement in a human with quadriplegia. *Nature* **533**, 247–250 (2016).

182. Lorach, H. *et al.* Walking naturally after spinal cord injury using a brain–spine interface. *Nature* **618**, 126–133 (2023).

183. Hong, G. & Lieber, C. M. Novel electrode technologies for neural recordings. *Nature Reviews Neuroscience* **20**, 330–345 (2019).

184. Harris, K. D., Quiroga, R. Q., Freeman, J. & Smith, S. L. Improving data quality in neuronal population recordings. *Nat Neurosci* **19**, 1165–1174 (2016).

185. Kajikawa, Y. & Schroeder, C. E. How Local Is the Local Field Potential? *Neuron* **72**, 847–858 (2011).

186. Bédard, C., Kröger, H. & Destexhe, A. Modeling Extracellular Field Potentials and the Frequency-Filtering Properties of Extracellular Space. *Biophysical Journal* **86**, 1829–1842 (2004).

187. Buzsáki, G., Anastassiou, C. A. & Koch, C. The origin of extracellular fields and currents — EEG, ECoG, LFP and spikes. *Nat Rev Neurosci* **13**, 407–420 (2012).

188. Buzsáki, G. Theta Oscillations in the Hippocampus. *Neuron* **33**, 325–340 (2002).

189. Agarwal, G. *et al.* Spatially Distributed Local Fields in the Hippocampus Encode Rat Position. *Science* **344**, 626–630 (2014).

190. Rattay, F. *et al.* Mechanisms of Electrical Stimulation with Neural Prostheses. *Neuromodulation: Technology at the Neural Interface* **6**, 42–56 (2003).

191. Guidelines to Study and Develop Soft Electrode Systems for Neural Stimulation. *Neuron* **108**, 238–258 (2020).

192. McIntyre, C. C. & Grill, W. M. Selective Microstimulation of Central Nervous System Neurons. *Annals of Biomedical Engineering* **28**, 219–233 (2000).

193. Fang, Z.-P. & Mortimer, J. T. Selective activation of small motor axons by quasitrapezoidal current pulses. *IEEE Transactions on Biomedical Engineering* **38**, 168–174 (1991).

194. McIntyre, C. C. & Grill, W. M. Extracellular Stimulation of Central Neurons: Influence of Stimulus Waveform and Frequency on Neuronal Output. *Journal of Neurophysiology* **88**, 1592–1604 (2002).

195. Cogan, S. F., Ludwig, K. A., Welle, C. G. & Takmakov, P. Tissue damage thresholds during therapeutic electrical stimulation. *J. Neural Eng.* **13**, 021001 (2016).

196. Shannon, R. V. A model of safe levels for electrical stimulation. *IEEE Transactions on Biomedical Engineering* **39**, 424–426 (1992).

197. Bianchi, M. *et al.* Poly(3,4-ethylenedioxythiophene)-Based Neural Interfaces for Recording and Stimulation: Fundamental Aspects and In Vivo Applications. *Advanced Science* **9**, 2104701 (2022).

198. Ramantani, G. *et al.* Simultaneous subdural and scalp EEG correlates of frontal lobe epileptic sources. *Epilepsia* **55**, 278–288 (2014).

199. Hefft, S. *et al.* Safety of Hybrid Electrodes for Single-Neuron Recordings in Humans. *Neurosurgery* **73**, 78 (2013).

200. Song, E., Li, J., Won, S. M., Bai, W. & Rogers, J. A. Materials for flexible bioelectronic systems as chronic neural interfaces. *Nat. Mater.* **19**, 590–603 (2020).

201. Ball, T., Kern, M., Mutschler, I., Aertsen, A. & Schulze-Bonhage, A. Signal quality of simultaneously recorded invasive and non-invasive EEG. *NeuroImage* **46**, 708–716 (2009).

202. Thakor, N. V. Translating the Brain-Machine Interface. *Science Translational Medicine* **5**, 210ps17-210ps17 (2013).

203. Miller, J. F. *et al.* Neural Activity in Human Hippocampal Formation Reveals the Spatial Context of Retrieved Memories. *Science* **342**, 1111–1114 (2013).

204. Rousche, P. J. & Normann, R. A. Chronic recording capability of the Utah Intracortical Electrode Array in cat sensory cortex. *Journal of Neuroscience Methods* **82**, 1–15 (1998).

205. Dai, X., Zhou, W., Gao, T., Liu, J. & Lieber, C. M. Three-dimensional mapping and regulation of action potential propagation in nanoelectronics-innervated tissues. *Nature Nanotech* **11**, 776–782 (2016).

206. Montgomery, K. L. *et al.* Wirelessly powered, fully internal optogenetics for brain, spinal and peripheral circuits in mice. *Nat Methods* **12**, 969–974 (2015).

207. Boys, A. J. *et al.* 3D Bioelectronics with a Remodellable Matrix for Long-Term Tissue Integration and Recording. *Advanced Materials* **35**, 2207847 (2023).

208. Minev, I. R. *et al.* Electronic dura mater for long-term multimodal neural interfaces. *Science* **347**, 159–163 (2015).

209. Luan, L. *et al.* Ultraflexible nanoelectronic probes form reliable, glial scar–free neural integration. *Science Advances* **3**, e1601966 (2017).

210. Rochford, A. E., Carnicer-Lombarte, A., Curto, V. F., Malliaras, G. G. & Barone, D. G. When Bio Meets Technology: Biohybrid Neural Interfaces. *Advanced Materials* **32**, 1903182 (2020).

211. Liang, Q. *et al.* Electron Conductive and Transparent Hydrogels for Recording Brain Neural Signals and Neuromodulation. *Advanced Materials* **35**, 2211159 (2023).

212. Cea, C. *et al.* Integrated internal ion-gated organic electrochemical transistors for stand-alone conformable bioelectronics. *Nat. Mater.* **22**, 1227–1235 (2023).

213. Strakosas, X. *et al.* Metabolite-induced in vivo fabrication of substrate-free organic bioelectronics. *Science* **379**, 795–802 (2023).

214. Fromherz, P. Joining microelectronics and microionics: Nerve cells and brain tissue on semiconductor chips. *Solid-State Electronics* **52**, 1364–1373 (2008).

215. Hutzler, M. & Fromherz, P. Silicon chip with capacitors and transistors for interfacing organotypic brain slice of rat hippocampus. *European Journal of Neuroscience* **19**, 2231–2238 (2004).

216. Viventi, J. *et al.* Flexible, foldable, actively multiplexed, high-density electrode array for mapping brain activity in vivo. *Nat Neurosci* **14**, 1599–1605 (2011).

217. Kittlesen, G. P., White, H. S. & Wrighton, M. S. Chemical derivatization of microelectrode arrays by oxidation of pyrrole and N-methylpyrrole: fabrication of molecule-based electronic devices. *J. Am. Chem. Soc.* **106**, 7389–7396 (1984).

218. Khodagholy, D. *et al.* In vivo recordings of brain activity using organic transistors. *Nat Commun* **4**, 1575 (2013).

219. Rivnay, J. *et al.* Organic electrochemical transistors. *Nature Reviews Materials* (2018) doi:10.1038/natrevmats.2017.86.

220. Strakosas, X., Wei, B., Martin, D. C. & Owens, R. M. Biofunctionalization of polydioxythiophene derivatives for biomedical applications. *J. Mater. Chem. B* **4**, 4952–4968 (2016).

221. Braendlein, M. *et al.* Lactate Detection in Tumor Cell Cultures Using Organic Transistor Circuits. *Advanced Materials* **29**, 1605744 (2017).

222. Hutter, P. C., Rothlander, T., Scheipl, G. & Stadlober, B. All Screen-Printed Logic Gates Based on Organic Electrochemical Transistors. *IEEE Trans. Electron Devices* **62**, 4231–4236 (2015).

223. Huang, W. *et al.* Vertical organic electrochemical transistors for complementary circuits. *Nature* **613**, 496–502 (2023).

224. Friedlein, J. T., McLeod, R. R. & Rivnay, J. Device physics of organic electrochemical transistors. *Organic Electronics* **63**, 398–414 (2018).

225. Bernards, D. A. & Malliaras, G. G. Steady-state and transient behavior of organic electrochemical transistors. *Advanced Functional Materials* (2007) doi:10.1002/adfm.200601239.

226. Sakurai, T. & Newton, A. R. A simple MOSFET model for circuit analysis. *IEEE Transactions on Electron Devices* **38**, 887–894 (1991).

227. Nielsen, C. B. *et al.* Molecular Design of Semiconducting Polymers for High-Performance Organic Electrochemical Transistors. *J Am Chem Soc* **138**, 10252–10259 (2016).

228. Macchia, E. *et al.* About the amplification factors in organic bioelectronic sensors. *Mater. Horiz.* **7**, 999–1013 (2020).

229. Donahue, M. J. *et al.* High-Performance Vertical Organic Electrochemical Transistors. *Advanced Materials* **30**, 1–5 (2018).

230. Rivnay, J. *et al.* High-performance transistors for bioelectronics through tuning of channel thickness. *Science Advances* **1**, 1–5 (2015).

231. MOSFETs. in *Physics of Semiconductor Devices* 293–373 (John Wiley & Sons, Ltd, 2006). doi:10.1002/9780470068328.ch6.

232. Sun, H. *et al.* Complementary Logic Circuits Based on High-Performance n-Type Organic Electrochemical Transistors. *Advanced Materials* **30**, 1704916 (2018).

233. Cicoira, F. *et al.* Influence of Device Geometry on Sensor Characteristics of Planar Organic Electrochemical Transistors. *Advanced Materials* **22**, 1012–1016 (2010).

234. Koutsouras, D. A., Torricelli, F., Gkoupidenis, P. & Blom, P. W. M. Efficient Gating of Organic Electrochemical Transistors with In-Plane Gate Electrodes. *Advanced Materials Technologies* **n/a**, 2100732.

235. Bernards, D. A. *et al.* Enzymatic sensing with organic electrochemical transistors. *J. Mater. Chem.* **18**, 116–120 (2007).

236. Friedlein, J. T., Donahue, M. J., Shaheen, S. E., Malliaras, G. G. & McLeod, R. R. Microsecond Response in Organic Electrochemical Transistors: Exceeding the Ionic Speed Limit. *Advanced Materials* **28**, 8398–8404 (2016).

237. Campana, A., Cramer, T., Simon, D. T., Berggren, M. & Biscarini, F. Electrocardiographic recording with conformable organic electrochemical transistor fabricated on resorbable bioscaffold. *Advanced Materials* (2014) doi:10.1002/adma.201400263.

238. Faria, G. C., Duong, D. T. & Salleo, A. On the transient response of organic electrochemical transistors. *Organic Electronics* **45**, 215–221 (2017).

239. Drieschner, S. *et al.* Frequency response of electrolyte-gated graphene electrodes and transistors. *J. Phys. D: Appl. Phys.* **50**, 095304 (2017).

240. Paulsen, B. D., Tybrandt, K., Stavrinidou, E. & Rivnay, J. Organic mixed ionic–electronic conductors. *Nat. Mater.* **19**, 13–26 (2020).

241. Rolin, C. *et al.* Charge carrier mobility in thin films of organic semiconductors by the gated van der Pauw method. *Nature Communications* **8**, (2017).

242. Friedlein, J. T. *et al.* Influence of disorder on transfer characteristics of organic electrochemical transistors. *Applied Physics Letters* (2017) doi:10.1063/1.4993776.

243. Bihar, E. *et al.* A Disposable paper breathalyzer with an alcohol sensing organic electrochemical transistor. *Scientific Reports* (2016) doi:10.1038/srep27582.

244. Paterson, A. F. *et al.* On the Role of Contact Resistance and Electrode Modification in Organic Electrochemical Transistors. *Advanced Materials* (2019) doi:10.1002/adma.201902291.

245. Kaphle, V., Liu, S., Al-Shadeedi, A., Keum, C.-M. & Lüssem, B. Contact Resistance Effects in Highly Doped Organic Electrochemical Transistors. *Advanced Materials* **28**, 8766–8770 (2016).

246. Liu, C. *et al.* Device Physics of Contact Issues for the Overestimation and Underestimation of Carrier Mobility in Field-Effect Transistors. *Physical Review Applied* (2017) doi:10.1103/PhysRevApplied.8.034020.

247. Van Der Pauw, L. A method of measuring resistivity and Hall effect of lamellae of arbitrary shape. *Philips Tech Rev* (1958).

248. Jiang, S. *et al.* Probing Coulomb Interactions on Charge Transport in Few-Layer Organic Crystalline Semiconductors by the Gated van der Pauw Method. *Advanced Electronic Materials* (2020) doi:10.1002/aelm.202000136.

249. Wang, S., Ha, M., Manno, M., Daniel Frisbie, C. & Leighton, C. Hopping transport and the Hall effect near the insulator–metal transition in electrochemically gated poly(3-hexylthiophene) transistors. *Nat Commun* **3**, 1210 (2012).

250. Nawaz, A., Liu, Q., Leong, W. L., Fairfull-Smith, K. E. & Sonar, P. Organic Electrochemical Transistors for In Vivo Bioelectronics. *Advanced Materials* **33**, 2101874 (2021).

251. Lee, W. *et al.* Integration of Organic Electrochemical and Field-Effect Transistors for Ultraflexible, High Temporal Resolution Electrophysiology Arrays. *Advanced Materials* **28**, 9722–9728 (2016).

252. Lee, W. *et al.* Transparent, conformable, active multielectrode array using organic electrochemical transistors. *Proc Natl Acad Sci USA* **114**, 10554–10559 (2017).

253. Diacci, C. *et al.* Diurnal in vivo xylem sap glucose and sucrose monitoring using implantable organic electrochemical transistor sensors. *iScience* **24**, 101966 (2021).

254. Fu, Y. *et al. Ultrasensitive Detection of RNA Biomarkers Using Portable Sensing Platforms Based on Organic Electrochemical Transistors*. https://papers.ssrn.com/abstract=3813281 (2021) doi:10.2139/ssrn.3813281.

255. Yu, J. *et al.* Highly sensitive detection of caspase-3 activity based on peptide-modified organic electrochemical transistor biosensors. *Nanoscale* **13**, 2868–2874 (2021).

256. Macchia, E. *et al.* Ultra-sensitive protein detection with organic electrochemical transistors printed on plastic substrates. *Flex. Print. Electron.* **3**, 034002 (2018).

257. Decataldo, F. *et al.* Organic Electrochemical Transistors: Smart Devices for Real-Time Monitoring of Cellular Vitality. *Advanced Materials Technologies* **4**, 1900207 (2019).

258. Khalili, A. A. & Ahmad, M. R. A Review of Cell Adhesion Studies for Biomedical and Biological Applications. *International Journal of Molecular Sciences* **16**, 18149–18184 (2015).

259. Lasky, L. A. *et al.* An endothelial ligand for L-selectin is a novel mucin-like molecule. *Cell* **69**, 927–938 (1992).

260. Okegawa, T., Pong, R.-C., Li, Y. & Hsieh, J.-T. The role of cell adhesion molecule in cancer progression and its application in cancer therapy. *Acta Biochim Pol* **51**, 445–457 (2004).

261. Perinpanayagam, H. *et al.* Early cell adhesion events differ between osteoporotic and non-osteoporotic osteoblasts. *J Orthop Res* **19**, 993–1000 (2001).

262. Simon, S. I. & Green, C. E. Molecular mechanics and dynamics of leukocyte recruitment during inflammation. *Annu Rev Biomed Eng* **7**, 151–185 (2005).

263. Lekka, M., Gnanachandran, K., Kubiak, A., Zieliński, T. & Zemła, J. Traction force microscopy – Measuring the forces exerted by cells. *Micron* **150**, 103138 (2021).

264. Gómez-González, M., Latorre, E., Arroyo, M. & Trepat, X. Measuring mechanical stress in living tissues. *Nat Rev Phys* **2**, 300–317 (2020).

265. Helenius, J., Heisenberg, C.-P., Gaub, H. E. & Muller, D. J. Single-cell force spectroscopy. *Journal of Cell Science* **121**, 1785–1791 (2008).

266. Castelain, M., Rouxhet, P. G., Pignon, F., Magnin, A. & Piau, J.-M. Single-cell adhesion probed in-situ using optical tweezers: A case study with Saccharomyces cerevisiae. *Journal of Applied Physics* **111**, 114701 (2012).

267. Ito, H. & Kaneko, M. On-chip cell manipulation and applications to deformability measurements. *ROBOMECH Journal* **7**, 3 (2020).

268. Tang, Z. *et al.* Shear stress-dependent cell detachment from temperature-responsive cell culture surfaces in a microfluidic device. *Biomaterials* **33**, 7405–7411 (2012).

269. Janshoff, A. *et al.* Cell Adhesion Monitoring Using Substrate-Integrated Sensors. *Journal of Adhesion Science and Technology* **24**, 2079–2104 (2010).

270. Faria, G. C. *et al.* Organic electrochemical transistors as impedance biosensors. *MRS Communications* **4**, 189–194 (2014).

271. Lieberth, K. *et al.* Current-Driven Organic Electrochemical Transistors for Monitoring Cell Layer Integrity with Enhanced Sensitivity. *Advanced Healthcare Materials* **10**, 2100845 (2021).

272. Rivnay, J. *et al.* Organic electrochemical transistors for cell-based impedance sensing. *Applied Physics Letters* **106**, (2015).

273. Shah, P., Zhu, X., Zhang, X., He, J. & Li, C. Microelectromechanical System-Based Sensing Arrays for Comparative in Vitro Nanotoxicity Assessment at Single Cell and Small Cell-Population Using Electrochemical Impedance Spectroscopy. *ACS Appl. Mater. Interfaces* **8**, 5804–5812 (2016).

274. Wu, Z. & Lin, L. Nanofluidics for single-cell analysis. 8.

275. Hempel, F. *et al.* PEDOT:PSS organic electrochemical transistors for electrical cell-substrate impedance sensing down to single cells. *Biosensors and Bioelectronics* **180**, 113101–113101 (2021).

276. Zahn, R., Vörös, J. & Zambelli, T. Swelling of electrochemically active polyelectrolyte multilayers. *Current Opinion in Colloid & Interface Science* **15**, 427–434 (2010).

277. Zhu, X., Hu, Y., Wu, G., Chen, W. & Bao, N. Two-Dimensional Nanosheets-Based Soft Electro-Chemo-Mechanical Actuators: Recent Advances in Design, Construction, and Applications. *ACS Nano* **15**, 9273–9298 (2021).

278. Yamada, M. *et al.* Photomobile Polymer Materials: Towards Light-Driven Plastic Motors. *Angewandte Chemie International Edition* **47**, 4986–4988 (2008).

279. Hu, F., Xue, Y., Xu, J. & Lu, B. PEDOT-Based Conducting Polymer Actuators. *Frontiers in Robotics and AI* **6**, (2019).

280. Smela, E. & Gadegaard, N. Volume Change in Polypyrrole Studied by Atomic Force Microscopy. *J. Phys. Chem. B* **105**, 9395–9405 (2001).

281. Smela, E. & Gadegaard, N. Surprising Volume Change in PPy(DBS): An Atomic Force Microscopy Study. *Advanced Materials* **11**, 953–957 (1999).

282. Yan, B., Wu, Y. & Guo, L. Recent Advances on Polypyrrole Electroactuators. *Polymers* **9**, 446 (2017).

283. Posey, F. A. & Morozumi, T. Theory of Potentiostatic and Galvanostatic Charging of the Double Layer in Porous Electrodes. *J. Electrochem. Soc.* **113**, 176 (1966).

284. Otero, T. F. & Boyano, I. Comparative Study of Conducting Polymers by the ESCR Model. *J. Phys. Chem. B* **107**, 6730–6738 (2003).

285. Smela, E. Conjugated polymer actuators. *MRS Bulletin* (2008) doi:10.1557/mrs2008.45.

286. Chang, L. *et al.* Ionic Electroactive Polymers Used in Bionic Robots: A Review. *J Bionic Eng* **15**, 765–782 (2018).

287. Zahn, R., Vörös, J. & Zambelli, T. Tuning the electrochemical swelling of polyelectrolyte multilayers toward nanoactuation. *Langmuir* **30**, 12057–12066 (2014).

288. Maia, G., Torresi, R. M., Ticianelli, E. A. & Nart, F. C. Charge Compensation Dynamics in the Redox Processes of Polypyrrole-Modified Electrodes. *J. Phys. Chem.* **100**, 15910–15916 (1996).

289. Temmer, R. *et al.* In search of better electroactive polymer actuator materials: PPy versus PEDOT versus PEDOT–PPy composites. *Smart Mater. Struct.* **22**, 104006 (2013).

290. Melling, D., Martinez, J. G. & Jager, E. W. H. Conjugated Polymer Actuators and Devices: Progress and Opportunities. *Advanced Materials* **31**, 1808210 (2019).

291. Savva, A., Wustoni, S. & Inal, S. Ionic-to-electronic coupling efficiency in PEDOT:PSS films operated in aqueous electrolytes. *J. Mater. Chem. C* **6**, 12023–12030 (2018).

292. Wu, R., Paulsen, B. D., Ma, Q. & Rivnay, J. Mass and Charge Transport Kinetics in an Organic Mixed Ionic–Electronic Conductor. *Chem. Mater.* **34**, 9699–9710 (2022).

293. Wang, X. & Smela, E. Color and volume change in PPy(DBS). *Journal of Physical Chemistry C* (2009) doi:10.1021/jp802937v.

294. Ghodbane, O., Ataherian, F., Wu, N.-L. & Favier, F. In situ crystallographic investigations of charge storage mechanisms in MnO2-based electrochemical capacitors. *Journal of Power Sources* **206**, 454–462 (2012).

295. Prehal, C. *et al.* A carbon nanopore model to quantify structure and kinetics of ion electrosorption with in situ small-angle X-ray scattering. *Phys. Chem. Chem. Phys.* **19**, 15549–15561 (2017).

296. Lyu, D. *et al.* Operando NMR electrochemical gating studies of ion dynamics in PEDOT:PSS. *Nat. Mater.* **22**, 746–753 (2023).

297. Li, Y. *et al.* Stretchable Zn-Ion Hybrid Battery with Reconfigurable V2CTx and Ti3C2Tx MXene Electrodes as a Magnetically Actuated Soft Robot. *Advanced Energy Materials* **11**, 2101862 (2021).

298. Chen, J. & Lee, P. S. Electrochemical Supercapacitors: From Mechanism Understanding to Multifunctional Applications. *Advanced Energy Materials* **11**, 2003311 (2021).

299. Black, J. M. *et al.* Strain-Based In Situ Study of Anion and Cation Insertion into Porous Carbon Electrodes with Different Pore Sizes. *Advanced Energy Materials* **4**, 1300683 (2014).

300. Fonner, J. M. *et al.* Biocompatibility implications of polypyrrole synthesis techniques. *Biomed. Mater.* **3**, 034124 (2008).

301. Higgins, M. J., McGovern, S. T. & Wallace, G. G. Visualizing Dynamic Actuation of Ultrathin Polypyrrole Films. *Langmuir* **25**, 3627–3633 (2009).

302. Amorini, F. *et al.* Electrically Controlled 'Sponge Effect' of PEDOT:PSS Governs Membrane Potential and Cellular Growth. *ACS Appl Mater Interfaces* **9**, 6679–6689 (2017).

303. Giridharagopal, R. *et al.* Electrochemical strain microscopy probes morphology-induced variations in ion uptake and performance in organic electrochemical transistors. *Nature Mater* **16**, 737–742 (2017).

304. Deng, Q. *et al.* Progress and prospective of electrochemical actuator materials. *Composites Part A: Applied Science and Manufacturing* **165**, 107336 (2023).

305. Baughman, R. H. Conducting polymer artificial muscles. *Synthetic Metals* **78**, 339–353 (1996).

306. Pei, Q., Inganas, O. & Lundstrom, I. Bending bilayer strips built from polyaniline for artificial electrochemical muscles. *Smart Mater. Struct.* **2**, 1 (1993).

307. Shoa, T., Madden, J. D., Munce, N. R. & Yang, V. Analytical modeling of a conducting polymer-driven catheter. *Polymer International* **59**, 343–351 (2010).

308. Jager, E. W., Smela, E. & Inganas, O. Microfabricating conjugated polymer actuators. *Science* **290**, 1540–1545 (2000).

309. Smela, E., Inganäs, O. & Lundström, I. Controlled Folding of Micrometer-Size Structures. *Science* **268**, 1735–1738 (1995).

310. Hiraoka, M. *et al.* Miniature conductive polymer actuators for high pressure generation in lab on chip systems. *Sensors and Actuators A: Physical* **177**, 23–29 (2012).

311. Löffler, S., Libberton, B. & Richter-Dahlfors, A. Organic Bioelectronic Tools for Biomedical Applications. *Electronics* **4**, 879–908 (2015).

312. Jager, E. W. H., Inganäs, O. & Lundström, I. Microrobots for Micrometer-Size Objects in Aqueous Media: Potential Tools for Single-Cell Manipulation. *Science* **288**, 2335–2338 (2000).

313. Sharma, M., Waterhouse, G. I. N., Loader, S. W. C., Garg, S. & Svirskis, D. High surface area polypyrrole scaffolds for tunable drug delivery. *International Journal of Pharmaceutics* **443**, 163–168 (2013).

314. Abidian, M. R., Kim, D.-H. & Martin, D. C. Conducting-Polymer Nanotubes for Controlled Drug Release. *Advanced Materials* **18**, 405–409 (2006).

315. Jiang, S. *et al.* Enhanced drug loading capacity of polypyrrole nanowire network for controlled drug release. *Synthetic Metals* **163**, 19–23 (2013).

316. Valdés-Ramírez, G. *et al.* Multiplexed and switchable release of distinct fluids from microneedle platforms via conducting polymer nanoactuators for potential drug delivery. *Sensors and Actuators B: Chemical* **161**, 1018–1024 (2012).

317. Park, S., Kang, Y. J. & Majd, S. A Review of Patterned Organic Bioelectronic Materials and their Biomedical Applications. *Advanced Materials* **27**, 7583–7619 (2015).

318. Emslie, A. G., Bonner, F. T. & Peck, L. G. Flow of a Viscous Liquid on a Rotating Disk. *Journal of Applied Physics* **29**, 858–862 (2004).

319. Verdi, M. <1995>. Hybrid lead-halide perovskites as novel materials for thin film direct and flexible ionizing radiation detectors. (Alma Mater Studiorum - Università di Bologna, 2023). doi:10.48676/unibo/amsdottorato/10690.

320. Charlot, B. *et al.* Micropatterning PEDOT:PSS layers. *Microsystem Technologies* **19**, 895–903 (2013).

321. Hickling, A. Studies in electrode polarisation. Part IV.—The automatic control of the potential of a working electrode. *Trans. Faraday Soc.* **38**, 27–33 (1942).

322. Wang, S. *et al.* Electrochemical impedance spectroscopy. *Nat Rev Methods Primers* **1**, 41 (2021).

323. Marti, O., Drake, B. & Hansma, P. K. Atomic force microscopy of liquid-covered surfaces: Atomic resolution images. *Applied Physics Letters* **51**, 484–486 (1987).

324. Mironov, V. *Fundamentals of Scanning Probe Microscopy*. (2014).

325. García, R., Magerle, R. & Perez, R. Nanoscale compositional mapping with gentle forces. *Nat Mater* **6**, 405–411 (2007).

326. Lyubchenko, Y. L. AFM Imaging in Liquid of DNA and Protein–DNA Complexes. in *Atomic Force Microscopy in Liquid* 231–258 (John Wiley & Sons, Ltd, 2012). doi:10.1002/9783527649808.ch9.

327. Phosphate-buffered saline (PBS). *Cold Spring Harb Protoc* **2006**, pdb.rec8247 (2006).

328. Koon, D. W., Bahl, A. A. & Duncan, E. O. Measurement of contact placement errors in the van der Pauw technique. *Review of Scientific Instruments* **60**, 275–276 (1989).

329. Bernards, D. A. & Malliaras, G. G. Steady-state and transient behavior of organic electrochemical transistors. *Advanced Functional Materials* (2007) doi:10.1002/adfm.200601239.

330. Volkov, A. V. *et al.* Understanding the Capacitance of PEDOT:PSS. *Advanced Functional Materials* **27**, (2017).

331. Proctor, C. M., Rivnay, J. & Malliaras, G. G. Understanding volumetric capacitance in conducting polymers. *Journal of Polymer Science, Part B: Polymer Physics* **54**, 1433–1436 (2016).

332. van der Pauw, L. J. A method of measuring the resistivity and Hall coefficient on lamellae of arbitrary shape. *Philips Technical Review* Preprint at (1958).

333. Rivnay, J. *et al.* High-performance transistors for bioelectronics through tuning of channel thickness. *Science Advances* **1**, 1–5 (2015).

334. Mariani, F. *et al.* Microscopic Determination of Carrier Density and Mobility in Working Organic Electrochemical Transistors. *Small* (2019) doi:10.1002/smll.201902534.

335. Arkhipov, V. I., Heremans, P., Emelianova, E. V., Adriaenssens, G. J. & Bässler, H. Charge carrier mobility in doped semiconducting polymers. *Applied Physics Letters* (2003) doi:10.1063/1.1572965.

336. Yamashita, M., Otani, C., Okuzaki, H. & Shimizu, M. Nondestructive measurement of carrier mobility in conductive polymer PEDOT:PSS using terahertz and infrared spectroscopy. in *2011 30th URSI General Assembly and Scientific Symposium, URSIGASS 2011* (2011). doi:10.1109/URSIGASS.2011.6050616.

337. Liu, C. *et al.* Device Physics of Contact Issues for the Overestimation and Underestimation of Carrier Mobility in Field-Effect Transistors. *Physical Review Applied* (2017) doi:10.1103/PhysRevApplied.8.034020.

338. Uemura, T. *et al.* On the Extraction of Charge Carrier Mobility in High-Mobility Organic Transistors. *Advanced Materials* (2016) doi:10.1002/adma.201503133.

339. Kaphle, V., Liu, S., Al-Shadeedi, A., Keum, C.-M. & Lüssem, B. Contact Resistance Effects in Highly Doped Organic Electrochemical Transistors. *Advanced Materials* **28**, 8766–8770 (2016).

340. Kaphle, V., Paudel, P. R., Dahal, D., Radha Krishnan, R. K. & Lüssem, B. Finding the equilibrium of organic electrochemical transistors. *Nature Communications* (2020) doi:10.1038/s41467-020-16252-2.

341. Nikolou, M. & Malliaras, G. G. Applications of poly (3,4-ethylenedioxythiophene) doped with poly(styrene sulfonic acid) transistors in chemical and biological sensors. *Chemical Record* (2008) doi:10.1002/tcr.20133.

342. Braun, S., Salaneck, W. R. & Fahlman, M. Energy-level alignment at organic/metal and organic/organic interfaces. *Advanced Materials* (2009) doi:10.1002/adma.200802893.

343. Groenendaal, L., Jonas, F., Freitag, D., Pielartzik, H. & Reynolds, J. R. Poly(3,4-ethylenedioxythiophene) and its derivatives: past, present, and future. *Advanced Materials* (2000) doi:10.1002/(SICI)1521-4095(200004)12:7<481::AID-ADMA481>3.0.CO;2-C.

344. Friedlein, J. T. *et al.* Influence of disorder on transfer characteristics of organic electrochemical transistors. *Applied Physics Letters* (2017) doi:10.1063/1.4993776.

345. Rolin, C. *et al.* Charge carrier mobility in thin films of organic semiconductors by the gated van der Pauw method. *Nature Communications* **8**, (2017).

346. Tsuno, M. *et al.* Physically-based threshold voltage determination for MOSFET's of all gate lengths. *IEEE Transactions on Electron Devices* (1999) doi:10.1109/16.772487.

347. Pesavento, P. V., Chesterfield, R. J., Newman, C. R. & Frisble, C. D. Gated four-probe measurements on pentacene thin-film transistors: Contact resistance as a function of gate voltage and temperature. *Journal of Applied Physics* (2004) doi:10.1063/1.1806533.

348. Bonafè, F., Decataldo, F., Cramer, T. & Fraboni, B. Ionic Solvent Shell Drives Electroactuation in Organic Mixed Ionic-Electronic Conductors. *Advanced Science* **n/a**, 2308746.

349. Zhanshayeva, L., Favaron, V. & Lubineau, G. Macroscopic Modeling of Water Uptake Behavior of PEDOT:PSS Films. *ACS Omega* **4**, 21883–21890 (2019).

350. O'M. B., J. Review: Ionic hydration in chemistry and biophysics, by B. E. Conway, Elsevier Publishing Company, 1981. *J Solution Chem* **11**, 221–222 (1982).

351. Isaksson, J. *et al.* Electronic control of Ca2+ signalling in neuronal cells using an organic electronic ion pump. *Nature Mater* **6**, 673–679 (2007).

352. Paasch, G., Micka, K. & Gersdorf, P. Theory of the electrochemical impedance of macrohomogeneous porous electrodes. *Electrochimica Acta* **38**, 2653–2662 (1993).

353. Proctor, C. M., Rivnay, J. & Malliaras, G. G. Understanding volumetric capacitance in conducting polymers. *Journal of Polymer Science, Part B: Polymer Physics* **54**, 1433–1436 (2016).

354. de Levie, R. On porous electrodes in electrolyte solutions: I. Capacitance effects. *Electrochimica Acta* **8**, 751–780 (1963).

355. Conway, B. E. Ionic hydration in chemistry and biophysics. (1981).

356. Zhang, Z. *et al.* Capturing the swelling of solid-electrolyte interphase in lithium metal batteries. *Science* **375**, 66–70 (2022).

357. Snook, G. A., Kao, P. & Best, A. S. Conducting-polymer-based supercapacitor devices and electrodes. *Journal of Power Sources* **196**, 1–12 (2011).

358. Xie, K. *et al.* Delamination and Wrinkling of Flexible Conductive Polymer Thin Films. *Advanced Functional Materials* **31**, 2009039 (2021).

359. Time-Constant Dispersion. in *Electrochemical Impedance Spectroscopy* 233–263 (John Wiley & Sons, Ltd, 2008). doi:10.1002/9780470381588.ch13.

360. Monclus, M. A., Young, T. J. & Di Maio, D. AFM indentation method used for elastic modulus characterization of interfaces and thin layers. *J Mater Sci* **45**, 3190–3197 (2010).

361. Spinks, G. m., Liu, L., Wallace, G. g. & Zhou, D. Strain Response from Polypyrrole Actuators under Load. *Advanced Functional Materials* **12**, 437–440 (2002).

362. Wang, N., Liu, Y., Fu, Y. & Yan, F. AC Measurements Using Organic Electrochemical Transistors for Accurate Sensing. *ACS Applied Materials and Interfaces* **10**, 25834–25840 (2018).

363. Faria, G. C., Duong, D. T. & Salleo, A. On the transient response of organic electrochemical transistors. *Organic Electronics* **45**, 215–221 (2017).

364. Tybrandt, K., Zozoulenko, I. V. & Berggren, M. Chemical potential-electric double layer coupling in conjugated polymer-polyelectrolyte blends. *Science Advances* **3**, (2017).

365. Khodagholy, D. *et al.* High transconductance organic electrochemical transistors. *Nature Communications* (2013) doi:10.1038/ncomms3133.

366. Kalluri, R. Basement membranes: structure, assembly and role in tumour angiogenesis. *Nat Rev Cancer* **3**, 422–433 (2003).

367. Deshmukh, M. A., Jeon, J.-Y. & Ha, T.-J. Carbon nanotubes: An effective platform for biomedical electronics. *Biosensors and Bioelectronics* **150**, 111919 (2020).

368. Peña-Bahamonde, J., Nguyen, H. N., Fanourakis, S. K. & Rodrigues, D. F. Recent advances in graphene-based biosensor technology with applications in life sciences. *J Nanobiotechnol* **16**, 75 (2018).

369. Amorini, F. *et al.* Electrically Controlled “Sponge Effect” of PEDOT:PSS Governs Membrane Potential and Cellular Growth. *ACS Appl. Mater. Interfaces* **9**, 6679–6689 (2017).

370. Koutsouras, D. A. *et al.* Impedance Spectroscopy of Spin-Cast and Electrochemically Deposited PEDOT:PSS Films on Microfabricated Electrodes with Various Areas. *ChemElectroChem* **4**, 2321–2327 (2017).

Acknowledgments

The completion of this thesis concludes a three-year journey full of stimulating and rewarding experiences. This work has been possible thanks to the unlimited support of those I have worked and lived with in these years.

First, I thank my supervisor Prof. Beatrice Fraboni for her guidance during this period. She always supported my work with her leadership and advice, but also left me free of experimenting, while helping me to stay on the right track. I also thank her for the great work environment she has created in the "Semiconductor Physics Group", making it a place where you can really feel at home.

I thank Tobias, my co-supervisor, mentor and inexhaustible source of suggestions, scientific discussions, and ideas; he was the brain, and I was the "brawn" for most of the work you can read in these pages. I thank Francesco, who accompanied me throughout the initial phase of my PhD and remains a precious collaborator and friend, always ready to assist me with his enthusiasm and passion.

I thank all the scientific collaborators I have worked with during these years. I thank Isabella Zironi from Prof. Daniel Remondini's group for her work with cells during the development of *in-vitro* bioelectronic sensors. I thank the research group of Prof. Roberto Amici and Matteo Cerri from the Department of Biomedical and Neuromotor Sciences of the University of Bologna, in particular Timna and Emiliana, for their competent and passionate work on animal surgery for *in-vivo* electrocorticography experiments. I acknowledge the group of Prof. Erika Scavetta from the Department of Industrial Chemistry of the University of Bologna for the strong and fruitful collaboration regarding electrochemical sensors and neuromorphic devices based on organic electrochemical transistors. I finally want to express my gratitude to Prof. George Malliaras for hosting me for a six-month internship at his Bioelectronics Laboratory in Cambridge. That experience gave me the opportunity to work in a high-level and exciting research environment. A big thank to Chaoqun Dong for her supervision and fruitful collaboration on electrochemical actuators based on polypyrrole. Our challenging project taught me that perseverance is the key to achieve great results.

I thank my colleagues with whom I've shared my time in the Department over these years. I thank the "Original DIFA" friends Matteo (Green), Giovanni, Luca Pos., Ilaria, and Alberto. You helped me to face my PhD adventure with your example of work attitude, you helped me with my lab sufferings, we had great times in and outside the lab. I thank Lorenzo, Pierpaolo, and Jonathan, who accompanied me on the long journey from the Bachelor to the end of the PhD. I thank the "New DIFA" friends Lufa, Lia, Camilla, Irene, Marco, Luca B., Matteo (Marke), Sara, Aleksandra for sharing lab time, lunch breaks, but also aperitives, dinners,

parties, and other beautiful moments together. I thank postdocs and researchers in the Semiconductor Group including Vito, Andrea, and Laura for their constant support. Last, but not least, I thank all the students who worked in the lab with me during their Bachelor/Master thesis preparation, including Caja, Giacomo, Chiara, Hong, Marco, and Riccardo.

I thank Antonio, Margaux, Atharva, Cate, Luigi, Tugce, Ana, and all the other friends from the Bioelectronic Laboratory. You made my life in Cambridge a special experience I will never forget.

I thank my long-term friends Giulia and Alex, Francesco and Francesca, and the "barbecue heroes group" Daniele, Enrico, Alessandro, Bugo, Vittorio, and Samuele for all the beautiful moments spent together. I thank the huge "Summer Vacation Group" from Florence for our beautiful holidays around Italy and Europe in minivan. I thank Mattia, Lif, and Elisa for the winter expeditions of "intense" skiing.

I thank "my" woods and mountains in Monghidoro, the magnificent peaks in Dolomites, the green grasslands of England, the endless hills in Andalucia, the shiny water of the West Coast that I would have never bet on being able to see. Thanks to these experiences I felt alive, and I found new energies and motivations.

Ringrazio infine la mia famiglia per avermi dato tutto. Ringrazio la mia mamma, alla quale dedico questa tesi. Ringrazio mio papà, gli zii, i nonni, mio cugino Federico. Ogni singola parola in questo lungo ed "incompresibile" documento è scritta grazie a voi. Ringrazio Loretta, Marino, Mattia. Ringrazio Elisa, per tutto quello che è stato, che è, che sarà. Infinitamente grato a tutti voi.